이학박사 학위논문

Dynamics and Modeling of Thermally and Orographically Forced Flows and Convection

열과 산악이 유도하는 흐름과 대류의 역학 및 모델링

2018 년 2 월

서울대학교 대학원

지구환경과학부

서 재 명

Dynamics and Modeling of Thermally and Orographically Forced Flows and Convection

By

Jaemyeong Mango Seo

A Dissertation Submitted to the Faculty of the Graduate School of Seoul National University in Partial Fulfillment of the Requirements for the Degree of Doctor of Philosophy

February 2018

Advisory Committee:

Professor Seok-Woo Son, Chair

Professor Jong-Jin Baik, Advisor

Professor Sungsu Park

Professor Jae Gyoo Lee

Doctor Young-San Park

Abstract

Many big cities around the world are located near the mountains. In city-mountain regions, thermally and topographically forced local winds are produced and they affect the transport of pollutants emitted into the urban atmosphere. A better understanding of the dynamics of thermally and topographically forced local winds is necessary to improve the prediction of local winds and to cope with environmental problems. In this study, the interactions of urban breezes with mountain slope winds in the presence of basic-state wind are theoretically examined within the context of the response of a stably stratified atmosphere to prescribed thermal and mechanical forcing. The interactions between urban breezes and mountain slope winds are viewed through the linear superposition of individual analytical solutions for urban thermal forcing, mountain thermal forcing, and mountain mechanical forcing. A setting in which a city is located downwind of a mountain is considered. In the nighttime, in the mountain-side urban area, surface/near-surface horizontal flows induced by mountain cooling and mountain mechanical forcing cooperatively interact with urban breezes, resulting in strengthened winds. In the daytime, in the urban area, surface/near-surface horizontal flows induced by mountain heating are opposed to urban breezes, giving rise to weakened winds. It is shown that the degree to which urban breezes and mountain slope winds interact is sensitive to the mountain height and the basic-state wind speed. Particularly, a change in the basic-state wind speed affects not only the strength of thermally and mechanically induced flows (internal gravity waves) but also their vertical wavelengths and decay rates. The examination of a case in a setting in which a city is located upwind of a mountain reveals that the direction

of basic-state wind significantly affects the interactions between urban breezes and mountain slope winds.

The urban breeze circulation (UBC) is a thermally forced mesoscale circulation characterized by low-level inward flows toward the urban center, updrafts near the urban center, upper-level outward flows, and weak downdrafts outside the urban area. Previous numerical modeling studies indicate that in the early morning the direction of the UBC can be reversed. Here, the dynamics of a reversed UBC is studied in the context of the response of the atmosphere to a specified thermal forcing, which represents the diurnally varying urban heating. For this, linearized, two-dimensional, hydrostatic, and Boussinesq airflow system in a rotating frame with a specified thermal forcing is solved using the Fourier transform method. The occurrence of a reversed UBC in the early morning is confirmed. The Coriolis parameter affects the strength and vertical structure of the UBC, whose role is similar to that of the coefficient of Rayleigh friction and Newtonian cooling. The occurrence condition, strength, and vertical structure of a reversed UBC are examined. The Coriolis force as well as urban heating alters the occurrence time of the reversed UBC. For a strongly viscous system, a reversed UBC occurs only in high latitudes with low occurrence possibility. A simple oscillation-type model for the horizontal velocity is constructed to get some dynamical insights into a reversed UBC. The analysis results also show that the Coriolis force alters the occurrence time of the reversed UBC.

Dynamical aspects of flows forced by either convective heating or a mountain have been extensively studied, but those forced by both convective heating and a mountain have been less studied. Here, we theoretically examine the orographic-

convective flows, gravity-wave reflection, and gravity-wave momentum fluxes in stably stratified two-layer hydrostatic and nonhydrostatic atmospheres. The upper layer (stratosphere) has a larger static stability than the lower layer (troposphere), and the basic-state wind has a constant shear in the troposphere and is uniform in the stratosphere. The equations governing small-amplitude perturbations in a two-dimensional, steady-state, and nonrotating system in the presence of orographic forcing and convective forcing are analytically solved. Then, the analytic solutions are analyzed to understand how orographically and convectively forced flows vary with changes in the basic-state wind speed, stratospheric static stability, and the location of the convection relative to the mountain.

In a two-layer hydrostatic atmosphere, over the upslope of the mountain, the convectively forced deep upward motion is positively combined with the orographic uplift, thus giving rise to enhanced upward motions there. The ratio of the convectively forced vertical velocity to the orographically forced vertical velocity at the cloud base height over an upslope location of the mountain is analyzed to further understand the linear interaction between orographically and convectively forced flows. The gravity-wave reflection at the tropopause plays an important role in orographic-convective flows. The gravity-wave reflection at the tropopause acts to amplify the symmetric (anti-symmetric) structure of orographically (convectively) forced waves. The vertical fluxes of the horizontal momentum are analytically obtained. The total momentum flux contains the component resulting from the nonlinear interaction between orographically and convectively forced waves. It is found that the nonlinear interaction component can be as

important as each of the orographic and convective components in the total momentum flux depending on the location of the convection relative to the mountain.

A nondimensional governing equation system including the Rayleigh friction and the Newtonian cooling is considered to theoretically investigate the nonhydrostatic effects on convectively forced flows in a single layer nonhydrostatic atmosphere. The nondimensionalized airflow system contains the nonhydrostaticity factor β (= U/Na, where U is the basic-state wind speed, a is the half-width of the convective forcing, and N is the basic-state buoyancy frequency). In an inviscid-limit system, the solutions for vertical velocity are classified into the propagating mode ($k \leq \beta^{-1}$, where k is the nondimensional horizontal wavenumber) and the evanescent mode ($k > \beta^{-1}$). As β increases, an alternating wavy pattern of updrafts and downdrafts appears downstream of the convective forcing with a horizontal wavelength of $2\pi\beta$ corresponding to the critical horizontal wavenumber $k_c = \beta^{-1}$. The momentum flux analysis shows that the alternating updrafts and downdrafts are almost horizontally propagating gravity waves of the propagating mode whose k is slightly smaller than k_c and that these gravity waves strengthen the momentum flux above the convective forcing. In a viscid system, the solution for vertical velocity has propagating and decaying components simultaneously such that they cannot be explicitly separated. Here, the propagating mode and two evanescent modes are defined by comparing the magnitudes of the vertical wavenumber and decay rate. For large viscous coefficient, the k-range of the propagating mode becomes narrow and the alternating updrafts and downdrafts dissipate. As β increases, the propagating mode, which strengthens the momentum flux above the convective forcing, effectively dissipates even with small viscous coefficient.

In a two-layer nonhydrostatic atmosphere, the wave components form modified Bessel functions of the purely imaginary order. The wave components in the stratosphere are sinusoidal or exponential depending on the horizontal wave number, tropospheric basic-state wind shear, and stratospheric static stability. Resonant waves corresponding to the horizontal wavelength of the zeros of the denominator of the solution are nonhydrostatically generated downstream of the convective forcing. Without stratospheric stability jump, the horizontal wavelengths of resonant waves are the zeros of $K_{i\mu}(\xi_0)$. Relatively short waves are trapped at a certain height because the wave behavior changes from sinusoidal to exponential. Most of the resonant waves are in the range of the sinusoidal asymptotic of the modified Bessel function. Using that fact, the wavelengths of resonant waves in the case of Ri = 9, 36, and 144 are approximated. Stratospheric stability jump conditionally reflects totally or partially and transmits the resonant waves. Relatively short waves are totally trapped in the troposphere by the gravity-wave reflection and the window is broader in the case with stronger wind shear. The transmitted resonant waves vertically propagate in the stratosphere and transport wave energy.

Aerosol effects on orographic precipitation from shallow and deep convective clouds over mountains with different windward-widths are numerically studied using the Weather Research and Forecasting model which includes a bin microphysics scheme. Forced uplift by a mountain in a potentially unstable atmosphere results in cellular-type convective orographic clouds.

In the cases with shallow and warm clouds, more cloud droplets are produced under higher aerosol number concentration. As a result, the growth of cloud droplets into

raindrops is inhibited, the total and maximum precipitation amounts decrease, and the maximum precipitation occurs downstream. In addition, stronger convection is generated because of stronger condensational heat release, and more liquid drops of small sizes are distributed in a deeper layer. In the case of narrower windward-width, compared to the case with symmetric mountain, the steeper upslope generates stronger convection with a shorter advection time scale, hence stronger precipitation is concentrated over a narrower area. Accordingly, the aerosol effects, which result in a decrease in the total precipitation amount and a downstream shift of the location of the maximum precipitation, are clearer here than in the cases with the symmetric mountain. In the case with a wider windward-width, the gentler upslope generates a weaker convection, while a large portion of liquid drops precipitate over the wide upslope with a long-enough advection time scale. The orographic precipitation amount and the location of its maximum are more sensitive to the aerosol number concentration when the mountain upslope is steeper.

In the cases with deep and mixed-phase clouds, orographic precipitation occurs mainly from lower-level clouds and its dependency on the aerosol number concentration and upslope steepness is similar to that in the case with shallow and warm convective clouds in the early stage. As time goes on, lower-level convective clouds vigorously develop and an upper-level mixed-phase cloud extends upstream depending on the case, and strong interactions between lower- and upper-level clouds result in strong precipitation via melting or direct sedimentation of ice-phased particles if both conditions are satisfied. The mixed-phase processes (freezing, WBF process, and riming) during the interaction is stronger in the case of higher aerosol number concentration, resulting in enhanced surface precipitation on the symmetric mountain. In the cases with asymmetric

mountains, the trends are not monotonic. In the case with steep upslope, the liquid drop growth is slower compared to the clean case and the condensational latent heating is weaker compared to the polluted case, and these characteristics inhibit the interaction between lower- and higher-level clouds and the mixed-phase processes result in the minimal surface precipitation amount in the control case. In the case with a gentle upslope, on the other hand, stronger condensational heating than the clean case and faster growth of liquid drops than the polluted case enhance the interaction between lower- and higher-level clouds and the mixed-phase processes result in the maximal surface precipitation amount in the control case.

A real orographic precipitation event over the Taebaek Mountains from 26 to 27 June 2015 with three different aerosol number concentrations is numerically simulated to examine aerosol effects on real orographic precipitation. Near Sokcho, orographic clouds are warm-phased. In this region, an increase in aerosol number concentration results in the increased cloud droplet mixing ratio and the decreased raindrop mixing ratio. However, the change of the surface precipitation amount is not monotonic. Both the increased raindrop mixing ratio in the clean case and the decreased cloud droplet mixing ratio in the polluted case result in enhanced surface precipitation. Near Mt. Kumgang, ice particles in the upper-level cloud play an important role in controlling the surface precipitation amount. In this region, the increase in aerosol number concentration results in the increased surface precipitation amount through the increase the ice-phased particle mixing ratio.

Keywords: stably stratified atmosphere, urban breeze circulation, orographic-convective

flows, gravity-wave momentum fluxes, aerosol-cloud-precipitation interaction, orographic precipitation

Student Number: 2009-20371

Contents

List of Figures

List of Tables

1 Overview

To examine various atmospheric phenomena, we conceptually simplify the system into a mathematically expressible frame. Mathematically expressed atmospheric systems are widely used to fundamentally and systematically understand atmospheric phenomena. Many atmospheric processes are driven by external forcings. Topography of the Earth's surface mechanically perturbs atmospheric movements. Spatial and temporal variations of thermal forcings also initiate atmospheric phenomena. The urban breeze circulation (UBC) is a characteristic local circulation which originates from the thermal imbalance between urban and rural areas. A city near or on a mountainous region is influenced by the mechanical forcing of the mountains and the thermal forcing from the mountains and the urban area. In Chapter 2, the interactions between urban breezes and mountain slope winds in the presence of basic-state wind are examined. The circulation direction of UBC can be reversed in a rotating frame. Detailed dynamics of the reversed UBC is provided in Chapter 3.

Another well examined thermal forcing is latent heat released from clouds. This heating originates from the condensation, freezing and sublimation of the hydrometeors in clouds. To represent a flow forced by latent heating from convective clouds, many studies include a finite-depth diabatic heating function in the thermodynamic energy equation as an external thermal forcing. The orographic rainfall related system can be represented as an atmosphere influenced by the mechanical forcing of mountain and the thermal forcing from a convective thermal heating. Chapter 4 provides dynamics related to orographically and convectively forced flows in a two-layer hydrostatic atmosphere. In

Chapter 5, nonhydrostatic effects of the convectively forced flows in a uniformly stratified atmosphere with constant basic-state wind speed are theoretically examined. Chapter 6 extends the study in Chapter 5 to orographic-convective flows and waves in a two-layer nonhydrostatic atmosphere.

The mathematically expressed atmospheric system is also used to numerically simulate complicated atmospheric phenomena which have too many causality factors and are difficult to simplify. Cloud microphysics is one of the important but conceptually complicating processes. Because of the computational scarcity, cloud microphysics tends to be over-simplified. The bin microphysics method is a realistic method to represent detailed microphysical processes involved in precipitation events; however, the detailed study of orographic precipitation using the bin microphysics is still at an early stage due to the excessive computational needs. As an extended study of the theoretical study of orographic-convective flows, we numerically simulate an orographic-convective precipitation from clouds. Chapter 7 and Chapter 8 discuss the orographic precipitation from shallow-warm convection and from deep and mixed-phase convection, respectively. Finally, a real simulation study of orographic precipitation over The Taebaek Mountains with different aerosol number concentrations is provided in Chapter 9 to re-visit our findings of Chapter 7 and Chapter 8. The main results of this study are summarized in Chapter 10.

2 Dynamics of interactions between urban breezes and mountain slope winds in the presence of basic-state wind

2.1 Introduction

Many interesting thermally or mechanically driven local-wind phenomena are observed in the atmosphere, including urban breezes, land/sea breezes, mountain/valley winds, severe downslope storms, etc. Over the past few decades, these local-wind phenomena have been extensively studied and substantial progress in understanding the basic dynamics of each local-wind phenomenon has been made [see references in Simpson (1994), Lin (2007), and Markowski and Richardson (2010)]. In many regions of the world, local-wind systems interact with each other. The degree of interactions between local-wind systems differs depending on location, time of day, etc. For example, daytime urban breezes interact with sea breezes in and around coastal/inland cities and the degree of the interactions differs depending on many factors, such as sea surface temperature, city size, urban heat island intensity, and time of day (e.g., Yoshikado 1992; Freitas et al. 2007; Ryu and Baik 2013). Understanding the dynamics of interactions between local-wind systems is one of the important issues in mesoscale dynamics and helps to cope with environmental problems with which big cities located near mountains or in complex terrain or adjacent to seas are faced. Fernando (2010) reviewed the fluid dynamics of mesoscale urban airflows in complex terrain.

Thermally or mechanically driven winds/flows can be theoretically investigated from the viewpoint of the response of a stably stratified atmosphere to prescribed thermal or mechanical forcing. From this angle, extensive theoretical studies, particularly focusing on mountain waves or convectively forced flows, have been performed to better understand thermally or mechanically driven winds/flows (e.g., Queney 1948; Smith 1980; Lin 1987; Song and Chun 2005). The interactions between mountain waves and convectively forced flows with application to the dynamics of orographic rain are well described in a theoretical study of Smith and Lin (1982).

Recently, Ganbat et al. (2015b) theoretically examined the interactions of urban breezes with mountain slope winds in the absence of basic-state wind. When there is no basic-state wind, mountains cannot mechanically induce mountain waves in a stably stratified atmosphere. Hence, mountain slope winds are produced only by mountain thermal forcing (mountain heating in the daytime and mountain cooling in the nighttime). In this study, we extend our previous study by including basic-state wind and mountain mechanical forcing and further examine the interactions of urban breezes with mountain slope winds. The sensitivities of the interactions to mountain mechanical forcing and basic-state wind speed are also investigated. In this study, mountain slope winds are produced by both mountain thermal forcing and mountain mechanical forcing. In section 2.2, governing equations and solutions are provided. In section 2.3, values of parameters for calculations are provided. In section 2.4, calculation results are presented and discussed.

2.2 Governing equations and analytic solutions

In this study, a two-dimensional, hydrostatic, nonrotating, Boussinesq airflow system in the presence of thermal forcing and topography is considered. Linearized equations in the presence of uniform basic-state horizontal wind can be expressed as follows (Lin 2007; Ganbat et al. 2015b):

$$\frac{\partial u}{\partial t} + U\frac{\partial u}{\partial x} = -\frac{\partial \pi}{\partial x} - \nu u, \tag{2.1}$$

$$\frac{\partial \pi}{\partial z} = b, \tag{2.2}$$

$$\frac{\partial b}{\partial t} + U\frac{\partial b}{\partial x} + N^2 w = \frac{g}{c_p T_0} q - \nu b, \tag{2.3}$$

$$\frac{\partial u}{\partial x} + \frac{\partial w}{\partial z} = 0. \tag{2.4}$$

Here, u is the perturbation velocity in the x-direction, w is the perturbation vertical velocity in the z-direction, π is the perturbation kinematic pressure, and b is the perturbation buoyancy. U is the basic-state wind speed in the x-direction, N is the buoyancy frequency (constant in this study), g is the gravitational acceleration, c_p is the specific heat of air at constant pressure, T_0 is the reference temperature, and ν is the coefficient of Rayleigh friction and Newtonian cooling. q in Eq. (2.3) represents thermal forcing (heating or cooling) and is specified as

$$q(x,z,t) = q_0 \frac{a_q^{\,2}}{(x-c_q)^2 + a_q^{\,2}} e^{-z/H} \,\mathrm{Re}\{e^{i\Omega t}\}. \tag{2.5}$$

Here, q_0 is the magnitude of the thermal forcing, a_q is the half-width of the bell-shaped function, c_q is the horizontal location of the center of the thermal forcing, and H is the e-folding depth of the thermal forcing. Ω is the angular frequency of the diurnal variation. A bell-shaped mountain is considered in this study, which is given by

$$h(x) = h_m \frac{a_h^{\,2}}{(x-c_h)^2 + a_h^{\,2}}, \tag{2.6}$$

where h_m is the maximum mountain height, a_h is the half-width of the bell-shaped mountain, and c_h is the horizontal location of the mountain center. A bell-shaped function is widely used in theoretical studies to represent thermal forcing and mountain shape (e.g., Queney 1948; Smith and Lin 1982; Baik 1992) because it imitates real heating/cooling and an isolated mountain well and the Fourier transform of the bell-shaped function is mathematically simple.

Eqs. (2.1)–(2.4) can be combined to yield a single equation for the perturbation vertical velocity.

$$\left(\frac{\partial}{\partial t} + U\frac{\partial}{\partial x} + \nu\right)^2 \frac{\partial^2 w}{\partial z^2} + N^2 \frac{\partial^2 w}{\partial x^2} = \frac{g}{c_p T_0} \frac{\partial^2 q}{\partial x^2}. \tag{2.7}$$

Eq. (2.7) is Fourier-transformed in x ($\rightarrow k$) and t ($\rightarrow \omega$) to get

$$\frac{d^2\hat{w}}{dz^2} + N^2\lambda^2\hat{w} = \frac{g}{c_p T_0}\lambda^2\hat{q}, \tag{2.8}$$

where

$$\lambda = \frac{k}{(\omega + Uk) - i\nu},$$

$$\hat{q}(k, z, \omega) = q_0 a_q e^{-ic_q k} e^{-a_q k} e^{-z/H} \frac{\delta(\omega - \Omega) + \delta(\omega + \Omega)}{2}.$$

Here, δ is the delta function. The solution of Eq. (2.8) is obtained by imposing an upper radiation condition ($U > 0$ in this study so that $B = 0$) and a lower boundary condition of $\hat{w} = ikU\hat{h}$ at z = 0.

$$\hat{w}(k, z, \omega) = ikU\hat{h}e^{iN\lambda z} + C\frac{\lambda^2}{1 + N^2\lambda^2 H^2} e^{-ic_q k} e^{-a_q k} \frac{\delta(\omega - \Omega) + \delta(\omega + \Omega)}{2}\left(e^{-z/H} - e^{iN\lambda z}\right), \tag{2.9}$$

where

$$\hat{h}(k, \omega) = h_m a_h e^{-ic_h k} e^{-a_h k}\delta(\omega),$$

$$C = \frac{g}{c_p T_0} q_0 a_q H^2.$$

Time-invariant property of $h(x)$ is represented by $\delta(\omega)$ in wavenumber-frequency space.

The first term on the right-hand side of Eq. (2.9) represents the perturbation vertical velocity in the wavenumber-frequency space induced by the mountain mechanical forcing. The second term on the right-hand side of Eq. (2.9) represents the perturbation vertical velocity in the wavenumber-frequency space induced by the thermal forcing. To obtain the solution for the perturbation vertical velocity in physical space, the inverse Fourier transform in k ($\rightarrow x$) and ω ($\rightarrow t$) upon Eq. (2.9) is performed and then the real part is taken.

$$
\begin{aligned}
w(x,z,t) = &-Uh_{\mathrm{m}}a_{\mathrm{h}}\int_0^{\infty} ke^{-a_{\mathrm{h}}k}e^{-\gamma_0 z}\sin[k(x-c_{\mathrm{h}})+m_0 z]\,dk \\
&+\frac{C}{2}\int_0^{\infty} k^2 e^{-a_{\mathrm{q}}k}\Big\langle X_{\mathrm{R}}\left\{e^{-z/H}\cos[k(x-c_{\mathrm{q}})+\Omega t]-e^{-\gamma z}\cos[k(x-c_{\mathrm{q}})+mz+\Omega t]\right\} \\
&\qquad -X_{\mathrm{I}}\left\{e^{-z/H}\sin[k(x-c_{\mathrm{q}})+\Omega t]-e^{-\gamma z}\sin[k(x-c_{\mathrm{q}})+mz+\Omega t]\right\} \\
&\qquad +X_{\mathrm{R}}'\left\{e^{-z/H}\cos[k(x-c_{\mathrm{q}})-\Omega t]-e^{-\gamma' z}\cos[k(x-c_{\mathrm{q}})+m'z-\Omega t]\right\} \\
&\qquad -X_{\mathrm{I}}'\left\{e^{-z/H}\sin[k(x-c_{\mathrm{q}})-\Omega t]-e^{-\gamma' z}\sin[k(x-c_{\mathrm{q}})+m'z-\Omega t]\right\}\Big\rangle dk,
\end{aligned}
\tag{2.10}
$$

where

$$
X_{\mathrm{R}} = \frac{(\Omega+Uk)^2+N^2H^2k^2-\nu^2}{\left[(\Omega+Uk)^2+N^2H^2k^2-\nu^2\right]^2+4\nu^2(\Omega+Uk)^2},
$$

$$
X_{\mathrm{I}} = \frac{2\nu(\Omega+Uk)}{\left[(\Omega+Uk)^2+N^2H^2k^2-\nu^2\right]^2+4\nu^2(\Omega+Uk)^2},
$$

$$
X_{\mathrm{R}}' = \frac{(\Omega-Uk)^2+N^2H^2k^2-\nu^2}{\left[(\Omega-Uk)^2+N^2H^2k^2-\nu^2\right]^2+4\nu^2(\Omega-Uk)^2},
$$

$$X_{\mathrm{I}}' = \frac{-2\nu(\Omega - Uk)}{\left[(\Omega - Uk)^2 + N^2H^2k^2 - \nu^2\right]^2 + 4\nu^2(\Omega - Uk)^2},$$

$$\gamma_0 = \frac{Nk\nu}{U^2k^2 + \nu^2},\ m_0 = \frac{NUk^2}{U^2k^2 + \nu^2},$$

$$\gamma = \frac{Nk\nu}{(\Omega + Uk)^2 + \nu^2},\ m = \frac{Nk(\Omega + Uk)}{(\Omega + Uk)^2 + \nu^2},$$

$$\gamma' = \frac{Nk\nu}{(\Omega - Uk)^2 + \nu^2},\ m' = \frac{-Nk(\Omega - Uk)}{(\Omega - Uk)^2 + \nu^2}.$$

Using the forward Euler scheme, the numerical integration with respect to k in Eq. (2.10) is made. We use $k_n = 2n\pi/10^5$ m^{-1} (n = 1, 2, ⋯, 10000) which gives L_x = 10–10^5 m (L_x: wavelength in the x-direction). The choice of the domain size does not matter if L_x corresponding to the smallest k (k_1) covers the entire domain and L_x corresponding to the largest k (k_{10000}) is smaller than the x-directional resolution. In this study, Δx = 100 m is used. Using Eq. (2.10) and the Fourier-transformed equations of Eqs. (2.1)–(2.4), the solutions for the perturbation horizontal velocity, perturbation kinematic pressure, and perturbation buoyancy can be obtained. Note that in the absence of the mountain mechanical forcing the solution w becomes identical to that of Ganbat et al. (2015b).

2.3 Parameters

The solution that represents the linear interactions of urban breezes with mountain slope winds is obtained by the linear superposition of solutions that correspond to urban thermal forcing, mountain thermal forcing, and mountain mechanical forcing. The thermal forcing that induces urban breezes and the thermal forcing that induces mountain

slope winds are supposed to have steady components (Ω = 0 s^{-1}) and diurnally varying components ($\Omega = 2\pi/24$ h^{-1}) (Ganbat et al. 2015b). Mountain mechanical forcing has a steady component only. The solution for the perturbation vertical velocity is the sum of solutions corresponding to each forcing, which is given by

$$w(x,z,t) = w_{\mathrm{us}}(x,z) + w_{\mathrm{ud}}(x,z,t-\tau_{\mathrm{u}}) + w_{\mathrm{ms}}(x,z) + w_{\mathrm{md}}(x,z,t-\tau_{\mathrm{m}}) + w_{\mathrm{h}}(x,z). \tag{2.11}$$

Here, w_{us}, w_{ud}, w_{ms}, and w_{md} are the perturbation vertical velocities corresponding to the steady urban thermal forcing, diurnally varying urban thermal forcing, steady mountain thermal forcing, and diurnally varying mountain thermal forcing, respectively. The magnitudes of steady urban thermal forcing, diurnally varying urban thermal forcing, steady mountain thermal forcing, and diurnally varying mountain thermal forcing are denoted by q_{us}, q_{ud}, q_{ms}, and q_{md}, respectively. τ_{u} is the time of maximum urban thermal forcing, and τ_{m} is the time of maximum mountain thermal forcing. w_{h} is the perturbation vertical velocity corresponding to steady mountain mechanical forcing.

Consider a setting in which a city is located downwind of a mountain. The center of the city (mountain) is located at x = 10 km (x = –10 km). Following Ganbat et al. (2015b), the following parameter values are used in the calculations: q_{us} = 0.20 J kg^{-1} s^{-1}, q_{ud} = 0.15 J kg^{-1} s^{-1}, q_{ms} = 0.05 J kg^{-1} s^{-1}, q_{md} = 0.20 J kg^{-1} s^{-1}, c_{u} = 10 km, c_{m} = –10 km, τ_{u} = 1700 LT, τ_{m} = 1400 LT, a_{u} = a_{m} = 5 km, H_{u} = 750 m (urban H), H_{m} = 500 m (mountain H), N = 0.01 s^{-1}, T_0 = 283 K, and ν = 1/7200 s^{-1}. Even though the time variation of buoyancy frequency affects thermally or mechanically induced flows, N is treated as a constant because of mathematical difficulty in handling time-dependent

buoyancy frequency. For simplicity, a region of x = 0 to 20 km (x = –20 to 0 km) is called the urban (mountain) area. In a control case, the basic-state wind speed is specified as 2 m s^{-1}, and the maximum mountain height is specified as 100 m. Sensitivities to mountain height and basic-state wind speed are examined.

The horizontal variations of urban thermal forcing and mountain thermal and mechanical forcings normalized by the maximum of each forcing are plotted in Fig. 2.1a. Figure 1a also shows the names of the areas which are used in this study (mountain-side urban area, rural-side urban area, urban-side mountain area, and plain-side mountain area). The dark gray (gray) box on the x-axis indicates the urban (mountain) area. The temporal variations of urban thermal forcing and mountain thermal forcing at the center of each thermal forcing and z = 0 km are shown in Fig. 2.1b, which is from Ganbat et al. (2014). Note that urban (mountain) thermal forcing is the sum of steady urban (mountain) thermal forcing and the diurnally varying urban (mountain) thermal forcing. Urban thermal forcing is positive at all times (urban heating), and mountain thermal forcing is positive from 0700 to 2100 LT (mountain heating) and negative from 2100 to 0700 LT (mountain cooling) (Fig. 2.1b). In the following sections, the perturbation vertical velocity, perturbation horizontal velocity, perturbation velocity vector, perturbation buoyancy, and perturbation kinematic pressure are called as the vertical velocity, horizontal velocity, velocity vector, buoyancy, and kinematic pressure for brevity, respectively.

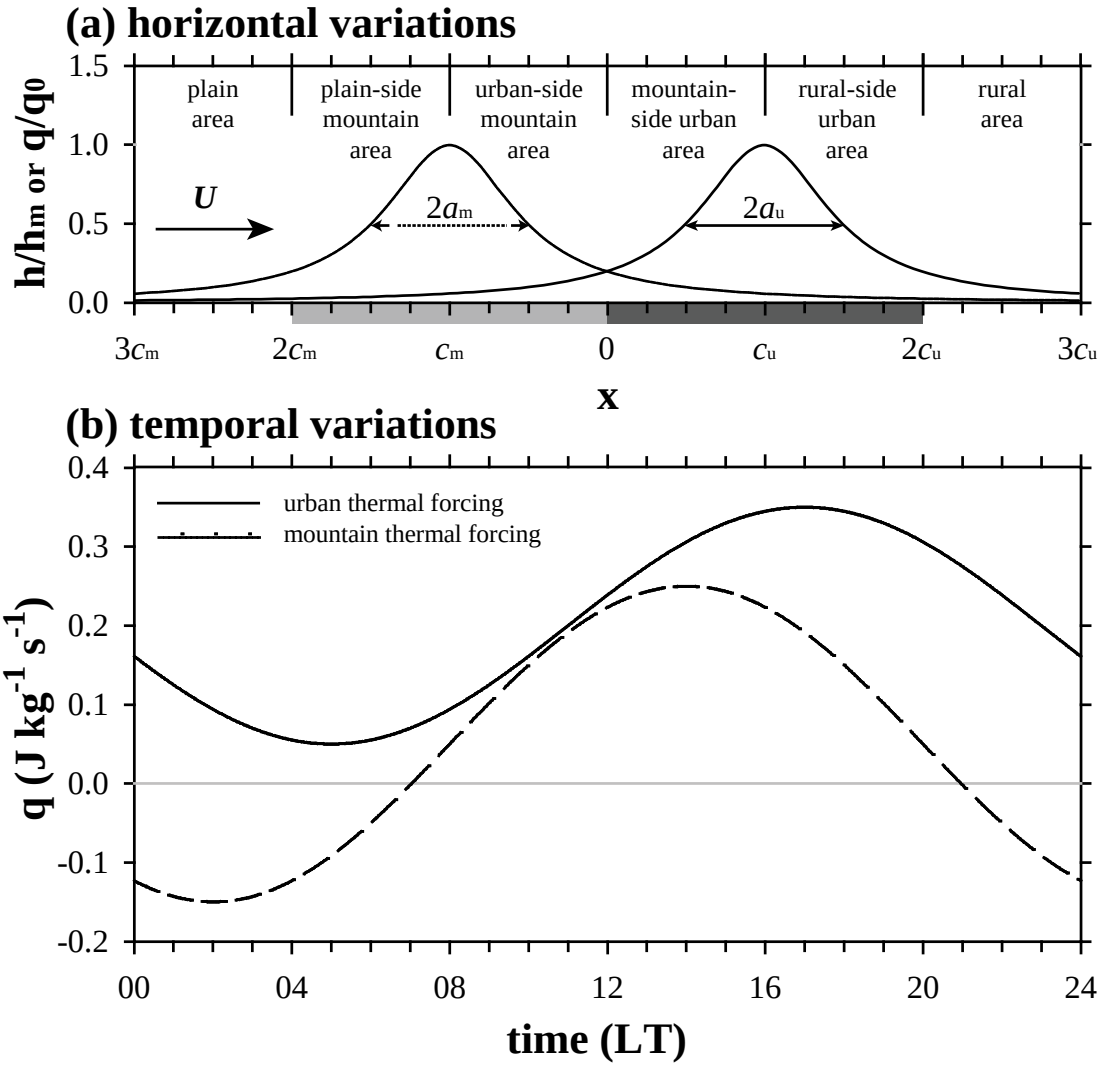

Figure 2.1 (a) Horizontal variations of urban thermal forcing (solid line) and mountain thermal and mechanical forcings (dashed line) normalized by the maximum of each forcing. The dark gray (gray) box on the *x*-axis indicates the urban (mountain) area. The names of the areas used in this study are given. (b) Temporal variations of urban thermal forcing at $x = c_u$ and $z = 0$ km (solid line) and mountain thermal forcing at $x = c_m$ and $z = 0$ km (dashed line). Fig. 2.1b is from Ganbat et al. (2015b).

2.4 Results and Discussion

2.4.1 Cases with each forcing only

To facilitate an investigation of the interactions of urban breezes with mountain slope winds, the results of cases with each forcing only are first presented. Figure 2.2 shows the vertical velocity, velocity vector, buoyancy, and kinematic pressure fields at 0200 and 1700 LT in the cases with urban thermal forcing only, mountain thermal forcing only, and mountain mechanical forcing only. In all three cases, the basic-state wind speed is specified as 2 m s^{-1}. In the case with mountain mechanical forcing only, the maximum mountain height is specified as 100 m. In all three cases, updraft and downdraft bands in the vertical direction are evident, especially in the case with mountain mechanical forcing only. These updraft and downdraft bands are internal gravity waves forced by thermal or mechanical forcing in a stably stratified atmosphere (Baik and Chun 1997). Wave amplitudes decrease with height because of the exponential decay of urban or mountain thermal forcing (thermal forcing is zero in the case with mountain mechanical forcing only) and the Rayleigh friction and Newtonian cooling. Phase lines are tilted upwind, implying upward propagation of wave energy (Chun and Baik 1998).

In the case with urban heating only (Fig. 2.2a, b), the buoyancy and kinematic pressure gradient in the urban area are larger at 1700 LT than at 0200 LT because of stronger urban heating at 1700 LT. This leads to stronger circulation at 1700 LT than at 0200 LT. At 1700 LT, relatively strong upward motion is observed downwind of the urban heating center (x = 10 km), while weak downward motion is observed upwind of the urban heating center. This result is consistent with that of Baik (1992). In the urban area, positive surface/near-surface (perturbation) horizontal flows are observed and they

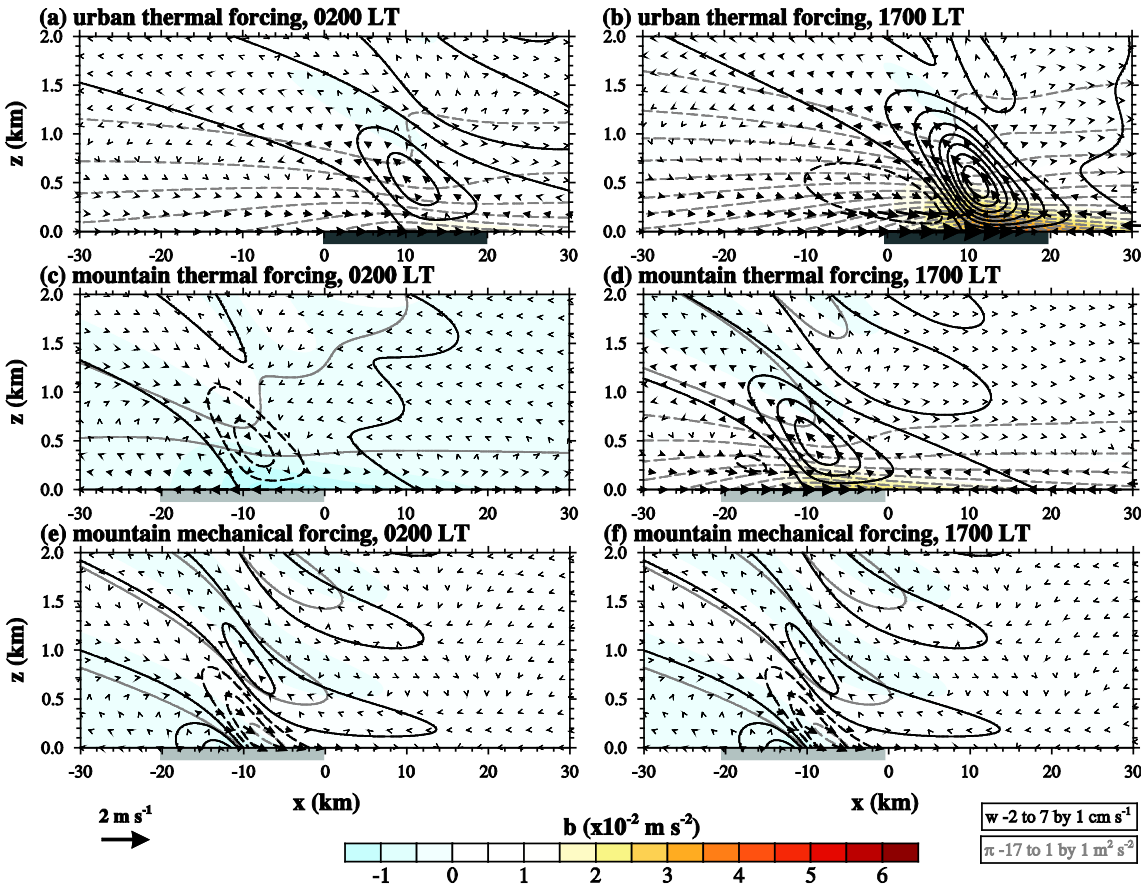

Figure 2.2 Vertical velocity (black lines), velocity vector, buoyancy (shaded), and kinematic pressure (gray lines) fields at 0200 LT (left) and 1700 LT (right) in the cases with (a), (b) urban thermal forcing only, (c), (d) mountain thermal forcing only, and (e), (f) mountain mechanical forcing only. The basic-state wind speed is specified as 2 m s^{-1}. In the case with mountain mechanical forcing only, the maximum mountain height is specified as 100 m. The dark gray (gray) box on the *x*-axis (also, in Figs. 2.3–2.6) indicates the urban (mountain) area.

diverge and then converge as going downwind. The location of maximum surface convergence, which is x = 14.2 km at 1700 LT, is situated downwind of the urban heating center. In x = –10 to 0 km, there are positive horizontal flows at low levels. These features are also observed at 0200 LT, although urban-heating induced flows are weaker. In the case with mountain thermal forcing only (Fig. 2.2c, d), there is mountain cooling at 0200 LT and mountain heating at 1700 LT (Fig. 2.1b). In x = –10 to 0 km, downward motion at 0200 LT and upward motion at 1700 LT exist. In the mountain area, there exists negative surface/near-surface horizontal flows except near x = 0 km at 0200 LT and positive surface/near-surface horizontal flows at 1700 LT. In x = 0 to 10 km, positive horizontal flows at 0200 LT and negative horizontal flows at 1700 LT are observed at low levels. In the case with mountain mechanical forcing only (Fig. 2.2e, f), the perturbation field at 0200 LT is identical to that at 1700 LT because mountain mechanical forcing is steady. At low levels, downslope winds (downward motion with positive horizontal flows) are produced in x = –10 to 0 km. In x = 0 to 10 km, positive surface/near-surface horizontal flows are produced, but their intensity is very weak.

2.4.2 Control case

The control case is equal to a case that linearly combines the three cases with each forcing only (Fig. 2.2). Figure 2.3 shows the vertical velocity, velocity vector, buoyancy, and kinematic pressure fields at 0200, 0800, 1100, 1400, 1700, and 2000 LT in the control case (U = 2 m s^{-1} and h_m = 100 m). Flow patterns in the presence of basic-state wind (Fig. 2.3) are quite different from those in the absence of basic-state wind (Ganbat

et al. 2015b). Unlike in Ganbat et al. (2015b), updraft and downdraft bands in the vertical direction with phase lines tilted upwind are produced in the control case.

At 0200 LT (Fig. 2.3a), urban heating produces upward motion in the rural-side urban area (x = 10 to 20 km). Mountain cooling produces downward motion on the urban-side mountain slope (x = –10 to 0 km), and mountain mechanical forcing produces downslope winds on the urban-side mountain slope. On the urban-side mountain slope, downward motion induced by mountain cooling is cooperatively combined with downslope winds induced by mountain mechanical forcing, resulting in strengthened downward motion. On the other hand, on the urban-side mountain slope negative surface/near-surface horizontal flows induced by mountain cooling are opposed to the horizontal component of downslope winds induced by mountain mechanical forcing, resulting in weakened positive surface/near-surface horizontal flows. In the mountain-side urban area (x = 0 to 10 km), positive surface/near-surface horizontal flows induced by mountain cooling and very weak positive surface/near-surface horizontal flows induced by mountain mechanical forcing are cooperatively combined with urban breezes, giving rise to strengthened winds. At 0800 LT (Fig. 2.3b), mountain heating is weak (Fig. 2.1b), so mountain mechanical forcing plays an important role in producing mountain slope winds. Upward motion in the rural-side urban area is weaker at 0800 LT than at 0200 LT. Urban heating at 0800 LT is the same as that at 0200 LT, and mountain mechanical forcing is steady. Hence, mountain heating is responsible for the weaker upward motion at 0800 LT in the rural-side urban area, which is associated with weaker surface/near-surface convergence. At 1100 LT (Fig. 2.3c), both urban heating and mountain heating increase (Fig. 2.1b). Upward motion in the rural-side urban area is

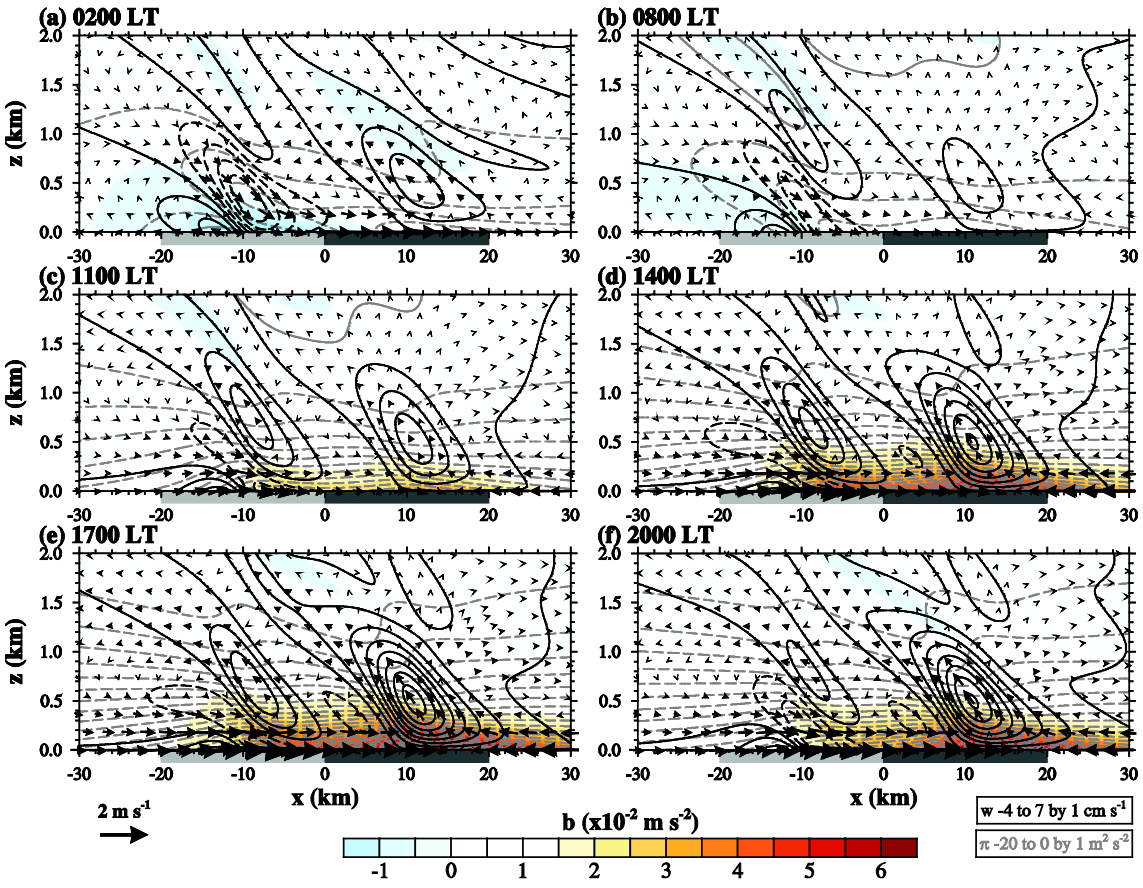

Figure 2.3 Vertical velocity (black lines), velocity vector, buoyancy (shaded), and kinematic pressure (gray lines) fields at (a) 0200, (b) 0800, (c) 1100, (d) 1400, (e) 1700, and (f) 2000 LT in the control case.

further intensified.

At 1400 LT (Fig. 2.3d), mountain heating is the strongest (Fig. 2.1b), producing strong upward motion on the urban-side mountain area (x = –10 to 0 km). On the urban-side mountain slope, downslope winds induced by mountain mechanical forcing and upward motion induced by mountain heating act oppositely to give rise to weakened downward motion. Because urban heating is also strong at 1400 LT, upward motion stronger than at 1100 LT develops in the rural-side urban area. Because of the influences of downslope winds induced by mountain mechanical forcing and urban breezes induced by urban heating, winds on the urban-side mountain slope are directed toward the urban center. At 1700 LT (Fig. 2.3e), urban heating is the strongest (Fig. 2.1b) and the buoyancy in the urban area is positive and large, producing well-developed urban circulation with strong upward motion. The buoyancy in the urban area is larger in the control case than in the case with urban heating only (Fig. 2.2b). This is a result of the influence of mountain heating and the interactions of urban breezes with mountain slope winds. Because of strengthened urban breezes, winds toward the urban center on the urban-side mountain slope become strong. At 2000 LT (Fig. 2.3f), mountain heating is weak (Fig. 2.1b) and mountain mechanical forcing is mainly responsible for mountain slope winds.

As should be expected, Fig. 2.3 shows that the interactions of urban breezes with mountain slope winds are stronger in the area between the mountain center and the urban center than in other areas, simply because of larger superposition of urban heating, mountain thermal forcing, and mountain mechanical forcing. In the mountain-side urban area, in the nighttime and daytime surface/near-surface winds are directed toward the

urban center due to urban heating, but their intensity changes with time, depending on diurnally varying interactions between urban breezes and mountain slope winds. In the urban-side mountain area, mountain cooling in the nighttime and mountain heating in the daytime play a crucial role in diurnally varying interactions between urban breezes and mountain slope winds.

2.4.3 Sensitivities to mountain height and basic-state wind speed

The degree of interactions between urban breezes and mountain slope winds can vary depending on the magnitudes of basic-state wind speed and stability as well as on the intensities of urban thermal forcing, mountain thermal forcing, and mountain mechanical forcing. In this subsection, we examine the sensitivities of the interactions of urban breezes with mountain slope winds to mountain height and basic-state wind speed. The maximum mountain height (h_m) is a parameter that controls the intensity of mountain mechanical forcing.

Figure 2.4 shows the vertical velocity, velocity vector, buoyancy, and kinematic pressure fields at 0200 and 1700 LT in the cases with h_m = 50 and 200 m. These two cases are the same as the control case (h_m = 100 m) except for the maximum mountain height. 0200 LT and 1700 LT are selected because representative nighttime and daytime flow features are well captured at these times. Eq. (2.10) indicates that the vertical velocity induced by mountain mechanical forcing is proportional to maximum mountain height. Therefore, stronger (weaker) mountain mechanical forcing corresponding to a larger (smaller) maximum mountain height produces stronger (weaker) mountain waves

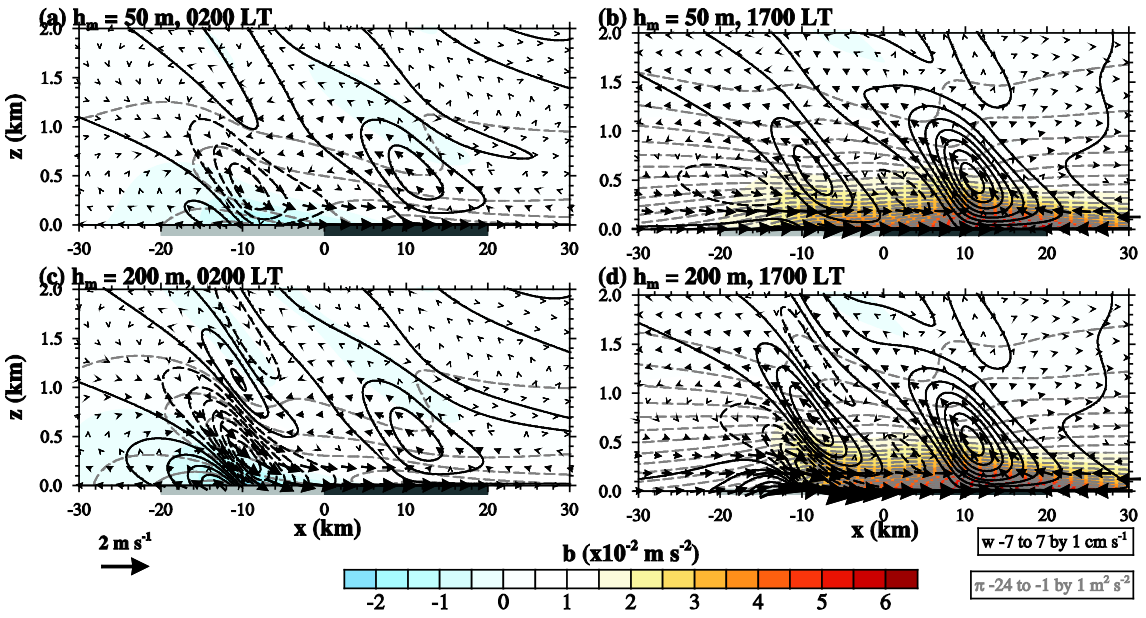

Figure 2.4 Vertical velocity (black lines), velocity vector, buoyancy (shaded), and kinematic pressure (gray lines) fields at 0200 LT (left) and 1700 LT (right) in the cases with (a), (b) h_m = 50 m and (c), (d) h_m =200 m. The basic-state wind speed is specified as 2 m s^{-1}.

in the mountain area, as seen in Figs. 2.3a, e and 2.4. At 0200 LT, as mountain height increases, downward motion on the urban-side mountain slope, which is produced by downward motion induced by mountain cooling being combined with downslope winds induced by mountain mechanical forcing, is strengthened (Figs. 2.3a and 2.4a, c). On the urban-side mountain slope, downslope winds whose horizontal component is weakened due to negative horizontal flows induced by mountain cooling intensify with increasing mountain height. Stronger downslope winds toward the city center for stronger mountain mechanical forcing are cooperatively combined with urban breezes in the mountain-side urban area. This leads to strengthened winds in the mountain-side urban area with increasing mountain height, as seen in Figs. 2.3a and 2.4a, c. The intensity of upward motion in the rural-side urban area changes little with mountain height. At 1700 LT, winds on the urban-side mountain slope intensify and accordingly winds in the mountain-side urban area also intensify as mountain height increases (Figs. 2.3e and 2.4b, d).

Sensitivity to basic-state wind speed is shown in Fig. 2.5, depicting the vertical velocity, velocity vector, buoyancy, and kinematic pressure fields at 0200 and 1700 LT in the cases with U = 1 and 4 m s^{-1}. These two cases are the same as the control case (U = 2 m s^{-1}) except for basic-state wind speed. A change in basic-state wind speed affects not only the strength of thermally and mechanically induced flows (internal gravity waves) but also their vertical wavelength and decaying rate (Eq. 2.10). As basic-state wind speed increases, thermally and mechanically induced flows are extended deeper in the vertical direction, mountain waves induced by mountain mechanical forcing intensify, and the vertical wavelength of updraft and downdraft bands increases (Figs. 2.3a, e and 2.5). As basic-state wind speed increases, at 0200 LT surface/near-surface horizontal flows

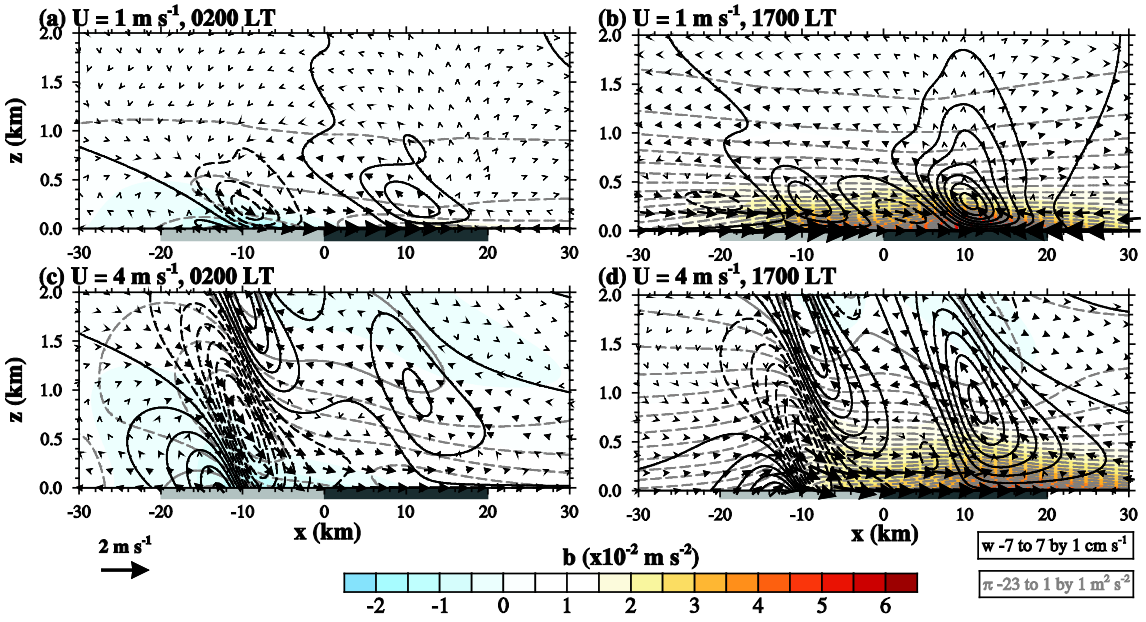

Figure 2.5 Vertical velocity (black lines), velocity vector, buoyancy (shaded), and kinematic pressure (gray lines) fields at 0200 LT (left) and 1700 LT (right) in the cases with (a), (b) U = 1 m s^{-1} and (c), (d) U = 4 m s^{-1}. The maximum mountain height is specified as 100 m.

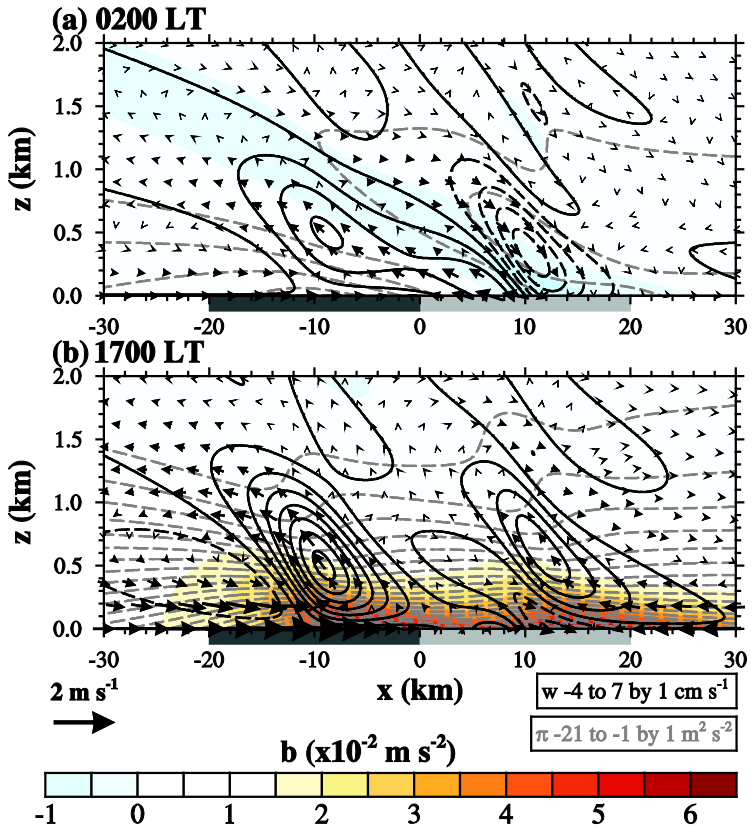

Figure 2.6 Vertical velocity (black lines), velocity vector, buoyancy (shaded), and kinematic pressure (grey lines) fields at (a) 0200 LT and (b) 1700 LT in the case in which a city is located upwind of a mountain. The maximum mountain height and basic-state wind speed are specified as 100 m and 2 m s^{-1}, respectively.

directed toward the city center in the area between the mountain center and the urban center weaken. In the case with U = 4 m s^{-1}, positive surface/near-surface horizontal flows are present outside of the urban area as well as in the urban area (Fig. 2.5c). At 1700 LT, winds on the urban-side mountain slope become strong and surface/near-surface horizontal flows in the mountain-side urban area strengthen as basic-state wind speed increases (Figs. 2.3e and 2.5b, d). The location of zero surface horizontal flows is shifted farther downwind with increasing basic-state wind speed (Figs. 2.3e and 2.5b, d). Because w_{h} is explicitly proportional to U, but w_{us}, w_{ud}, w_{ms} or w_{md} is approximately proportional to U^{-2} (Eq. 2.10), mountain mechanical forcing becomes more important with increasing basic-state wind speed, as clearly seen in Fig. 2.5.

Thus far, we have investigated the interactions of urban breezes with mountain slope winds in the cases in which a city is located downwind of a mountain. Here, we examine interactions between urban breezes and mountain slope winds in a setting in which a city is located upwind of a mountain. In a case considered, the urban area is situated upwind of the mountain area with the urban and mountain centers being located at x = –10 km and x = 10 km, respectively, and other specified parameter values are the same as those in the control case. This case is equivalent to the control case, but with basic-state wind blowing in the opposite direction (U < 0). At 0200 LT (Fig. 2.6a), strengthened upward motion by mountain cooling and mountain mechanical forcing on the urban-side mountain slope (x = 0 to 10 km) is connected with upward motion induced by urban heating on the mountain-side urban area (x = –10 to 0 km), forming a broad region of upward motion between the urban center and the mountain center. Surface/near-surface horizontal flows in the mountain-side urban area are weaker than those in the

control case (Figs. 2.3a and 2.6a). At 1700 LT (Fig. 2.6b), the connected upward motion still exists, but its intensity on the urban-side mountain slope is weaker than that at 0200 LT. This weaker intensity is because on the urban-side mountain slope upward motion induced by mountain mechanical forcing is combined with downward motion induced by mountain heating. On the urban-side mountain slope, surface/near-surface horizontal flows are very weak because negative surface/near-surface horizontal flows induced by urban heating are almost cancelled by positive surface/near-surface horizontal flows induced by mountain heating. Figures 2.3 and 2.6 indicate that basic-state wind direction is one of the important factors that significantly affect interactions between urban breezes and mountain slope winds.

3 Dynamics of reversed urban breeze circulation

3.1 Introduction

Weather and climate in urban areas are influenced by the local circulation induced by a thermal difference between urban and rural areas, which is called urban breeze circulation (UBC) or urban heat island circulation. UBC can interact with other local circulations such as sea-land breeze circulation and mountain-valley breeze circulation, depending on the geographical location (Dandou et al. 2009; Ryu and Baik 2013). UBC is one of the interesting problems in mesoscale meteorology, and a better understanding of UBC will help urban planning as well as urban weather and air quality prediction (Barlag and Kuttler 1990/91; Ryu et al. 2013b).

UBC has been extensively studied in the past decades. Observational studies have documented UBC and its features (Clarke 1969; Oke 1973; Shreffler 1978, 1979; Haeger-Eugensson and Holmer 1999; Lindén and Holmer 2011). Numerical modeling studies have illustrated the structure and evolution of simulated UBC (Draxler 1986; Lemonsu and Masson 2002; Ryu et al. 2013b). Theoretical studies have examined urban heating-induced circulation/flow by adding surface temperature perturbation in a mechanically viscous and thermally diffusive system (Estoque and Bhumralkar 1969; Olfe and Lee 1971) or thermal forcing in the thermodynamic energy equation (Lin and Smith 1986; Baik 1992; Han and Baik 2008).

To investigate a diurnal cycle of UBC in a theoretical frame, the observed diurnal variation of urban heating has to be considered. Observational studies indicate that the

urban heat island intensity exhibits a diurnal variation and its maximum occurs in the nighttime (Lee and Baik 2010). In the nighttime, however, urban heating-induced circulation/flow is weak because of strong static stability which suppresses upward motion. Many observational and numerical modeling studies show that the maximum intensity of UBC is observed in the daytime, more specifically in the late afternoon (Shreffler 1978, 1979; Oliveira et al. 2003; Ryu et al. 2013a; Ganbat et al. 2015a). To reflect this characteristic, theoretical studies that examine a diurnal cycle of UBC use the heating function that has a maximum in the late afternoon (Ganbat et al. 2015b; Chapter 2).

The general structure of UBC in the calm atmosphere consists of low-level inward flows toward the urban center, strong updrafts near the urban center, upper-level outward flows, and weak downdrafts outside the urban area. Interestingly, an idealized numerical modeling study indicates that reversed UBC in which the direction of circulation is opposite to that of the typical UBC is observed in the early morning when the Coriolis force is included, even though the urban area still releases heat (Savijärvi and Liya 2001). Using a numerical model, Ganbat et al. (2015a) confirmed the numerical modeling result of Savijärvi and Liya (2001). Savijärvi and Liya (2001) explained that reversed UBC (or anti-UBC) is generated as a result of the inertial rotation of the UBC with an inertial period of $12/|\sin\varphi|$ h (φ is the latitude) after surface heat transfer and vertical mixing are calmed down after sunset. However, the basic dynamics of reversed UBC has not yet been studied, motivating this study.

The purpose of this study is to understand the dynamics of UBC in a rotating system, particularly the dynamics of reversed UBC. The governing equations and

solutions are provided in section 3.2. In section 3.3, UBC in a rotating system and the dynamics of reversed UBC are presented and discussed.

3.2 Governing equations and solutions

To examine UBC in a rotating system, we consider a two-dimensional, linear, hydrostatic, Boussinesq airflow system with thermal forcing in the zero background wind. Equations that govern perturbations can be written as follows.

$$u_t - fv = -\pi_x - \alpha u, \tag{3.1}$$

$$v_t + fu = -\alpha v, \tag{3.2}$$

$$\pi_z = b, \tag{3.3}$$

$$b_t + N^2 w = \frac{g}{c_p T_0} q - \alpha b, \tag{3.4}$$

$$u_x + w_z = 0, \tag{3.5}$$

where u, v, and w are the velocities in the x-, y-, and z-direction (zonal, meridional, and vertical velocities), respectively, π is the perturbation kinematic pressure, b is the perturbation buoyancy, f is the Coriolis parameter, α is the coefficient of Rayleigh friction and Newtonian cooling (hereafter, called the frictional coefficient for simplicity), N is the buoyancy frequency, g is the gravitational acceleration, c_p is the specific heat of air at constant pressure, and T_0 is the reference temperature. The thermal forcing q represents the diurnally varying urban heating and is specified to be bell-shaped in the horizontal

and have an exponential decay in the vertical. The structure of the thermal forcing imitates the resultant spatial temperature pattern over cities.

$$q(x,z,t) = q_0 \frac{a^2}{x^2 + a^2} e^{-z/H} \,\mathrm{Re}\left\{e^{i\Omega t}\right\}, \tag{3.6}$$

where q_0 is the magnitude of urban heating, a is the half-width of the bell-shaped function, H is the e-folding depth of urban heating, and Ω is the angular frequency of the diurnal variation of urban heating. Note that equations (3.1)–(3.5) and the specified urban heating (3.6) are the same as those of Ganbat et al. (2015b), except that the momentum equation in the y-direction, the Coriolis force terms, and the zero background wind are considered in the present study.

Equations (3.1)–(3.5) can be combined into a single equation for w, which is expressed by

$$\left[\left(\partial_t + \alpha\right)^2 + f^2\right] w_{zz} + N^2 w_{xx} = \frac{g}{c_p T_0} q_{xx}\,. \tag{3.7}$$

Equation (3.7) is converted to an ordinary differential equation in z by taking the Fourier transform in x ($\rightarrow k$) and t ($\rightarrow \omega$) as follows.

$$\hat{w}_{zz} + N^2 \lambda^2 \hat{w} = \frac{g}{c_p T_0} \lambda^2 \hat{q}\,, \tag{3.8}$$

where

$$\lambda^2 = \frac{k^2}{(\omega - i\alpha)^2 - f^2}, \tag{3.9a}$$

$$\hat{q}(k,z,\omega) = q_0 a e^{-ak} e^{-z/H} \frac{\delta(\omega-\Omega)+\delta(\omega+\Omega)}{2}. \tag{3.9b}$$

Here, the Dirac delta function is denoted by δ. The general solution of Eq. (3.8) is given by

$$\hat{w}(k,z,\omega) = A(k,\omega)e^{iN\lambda z} + B(k,\omega)e^{-iN\lambda z} + \frac{\lambda^2 H^2}{1+N^2\lambda^2 H^2}\frac{g}{c_p T_0}\hat{q}, \tag{3.10}$$

where

$$\lambda(k,\omega) = \begin{cases} \dfrac{k}{\left(R^2+I^2\right)^{1/4}}\left[\cos\left(\dfrac{1}{2}\tan^{-1}\dfrac{I}{R}\right) + i\sin\left(\dfrac{1}{2}\tan^{-1}\dfrac{I}{R}\right)\right] & \text{for } R(\omega) \geq 0, \\ \dfrac{k}{\left(R^2+I^2\right)^{1/4}}\left[-\sin\left(\dfrac{1}{2}\tan^{-1}\dfrac{I}{R}\right) + i\cos\left(\dfrac{1}{2}\tan^{-1}\dfrac{I}{R}\right)\right] & \text{for } R(\omega) < 0, \end{cases} \tag{3.11a}$$

$$R(\omega) = \omega^2 - \left(\alpha^2 + f^2\right), \tag{3.11b}$$

$$I(\omega) = 2\alpha\omega. \tag{3.11c}$$

Note that the values of α, f, and ω determine the major behaviors of the solution. For $R(\omega) > 0$, the solution mainly exhibits a wave-like behavior in the vertical. On the other hand, for $R(\omega) < 0$, the solution mainly exhibits a decay in the vertical when the possible ranges of sine and cosine terms in $\lambda(k, \omega)$ are considered. In this study, the values of α, f, and ω which make $R(\omega)$ negative will be used to consider cases in which UBC exhibits very weak wave-like pattern in the vertical. For $R(\omega) < 0$, the real part of λ changes the sign by the sign of $I(\omega)$, whereas the imaginary part of λ is independent of the sign of $I(\omega)$.

Two unknown coefficients $A(k, \omega)$ and $B(k, \omega)$ in Eq. (3.10) are obtained by applying a flat bottom boundary condition ($\hat{w} = 0$ at $z = 0$) and eliminating the vertically amplifying component ($B(k, \omega) = 0$). Then, the solution in Fourier-transformed space is expressed by

$$\hat{w}(k,z,\omega) = \frac{C\lambda^2}{1+N^2\lambda^2H^2} e^{-ak} \frac{\delta(\omega-\Omega)+\delta(\omega+\Omega)}{2}\left(e^{-z/H} - e^{iN\lambda z}\right), \qquad (3.12)$$

where $C = gq_0aH^2/(c_pT_0)$.

By taking the inverse Fourier transform in k ($\rightarrow x$) and ω ($\rightarrow t$) and choosing the real part, we can obtain the solution of w in physical space.

$$\begin{aligned} w(x,z,t) = C\int_0^\infty k^2 e^{-ak} \cos kx \Big[& e^{-z/H}\left(X_{\mathrm{R}} \cos\Omega t - X_{\mathrm{I}} \sin\Omega t\right) \\ & - e^{-\gamma z}\left\{X_{\mathrm{R}} \cos(mz+\Omega t) - X_{\mathrm{I}} \sin(mz+\Omega t)\right\}\Big] dk, \end{aligned} \qquad (3.13)$$

where

$$X_{\mathrm{R}} = \frac{\Omega^2 + N^2H^2k^2 - \left(\alpha^2 + f^2\right)}{\left[\Omega^2 + N^2H^2k^2 - (\alpha^2 + f^2)\right]^2 + 4\alpha^2\Omega^2}, \tag{3.14a}$$

$$X_{\mathrm{I}} = \frac{2\alpha\Omega}{\left[\Omega^2 + N^2H^2k^2 - (\alpha^2 + f^2)\right]^2 + 4\alpha^2\Omega^2}, \tag{3.14b}$$

$$m = \mathrm{Re}\{N\lambda(k, \Omega)\}, \tag{3.14c}$$

$$\gamma = \mathrm{Im}\{N\lambda(k, \Omega)\}. \tag{3.14d}$$

Using Eq. (3.13) and the Fourier-transformed equations of Eqs. (3.1)–(3.5), we can obtain the solutions of u, v, π, and b. For example, the solutions of u and v are provided as follows.

$$\begin{aligned} u(x,z,t) = C\int_0^\infty ke^{-ak}\sin kx\Big[& e^{-z/H}\left(X_{\mathrm{R}}\cos\Omega t - X_{\mathrm{I}}\sin\Omega t\right)/H \\ & - e^{-\gamma z}\Big\langle m\left\{X_{\mathrm{R}}\sin\left(mz+\Omega t\right) + X_{\mathrm{I}}\cos\left(mz+\Omega t\right)\right\} \\ & - \gamma\left\{X_{\mathrm{R}}\cos\left(mz+\Omega t\right) - X_{\mathrm{I}}\sin\left(mz+\Omega t\right)\right\}\Big\rangle\Big]dk, \end{aligned} \tag{3.15}$$

$$\begin{aligned} v(x,z,t) = -Cf\int_0^\infty ke^{-ak}\sin kx\Big[& e^{-z/H}\left(Y_{\mathrm{R}}\cos\Omega t + Y_{\mathrm{I}}\sin\Omega t\right)/H \\ & + e^{-\gamma z}\Big\langle m\left\{Y_{\mathrm{R}}\cos\left(mz+\Omega t\right) - Y_{\mathrm{I}}\sin\left(mz+\Omega t\right)\right\} \\ & - \gamma\left\{Y_{\mathrm{R}}\sin\left(mz+\Omega t\right) + Y_{\mathrm{I}}\cos\left(mz+\Omega t\right)\right\}\Big\rangle\Big]dk, \end{aligned} \tag{3.16}$$

where

$$Y_{\mathrm{R}} = \frac{\Omega X_{\mathrm{R}} - \alpha X_{\mathrm{I}}}{\Omega^2 + \alpha^2}, \tag{3.17a}$$

$$Y_{\mathrm{I}} = \frac{\alpha X_{\mathrm{R}} + \Omega X_{\mathrm{I}}}{\Omega^2 + \alpha^2}. \tag{3.17b}$$

To examine a diurnal cycle of UBC, the solution of w which corresponds to the urban heating component that is constant with time (w_{c}; $\Omega_{\mathrm{c}} = 0$ s^{-1}) and the solution of w which corresponds to the urban heating component that varies diurnally (w_{d}; $\Omega_{\mathrm{d}} = 2\pi/24$ h^{-1}) are linearly superposed. The magnitudes of urban heating $q_{\mathrm{c}} = 0.2$ J kg^{-1} s^{-1} and $q_{\mathrm{d}} = 0.19$ J kg^{-1} s^{-1} are selected for w_{c} and w_{d}, respectively. Other parameter values are specified as $N = 0.01$ s^{-1}, $T_0 = 283.15$ K, $a = 5$ km, and $H = 750$ m (Ganbat et al. 2015b). Urban heating is specified to have a maximum at 1700 LT and a minimum at 0500 LT by applying the (t – 17 h) to the time t. Many previous studies which consider the local circulation induced by diurnally varying thermal forcing (sea-land breeze circulation and UBC) have used different frictional coefficients [(3.2 h)$^{-1}$ in Dalu and Pielke (1989); (2 h)$^{-1}$ in Ganbat et al. (2015b); (8.9 h)$^{-1}$ in Li and Chao (2016)]. These studies focused on the circulations in the daytime. This study focuses the evolution of the UBC in the nighttime and early morning with weaker turbulent activity. In this study, $\alpha = 2 \times 10^{-5}$ s^{-1} [= (13.9 h)$^{-1}$], which is smaller than the frictional coefficient used in the previous studies, is chosen. The integrations in Eqs. (3.13), (3.15), and (3.16) are numerically calculated using the forward scheme with $\Delta k = 2n\pi/10^5$ m^{-1} ($n = 0, 1, 2, \ldots, 10^4$).

3.3 Results and discussion

3.3.1 UBC in a rotating system

Ganbat et al. (2015b) investigated the UBC induced by urban heating in the resting basic-state wind and a non-rotating frame. In Ganbat et al. (2015b), $\alpha = 1/7200\ s^{-1}$, $q_c = 0.2\ J\ kg^{-1}\ s^{-1}$, and $q_d = 0.15\ J\ kg^{-1}\ s^{-1}$ are used. Here, a brief description of their results is given. In the nighttime, the low pressure and the positive buoyancy drive low-level converging flows toward the urban center. Subsequently, updrafts near the urban center, upper-level diverging flows, and then weak downdrafts outside the urban area are induced. This kind of circulation is maintained with diurnal variations in strength and horizontal/vertical scale. The UBC strengthens with time from 0800 LT and attains its maximum intensity in the late afternoon. Although the time of the strongest urban heating is 1700 LT, the strongest horizontal and vertical velocities occur 2 h 2 min and 36 min later than the time of the strongest daytime urban heating, respectively. The time lags between weakest nighttime urban heating and the weakest horizontal and vertical velocities are the same as in the above. Expectably, urban heating induces the typical UBC in terms of circulation direction over an entire day.

Figure 3.1 shows meridional and vertical velocities, perturbation kinematic pressure, and velocity vector fields (u, w) in the case with the Coriolis force terms. The selected times are 0200, 0600, and 1200 LT, and the Coriolis parameter is evaluated at φ = 30°N. At 0200 LT, thermally induced zonal converging flows and updrafts in the urban area are evident (Fig 3.1a). Generally, the meridional velocity is positive (negative) in the region with negative (positive) zonal velocity, due to the Coriolis effect. At 0600 LT, near-surface zonal diverging flows accompanied with broad and weak downdrafts of ~0.3

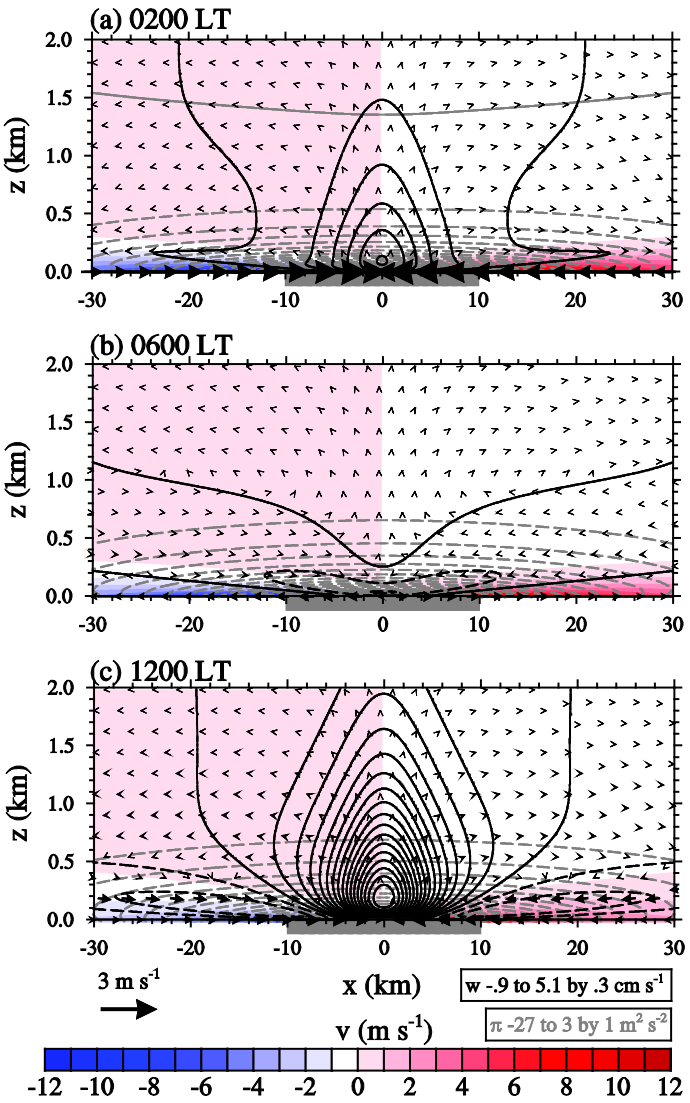

FIG. 3.1. Meridional (shaded) and vertical (black contours) velocities, perturbation kinematic pressure (gray contours), and velocity vector fields at (a) 0200, (b) 0600, and (c) 1200 LT in the case with the Coriolis force terms. The Coriolis parameter is evaluated at φ = 30°N. The gray box on the *x*-axis indicates the urban area in which urban heating is concentrated.

to ~1 km depth are developed (Fig. 3.1b), forming reversed UBC. Reversed UBC is opposite to typical UBC in terms of circulation direction, even though the kinematic pressure perturbation is negative in the urban area and the thermal forcing is positive (heating). As time goes on, the main updrafts above the downdraft layer strengthen and touch the surface and the circulation direction goes back to that of typical UBC. At 1200 LT, typical UBC is well established (Fig. 3.1c). The zonal converging flows are deeper at 1200 LT than at 0200 LT (Figs. 3.1a and 3.1c).

To investigate the latitude dependence of the UBC, we calculate differences in meridional and vertical velocities, perturbation kinematic pressure, and velocity vector between φ = 40 and 30°N (φ = 40°N case minus φ = 30°N case) (Fig. 3.2). At 0200 LT (1200 LT), zonal converging near-surface flows are weaker (stronger) in the higher latitude case. At 0600 LT, the difference in vertical velocity is positive because weaker low-level downdrafts associated with reversed UBC are induced in the higher latitude case. This is related to the fact that the inertial period in the higher latitude is shorter than that in the lower latitude. In section 3b, some discussion of the inertial rotation is provided.

Figure 3.3 shows differences in meridional and vertical velocities, perturbation kinematic pressure, and velocity vector between the cases with and without the Coriolis force terms (case with the Coriolis force terms minus case without the Coriolis force terms). The Coriolis parameter in the case with the Coriolis force terms is evaluated at φ = 30°N. We use $\alpha = 1/7200$ s^{-1} in these cases because $R(\Omega_d)$ is positive in the case with $\alpha = 2 \times 10^{-5}$ s^{-1} and no Coriolis force. The addition of the Coriolis force terms results in the weakening of zonal converging flows and updrafts during the entire day. Note that in this

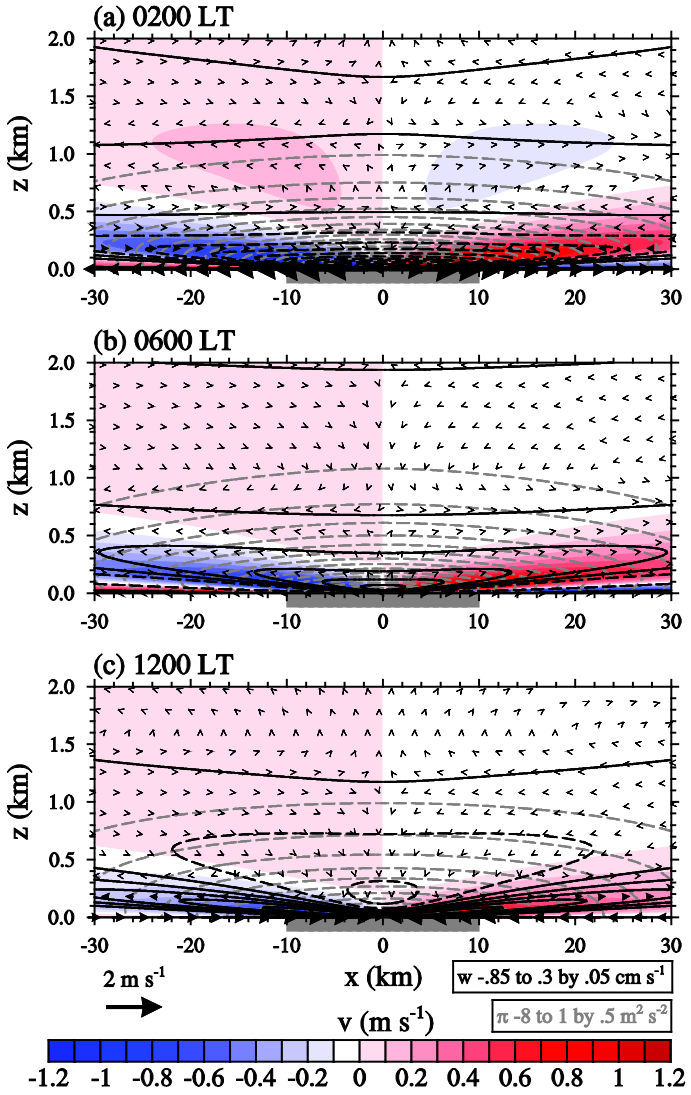

FIG. 3.2. Fields of differences in meridional (shaded) and vertical (black contours) velocities, perturbation kinematic pressure (gray contours), and velocity vector at (a) 0200, (b) 0600, and (c) 1200 LT between the case of φ = 40°N and the case of 30°N.

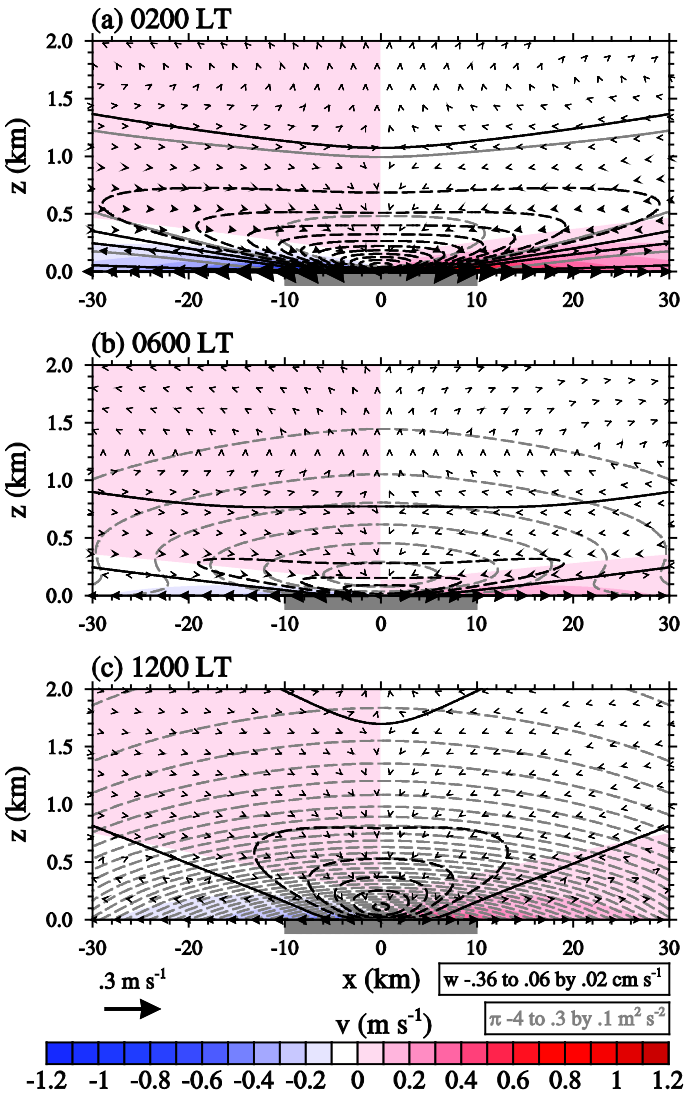

FIG. 3.3. Fields of differences in meridional (shaded) and vertical (black contours) velocities, perturbation kinematic pressure (gray contours), and velocity vector at (a) 0200, (b) 0600, and (c) 1200 LT between the case with the Coriolis force terms and the case without the Coriolis force terms. The Coriolis parameter in the case with the Coriolis force terms is evaluated at φ = 30°N.

this rotational case with strong friction, reversed UBC does not appear.

Figure 3.4 shows the hodographs of the diurnally varying component of surface horizontal velocity at x = –5, –10, and –20 km with $\alpha = 2 \times 10^{-5}$ s^{-1} and 1/7200 s^{-1}. The Coriolis parameter is evaluated at φ = 30°N. The black circle on each trajectory indicates the surface horizontal velocity at 0000 LT, and the spiral curve from the black circle indicates the vertical change of the horizontal velocity at x = –5 km and at 0000 LT. The surface horizontal velocity rotates clockwise with time, and the horizontal velocity rotates clockwise with height (see the spiral curves in Fig. 3.4). At x = –5 km and at 0000 LT, the height from the surface at which the zonal velocity first becomes zero is 20 m (40 m) in the case with $\alpha = 2 \times 10^{-5}$ s^{-1} (α = 1/7200 s^{-1}). In the case with the smaller frictional coefficient (Fig. 3.4a), the range of diurnal variation in surface zonal velocity is similar to that in surface meridional velocity and the strongest surface horizontal velocity (6.4 m s^{-1}) appears at ~2200 (~1000) LT. The daily constant components of surface horizontal velocity in this case are (4.3, –15.5), (3.2, –11.8), and (1.7, –6.2) in m s^{-1} at x = –5, –10, and –20 km, respectively. Hence, at these locations, the surface zonal velocity changes the sign from 0600 to 1000 LT and the surface meridional velocity does not change the sign. Note that the strongest zonal and meridional velocities are –5.8 m s^{-1} at ~0800 LT and 5.6 m s^{-1} at ~1300 LT, respectively. In the case with the larger frictional coefficient (Fig. 3.4b), the range of the diurnally varying component is larger in the zonal direction than in the meridional direction and the surface horizontal velocity is the strongest at ~1900 (~0700) LT. The strongest surface horizontal wind speed in this case is 1.9 m s^{-1} and is 4.5 m s^{-1} weaker than that in the case with $\alpha = 2 \times 10^{-5}$ s^{-1}. The daily constant components of surface horizontal velocity are (1.9, –1.0), (1.4, –0.7), and (0.7, –0.4) in

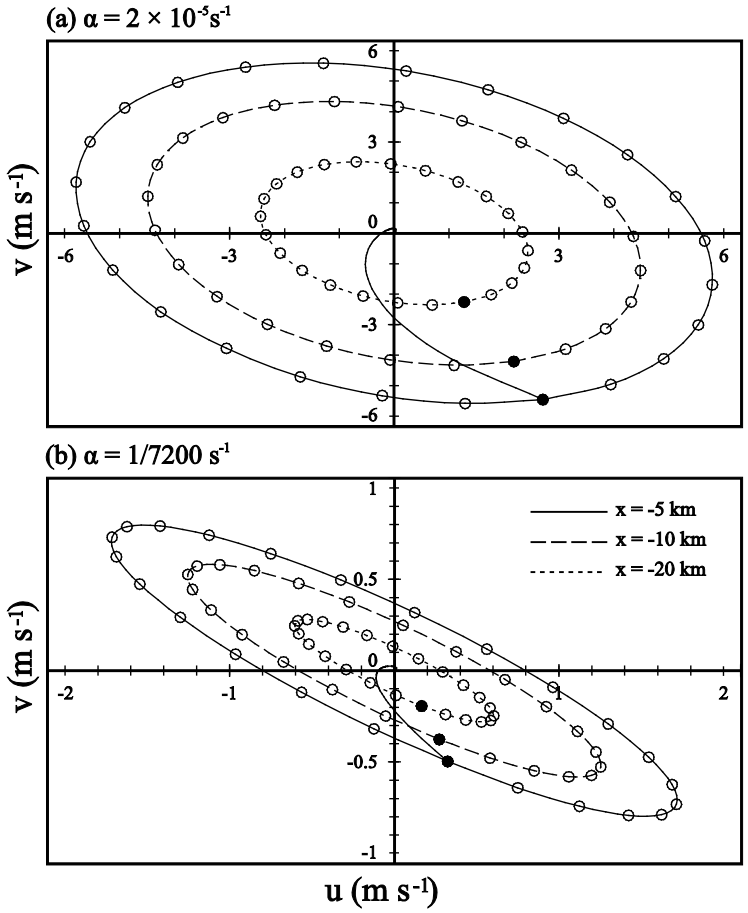

FIG. 3.4. Hodographs of the diurnally varying component of surface horizontal velocity at x = –5, –10, and –20 km and at φ = 30°N with (a) $\alpha = 2 \times 10^{-5}$ s^{-1} and (b) α = 1/7200 s^{-1}. The black circle on each trajectory indicates the surface horizontal velocity at 0000 LT, and the spiral curve from the black circle indicates the vertical change of the horizontal velocity at x = –5 km and at 0000 LT.

m s^{-1} at x = –5, –10, and –20 km, respectively. In this case, the sign of surface zonal and meridional velocities does not change during the entire day. Note that the strongest zonal and meridional velocities are 1.7 m s^{-1} at ~0700 LT and 0.8 m s^{-1} at ~0900 LT, respectively. The horizontal wind speed decreases rapidly with height in both the cases.

3.3.2 Dynamics of reversed UBC

The occurrence of reversed UBC is possible if the maximum amplitude of the diurnally varying component of the velocity in the zonal or vertical direction exceeds the value of its daily constant component. To examine the occurrence condition of reversed UBC, we calculate the maximum value of the diurnally varying vertical velocity ($w_{d,\,max}$) for the ranges of the latitude and frictional coefficient. Also, we calculate the ratio of $w_{d,\,max}$ to the daily constant vertical velocity (w_c) at the occurrence location and time ($t = t_{max}$) of $w_{d,\,max}$. In this analysis, we use $q_c = q_d = 0.2$ J kg^{-1} s^{-1} to emphasize that the occurrence condition of reversed UBC is the circulation direction that can be reversed even though the thermal forcing has a positive sign. In the case of $q_d > q_c$, a reversed UBC can appear more easily. Figure 3.5 shows $w_{d,\,max}$, $w_{d,\,max}/w_c$, and the occurrence time and height (z_{max}) of $w_{d,\,max}$. The parameter r is the ratio of the frictional coefficient to the angular frequency of Earth's rotation. The gray area in Fig. 3.5 indicates the range of $R(\Omega_d) \geq 0$ ($r^2 \leq 1 - 4\sin^2\varphi$). We can regard that reversed UBC appears at $z = z_{max}$ after 12 hours of $t = t_{max}$ with the strength $w_{d,\,max} - w_c$ because the diurnally varying component has the opposite sign with the same strength after 12 hours of $t = t_{max}$.

The results shown in Fig. 3.5 are sensitive near φ = 30°N for small r. The ratio $w_{d,\,max}/w_c$ is maximum at $\varphi \sim$ 30°N and $r \sim 0$ and generally decreases (increases) with latitude

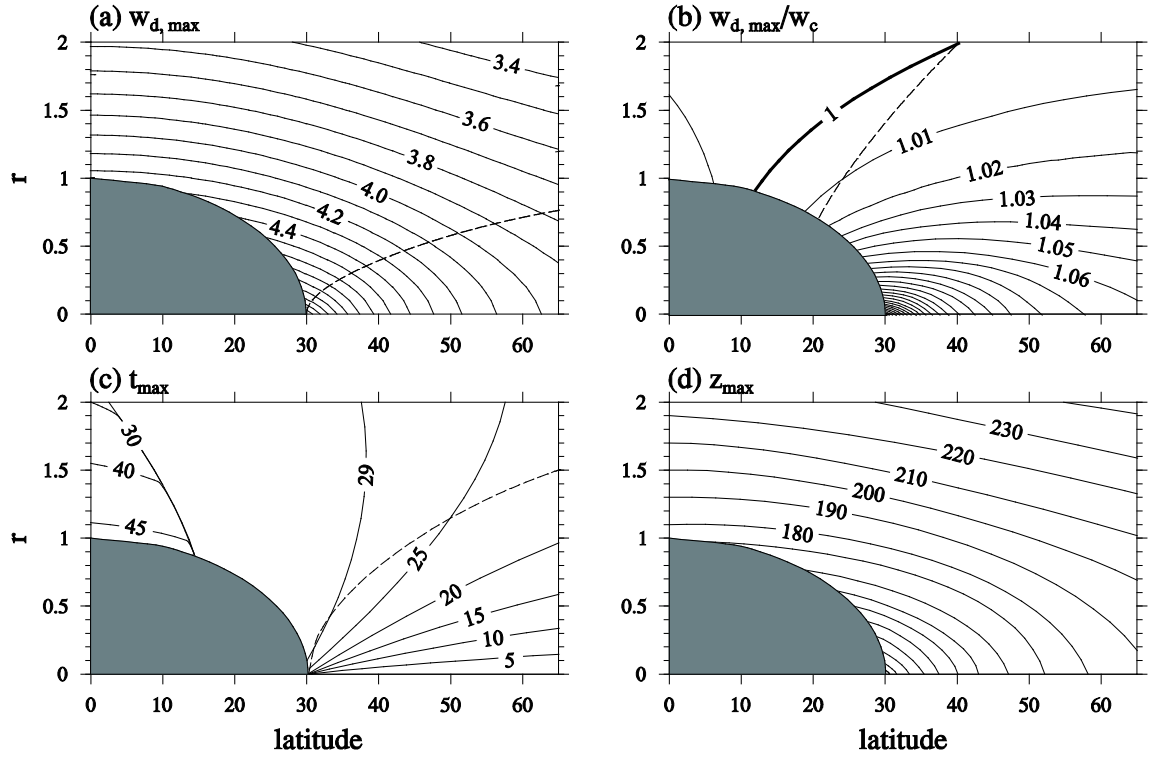

FIG. 3.5. (a) Maximum diurnally varying vertical velocity (cm s^{-1}), (b) ratio of the maximum diurnally varying vertical velocity to the daily constant vertical velocity, and (c) occurrence time and (d) height (m) of the maximum diurnally varying vertical velocity as a function of latitude and r ($= \alpha/\Omega_d$). Here, we use $q_c = q_d = 0.2$ J kg^{-1} s^{-1}. In (c), the hour of the occurrence time is 17 h and the minute of the occurrence time is contoured. The gray area in which $r^2 \leq 1 - 4\sin^2\varphi$ indicates the condition of $R(\Omega_d) \geq 0$. The dashed line in (b) is $r^2 = 12\sin^2\varphi - 1$, and the dashed line in (c) is $r^2 = 4\sin^2\varphi - 1$ For a given φ, the range below the dashed line in (a) indicates $|F_d| \geq |F_c|$ in Eqs. (3.21) and (3.22).

for small (large) r. For a given latitude, the ratio $w_{d,\,max}/w_c$ decreases with r except in very low latitude. Figure 3.5b indicates that reversed UBC exists only in high latitude for a strongly viscous system and that the Coriolis force plays an important role for a weakly viscous system. In the tropics, reversed UBC does not occur for a strongly viscous system. The Coriolis parameter in λ, X_R, and X_I in Eqs. (3.11) and (3.14) acts as a frictional coefficient. In detail, $(\alpha^2 + f^2)$ is applied in a rotating system in place of α^2 in a nonrotating system such as Eq. (3.11) in Ganbat et al. (2015b) and Eq. (3.10) in Seo et al. (2017b). Olfe and Lee (1971) also indicated that the Coriolis force damps the heat island-type flows. In the system considered in this study, the zonal pressure gradient produced by urban heating generates zonal flows. In terms of energetics, the Coriolis force diverts part of the driving energy to generate meridional flows, while friction consumes energy on both zonal and meridional flows. In this way, the zonal circulation is weakened by the Coriolis force. For a given r, $w_{d,\,max}$ decreases with latitude (Fig. 3.5a) and z_{max} increases with latitude (Fig. 3.5d). For a given latitude, $w_{d,\,max}$ also decreases with r (Fig. 3.5a) and z_{max} also increases with r (Fig. 3.5d). The occurrence time of $w_{d,\,max}$ for a given latitude higher than ~30°N is delayed with r, but the occurrence time of $w_{d,\,max}$ decreases with r for the cases with t_{max} larger than 30 min in a limited range of latitude and r (Fig. 3.5c).

The resonance-like pattern of the ratio $w_{d,\,max}/w_c$ at $\varphi \sim 30°$N and $r \sim 0$ recalls the work of Rotunno (1983). Rotunno (1983) examined the sea-land breeze represented by an atmospheric response to diurnally varying thermal forcing in the equation system similar to that of this study. Without viscous effects, generated circulation is confined to the neighborhood of the thermal forcing in the case of $f > \Omega_d$, while generated circulation is in the form of internal-inertial waves in the case of $f < \Omega_d$. The system is singular at the

critical latitude of 30°N. The reversal of the UBC is related to the frictionally decayed resonance of the diurnally varying component of the vertical velocity at φ = 30°N. This is because at φ = 30°N, the strength of the diurnally varying component has its maximum, whereas that of the daily constant component of the vertical velocity does not have [Eqs. (3.13) and (3.14)].

The solution obtained in this study contains diurnally varying and uniform components because we consider such thermal forcing functions. In a rotating system, thermally induced flow/circulation is always affected by the Coriolis force. By combining Eqs. (3.1) and (3.2), we can obtain an equation for the zonal velocity.

$$\left[\left(\partial_t + \alpha\right)^2 + f^2\right]u = -\left(\partial_t + \alpha\right)\pi_x. \tag{3.18}$$

On the western side of the urban center near the surface, $-\pi_x$ has a positive sign for urban heating. If $-\pi_x$ takes a form of $P_\mathrm{d}\cos\Omega(t - t_0) + P_\mathrm{c}$, Eq. (3.18) can be written as

$$\left[\left(d_t + \alpha\right)^2 + f^2\right]u = \alpha P_\mathrm{d}\cos\Omega(t-t_0) - \Omega P_\mathrm{d}\sin\Omega(t-t_0) + \alpha P_\mathrm{c}. \tag{3.19}$$

Equation (3.19) is an oscillation-type equation with the imposed time-dependent forcing. The solutions of u and v are

$$u(t) = \mathrm{Re}\left\{\tilde{U}_0 e^{(if-\alpha)(t-t_0)}\right\} + D_\mathrm{d}\cos\Omega(t-t_0) + E_\mathrm{d}\sin\Omega(t-t_0) + D_\mathrm{c}, \tag{3.20}$$

$$v(t) = \mathrm{Re}\left\{i\tilde{U}_0 e^{(if-\alpha)(t-t_0)}\right\} + F_\mathrm{d}\cos\Omega(t-t_0) + G_\mathrm{d}\sin\Omega(t-t_0) + F_\mathrm{c}, \tag{3.21}$$

where

$$D_{\mathrm{d}} = \alpha \frac{\Omega^2 + \alpha^2 + f^2}{R^2(\Omega) + I^2(\Omega)} P_{\mathrm{d}}, \tag{3.22a}$$

$$E_{\mathrm{d}} = \Omega \frac{\Omega^2 + \alpha^2 - f^2}{R^2(\Omega) + I^2(\Omega)} P_{\mathrm{d}}, \tag{3.22b}$$

$$D_{\mathrm{c}} = -\frac{\alpha}{R(0)} P_{\mathrm{c}}, \tag{3.22c}$$

$$F_{\mathrm{d}} = f \frac{R(\Omega)}{R^2(\Omega) + I^2(\Omega)} P_{\mathrm{d}}, \tag{3.22d}$$

$$G_{\mathrm{d}} = -f \frac{I(\Omega)}{R^2(\Omega) + I^2(\Omega)} P_{\mathrm{d}}, \tag{3.22e}$$

$$F_{\mathrm{c}} = \frac{f}{R(0)} P_{\mathrm{c}}. \tag{3.22f}$$

Here, $\tilde{U}_0$ (= $u_0 + iv_0$) is the complex velocity at $t = t_0$. Equations (3.20) and (3.21) indicate that the solutions of the zonal and meridional velocities induced by a diurnally varying perturbation kinematic pressure gradient have a temporally decaying inertial rotation term, diurnally varying terms, and a constant term. If we consider $t \sim t_0$ as a late afternoon time at which UBC is the strongest, we can estimate the time evolution of horizontal velocity after $t \sim t_0$, which is affected by the Coriolis force and the diurnally varying perturbation kinematic pressure gradient.

The sum of the second and fourth terms in the right-hand side of Eqs. (3.20) and (3.21) has a minimum at $t = t_0 + 12$ h. The minimum value of the sum at $t = t_0 + 12$ h has

a sign opposite to the maximum value if $|D_d|$ and $|F_d|$ are larger than $|D_c|$ and $|F_c|$, respectively. The condition for $|D_d| \geq |D_c|$ is $r^2 \leq 12\sin^2\varphi - 1$, and the limit curve is drawn in Fig. 3.5b. Note that the limit curve is closer to $w_{d,\,max}/w_c = 1$ curve for large r. The third term in the right-hand side of Eqs. (3.20) and (3.21) shifts the phase of the times that the maximum and minimum occur. The positive (negative) E_d and G_d indicate that the sum of the second, third, and fourth terms has a minimum value after (before) $t = t_0 + 12$ h. For a given latitude, t_{max} increases with r in the range of $r^2 \leq 4\sin^2\varphi - 1$ (for $\varphi \geq 30°$N). The limit curve is drawn in Fig. 3.5c. Outside of the limit curve, especially for $\varphi < 30°$N, t_{max} tends to decrease with r for a given latitude. Similarly, we can obtain the condition for $|F_d| \geq |F_c|$ (the limit curve is drawn in Fig. 3.5a). However, as discussed earlier, there is no sign change of meridional velocity at a given location under all conditions. This is because we consider $v_c \propto -(u_c\sin\varphi)/r$ and $v_d \propto -(ru_d\sin\varphi)/(1 + r^2)$ in the equation system. Note that these relations can be obtained by applying 0, $i\Omega_d v_d$, $2\Omega_d\sin\varphi$, and $r\Omega_d$ to $\partial_t v_c$, $\partial_t v_d$, f, and α in Eq. (3.2), respectively. The relations indicate that v_c has a larger value than v_d with comparable u_c and u_d for a given latitude.

The complex velocity $\tilde{U}_0$ in the first term in the right-hand side of Eqs. (3.20) and (3.21) inertially rotates 180 degrees during half an inertial period ($12/|\sin\varphi|$ h). Therefore, for a given r, the minimum of the resultant zonal velocity occurs earlier than the time which is determined by the last three terms in the right-hand side of Eqs. (3.20) and (3.21) in higher latitude. This effect is stronger for smaller r.

Figure 6 shows the time series of $u(t + t_0)$ in Eq. (3.20) with $r = 0.5$ and 1.5. Here, $(u_0, v_0) = (5, 0)$ m s^{-1} and $P_c = P_d = 2.5 \times 10^{-4}$ m s^{-2} are used. For $r = 0.5$, the minimum value of the diurnally varying u, which is marked by circles, occurs later (earlier) than

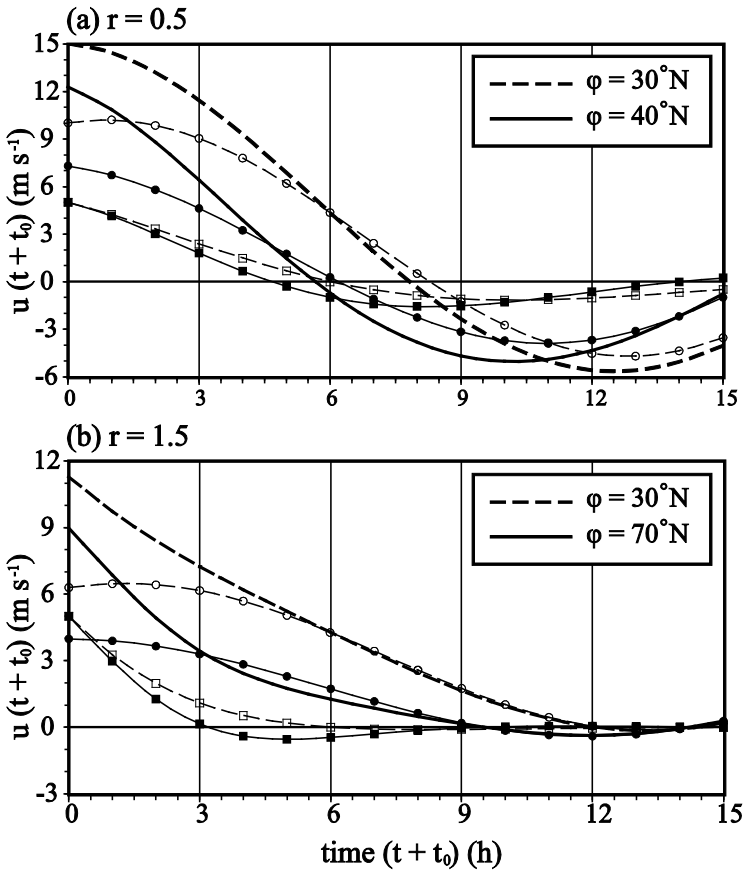

FIG. 3.6. Time series of $u(t + t_0)$ in Eq. (3.20) with r = (a) 0.5 at φ = 30 and 40°N and (b) 1.5 at φ = 30 and 70°N. The first term (inertial rotation) is marked by squares and the sum of the other three terms (diurnal variation) is marked by circles. The thick solid and dashed lines without marks are total $u(t + t_0)$.

$t = t_0 + 12$ h at $\varphi = 40°$N ($\varphi = 30°$N) following the sign of E_d. Note that the sign of E_d is negative at $\varphi = 40°$N and positive at $\varphi = 30°$N. Moreover, shorter inertial period at $\varphi = 40°$N causes the minimum of total u to occur earlier. From Fig. 3.6a, we can deduce that the strongest reversed UBC appears earlier and is weaker at $\varphi = 40°$N than at $\varphi = 30°$N. This explains the positive difference in the vertical velocity in Fig. 3.2b. For $r = 1.5$, negative E_d appears only in $\varphi \geq 64.3°$N and the inertial rotation term is strongly dampened in the nighttime (Fig. 3.6b). For this reason, it is difficult for reversed UBC to occur in the strongly viscous system.

4 Dynamics of orographic-convective flows in a two-layer hydrostatic atmosphere

4.1 Introduction

Forcings, such as mountains, convection, and fronts, in a stably stratified atmosphere generate mesoscale flows and internal gravity waves. Orographic forcing is a mechanical forcing of mountain, while convective forcing is a thermal forcing which represents latent heat released by condensation in convective clouds. In many cases, convective clouds are located in/near a mountainous area. Lin (1986) showed that orographically forced updrafts generate clouds and that the latent heat released from the induced clouds disturbs the stably stratified atmosphere. Jiang (2003) emphasized that latent heat release near a mountain affects upslope winds and the generation and development of orographic precipitation.

Orographically forced flows in a stably stratified atmosphere have been theoretically studied for a long time (e.g., Queney 1948; Smith 1980; Durran 1992). The linear dynamics of flows forced by an isolated mountain in a hydrostatic system indicate that orographically forced flows are characterized as vertically propagating mountain waves. The structure and strength of orographic gravity waves depend on environmental factors such as basic-state static stability and wind speed. Wurtele et al. (1987) and Keller (1994) examined the effects of tropospheric wind shear and static stability jump at the tropopause on orographic flows and momentum fluxes in hydrostatic/nonhydrostatic atmospheres, demonstrating that wave reflection at and wave transmission through the

tropopause affect orographic flows.

Theoretical studies of convectively forced flows have considered the diabatic forcing in the thermodynamic energy equation to represent latent heat release. Lin and Smith (1986) examined the transient response of a stably stratified airflow forced by a local heat source and found that in a steady state, the vertical displacement of the airflow is negative near the heating center and positive downstream. The deep convective forcing, which represents latent heat release from deep convection, induces a deep updraft area accompanied by a low-level compensating downward motion on the upstream of the convective forcing (Lin 1987; Lin and Li 1988; Han and Baik 2009). Lin and Li (1988) and Han and Baik (2010) examined the effects of basic-state wind shear on convectively forced flows in a single-layer atmosphere. Chun (1995) examined the response of a stably stratified two-layer atmosphere to low-level heating. In Chun (1995), the amplification of the flows/waves due to the wave reflection caused by the static stability jump is emphasized.

To theoretically analyze the mesoscale flows related to orographic precipitation, the perturbative motion resulted from the addition of a heat source in a mountainous area in a stably stratified atmosphere has been considered. In a single-layer atmospheric setting, Smith and Lin (1982) and Lin and Smith (1986) showed that the linear combination of orographically and convectively forced flows determine total flows in the region where orographic precipitation occurs. Davies and Schár (1986) considered diabatic heat released from non-precipitating clouds accompanied by mountain lee waves in a single-layer atmosphere. To better understand combined flows due to both orographic and convective forcings in a more realistic atmospheric setting, the

consideration of tropospheric wind shear and stability jump at the tropopause is needed.

Internal gravity waves transport wave energy and horizontal momentum in the horizontal and vertical (Eliassen and Palm 1960; Bretherton 1969; Bretherton 1988). Internal gravity waves penetrate into the upper atmosphere, and their energy is deposited through the gravity wave breaking/drag (Linzen 1981; Holton 1982). Many researchers have developed the parameterizations of orographic gravity-wave drag (e.g., Palmer et al. 1986; Pierrehumbert 1986) and have shown that the parameterizations can be applied to improve weather prediction or climate simulations (McFarlane 1987; Iwasaki et al. 1989). The reduction of the westerly bias of the Northern Hemispheric mean flow in winter is one example (Palmer et al. 1986). The dominant portion of stationary gravity waves originates from mountains. However, the significant magnitude of momentum fluxes of gravity waves with high frequencies has been observed and convectively forced gravity waves have been regarded as a main source, especially in summer. Many investigators have proposed convective gravity wave drag parameterizations (e.g., Chun and Baik 1998, 2002; Beres 2004; Song and Chun 2005, 2008) and applied them to large-scale numerical models to better simulate climate (Song et al. 2007). An overview of gravity-wave drag parameterizations is given in Kim et al. (2003). Smith and Lin (1982) presented an analytic expression for the vertical flux of the horizontal momentum in the case of uniform basic-state wind speed and static stability. In their expression, there is the momentum flux cross term which is resulted from the nonlinear interaction between orographically and convectively forced flows. Considering the importance of gravity-wave drag parameterizations in large-scale numerical models, further formulation and analysis of gravity-wave momentum flux cross term in a more realistic atmospheric

setting are needed.

In this study, orographic-convective flows, gravity-wave reflection, and gravity-wave momentum fluxes in a two-layer hydrostatic atmosphere are examined. In Section 4.2, the analytic solutions of the governing equations are obtained. In Section 4.3.1, the orographic-convective flows are described using the obtained analytic solutions. In Section 4.3.2, the gravity-wave reflection at the tropopause is analysed to deeply understand its effects on orographic-convective flows. In Section 4.3.3, the analytic expressions of gravity-wave momentum fluxes forced by orographic forcing, convective forcing, and both orographic and convective forcings are provided and are analyzed.

4.2 Governing equations and solutions

A two-dimensional (*x*-*z* plane), linear, steady-state, inviscid, nonrotating equation system that satisfies hydrostatic and Boussinesq approximations is considered. The governing equations of perturbation variables are as follows.

$$Uu_x + wU_z = -\pi_x, \tag{4.1}$$

$$\pi_z = b, \tag{4.2}$$

$$Ub_x + N^2 w = \frac{g}{c_p T_0} q, \tag{4.3}$$

$$u_x + w_z = 0, \tag{4.4}$$

where u and w are the perturbation horizontal and vertical velocities, respectively, π is the perturbation kinematic pressure, b is the perturbation buoyancy, U is the basic-state wind

speed in the horizontal direction, N is the buoyancy frequency, g is the gravitational acceleration, c_p is the specific heat of air at constant pressure, T_0 is the reference temperature, and q is the convective forcing.

Figure 4.1 shows the schematic of a two-layer atmosphere considered in this study. The lower and upper layers represent the troposphere and stratosphere, respectively. The tropopause height is H. The stratospheric static stability N_S is larger than the tropospheric static stability N_T. The basic-state wind speed has a constant wind shear in the troposphere ($U = U_0 + sz$, where U_0 is the basic-state wind speed at the surface and s is the basic-state wind shear) and is constant in the stratosphere ($U = U_H$). Only positive U_0 and s are considered in this study. The convective forcing q represents the latent heat release from convective clouds and is specified as

$$q(x,z) = q_0 \left\{ \frac{a_c^2}{(x-c_c)^2 + a_c^2} - \frac{a_c b_c}{(x-c_c)^2 + b_c^2} \right\}, \tag{4.5}$$

where q_0 is the magnitude of the convective forcing, a_c is the half-width of the bell-shaped heating function, b_c is a constant ($b_c > a_c$), and c_c is the center of the convective forcing in the x-direction. The convective forcing is present from $z = h_1$ to $z = h_2$, where h_1 and h_2 are the bottom and top heights of the convective forcing, respectively (see Fig. 4.1). The mountain is represented as

$$h(x) = h_m \frac{a_m^2}{(x-c_m)^2 + a_m^2}, \tag{4.6}$$

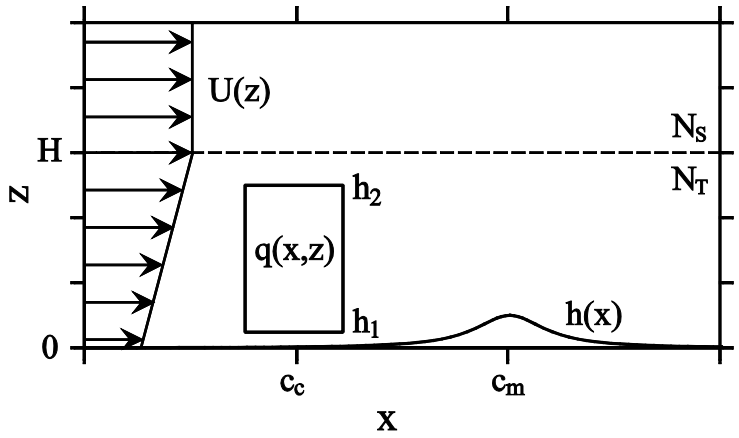

Figure 4.1. Structure of a two-layer atmosphere in the presence of convective forcing and a mountain considered in this study.

where h_m is the maximum height of the mountain, a_m is the half-width of the bell-shaped mountain function, and c_m is the center of the mountain in the x-direction.

Equations (4.1)–(4.4) can be combined into a single equation for the perturbation vertical velocity, which is Fourier-transformed ($x \rightarrow k$) to obtain

$$U^2 \hat{w}_{zz} + N^2 \hat{w} = \hat{F}, \tag{4.7a}$$

where

$$\hat{F}(k,z) = \frac{g q_0 a_c}{c_p T_0 N_T^2} (e^{-a_c k} - e^{-b_c k}) e^{-ikc_c}. \tag{4.7b}$$

The general solutions of Eq. (4.7a) for $0 \le z \le H$ and $z > H$ are given, respectively, by

$$\hat{w}_T(k,z) = AU^{\frac{1}{2}+i\mu} + BU^{\frac{1}{2}-i\mu} + \hat{F}, \tag{4.8a}$$

$$\hat{w}_S(k,z) = Ce^{imz} + De^{-imz}. \tag{4.8b}$$

Here, $\mu = (\mathrm{Ri} - 0.25)^{1/2}$, where Ri ($= N_T^2/s^2$) is the tropospheric Richardson number, and m ($= N_S/U_H$) is the vertical wavenumber of the internal gravity wave in the stratosphere. By imposing bottom boundary condition [$\hat{w} = ikU_0\hat{h} \equiv \hat{G}$; $\hat{h} = h_m a_m \exp\{-k(a_m + ikc_m)\}$], upper radiation condition ($D = 0$ with $U_H > 0$), and interfacial boundary conditions ($\hat{w}$ and $\partial\hat{w}/\partial z$ are continuous at $z = h_1$, h_2, and H), the analytic solutions in Fourier-transformed space for $0 \le z \le h_1$, $h_1 < z \le h_2$, $h_2 < z \le H$, and $z > H$ are obtained, which are given, respectively, by

$$\hat{w}_1(k,z) = \hat{G}\left(\frac{1-RZ_0^{-2i\mu}}{1-R}\right)Z_0^{\frac{1}{2}+i\mu} - \hat{F}\left(\frac{1-Z_0^{-2i\mu}}{1-R}\right)\left\{PR(Z_1^{\frac{1}{2}+i\mu} - Z_2^{\frac{1}{2}+i\mu}) + QZ_0^{2i\mu}(Z_1^{\frac{1}{2}-i\mu} - Z_2^{\frac{1}{2}-i\mu})\right\}, \tag{4.9a}$$

$$\hat{w}_2(k,z) = \hat{w}_1 - \hat{F}(PZ_1^{\frac{1}{2}+i\mu} + QZ_1^{\frac{1}{2}-i\mu} - 1), \tag{4.9b}$$

$$\hat{w}_3(k,z) = \hat{w}_1 - \hat{F}\left\{P(Z_1^{\frac{1}{2}+i\mu} - Z_2^{\frac{1}{2}+i\mu}) + Q(Z_1^{\frac{1}{2}-i\mu} - Z_2^{\frac{1}{2}-i\mu})\right\}, \tag{4.9c}$$

$$\hat{w}_4(k,z) = \left(\frac{1-RZ_{H0}^{-2i\mu}}{1-R}\right)\left[\hat{G}Z_{H0}^{\frac{1}{2}+i\mu} - \hat{F}\left\{P(Z_{H1}^{\frac{1}{2}+i\mu} - Z_{H2}^{\frac{1}{2}+i\mu}) + QZ_{H0}^{2i\mu}(Z_{H1}^{\frac{1}{2}-i\mu} - Z_{H2}^{\frac{1}{2}-i\mu})\right\}\right]e^{im\Delta z}, \tag{4.9d}$$

where

$$Z_i = \frac{U}{U_i}, \tag{4.9e}$$

$$Z_{Hi} = \frac{U_H}{U_i}, \tag{4.9f}$$

$$P = \frac{1}{2} + i\frac{1}{4\mu}, \tag{4.9g}$$

$$Q = \frac{1}{2} - i\frac{1}{4\mu}, \tag{4.9h}$$

$$R = \frac{\frac{1}{2} - i\left(\frac{N_S}{N_T}\sqrt{\mathrm{Ri}} - \mu\right)}{\frac{1}{2} - i\left(\frac{N_S}{N_T}\sqrt{\mathrm{Ri}} + \mu\right)}Z_{H0}^{2i\mu}, \tag{4.9i}$$

$$\Delta z = z - H. \tag{4.9j}$$

In Eqs. (4.9e) and (4.9f), i = 0, 1, and 2 are for z = 0, h_1, and h_2, respectively.

Equations (4.9a)–(4.9d) are the linear sum of orographically and convectively induced components. P (Q) represents the complex amplitude of upward (downward) propagating convectively forced internal gravity wave component generated at $z = h_1$ and h_2 (note that P and Q are a complex conjugate pair and $P + Q = 1$). R represents the complex reflection coefficient of the orographically/convectively forced internal gravity wave at the tropopause.

To get analytic solutions in physical space, we take the inverse Fourier transform ($k \rightarrow x$) of Eqs. (4.9a)–(4.9d) and select the real parts of the transformed solutions. The orographically forced components of the solutions for $0 \le z \le H$ (j = 1, 2, and 3) and $z > H$ are given, respectively, by

$$w_{jm}(x,z) = Z_0^{\frac{1}{2}}\Big[G_R\left\{R_1\cos(\theta_1+\theta_{z0}) - R_2\cos(\theta_2-\theta_{z0})\right\} - G_I\left\{R_1\sin(\theta_1+\theta_{z0}) - R_2\sin(\theta_2-\theta_{z0})\right\}\Big], \tag{4.10a}$$

$$w_{4m}(x,z) = Z_{H0}^{\frac{1}{2}}\Big[G_R\left\{R_1\cos(\theta_1+\theta_{H0}+m\Delta z) - R_2\cos(\theta_2-\theta_{H0}+m\Delta z)\right\} - G_I\left\{R_1\sin(\theta_1+\theta_{H0}+m\Delta z) - R_2\sin(\theta_2-\theta_{H0}+m\Delta z)\right\}\Big]. \tag{4.10b}$$

The convectively forced components of the solutions for $0 \le z \le h_1$, $h_1 < z \le h_2$, $h_2 < z \le H$, and $z > H$ are given, respectively, by

$$
\begin{aligned}
w_{1c}(x,z) = -\frac{N_T}{2s\mu}\Bigg[F_R \Bigg\langle R_1 \Bigg[& Z_1^{\frac{1}{2}} \left\{ \cos(\theta_1 + \Theta_{z1}^{+}) - \cos(\theta_1 - \Theta_{z1}^{-}) \right\} \\
& - Z_2^{\frac{1}{2}} \left\{ \cos(\theta_1 + \Theta_{z2}^{+}) - \cos(\theta_1 - \Theta_{z2}^{-}) \right\} \Bigg] \\
& + R_2 \Bigg[Z_1^{\frac{1}{2}} \left\{ \cos(\theta_2 + \Theta_{z1}^{-}) - \cos(\theta_2 - \Theta_{z1}^{+}) \right\} \\
& - Z_2^{\frac{1}{2}} \left\{ \cos(\theta_2 + \Theta_{z2}^{-}) - \cos(\theta_2 - \Theta_{z2}^{+}) \right\} \Bigg] \Bigg\rangle \\
& - F_I \Bigg\langle R_1 \Bigg[Z_1^{\frac{1}{2}} \left\{ \sin(\theta_1 + \Theta_{z1}^{+}) - \sin(\theta_1 - \Theta_{z1}^{-}) \right\} \\
& - Z_2^{\frac{1}{2}} \left\{ \sin(\theta_1 + \Theta_{z2}^{+}) - \sin(\theta_1 - \Theta_{z2}^{-}) \right\} \Bigg] \\
& + R_2 \Bigg[Z_1^{\frac{1}{2}} \left\{ \sin(\theta_2 + \Theta_{z1}^{-}) - \sin(\theta_2 - \Theta_{z1}^{+}) \right\} \\
& - Z_2^{\frac{1}{2}} \left\{ \sin(\theta_2 + \Theta_{z2}^{-}) - \sin(\theta_2 - \Theta_{z2}^{+}) \right\} \Bigg] \Bigg\rangle \Bigg],
\end{aligned}
\tag{4.11a}
$$

$$
w_{2c}(x,z) = w_{1c} - \left(\frac{N_T F_R}{s\mu} Z_1^{\frac{1}{2}} \cos\Theta_{z1}^{-} - F_R \right), \tag{4.11b}
$$

$$
w_{3c}(x,z) = w_{1c} - \frac{N_T F_R}{s\mu} \left(Z_1^{\frac{1}{2}} \cos\Theta_{z1}^{-} - Z_2^{\frac{1}{2}} \cos\Theta_{z2}^{-} \right), \tag{4.11c}
$$

$$
\begin{aligned}
w_{4c}(x,z) = -\frac{N_T}{s\mu} \Big[& F_R \left\{ R_1 \cos\left(\theta_1 + \theta_{H0} + m\Delta z\right) - R_2 \cos\left(\theta_2 - \theta_{H0} + m\Delta z\right) \right\} \\
& - F_I \left\{ R_1 \sin\left(\theta_1 + \theta_{H0} + m\Delta z\right) - R_2 \sin\left(\theta_2 - \theta_{H0} + m\Delta z\right) \right\} \Big] \times \\
& \left\{ Z_{H1}^{\frac{1}{2}} \cos\left(\theta_{10} - \tan^{-1}\frac{1}{2\mu} \right) - Z_{H2}^{\frac{1}{2}} \cos\left(\theta_{20} - \tan^{-1}\frac{1}{2\mu} \right) \right\}.
\end{aligned}
\tag{4.11d}
$$

In Eqs. (4.10) and (4.11),

$$
G_R + iG_I = -h_m a_m U_0 \frac{2a_m(x - c_m) + i\{(x - c_m)^2 - a_m^2\}}{(x - c_m)^2 + a_m^2}, \tag{4.12a}
$$

$$F_{\mathrm{R}} + iF_{\mathrm{I}} = \frac{q_0 g a_{\mathrm{c}}}{c_p T_0 N_{\mathrm{T}}^2} \left\{ \frac{a_{\mathrm{c}} + i(x - c_{\mathrm{c}})}{(x - c_{\mathrm{c}})^2 + a_{\mathrm{c}}^2} - \frac{b_{\mathrm{c}} + (x - c_{\mathrm{c}})}{(x - c_{\mathrm{c}})^2 + b_{\mathrm{c}}^2} \right\}, \tag{4.12b}$$

$$\frac{1}{1-R} \equiv R_1 e^{i\theta_1}, \tag{4.12c}$$

$$\frac{R}{1-R} \equiv R_2 e^{i\theta_2}, \tag{4.12d}$$

$$\theta_{zl} = \mu \ln \frac{U}{U_l}, \tag{4.12e}$$

$$\theta_{pq} = \mu \ln \frac{U_p}{U_q}, \tag{4.12f}$$

$$\Theta_{zj}^{\pm} = \theta_{z0} \pm \left(\theta_{j0} - \tan^{-1} \frac{1}{2\mu} \right). \tag{4.12g}$$

In Eq. (4.12e), l = 0, 1, and 2 are for z = 0, h_1, and h_2, respectively. In Eq. (4.12f), p and q = 0, 1, 2, and H are for z = 0, h_1, h_2, and H, respectively. In Eq. (4.12g), j = 1 and 2 are for $z = h_1$ and h_2, respectively.

We consider the finite-depth convective forcing which is located from $z = h_1$ = 1 km to $z = h_2$ = 11 km vertically and has the half-width of heating a_{c} = 10 km and $b_{\mathrm{c}} = 5a_{\mathrm{c}}$. The center of the bell-shaped mountain is c_{m} = 0 km with h_{m} = 500 m and a_{m} = 10 km. The tropospheric buoyancy frequency is specified as N_{T} = 0.01 s^{-1}, the basic-state wind speed at the surface as U_0 = 10 m s^{-1}, and the tropopause height as H = 12 km. The stratospheric buoyancy frequency N_{S}, the basic-state wind speed in the stratosphere U_H, and the center of the convective forcing c_{c} are different in each case. We name each case NxUyy in which N_{S} = 0.0x s^{-1} and U_H = yy m s^{-1} are used. The basic-state wind shear s is determined by U_0, U_H, and H, and the tropospheric Richardson number Ri by N_{T}, U_0, U_H,

and H. The magnitude of the convective forcing is specified as q_0 = 1 J kg^{-1} s^{-1}, and the reference temperature as T_0 = 273.15 K.

4.3 Results and discussion

4.3.1 Orographic-convective flows

The flows forced by each forcing are first presented before examining the linear interaction between orographic and convective flows. Figure 4.2 shows orographically and convectively forced perturbation vertical velocity fields in the cases of N1U10, N1U20, and N2U10 with c_m = 0 km and c_c = 0 km. Under the no-slip boundary condition at the surface, upward and downward flows are orographically generated on the upslope and downslope of the mountain, respectively (Figs. 4.2a–4.2c). Internal gravity waves are generated in the stably stratified atmosphere, and the perturbation vertical velocity fields exhibit a wavy structure in the vertical direction (Queney 1948; Durran 1992). The alternating pattern of the perturbation vertical velocity according to internal gravity waves generated at the surface is clear in the entire atmosphere. The convection forces a deep upward motion near the convective forcing center and a low-level compensating downward motion upstream of the convection (Figs. 4.2d–4.2f). These are well-known characteristics of convectively forced flows (Lin and Smith 1986; Han and Baik 2009). Above the convection top, the alternating pattern of the perturbation vertical velocity according to internal gravity waves clearly appears. Without the basic-state wind shear, the vertical wavelength of the internal gravity wave in the troposphere is $2\pi U_0/N_T$ = 6.28 km (cases of N1U10 and N2U10), as reported in many previous studies (e.g., Han and Baik 2009).

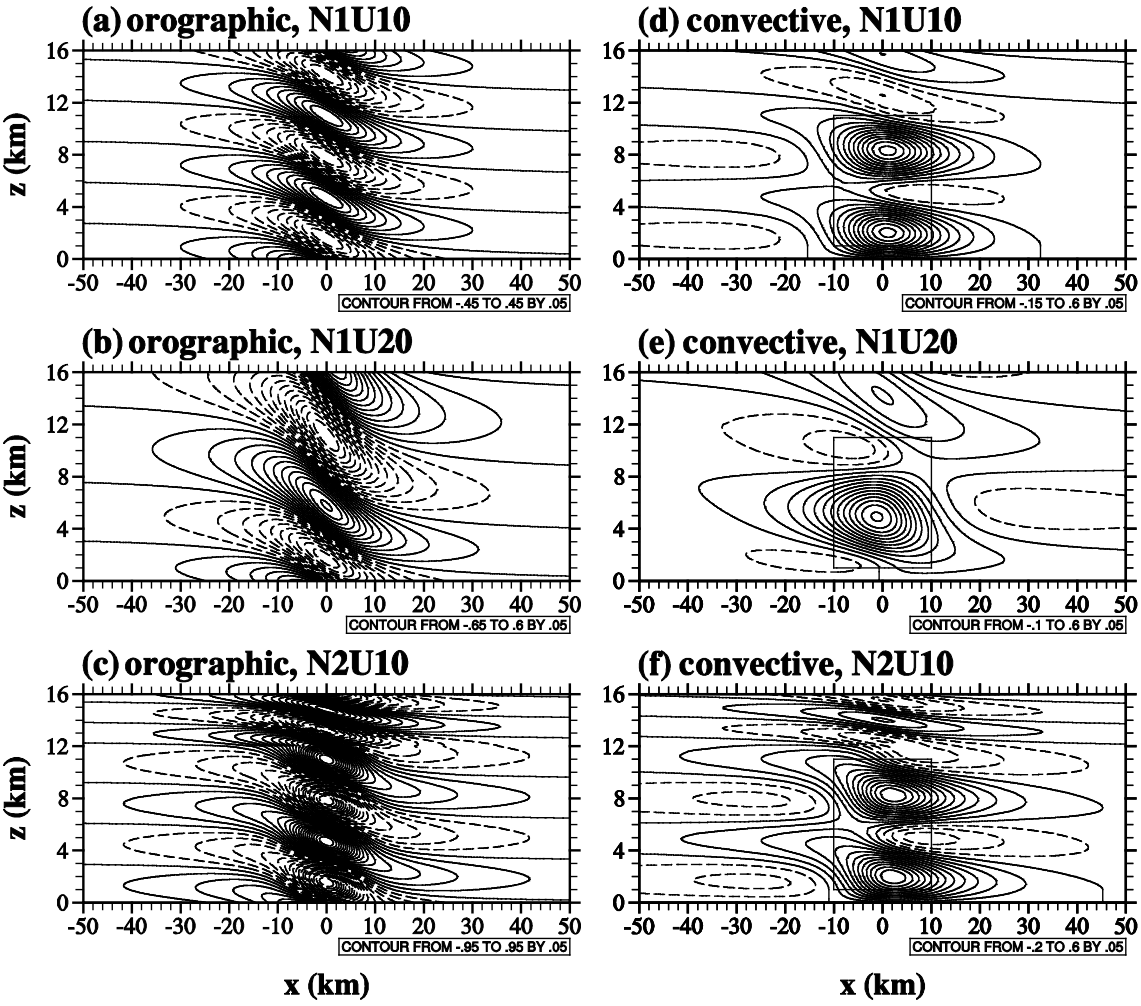

Figure 4.2. (a)–(c) Orographically and (d)–(f) convectively forced perturbation vertical velocity fields in the cases of N1U10 for (a) and (d), N1U20 for (b) and (e), and N2U10 for (c) and (f) with c_m = 0 km and c_c = 0 km. The rectangle in (d)–(f) represents the concentrated convective forcing region. The contour line information (unit: m s^{-1}) is given on the bottom of each panel.

In the case with wind shear, the increase of the basic-state wind speed with height strengthens the orographically forced perturbation vertical velocity (Fig. 4.2b). The vertical wavelength of the internal gravity wave is longer than that in the cases without wind shear due to the vertically increasing basic-state wind speed. The wavy structure of the convectively forced vertical velocity field in the troposphere is less clear in the case with wind shear (Fig. 4.2e). The main updraft is more concentrated and has a single-cell structure in the region of concentrated convective forcing. However, the compensating downward motion is weaker in the case with wind shear (Fig. 2e) than that in the cases without wind shear (Figure 4.2d and 4.2f). Compared to the cases without wind shear, the compensating downward motion is located closer to the convection center. In the cases without wind shear, on the upstream side, orographically forced waves are out of phase with convectively forced waves by ~180˚. For this reason, flows forced by convection over the mountain peak would be negatively combined with orographically forced flows on the upstream side. In the case with wind shear, the convectively forced single-cell shaped main upward motion would be positively (negatively) combined with the updraft (downdraft) near the convection center above the mountain peak (Figs. 4.2b and 4.2e). In the case of N2U10, the vertical wavelength of the internal gravity wave in the stratosphere is shorter than that in the case of N1U10 due to the higher stratospheric buoyancy frequency (Figs. 4.2c and 4.2f). The main structure of the perturbation vertical velocity field in the troposphere is similar to that in the case without stability jump. However, the induced flows are stronger in the case of N2U10 than in the case of N1U10. The wave reflection at the tropopause plays a role in strengthening the flows. The analysis of the wave reflection is provided in section 4.3.2.

The perturbation vertical velocity fields with the center of the convective forcing being located upstream of the mountain (c_c = –10 km) are shown in Figure 4.3. In all cases (N1U10, N1U20, N2U10, and N2U20), the convectively forced main upward motion is located over the upslope of the mountain. This upward motion is positively combined with orographically forced updrafts in the convection layer. As a result, a deep layer of strong updraft appears aloft upstream of the mountain (Figs. 4.3a and 4.3c). The main internal gravity wave bands generated by both forcings are concentrated slightly downstream of the mountain center (Figs. 4.3a and 4.3c). The convectively forced upward motion creates a deeper layer of strong updraft upslope of the mountain in the cases with wind shear than in the cases without wind shear (compare Figs. 4.3a and 4.3b and also Figs. 4.3c and 4.3d). However, the positive combination of the convectively forced upward motion with the low-level upslope wind is weaker in the cases with wind shear than in the cases without wind shear. The mountain waves are stronger and more concentrated over the mountain center in the cases with wind shear than in the cases without wind shear. The strong downdraft area of the mountain waves in the lower convection layer is broader in the cases with wind shear than in the cases without wind shear. As in Figure 4.2, the flows forced by both forcings are stronger in the cases with stability jump due to the wave reflection at the tropopause than in the cases with uniform stability in the entire atmosphere (compare Figure Figs. 4.3a and 4.3c and also Figs. 4.3b and 4.3d).

Figure 4.4 is the same as Figure 4.3 except for the center of the convective forcing being located lee of the mountain (c_c = 10 km). In the convection layer over the downslope of the mountain, the convectively forced upward motion positively interacts

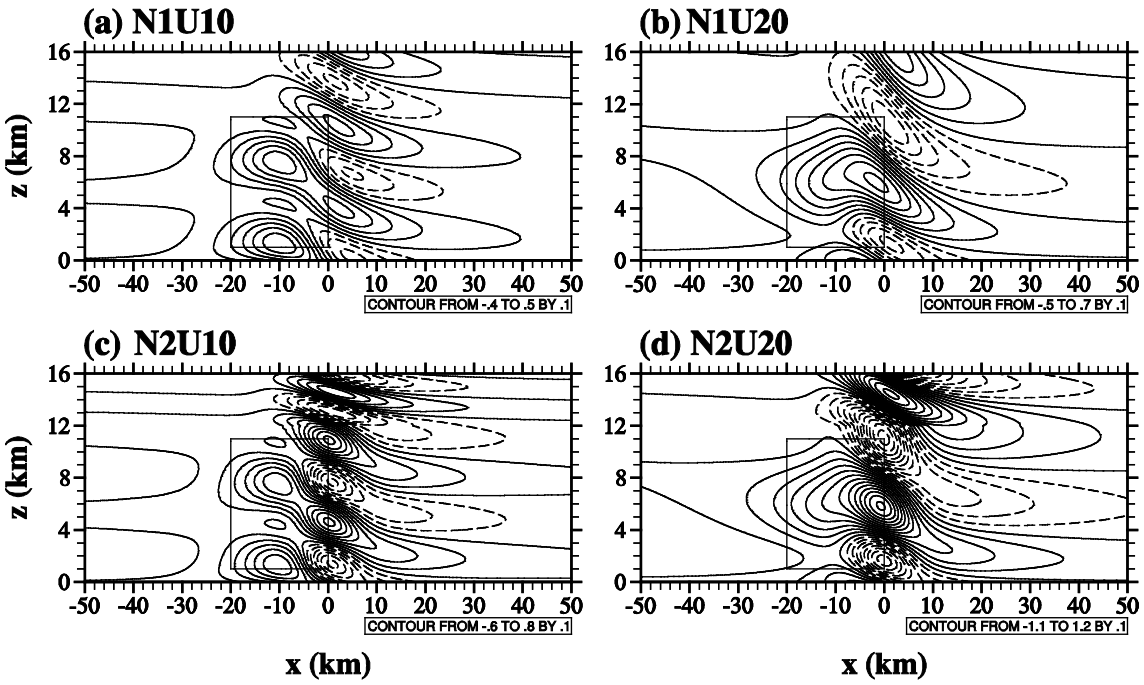

Figure 4.3. Perturbation vertical velocity fields in the cases of (a) N1U10, (b) N1U20, (c) N2U10, and (d) N2U20 with c_c = –10 km. The rectangle in the troposphere represents the concentrated convective forcing region. The contour line information (unit: m s^{-1}) is given on the bottom of each panel.

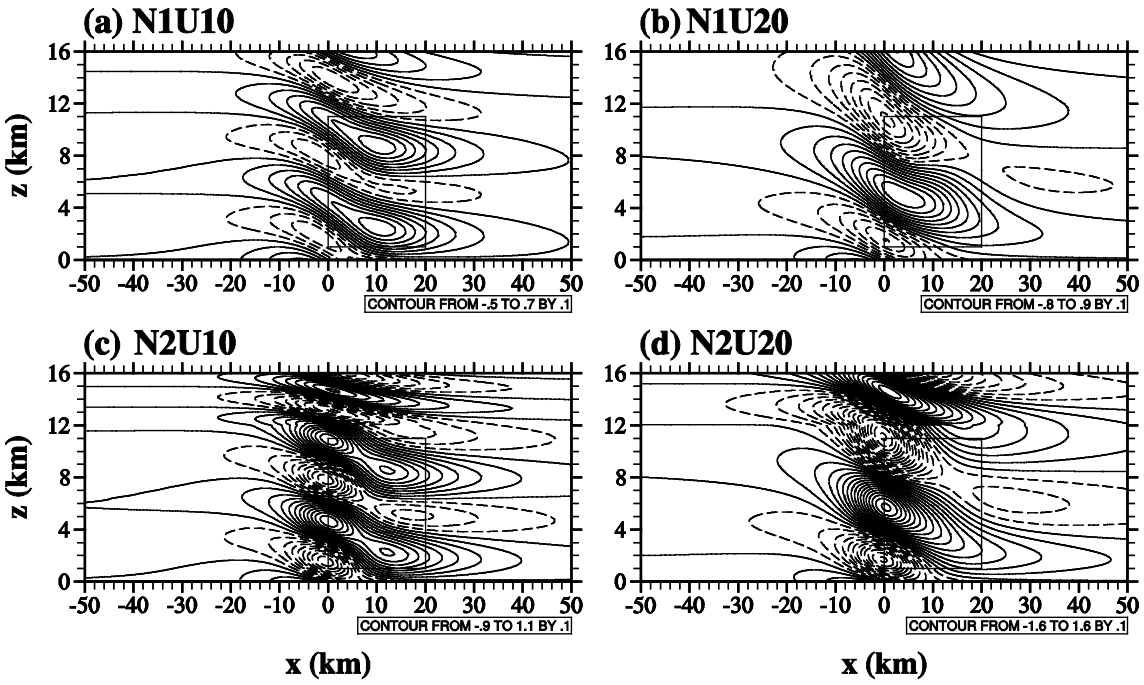

Figure 4.4. The same as Fig. 4.3 except for c_c = 10 km.

with the updrafts of mountain waves. In the cases without stability jump, the maximum amplitude of resultant waves appear above the downslope of the mountain as a result of the positive combination of orographically forced flows with convectively forced flows there (Figs. 4.4a and 4.4b). In the cases with stability jump, the maximum amplitude of the strengthened resultant waves over the mountain is located over the mountain peak (Figs. 4.4c and 4.4d).

Forced uplift of a moist air over the upslope of a mountain occasionally produces orographic clouds and precipitation. The horizontal and vertical motion forced by various factors, such as latent heating and local circulation, over the upslope of a mountain enhances or suppresses orographically forced uplift. To examine the effects of convectively forced vertical motion on orographically forced vertical motion on the upslope of the mountain, we calculate the ratio of the convectively forced perturbation vertical velocity to the orographically forced perturbation vertical velocity at $(x, z) = (c_m - a_m, h_1)$. Note that $c_m - a_m = -10$ km and $h_1 = 1$ km. The results are presented in Figure 4.5. The ratio is calculated as a function of c_c and U_H (Figs. 4.5a and 4.5b) and as a function of c_c and N_S (Figs. 4.5c and 4.5d).

When the convection center is located at $c_c \lesssim -10$ km, the convectively forced upward motion is positively combined with the orographic uplift. For weak wind shear ($s \lesssim 8.3 \times 10^{-4}$ s^{-1}; $U_H \lesssim 20$ m s^{-1}), the positive combination is stronger as wind shear becomes weaker (Figs. 4.5a and 4.5b). For strong wind shear, the convectively forced flows tend to be positively (negatively) combined with the orographic uplift when the convection center is located upstream (downstream) of the mountain, and the degree of the combination depends on the wind shear. When the convection center is located at

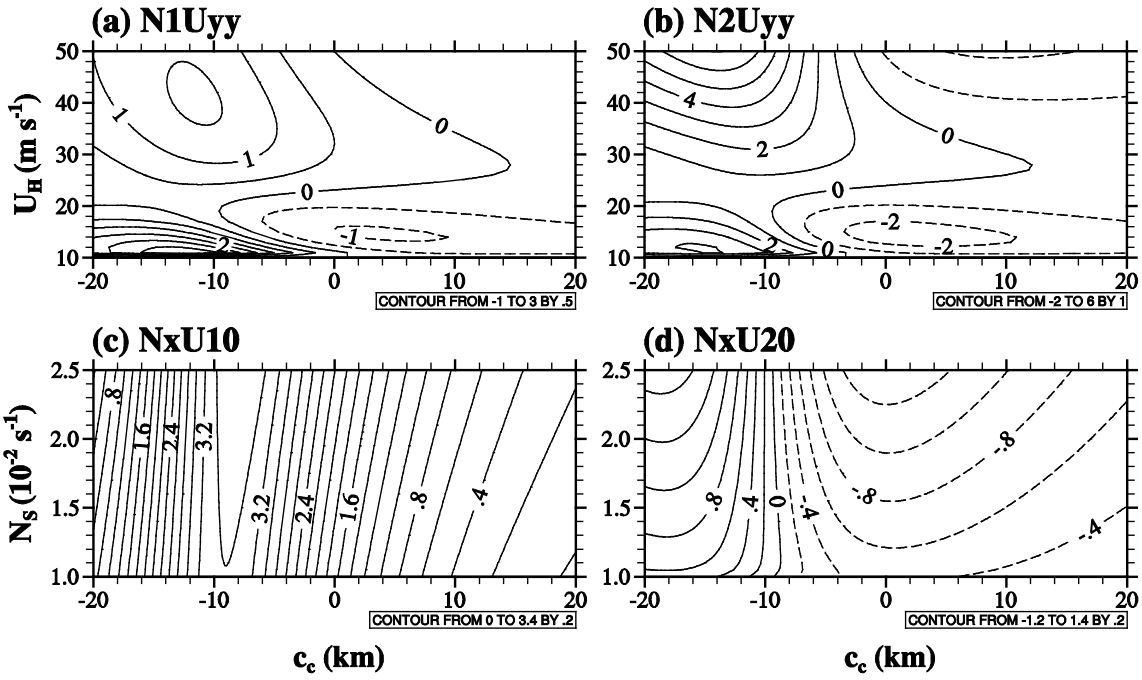

Figure 4.5. Fields of the ratio of the convectively forced perturbation vertical velocity to the orographically forced perturbation vertical velocity at (x, z) = ($c_m - a_m$, h_1) as a function of c_c and U_H in the cases of (a) N1Uyy and (b) N2Uyy and as a function of c_c and N_S in the cases of (c) NxU10 and (d) NxU20.

$c_c \gtrsim 0$ km, the convectively forced compensating downward motion is generally negatively combined with the orographic uplift. Depending on the location of the boundary between the convectively forced upward motion and the compensating downward motion, the ratio has different signs. For this reason, there is a range of wind shear in which the ratio is positive (negative), although the convective forcing is located above the lee (upstream) side of the mountain. The positive combination of the convectively forced upward motion with the orographic uplift and the negative combination of the convectively forced compensating downward motion with the orographic uplift are stronger in the case with large stability jump than in the case with small stability jump or without stability jump (compare Figs. 4.5a and 4.5b and also Figs. 4.5c and 4.5d). Without wind shear, the convection forces upward motion at $(x, z) = (c_m - a_m, h_1)$ in the wide range of c_c and N_S; because the compensating downward motion is located far upstream of the convection center. The positive interaction is strongest when the convection center is located at $x \sim -9$ km (Fig. 4.5c). When wind shear exists, however, the main upward motion (compensating downward motion) is positively (negatively) combined with the orographic uplift and the degree of the interaction is stronger with larger stability jump (Fig. 4.5d).

4.3.2 Gravity-wave reflection

As mentioned in section 4.3.1, the stability jump at the tropopause causes the reflection of the orographically/convectively forced internal gravity waves, and the reflected waves affect flows in both the troposphere and stratosphere. The complex reflection coefficient R at the tropopause is given in Eq. (4.9i). The complex reflection

coefficient R [$\equiv R_0\exp(i\theta_0)$, where R_0 is the reflectivity at the tropopause and θ_0 is the phase shift angle] can be rewritten as

$$R = \sqrt{\frac{\frac{1}{4}+\left(\frac{N_S}{N_T}\sqrt{\mathrm{Ri}}-\mu\right)^2}{\frac{1}{4}+\left(\frac{N_S}{N_T}\sqrt{\mathrm{Ri}}+\mu\right)^2}}\exp\left\{i\tan^{-1}\frac{\mu\left(1+2\ln Z_{H0}\right)}{\frac{1}{4}+\left(\frac{N_S}{N_T}\sqrt{\mathrm{Ri}}-\mu^2\right)}\right\}. \tag{4.13}$$

The orographically forced internal gravity waves propagate upward from the surface. At the tropopause, the waves are partially reflected due to the discontinuity of the static stability between the troposphere and stratosphere. The partially reflected waves at the tropopause are totally reflected at the surface and propagate upward again. As a result of infinite reflections, the upward propagating wave component is multiplied by $1/(1–R)$ and the downward propagating wave component is multiplied by $R/(1–R)$ [see Eqs. (4.9i), (4.12c), and (4.12d)]. The convectively forced internal gravity waves that originated from $z = h_1$ and h_2 propagate upward and downward with fractions of P and Q, respectively. Depending on the convection bottom/top heights and tropopause height, upward and downward propagating wave components are multiplied by $1/(1–R)$ and $R/(1–R)$, respectively, which are expressed as

$$\frac{1}{1-R} = \frac{1}{\sqrt{\left(1-R_0\cos\theta_0\right)^2+R_0^2\sin^2\theta_0}}\exp\left\{i\tan^{-1}\frac{R_0\sin\theta_0}{1-R_0\cos\theta_0}\right\}, \tag{4.14a}$$

$$\frac{R}{1-R} = \frac{R_0}{\sqrt{\left(\cos\theta_0-R_0\right)^2+\sin^2\theta_0}}\exp\left\{i\tan^{-1}\frac{\sin\theta_0}{\cos\theta_0-R_0}\right\}. \tag{4.14b}$$

Figure 4.6 shows R_0, R_1, R_2, θ_0, θ_1, and θ_2 as a function of the stratospheric buoyancy frequency and the Richardson number. For a given N_S, the reflectivity R_0 decreases as Ri increases. For a given N_S, R_0 is very sensitive to Ri when Ri is very small. For a given Ri, R_0 increases with increasing N_S. When Ri is large, R_0 tends to be independent of Ri for a given N_S and converges to

$$R_0 \approx \frac{N_S - N_T}{N_S + N_T} \ . \tag{4.15}$$

Note that R_0 in Eqs. (4.13) and (4.15) are always less than 1. The phase shift angle θ_0 ($-\pi/2 \le \theta_0 \le \pi/2$) is negative for large Ri. For very small Ri, the sign of θ_0 is changed to positive. This sudden phase reversal occurs when Ri = $[\{N_S + (N_S^2 + 2N_T^2)^{1/2}\}/2N_T]^2$. R_1 and R_2 are small when N_S and Ri are close to the boundary where the phase reversal of θ_0 occurs. For large Ri, both R_1 and R_2 increase with increasing N_S. For this reason, as stated, the resultant wave strengths are stronger in the presence of stability jump. The phase shift angles θ_1 and θ_2 are negative for large Ri. The magnitudes of both phase shift angles are smaller for larger Ri (weaker wind shear) and are increased with increasing N_S for a given large Ri. Both phase shift angles change the sign in a manner similar to θ_0. The phase shift angle θ_2 has additional sudden reversal when $R_0 = \cos\theta_0$. For a given N_S, the dependency of θ_2 on Ri is stronger than that of θ_1.

The analytic solutions for the orographically forced perturbation vertical velocity for $0 \le z \le H$ [Eq. (4.10a)] at the mountain center and the convectively forced perturbation vertical velocity for $0 \le z \le h_1$ [Eq. (4.11a)] at the convection center can be written as follows, respectively.

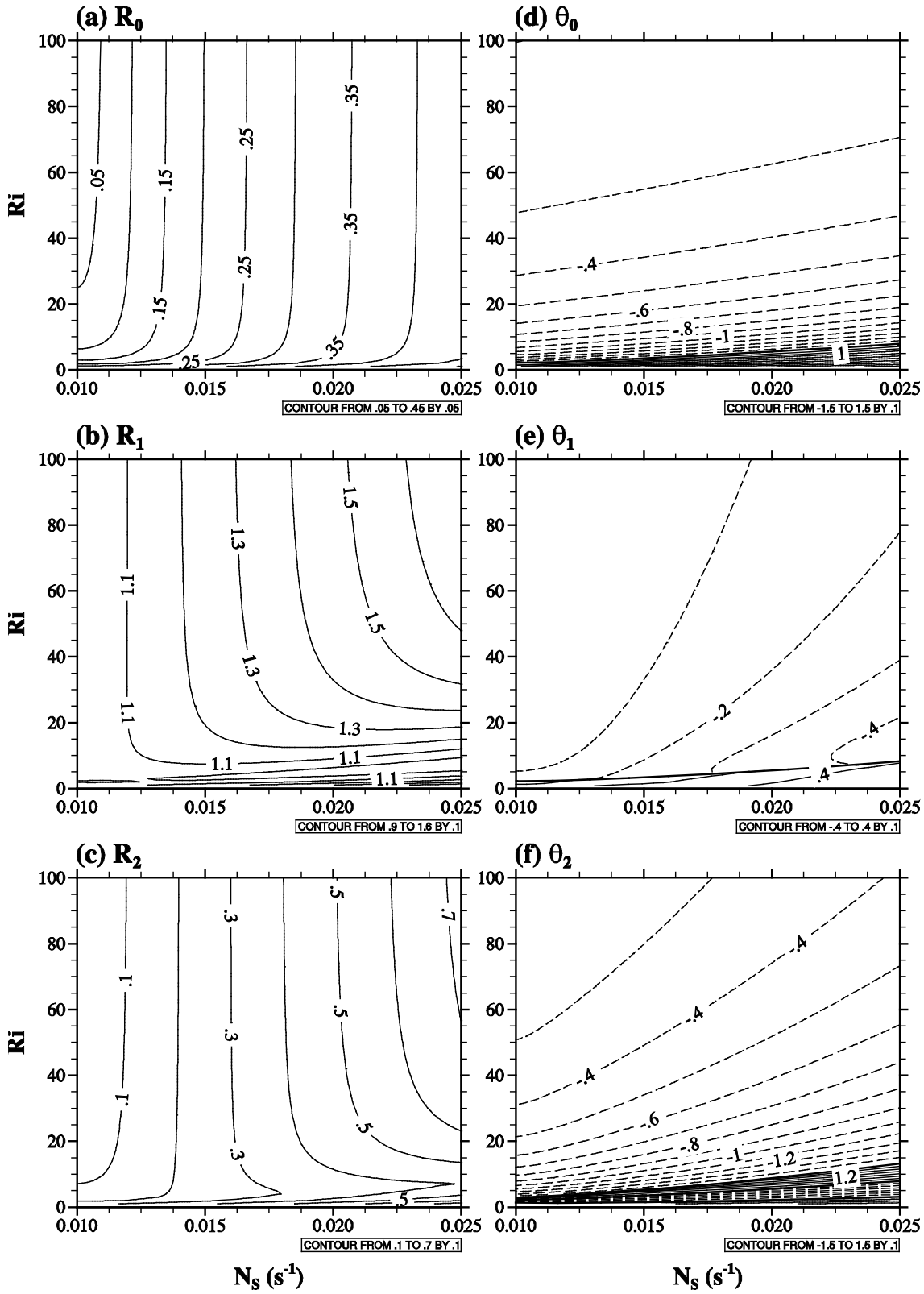
(a) R_0
(d) θ_0
(b) R_1
(e) θ_1
(c) R_2
(f) θ_2
Ri
N_S (s^{-1})
CONTOUR FROM .05 TO .45 BY .05
CONTOUR FROM -1.5 TO 1.5 BY .1
CONTOUR FROM .9 TO 1.6 BY .1
CONTOUR FROM -.4 TO .4 BY .1
CONTOUR FROM .1 TO .7 BY .1
CONTOUR FROM -1.5 TO 1.5 BY .1

Figure 4.6. (a) R_0, (b) R_1, (c) R_2, (d) θ_0, (e) θ_1, and (f) θ_2 as a function of the stratospheric buoyancy frequency and the Richardson number. The values of θ_0, θ_1, and θ_2 are in radian.

$$w_{\mathrm{m}}(z) = -G_{\mathrm{I}(x=0)} Z_0^{\frac{1}{2}} \left\{ \cos\theta_{z0}(R_1 \sin\theta_1 - R_2 \sin\theta_2) + \sin\theta_{z0}(R_1 \cos\theta_1 + R_2 \cos\theta_2) \right\}, \quad (4.16a)$$

$$\begin{aligned} w_{\mathrm{c}}(z) = -F_{\mathrm{R}(x=0)} \frac{N_{\mathrm{T}}}{s\mu} \sin\theta_{z0} \left(Z_1^{\frac{1}{2}} - Z_2^{\frac{1}{2}} \right) \Bigg\{ & \cos\left(\theta_{z0} - \tan^{-1}\frac{1}{2\mu} \right)(R_1 \sin\theta_1 - R_2 \sin\theta_2) \\ & + \sin\left(\theta_{z0} - \tan^{-1}\frac{1}{2\mu} \right)(R_1 \cos\theta_1 - R_2 \cos\theta_2) \Bigg\}. \end{aligned} \quad (4.16b)$$

Because the second terms on the right hand side of Eqs. (4.11b) and (4.11c) do not depend on the stratospheric buoyancy frequency, the terms in braces in Eqs. (4.16a) and (4.16b) determine the characteristics of the waves in the troposphere affected by the wave reflection at the tropopause.

The surface vertical velocity at the center of each forcing is zero and the vertically varying pattern of the vertical velocity at the center of each forcing is like a sine function rather than a cosine function (Fig. 4.2), and our calculation indicates that $R_1\sin\theta_1 - R_2\sin\theta_2$ is almost zero. Accordingly, among the two terms in braces in Eq. (4.16a) [also in Eq. (4.16b)], the second term which is related to $\sin\theta_{z0}$ is dominant. The horizontally symmetric structures of the orographically and convectively forced flows are mainly proportional to $R_1\cos\theta_1 + R_2\cos\theta_2$ and $R_1\cos\theta_1 - R_2\cos\theta_2$, respectively.

Figure 4.7 shows $R_1\cos\theta_1$ and $R_2\cos\theta_2$ as a function of the stratospheric buoyancy frequency and the Richardson number. The dependency of both $R_1\cos\theta_1$ and $R_2\cos\theta_2$ on N_{S} and Ri is similar to that of R_1 (Figs. 4.6b and 4.7). Because of the very similar pattern of $R_1\cos\theta_1$ and $R_2\cos\theta_2$, $R_1\cos\theta_1 - R_2\cos\theta_2$ is almost unity except for the range of N_{S} and Ri near the phase reversal occurrence. For this reason, the amplification of the flow at the center of each forcing by the infinite reflections is effective only for the orographically forced flows. Differences in orographically, convectively, and both orographically and

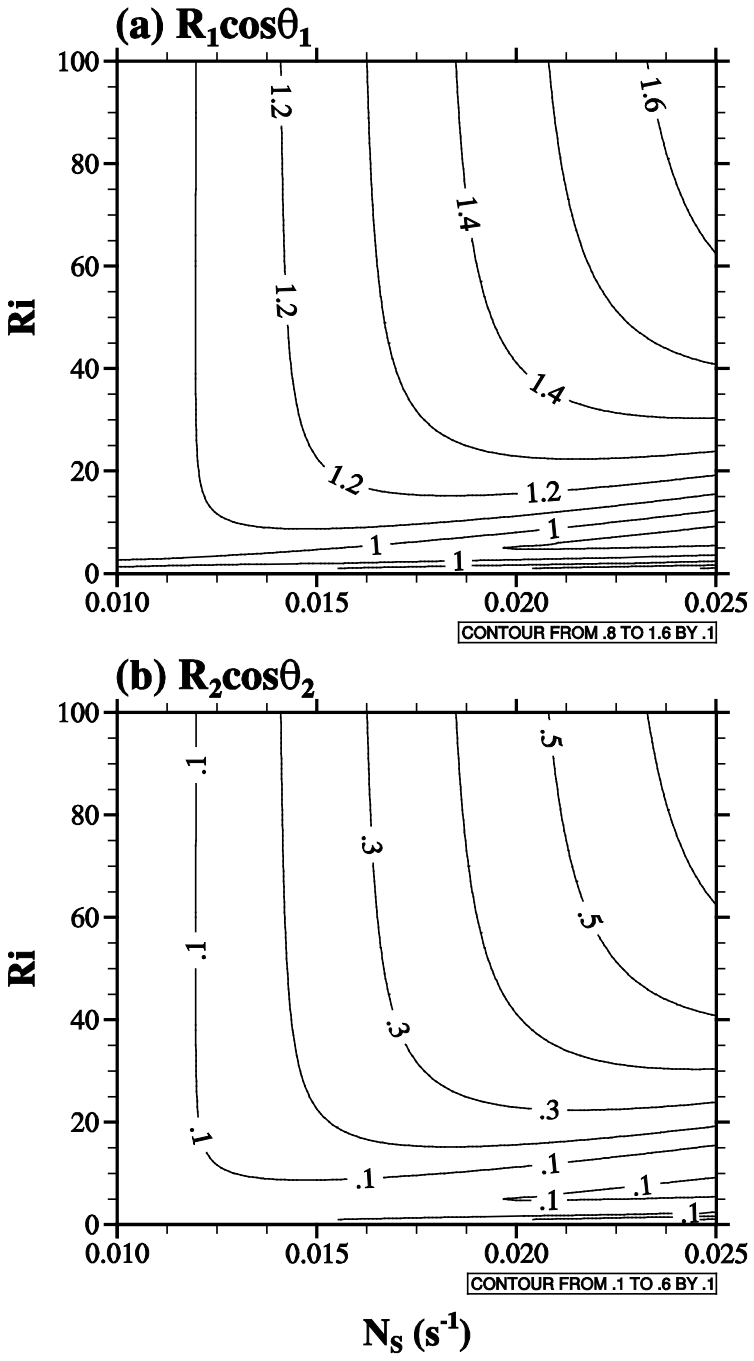

Figure 4.7. (a) $R_1\cos\theta_1$ and (b) $R_2\cos\theta_2$ as a function of the stratospheric buoyancy frequency and the Richardson number.

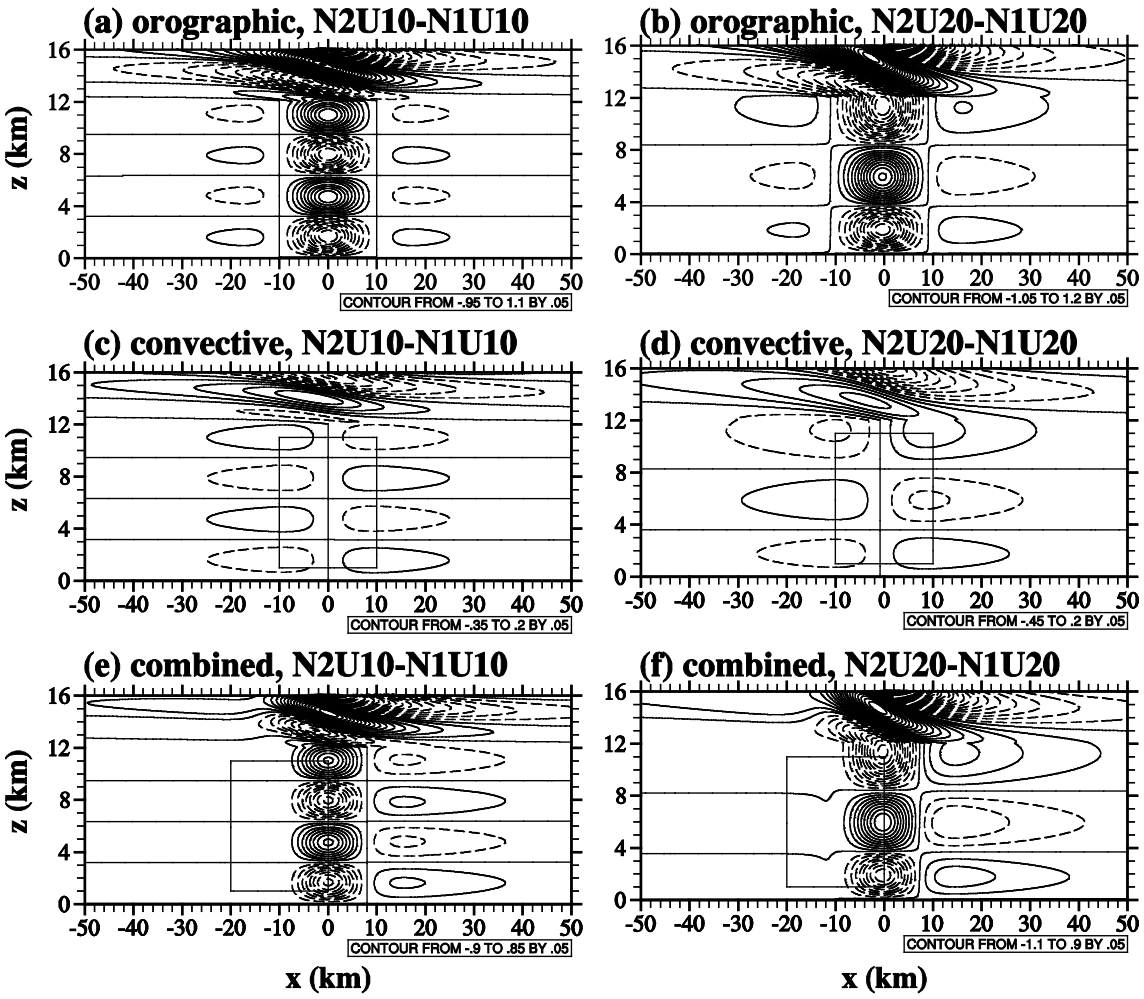

Figure 4.8. Differences in (a, b) orographically, (c, d) convectively, and (e, f) both orographically and convectively forced perturbation vertical velocity fields between the cases of N2U10 and N1U10 for the left column and between the cases of N2U20 and N1U20 for the right column. The center of the convective forcing is located at x = 0 km in (c, d) and x = –10 km in (e, f). The contour line information (unit: m s^{-1}) is given on the bottom of each panel.

convectively forced perturbation vertical velocity fields between the cases with and without stability jump at the tropopause are presented in Figure 4.8. Due to the wave reflection at the tropopause, the symmetric structure of the orographically forced flows in the troposphere is strengthened, and the pattern of the difference is not exactly symmetric for the case with tropospheric wind shear (Figs. 4.8a and 4.8b).

From an analysis similar to that about the horizontally symmetric structures of the orographically and convectively forced flows, it is revealed that the relations of the horizontally anti-symmetric structure of the orographically and convectively forced flows are mainly proportional to $R_1\cos\theta_1 - R_2\cos\theta_2$ and $R_1\cos\theta_1 + R_2\cos\theta_2$, respectively. This can be also seen in Figs. 4.8c and 4.8d. For this reason, the mountain waves tend to maintain the horizontally symmetric structure (Figs 4.2a and 4.2c), and the convectively forced compensating downward motion is strengthened and the maximal vertical velocity is moved downstream in the case with stability jump (Figs. 4.2d and 4.2f). The wave reflection at the tropopause has little effect on the positively combined strong updraft in the deep layer upstream of the mountain [from $x \sim -20$ km to ~ -10 km in Figs. 4.8e and 4.8f].

4.3.3 Gravity-wave momentum fluxes

In a stably stratified atmosphere, orographically/convectively forced internal gravity waves transport momentum vertically. The vertical flux of horizontal momentum can be obtained analytically by using the solutions of u and w, which is defined as

$$M \equiv \rho_0 \int_{-\infty}^{\infty} uw dx. \tag{4.17}$$

Here, ρ_0 is the reference air density. In this study, we consider the flows forced by the two forcings, and the resultant flows are obtained by the linear superposition of the flows forced by individual forcings. For this reason, the total momentum flux is divided into three components as follows.

$$\rho_0 \int_{-\infty}^{\infty} (u_{\mathrm{m}} + u_{\mathrm{c}})(w_{\mathrm{m}} + w_{\mathrm{c}})dx = M_{\mathrm{m}} + M_{\mathrm{c}} + M_{\mathrm{mc}}, \tag{4.18a}$$

where

$$M_{\mathrm{m}} = \rho_0 \int_{-\infty}^{\infty} u_{\mathrm{m}} w_{\mathrm{m}} dx, \tag{4.18b}$$

$$M_{\mathrm{c}} = \rho_0 \int_{-\infty}^{\infty} u_{\mathrm{c}} w_{\mathrm{c}} dx, \tag{4.18c}$$

$$M_{\mathrm{mc}} = \rho_0 \int_{-\infty}^{\infty} (u_{\mathrm{m}} w_{\mathrm{c}} + u_{\mathrm{c}} w_{\mathrm{m}}) dx. \tag{4.18d}$$

The total momentum flux has orographically forced component M_{m}, convectively forced component M_{c}, and component due to the nonlinear interaction between orographically and convectively forced components M_{mc}. The momentum flux components M_{m}, M_{c}, and M_{mc} in the stratosphere ($z > H$) are obtained as follows.

$$M_{\mathrm{m}} = -\frac{\rho_0 U_0^3}{4N_{\mathrm{T}}} \left(\frac{h_{\mathrm{m}} N_{\mathrm{T}}}{U_0} \right)^2 \left(\frac{N_{\mathrm{S}}}{N_{\mathrm{T}}} \right) \left\{ R_1^2 + R_2^2 - 2R_1 R_2 \cos\left(\theta_1 - \theta_2 + 2\theta_{H0} \right) \right\}, \tag{4.19}$$

$$M_{\mathrm{c}} = -\frac{\rho_0 U_0^3}{N_{\mathrm{T}}}\left(\frac{g q_0 a_{\mathrm{c}}}{c_p T_0 N_{\mathrm{T}} U_0^2}\right)^2 \ln\left\{\frac{\left(a_{\mathrm{c}}+b_{\mathrm{c}}\right)^2}{4 a_{\mathrm{c}} b_{\mathrm{c}}}\right\}\times$$
$$\frac{\dfrac{N_{\mathrm{T}}^2 Z_{H0}^{-1}}{s^2\mu^2}\left\{Z_{H1}^{\frac{1}{2}}\cos\left(\theta_{10}-\tan^{-1}\dfrac{1}{2\mu}\right)-Z_{H2}^{\frac{1}{2}}\cos\left(\theta_{20}-\tan^{-1}\dfrac{1}{2\mu}\right)\right\}^2\times}{\left(\dfrac{N_{\mathrm{S}}}{N_{\mathrm{T}}}\right)\left\{R_1^2+R_2^2-2R_1R_2\cos\left(\theta_1-\theta_2+2\theta_{H0}\right)\right\},} \tag{4.20}$$

$$M_{\mathrm{mc}} = -\frac{\rho_0 U_0^3}{N_{\mathrm{T}}}\left(\frac{g q_0 a_{\mathrm{c}}}{c_p T_0 N_{\mathrm{T}} U_0^2}\right)\left(\frac{h_{\mathrm{m}} N_{\mathrm{T}}}{U_0}\right)\times$$
$$\frac{2a_{\mathrm{m}}\left(c_{\mathrm{c}}-c_{\mathrm{m}}\right)\left\{\dfrac{1}{\left(a_{\mathrm{c}}+a_{\mathrm{m}}\right)^2+\left(c_{\mathrm{c}}-c_{\mathrm{m}}\right)^2}-\dfrac{1}{\left(b_{\mathrm{c}}+a_{\mathrm{m}}\right)^2+\left(c_{\mathrm{c}}-c_{\mathrm{m}}\right)^2}\right\}\times}{\dfrac{N_{\mathrm{T}} Z_{H0}^{-\frac{1}{2}}}{s\mu}\left\{Z_{H1}^{\frac{1}{2}}\cos\left(\theta_{10}-\tan^{-1}\dfrac{1}{2\mu}\right)-Z_{H2}^{\frac{1}{2}}\cos\left(\theta_{20}-\tan^{-1}\dfrac{1}{2\mu}\right)\right\}\times} \tag{4.21}$$
$$\left(\frac{N_{\mathrm{S}}}{N_{\mathrm{T}}}\right)\left\{R_1^2+R_2^2-2R_1R_2\cos\left(\theta_1-\theta_2+2\theta_{H0}\right)\right\}.$$

The orographically forced momentum flux component can be written as

$$M_{\mathrm{m}} = -\frac{\rho_0 U_0^3}{4N_{\mathrm{T}}}\mathrm{Fr}^{-2} c_3. \tag{4.22}$$

The parameter Fr = $U_0/(h_{\mathrm{m}}N_{\mathrm{T}})$ is the Froude number and is the nonlinearity factor of orographically forced internal gravity waves. The parameter $c_3 = (N_{\mathrm{S}}/N_{\mathrm{T}})\{R_1^2 + R_2^2 - 2R_1R_2\cos(\theta_1 - \theta_2 + 2\theta_{H0})\}$ is related to the wave transmission through the tropopause. When $N_{\mathrm{T}} = N_{\mathrm{S}}$ and $s = 0$, M_{m} is equal to the momentum flux given in Smith and Lin (1982) in which uniform basic-state wind and static stability are considered.

The convectively forced momentum flux component can be written as

$$M_{\mathrm{c}} = -\frac{\rho_0 U_0^3}{N_{\mathrm{T}}} \mu_{\mathrm{NL}}^2 c_1 c_2^2 c_3. \tag{4.23}$$

The parameter $\mu_{\mathrm{NL}} = (gq_0a_{\mathrm{c}})/(c_pT_0N_{\mathrm{T}}U_0^2)$ is the nonlinearity factor of thermally forced internal gravity waves (Chun and Baik 1994). The parameter $c_1 = \ln\{(a_{\mathrm{c}} + b_{\mathrm{c}})^2/4a_{\mathrm{c}}b_{\mathrm{c}}\}$ is related to the horizontal structure of the convective forcing. The parameter c_2^2 [underlined term in Eq. (4.20)] is related to the basic-state wind speed, tropospheric static stability, and the bottom and top heights of the convective forcing. The transmission related parameter c_3 is also multiplied. When $N_{\mathrm{T}} = N_{\mathrm{S}}$ and $s = 0$, M_{c} is equal to the momentum flux given in Chun and Baik (1998) in which uniform basic-state wind and static stability are considered.

The component caused by the nonlinear interaction between orographically and convectively forced internal gravity waves can be written as

$$M_{\mathrm{mc}} = -\frac{\rho_0 U_0^3}{N_{\mathrm{T}}} \mu_{\mathrm{NL}} \mathrm{Fr}^{-1} \frac{2\left(b_{\mathrm{c}} - a_{\mathrm{c}}\right)\left(a_{\mathrm{c}} + b_c + 2a_{\mathrm{m}}\right)\left(c_{\mathrm{c}} - c_{\mathrm{m}}\right)}{\left\{\left(a_{\mathrm{c}} + a_{\mathrm{m}}\right)^2 + \left(c_{\mathrm{c}} - c_{\mathrm{m}}\right)^2\right\}\left\{\left(b_{\mathrm{c}} + a_{\mathrm{m}}\right)^2 + \left(c_{\mathrm{c}} - c_{\mathrm{m}}\right)^2\right\}} c_2 c_3. \tag{4.24}$$

Equation (4.24) is the geometric average of Eqs. (4.22) and (4.23) except for the parameter related to the horizontal structure, which depends on the location of the convection relative to the mountain and the horizontal scales of the mountain and convection. The underlined term in Eq. (4.21) related to the horizontal structures of the mountain and convection is exactly the same as "cross terms proportional to *hQ*" in Eq. (65) of Smith and Lin (1982). The sign of the nonlinear interaction component depends

on the location of the convection relative to the mountain. When the convection center is equal to the mountain center ($c_c = c_m$), M_{mc} becomes zero. The nonlinear interaction component in the case with the convection center being located upslope (downslope) of the mountain has a positive (negative) value. As a function of the location of the convection relative to the mountain ($c_c - c_m$), M_{mc} has an anti-symmetric structure for given parameter values. In the case of $c_c - c_m < 0$ ($c_c - c_m > 0$), the positive maximum (negative minimum) of M_{mc} occurs when $6(c_c - c_m)^2 = a_c^2\{(r^4 + 14r^2 + 1)^{1/2} - (r^2 + 1)\}$, where $r = b_c/a_c$. In this study ($r = 5$), $(c_c - c_m)_{max/min} = \pm 0.93 a_c = \pm 9.3$ km.

Figure 4.9 shows the momentum fluxes forced by the mountain, convection, and orographic-convective interaction as a function of the stratospheric buoyancy frequency and the Richardson number. In this calculation, $\rho_0 = 0.7$ kg m^{-3} and $c_c - c_m = -10$ km are used. In an inviscid atmosphere without a critical level, the momentum flux above an a forcing does not vary with height and internal gravity waves that transport energy upward have a negative momentum flux (Eliassen and Palm 1960; Chun and Baik 1998). At/Near the boundary where the phase angle reversal occurs, the discontinuity of the momentum flux exists. For a given N_S, the magnitude of M_m (M_c) decreases (increases) as Ri increases (Figs 4.9a and 4.9b). M_c is more sensitive to Ri (also to s) compared to M_m. For a given Ri, both components M_m and M_c become large in magnitude as the stratospheric buoyancy frequency increases. The dependency of the magnitude of M_{mc} on N_S and Ri is similar to that of M_c (Fig. 4.9c). As discussed in section 4.3.2, the wave reflection at the tropopause strengthens the symmetric (anti-symmetric) structure of the orographically (convectively) forced flows. For this reason, the dependency of each momentum flux component on N_S and Ri is similar to that of $R_1\cos\theta_1 + R_2\cos\theta_2$ on N_S and Ri (Fig. 4.7).

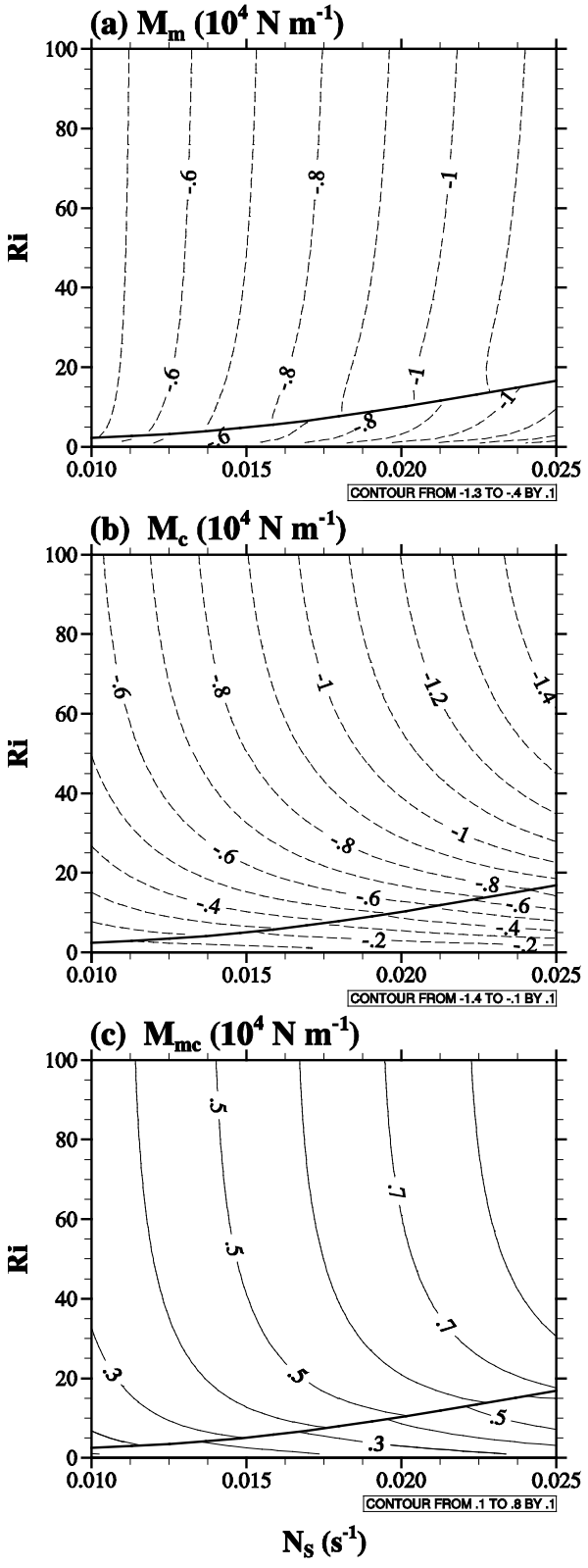
(a) M_m (10^4 N m^{-1})
Ri
CONTOUR FROM -1.3 TO -.4 BY .1
(b) M_c (10^4 N m^{-1})
Ri
CONTOUR FROM -1.4 TO -.1 BY .1
(c) M_{mc} (10^4 N m^{-1})
Ri
CONTOUR FROM .1 TO .8 BY .1
N_S (s^{-1})

Figure 4.9. Momentum fluxes forced by the (a) mountain, (b) convection, and (c) orographic-convective interaction as a function of the stratospheric buoyancy frequency and the Richardson number. Here, $c_c - c_m = -10$ km is used.

Note that the nonlinear interaction component has the same order of magnitude as each of the orographically and convectively components. Depending on the location of the convection relative to the mountain, the total momentum flux can be increased or decreased due to the orographic-convective interaction.

5 Dynamics of orographic-convective flows in a single layer nonhydrostatic atmosphere

5.1 Introduction

There are many mesoscale phenomena whose basic dynamics can be understood by theoretically examining the response of a stably stratified atmosphere to specified thermal forcing such as condensational heating in convective clouds or evaporative cooling of raindrops in the boundary layer. Along this research line, extensive studies have been performed to better understand the dynamics of thermally forced flows [see references in Lin (2007)]. The equation systems used so far are diverse, ranging from the simplest system of two dimensions and constant basic-state wind speed and buoyancy frequency (e.g., Lin and Smith 1986) to complex systems of, for example, three dimensions and shear flow with a critical level (e.g., Han and Baik 2010).

One of the troublesome factors in theoretical studies of thermally forced flows is the nonhydrostaticity of the airflow system. Hydrostatic approximation, which is valid in a system when the horizontal length scale of motion is much larger than the vertical length scale of motion, simplifies mathematical problems greatly because inertial terms in the vertical momentum equation are neglected under this approximation. However, in some deep convection problems, the vertical length scale of motion can be comparable to the horizontal length scale of motion, thus invalidating the hydrostatic approximation. In spite of this fact, very little attention has been paid to nonhydrostatic effects on convectively forced mesoscale flows.

Many studies of nonhydrostatic effects on orographically forced mesoscale flows, especially mountain waves, have been made. Queney (1948) indicated that in a nonhydrostatic system with vertically uniform basic-state wind speed and static stability, lee waves with the horizontal wavelength equal to $2\pi k_c^{-1}$, where k_c is the critical horizontal wavenumber, are evident when the half-width of a bell-shaped mountain is $\sim k_c^{-1}$. Smith (1979) overviewed the influence of mountains on the atmosphere. He classified the solution for the vertical velocity in wavenumber space into two modes depending on the sign of $l^2 - k^2$, where l is the Scorer parameter that is determined by the vertical structure of the basic-state wind speed and static stability. The solution with $k^2 < l^2$ represents vertically propagating gravity waves (propagating mode), and the solution with $k^2 > l^2$ represents vertically decaying gravity waves (evanescent mode).

In vertically structured atmospheres, vertically propagating gravity waves can be reflected according to the vertical structure of the Scorer parameter. The reflected gravity waves can be trapped in the lower atmosphere, and these trapped waves can form lee waves. Keller (1994) investigated nonhydrostatic effects on mountain waves in the presence of wind shear in the troposphere and a stability jump between the troposphere and stratosphere on the basis of Wurtele et al. (1987). Broutman et al. (2002, 2003) examined the behaviors of mountain waves in vertically structured hydrostatic and nonhydrostatic atmospheres using the ray theory. The nonhydrostatic effects on lee waves that are produced by a temperature inversion were investigated by Vosper (2004) and Teixeira et al. (2017).

A number of observational studies (Alexander et al. 2006; Grimsdell et al. 2010) have reported that convective clouds generate not only vertically propagating gravity

waves but also slantwise/horizontally propagating gravity waves. In a numerical modeling study of Alexander and Holton (2004), the slantwise/horizontally propagating gravity waves are clearly identified in the spectrum of convectively forced gravity waves in a nonhydrostatic atmosphere. To enhance our understanding of the dynamics of the slantwise/horizontally propagating gravity waves forced by convection, in-depth theoretical studies of nonhydrostatic effects on convectively forced gravity waves are required.

It is well-known that the wave energy transported by convectively forced gravity waves is one of the main energy sources that plays an important role in maintaining the circulation of the stratosphere and mesosphere [see references in Fritts and Alexander (2003)]. Many researchers have developed the parameterizations of convectively forced gravity-wave drag for use in large-scale or climate models (Beres 2004; Chun and Baik 1998, 2002; Song and Chun 2005, 2008; Choi and Chun 2011; Kang et al. 2017). Considering that current climate models adopt a nonhydrostatic system (e.g., Marsh et al. 2013; Walters et al. 2014), theoretical studies of nonhydrostatic effects on convectively forced gravity waves can provide some insight into the convectively forced gravity-wave drag parameterization in a nonhydrostatic system.

Using a nondimensional numerical model, Woo et al. (2013) studied nonhydrostatic effects on convectively forced mesoscale flows. They found that an alternating wavy pattern of updrafts and downdrafts appears downstream of the convective forcing and that the horizontal wavelength in the alternating wavy pattern is approximately $2\pi\beta$ (β: nonhydrostaticity factor). These results are consistent with those of Queney (1948). Although Woo et al. (2013) showed nonhydrostatic effects on

convectively forced mesoscale flows, the analysis is not sufficient to present the dynamics of convectively forced mesoscale flows in a nonhydrostatic system, particularly the dynamics of the alternating updrafts and downdrafts downstream of the convective forcing. This motivates the present study.

The main purpose of this study is to theoretically analyze nonhydrostatic effects on convectively forced flows, particularly focusing on the analysis of propagating and evanescent modes. In section 5.2, the governing equations and solutions are presented. In sections 5.3.1 and 5.3.2, nonhydrostatic effects in inviscid-limit and viscid systems are, respectively, presented and discussed. In section 5.3.3, nonhydrostatic effects on gravity-wave momentum flux are presented and discussed.

5.2 Governing equations and solutions

In this study, a two-dimensional, steady-state, nonrotating, Boussinesq airflow system with convective forcing is considered. The equations governing small-amplitude perturbations are expressed as follows.

$$U\frac{\partial u}{\partial x} = -\frac{\partial \pi}{\partial x} - \nu_m u, , \tag{5.1}$$

$$U\frac{\partial w}{\partial x} = -\frac{\partial \pi}{\partial z} + b - \nu_m w, , \tag{5.2}$$

$$U\frac{\partial b}{\partial x} + N^2 w = \frac{g}{c_p T_0} q - \nu_T b, , \tag{5.3}$$

$$\frac{\partial u}{\partial x} + \frac{\partial w}{\partial z} = 0, , \tag{5.4}$$

where u is the perturbation velocity in the x-direction, w is the perturbation velocity in the z-direction, π is the perturbation kinematic pressure, b is the perturbation buoyancy, U is the basic-state wind speed in the x-direction (U is constant with height in this study), v_m is the coefficient of Rayleigh friction, v_T is the coefficient of Newtonian cooling, N is the buoyancy frequency, g is the gravitational acceleration, c_p is the specific heat of air at constant pressure, T_0 is the reference temperature, and q is the convective forcing function.

To solve the above equation system, the Green function method is used (Han and Baik 2009, 2010). First, we obtain the solution for the perturbation vertical velocity in the equation system with line-type convective forcing that is given by

$$q(x) = q_0 \frac{a^2}{x^2 + a^2} \delta(z - h), \tag{5.5}$$

where q_0 and a are the strength and half-width of the bell-shaped convective forcing, respectively, δ is the Dirac delta function, and h is the height at which the line-type convective forcing is located. Then, we obtain the solution for the finite-depth convective forcing by integrating the solution for the perturbation vertical velocity induced by the line-type convective forcing with respect to h.

The following dimensionless variables (with tildes) are introduced (Han and Baik 2012; Woo et al. 2013).

$$x = a\tilde{x},\ a = a\tilde{a},\ z = \frac{U}{N}\tilde{z},\ h = \frac{U}{N}\tilde{h},\ h_1 = \frac{U}{N}\tilde{h}_1,\ h_2 = \frac{U}{N}\tilde{h}_2,$$

$$U = U\tilde{U},\ q = q_0\tilde{q},\ \nu_m = \frac{U}{a}\tilde{\nu}_m,\ \nu_T = \frac{U}{a}\tilde{\nu}_T,$$

$$u = \frac{gq_0a}{c_pT_0NU}\tilde{u},\ w = \frac{gq_0}{c_pT_0N^2}\tilde{w},\ \pi = \frac{gq_0a}{c_pT_0N}\tilde{\pi},\ b = \frac{gq_0a}{c_pT_0U}\tilde{b}. \tag{5.6}$$

After applying the above dimensionless variables to Eqs. (5.1)–(5.5), we obtain nondimensionalized governing equations and line-type convective forcing as follows.

$$\frac{\partial\tilde{u}}{\partial\tilde{x}} = -\frac{\partial\tilde{\pi}}{\partial\tilde{x}} - \tilde{\nu}_m\tilde{u}, \tag{5.7}$$

$$\beta^2\frac{\partial\tilde{w}}{\partial\tilde{x}} = -\frac{\partial\tilde{\pi}}{\partial\tilde{z}} + \tilde{b} - \beta^2\tilde{\nu}_m\tilde{w}, \tag{5.8}$$

$$\frac{\partial\tilde{b}}{\partial\tilde{x}} + \tilde{w} = \tilde{q} - \tilde{\nu}_T\tilde{b}, \tag{5.9}$$

$$\frac{\partial\tilde{u}}{\partial\tilde{x}} + \frac{\partial\tilde{w}}{\partial\tilde{z}} = 0, \tag{5.10}$$

$$\tilde{q}(\tilde{x},\tilde{z}) = \frac{\tilde{a}^2}{\tilde{x}^2 + \tilde{a}^2}\delta(\tilde{z} - \tilde{h}), \tag{5.11}$$

where β (= U/Na) is the nonhydrostaticity factor. Here, the half-width of the bell-shaped convective forcing a represents the horizontal length scale of the convective forcing. Note that the arbitrarily chosen horizontal length scale L is used in Woo et al. (2013). The nonhydrostaticity factor represents the degree of the contribution of the inertial term in the vertical momentum equation [Eq. (5.8)]. Hereafter, tildes are dropped to simplify the

notation.

Equations (5.7)–(5.10) can be combined into a single equation for the perturbation vertical velocity.

$$\left(\frac{\partial}{\partial x}+\nu_m\right)\left(\frac{\partial}{\partial x}+\nu_T\right)\left(\frac{\partial^2 w}{\partial z^2}+\beta^2\frac{\partial^2 w}{\partial x^2}\right)+\frac{\partial^2 w}{\partial x^2}=\frac{\partial^2 q}{\partial x^2}. \tag{5.12}$$

By taking the Fourier transform ($x \rightarrow k$) to Eq. (5.12), the differential equation for w in wavenumber space is obtained.

$$\frac{\partial^2 \hat{w}}{\partial z^2}+m^2\hat{w}=m_0^2\hat{q}, \tag{5.13a}$$

where

$$m^2=-k^2\left\{\frac{1}{(ik+\nu_m)(ik+\nu_T)}+\beta^2\right\}, \tag{5.13b}$$

$$m_0^2=-\frac{k^2}{(ik+\nu_m)(ik+\nu_T)}, \tag{5.13c}$$

$$\hat{q}=ae^{-ak}\delta(z-h). \tag{5.13d}$$

The general solution of Eq. (5.13a) is

$$\hat{w}_{\mathrm{L}}=A_1e^{imz}+B_1e^{-imz} \quad \text{for } 0\le z\le h, \tag{5.14a}$$

$$\hat{w}_{\mathrm{U}} = A_2 e^{imz} + B_2 e^{-imz} \text{ for } z > h. \tag{5.14b}$$

The coefficients A_1, A_2, B_1, and B_2 can be determined by applying the no-slip bottom boundary condition ($\hat{w}_{\mathrm{L}} = 0$ at $z = 0$), the upper radiation condition ($B_2 = 0$ with $U > 0$), and the interfacial boundary conditions at $z = h$ that are given by

$$\hat{w}_{\mathrm{L}} = \hat{w}_{\mathrm{U}}, \tag{5.15a}$$

$$\frac{\partial \hat{w}_{\mathrm{U}}}{\partial z} - \frac{\partial \hat{w}_{\mathrm{L}}}{\partial z} = a e^{-ak}. \tag{5.15b}$$

Then, the solution for the perturbation vertical velocity induced by the line-type convective forcing in wavenumber space is obtained.

$$\hat{w}_{\mathrm{L}} = i \frac{a m_0^2}{2m} \left\{ e^{im(z+h)} + e^{-im(z-h)} \right\} e^{-ak} \text{ for } 0 \le z \le h, \tag{5.16a}$$

$$\hat{w}_{\mathrm{U}} = i \frac{a m_0^2}{2m} \left\{ e^{im(z+h)} + e^{im(z-h)} \right\} e^{-ak} \text{ for } z > h. \tag{5.16b}$$

To get the solution induced by the finite-depth convective forcing, we integrate Eq. (5.16) with respect to h as follows.

$$\hat{w}_1 = \int_{h_1}^{h_2} \hat{w}_{\mathrm{L}} dh \text{ for } 0 \le z \le h_1, \tag{5.17a}$$

$$\hat{w}_2 = \int_{h_1}^{z} \hat{w}_{\mathrm{U}} dh + \int_{z}^{h_2} \hat{w}_{\mathrm{L}} dh \text{ for } h_1 < z \le h_2, \tag{5.17b}$$

$$\hat{w}_3 = \int_{h_1}^{h_2} \hat{w}_U dh \text{ for } z > h_2. \tag{5.17c}$$

After manipulation, we can obtain the following solution in wavenumber space.

$$\hat{w}_1 = (\hat{\Omega}^+_{+2} - \hat{\Omega}^+_{+1}) - (\hat{\Omega}^-_{-2} - \hat{\Omega}^-_{-1}) \text{ for } 0 \le z \le h_1, \tag{5.18a}$$

$$\hat{w}_2 = (\hat{\Omega}^+_{+2} - \hat{\Omega}^+_{+1}) - (\hat{\Omega}^-_{-2} - \hat{\Omega}^+_{-1}) \text{ for } h_1 < z \le h_2, \tag{5.18b}$$

$$\hat{w}_3 = (\hat{\Omega}^+_{+2} - \hat{\Omega}^+_{+1}) + (\hat{\Omega}^+_{-2} - \hat{\Omega}^+_{-1}) \text{ for } z > h_2, \tag{5.18c}$$

where

$$\hat{\Omega}^{\pm'}_{\pm n} = \frac{am_0^2}{2m^2}\left\{e^{\pm' im(z\pm h_n)} - 1\right\} e^{-ak}. \tag{5.18d}$$

In Eq. (5.18d), n = 1, 2. Each of $\hat{\Omega}^{\pm'}_{\pm n}$ represents the wave component induced by the convective forcing. The superscript of $\hat{\Omega}$ denotes the direction of wave energy propagation, positive (negative) sign denoting upward (downward) wave energy propagation. In the subscript of $\hat{\Omega}$, the positive (negative) sign denotes waves reflected at the surface (non-reflected waves) and n denotes the waves originated from $z = h_n$.

Finally, the solution in physical space is obtained by numerically integrating the real part as below.

$$w_j = \int_0^\infty \mathrm{Re}\left\{\hat{w}_j e^{ikx}\right\} dk = \int_0^\infty w_{jk} dk. \tag{5.19}$$

In Eq. (5.19), j = 1, 2, 3. The Euler forward scheme is used for the numerical integration. The convective forcing is located from $z = h_1 = 1$ to $z = h_2 = 9$. The half-width of the bell-shaped convective forcing is $a = 1$. Hereafter, for simplicity, the perturbation horizontal velocity and the perturbation vertical velocity are called the horizontal velocity and the vertical velocity, respectively.

5.3 Results and discussion

5.3.1 Inviscid-limit system

In an inviscid-limit system, i.e., both ν_m and ν_T are sufficiently small, individual wave components [Eq. (5.18d)] are approximated as

$$\hat{\Omega}_{\pm n}^{\pm'} \simeq \frac{a}{2m^2}\left\{e^{\pm' im(z\pm h_n)} - 1\right\} e^{-ak} . \tag{5.20}$$

In Eq. (5.20), the vertical wavenumber $m = (1 - \beta^2 k^2)^{1/2}$ is real if $k \leq \beta^{-1}$ and purely imaginary if $k > \beta^{-1}$. The wave component in the range of $k \leq \beta^{-1}$, which is sinusoidal with the vertical wavenumber m and propagates vertically, is called the propagating mode. The wave component in the range of $k > \beta^{-1}$, which exponentially decreases with a decay rate of $m' = (\beta^2 k^2 - 1)^{1/2} = -im$, is called the evanescent mode. This classification of wave components has been used in mountain-wave studies (Queney 1948; Smith 1979). Note that the k-boundary of both modes $k_c = \beta^{-1}$ is the critical horizontal wavenumber that was introduced by Queney (1948).

The spectral vertical velocity w_{jk} in Eq. (5.19) is obtained by applying Eq. (5.20) to Eq. (5.18) and choosing the real part of $\hat{w}_j e^{ikx}$. The spectral vertical velocity of the propagating mode ($k \le \beta^{-1}$) is given by

$$w_{1k} = -\frac{a}{m^2} e^{-ak} \sin mz \left\{ \sin\left(kx + mh_2\right) - \sin\left(kx + mh_1\right) \right\} \text{ for } 0 \le z \le h_1, \qquad (5.21a)$$

$$w_{2k} = -\frac{a}{m^2} e^{-ak} \left\{ \sin mz \sin\left(kx + mh_2\right) + \cos mh_1 \cos\left(kx + mz\right) - \cos kx \right\}$$

$$\text{for } h_1 < z \le h_2, \qquad (5.21b)$$

$$w_{3k} = \frac{a}{m^2} e^{-ak} \left(\cos mh_2 - \cos mh_1\right) \cos\left(kx + mz\right) \text{ for } z > h_2, \qquad (5.21c)$$

whereas the spectral vertical velocity of the evanescent mode ($k > \beta^{-1}$) is given by

$$w'_{1k} = -\frac{a}{m'^2} e^{-ak} \sinh m'z \left(e^{-m'h_2} - e^{-m'h_1}\right) \cos kx \text{ for } 0 \le z \le h_1, \qquad (5.22a)$$

$$w'_{2k} = \frac{a}{m'^2} e^{-ak} \left(e^{-m'h_2} \sinh m'z + e^{-m'z} \cosh m'h_1 - 1\right) \cos kx \text{ for } h_1 < z \le h_2, \qquad (5.22b)$$

$$w'_{3k} = -\frac{a}{m'^2} e^{-ak} e^{-m'z} \left(\cosh m'h_2 - \cosh m'h_1\right) \cos kx \text{ for } z > h_2. \qquad (5.22c)$$

Figure 5.1 shows the vertical velocity fields in the cases of the nonhydrostaticity factor β = 0.1, 0.3, 0.5, and 1 in the inviscid-limit system. For β = 0.1, the flow is close to the hydrostatic flow (Fig. 1a). As β increases, the flow gradually deviates from the hydrostatic flow and becomes more nonhydrostaic. For β = 0.3, 0.5, and 1, an alternating

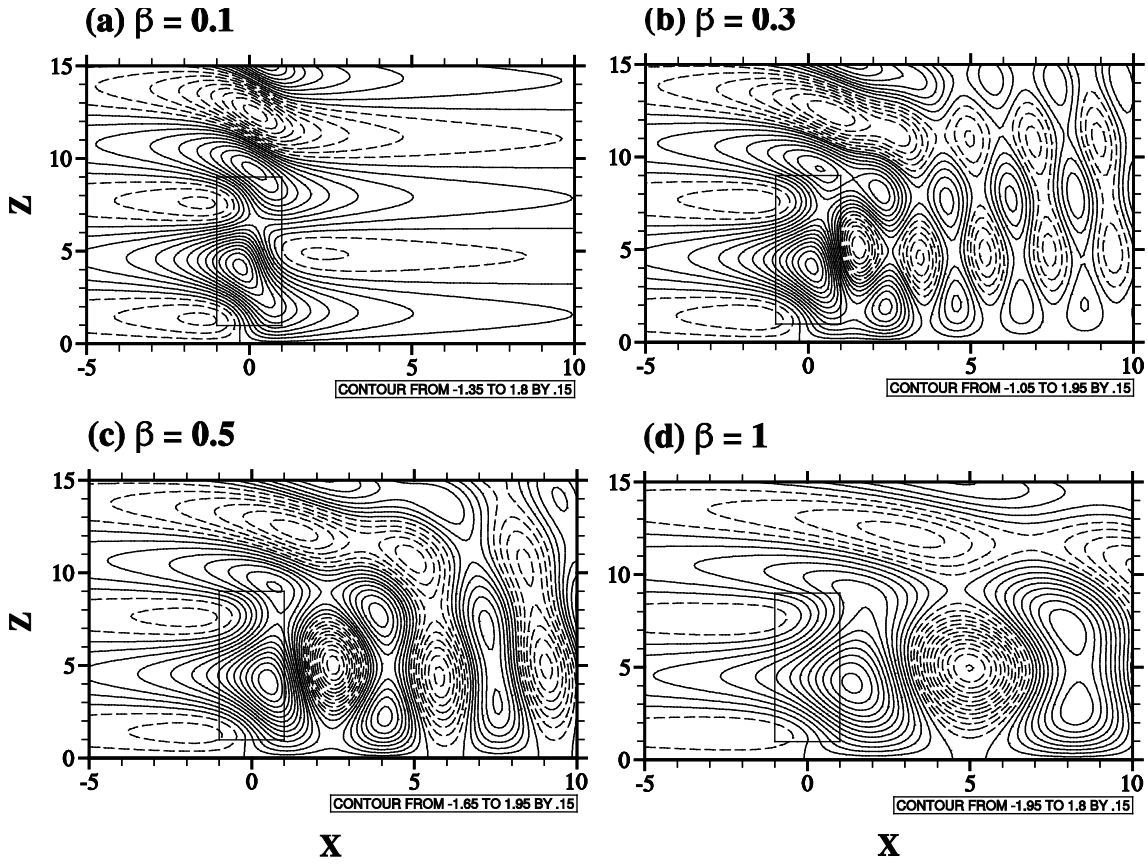

Figure. 5.1. Vertical velocity fields in the cases of β = (a) 0.1, (b) 0.3, (c) 0.5, and (d) 1 in the inviscid-limit system. The rectangle in each panel represents the concentrated convective forcing region. The contour line information is given at the bottom of each panel.

wavy pattern of updrafts and downdrafts appears downstream of the convective forcing (Figs. 5.1b–d). The horizontal wavelength ($2\pi k^{-1}$) of the alternating updrafts and downdrafts is $2\pi\beta$, which is 1.88 for $\beta = 0.3$, 3.14 for $\beta = 0.5$, and 6.28 for $\beta = 1$, where $k = k_c$. Note that the dimensional horizontal wavelength of the alternating updrafts and downdrafts is $2\pi U/N$, which is fixed for uniform basic-state wind speed and static stability. The nonhydrostaticity factor β can be controlled by changing the half-width of the bell-shaped convective forcing a for given environmental conditions (fixed U and N). Using Eq. (5.6), it can be easily seen that the alternating updrafts and downdrafts downstream of the convective forcing with the horizontal wavelength $2\pi U/N$ are generated as a decreases (β increases) in a dimensional frame. The alternating updrafts and downdrafts are almost horizontally propagating resonant waves. As the horizontal wavenumber k approaches k_c, the vertical wavenumber m of the propagating mode and the decay rate m' of the evanescent mode in the denominator of the wave components approach zero, thus amplifying corresponding wave components [see Eqs. (5.21) and (5.22)].

In their numerical modeling study, Woo et al. (2013) also found that the alternating updraft and downdraft cells appear downstream of the convective forcing and that the horizontal length scale of each cell is $\pi\beta$. Woo et al. (2013) speculated that the alternating updraft and downdraft cells are produced by the superposition of the horizontally propagating waves of the propagating mode and the horizontally wavy pattern of the evanescent mode. We calculate the propagating mode and evanescent mode of the vertical velocity field in the case of $\beta = 0.5$ (Fig. 5.2). As speculated in Woo et al. (2013), the evanescent mode exhibits a horizontally wavy pattern (Fig. 5.2b). However,

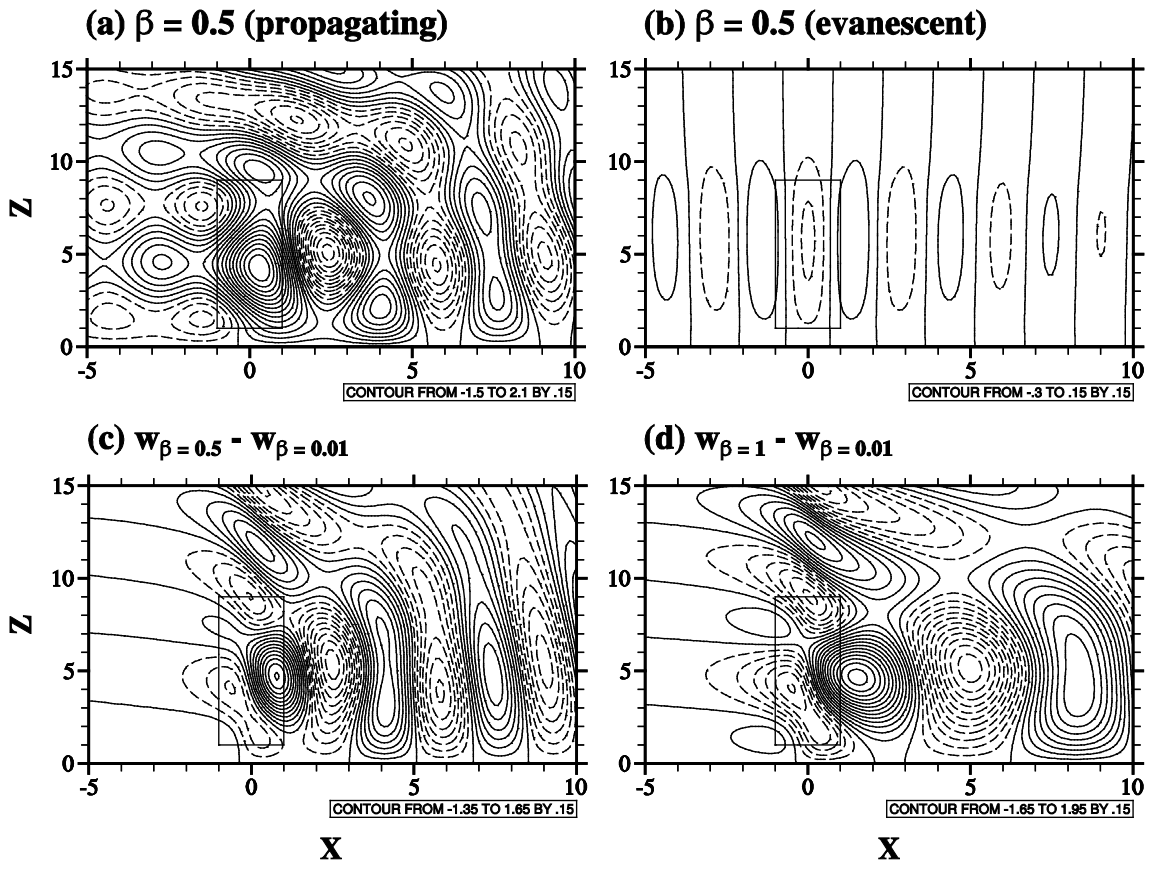

Figure 5.2. Vertical velocity fields in the case of β = 0.5: (a) propagating mode and (b) evanescent mode. Differences in vertical velocity field between the cases of (a) β = 0.5 and β = 0.01 and (d) β = 1 and β = 0.01. The rectangle in each panel represents the concentrated convective forcing region. The contour line information is given at the bottom of each panel. The inviscid-limit system is considered.

the vertical wavy pattern upstream of the convective forcing seems to be independent of β (Fig. 5.1). Differences in vertical velocity field between β = 0.5 and β = 0.01 (hydrostatic-limit system) (Fig. 5.2c) and between β = 1 and β = 0.01 (Fig.5. 2d) show that the nonhydrostatically generated alternating updrafts and downdrafts downstream of the convective forcing do not exhibit a wavy pattern in the vertical direction, so the vertical wavy pattern downstream of the convective forcing in Fig. 5.1 is also the β-independent hydrostatic-limit flow. Thus, it is deduced that the wavy pattern of the evanescent mode downstream of the convective forcing play a role in flattening the horizontally undulating pattern of the β-independent hydrostatic-limit flow like the role of the evanescent mode on the upstream of the convective forcing. In addition, the flow of the evanescent mode is much weaker than that of the propagating mode. For these reasons, in this study the alternating updrafts and downdrafts downstream of the convective forcing are regarded as the propagating mode.

5.3.2 Viscid system

In a viscid system that includes the Rayleigh friction and Newtonian cooling, the real part of the individual spectral wave components [Eqs. (5.18d) and (5.19)] are expressed as

$$\begin{aligned}\Omega_{\pm nk}^{\pm'} = \frac{a}{2}\Big[& X_R \left\{ e^{\mp' M_I (z \pm h_n)} \cos\left(kx \pm' M_R (z \pm h_n)\right) - \cos kx \right\} \\ & - X_I \left\{ e^{\mp' M_I (z \pm h_n)} \sin\left(kx \pm' M_R (z \pm h_n)\right) - \sin kx \right\} \Big],\end{aligned} \tag{5.23a}$$

where

$$X_R + iX_I \equiv \frac{m_0^2}{m^2} = \frac{\left\{1-\beta^2(k^2-\nu_m\nu_T)\right\} - i\left\{\beta^2 k(\nu_m+\nu_T)\right\}}{\left\{1-\beta^2(k^2-\nu_m\nu_T)\right\}^2 + \left\{\beta^2 k(\nu_m+\nu_T)\right\}^2}\ , \tag{5.23b}$$

$$m = M_R + iM_I$$
$$= \begin{cases} \dfrac{k(R^2+I^2)^{1/4}}{\sqrt{(k^2+\nu_m^2)(k^2+\nu_T^2)}}\left[\cos\left(\dfrac{1}{2}\tan^{-1}\dfrac{I}{R}\right) + i\sin\left(\dfrac{1}{2}\tan^{-1}\dfrac{I}{R}\right)\right] \text{ for } R \geq 0, \\ \dfrac{k(R^2+I^2)^{1/4}}{\sqrt{(k^2+\nu_m^2)(k^2+\nu_T^2)}}\left[-\sin\left(\dfrac{1}{2}\tan^{-1}\dfrac{I}{R}\right) + i\cos\left(\dfrac{1}{2}\tan^{-1}\dfrac{I}{R}\right)\right] \text{ for } R < 0, \end{cases} \tag{5.23c}$$

$$R = (k^2 - \nu_m\nu_T) - \beta^2(k^2+\nu_m^2)(k^2+\nu_T^2), \tag{5.23d}$$

$$I = (\nu_m + \nu_T)k. \tag{5.23e}$$

In the viscid system, the propagating mode and evanescent mode cannot be explicitly separated because the vertically propagating component with the vertical wavenumber M_R and the vertically decaying component with a decay rate M_I exist simultaneously in the entire range of k. In this study, we consider the case in which the coefficient of Rayleigh friction is equal to that of Newtonian cooling to examine a general role of the dissipation terms. Hereafter, we refer to $\nu = \nu_m = \nu_T$ as the viscous coefficient.

Figure 5.3 shows M_R, M_I, and R as a function of the horizontal wavenumber k in the cases of ν = 0.01, 0.3, 0.7, and 0.9. The nonhydrostaticity factor β is specified as 0.5. For ν = 0.01, M_R and M_I are similar to m and m' in the inviscid-limit case, respectively (Fig. 5.3a). Similar to the inviscid-limit case, M_R (M_I) is dominant in the range of $k \leq k_c$ ($k > k_c$), whereas M_I (M_R) is almost zero in the range of $k \geq k_c$ ($k < k_c$) (Fig. 3a). Noting that the vertical wavenumber M_R is larger (smaller) than M_I when R is positive (negative), we classify the propagating mode and evanescent mode based on the sign of R. The k-range

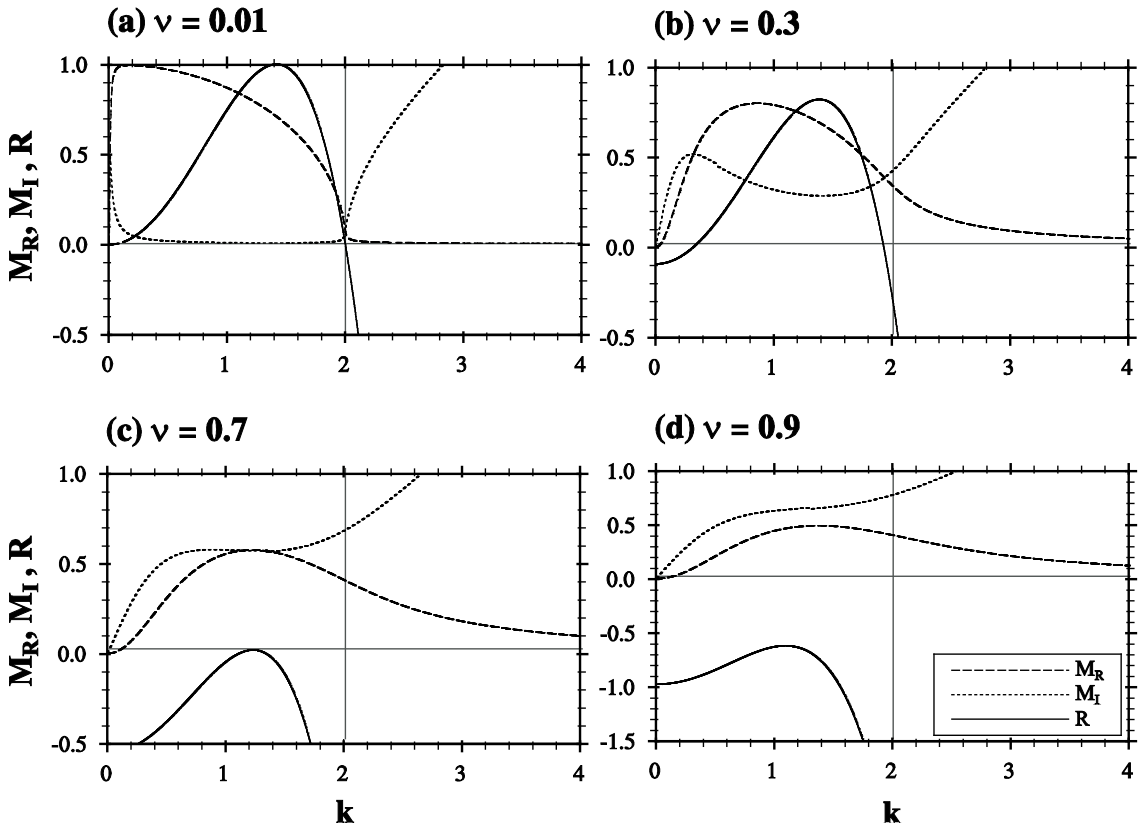

Figure 5.3. M_R, M_I, and R as a function of the horizontal wavenumber k in the cases of β = 0.5 and ν = (a) 0.01, (b) 0.3, (c) 0.7, and (d) 0.9.

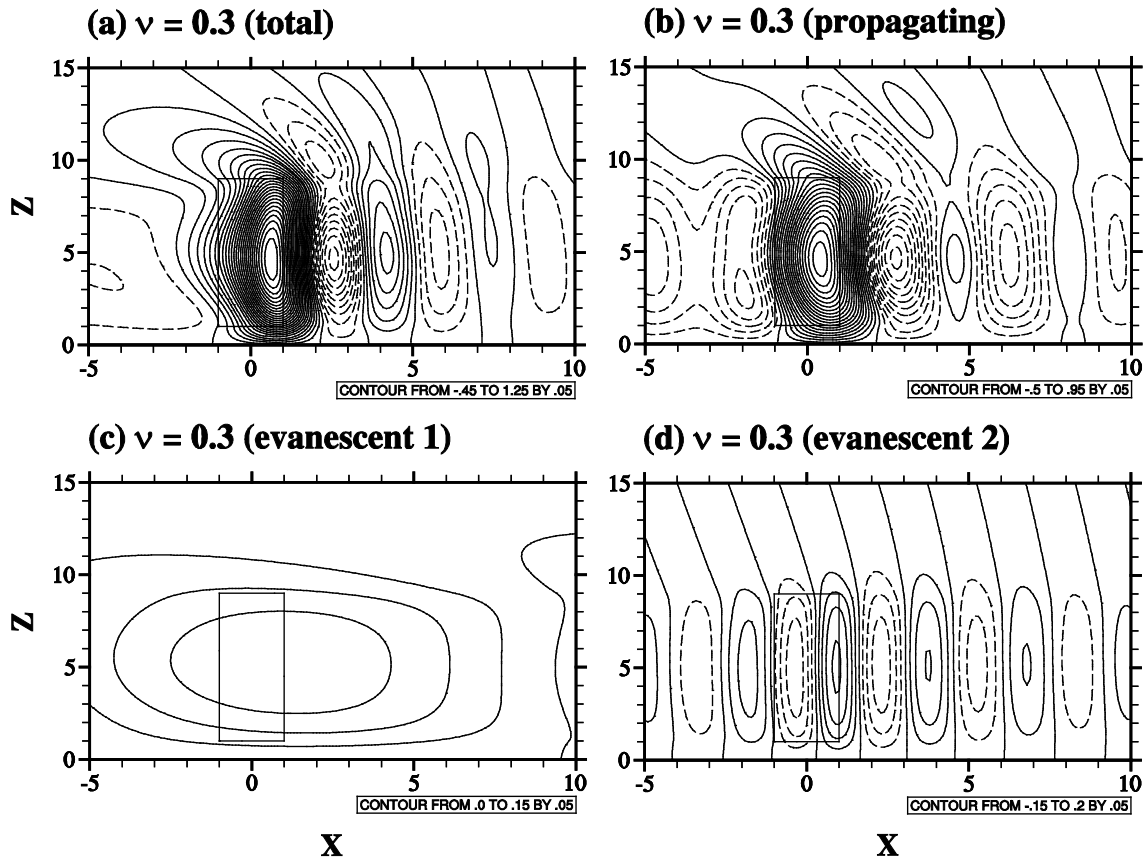

Figure 5.4. Vertical velocity fields in the case of β = 0.5 and ν = 0.3: (a) total, (b) propagating mode, (c) evanescent mode 1, and (d) evanescent mode 2. The rectangle in each panel represents the concentrated convective forcing region. The contour line information is given at the bottom of each panel.

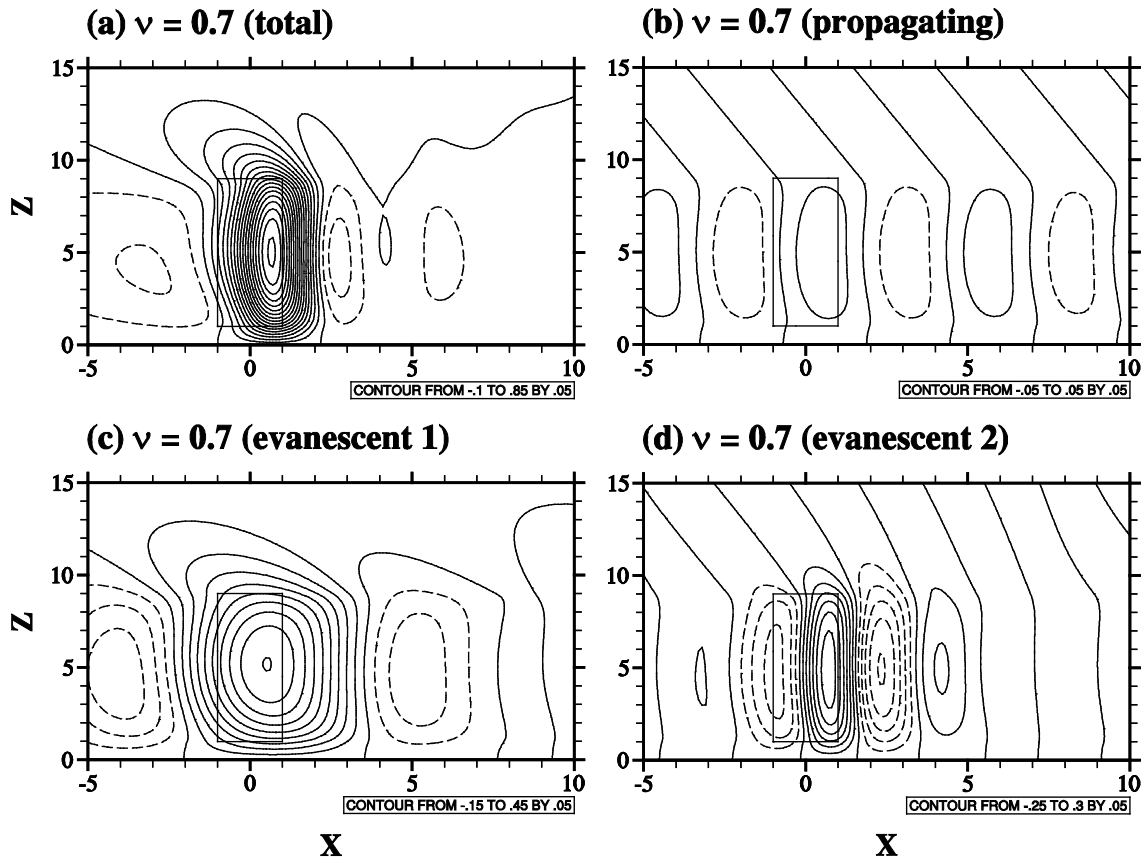

Figure 5.5. The same as Fig. 5.4 except for ν = 0.7.

in which R is positive is referred to as the propagating mode in the viscid system. The evanescent mode with k smaller (larger) than the k-minimum (maximum) in the k-range of the propagating mode is referred to as evanescent mode 1 (2). As ν increases, the k-range of the propagating mode becomes narrow and only the evanescent mode exists if ν exceeds a critical value. The critical viscous coefficient $\nu_c = 1/(2\sqrt{2}\beta)$ can be obtained under the condition that $R = 0$ does not have a solution. For $\beta = 0.5$, ν_c is 0.707.

Figure 5.4 shows the total vertical velocity field and the vertical velocity fields of the propagating mode, evanescent mode 1, and evanescent mode 2 in the case of $\beta = 0.5$ and $\nu = 0.3$. Similar to the inviscid-limit case, the alternating updrafts and downdrafts are clearly observed (Fig. 5.4a). The boundary of k between the propagating mode and evanescent mode 1 (2) is $k = 0.31$ (1.93), and the corresponding horizontal wavelength is 20.27 (3.26). In this case, the contribution of evanescent mode 1 to the total flow is not significant, while the other two modes, that is, the propagating mode and evanescent mode 2, play similar roles to the two modes in the inviscid-limit system. The alternating updrafts and downdrafts have a horizontal wavelength longer than that in the inviscid-limit system, and they weaken as further going downstream.

Figure 5.5 is the same as Fig. 5.4 except for $\nu = 0.7$, a larger viscous coefficient. Strong updraft near the convective forcing center, broad compensating downdraft upstream of the convective forcing, and narrow compensating downdraft downstream of the convective forcing are the major characteristics of the total vertical velocity field (Fig. 5.5a). The boundary of k between the propagating mode and evanescent mode 1 (2) is $k = 1.11$ (1.34), and the corresponding horizontal wavelength is 5.66 (4.69). When the flow system is strongly viscous, the alternating updrafts and downdrafts are almost dissipated

due to the very narrow k-range of the propagating mode. Evanescent modes 1 and 2 are dominant modes, and the contribution of the propagating mode to the total field is minor.

5.3.3 Gravity-wave momentum flux

To examine nonhydrostatic effects on gravity-wave momentum flux, the vertical flux of integrated horizontal momentum is derived by integrating the product of the spectral vertical velocity and the spectral horizontal velocity that is obtained using the Fourier-transformed continuity equation [$\hat{u}_j = (i/k)\partial\hat{w}_j/\partial z$].

$$M_j = \int_0^\infty M_{jk}\,dk = \int_0^\infty \lim_{L_x\to\infty} \frac{1}{L_x}\int_{-L_x/2}^{L_x/2} u_j w_j\,dx\,dk = \frac{1}{2}\int_0^\infty u_{jk} w_{jk}\,dk, \tag{5.24}$$

where L_x is the sufficiently large horizontal domain size and j = 1, 2, 3 depending on z [Eq. (5.18)]. Here, the orthogonality of the sinusoidal function is used.

In the inviscid-limit system, the gravity-wave momentum flux M_{2k} of the propagating mode for $h_1 < z \le h_2$ is

$$M_{2k} = -\frac{a^2}{2m^3 k} e^{-2ak}(\cos mh_2 - \cos mh_1)(\cos mz - \cos mh_1). \tag{5.25}$$

The gravity-wave momentum flux below the convective forcing is $M_{1k} = M_{2k}\,(z = h_1) = 0$. The gravity-wave momentum flux above the convective forcing is $M_{3k} = M_{2k}\,(z = h_2)$ = constant and satisfies the Eliassen-Palm theorem (Eliassen and Palm 1960). Note that the evanescent mode does not contribute to the momentum flux.

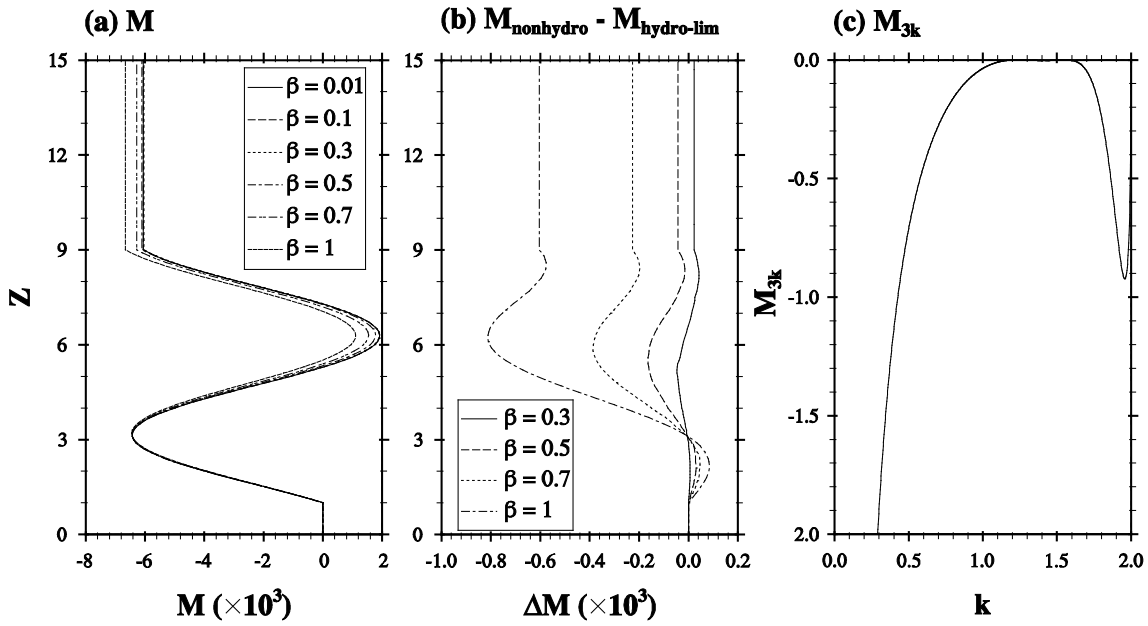

Figure 5.6. (a) Vertical profiles of gravity-wave momentum flux in the cases of β = 0.01, 0.1, 0.3, 0.5, 0.7, and 1. (b) Differences in gravity-wave momentum flux between the nonhydrostatic system in each case of β = 0.3, 0.5, 0.7, and 1 and the hydrostatic-limit system. (c) Spectral gravity-wave momentum flux above the convective forcing as a function of the horizontal wavenumber k in the case of β = 0.5. The inviscid-limit system is considered.

Figures 5.6a and 5.6b show the vertical profiles of gravity-wave momentum flux and its differences between the nonhydrostatic and hydrostatic-limit systems for various values of β. The inviscid-limit system is considered. As β increases, the gravity-wave momentum flux departs from that in the hydrostatic-limit system (Fig. 5.6a), so the magnitude of the gravity-wave momentum flux above $z \sim 3$ increases compared to that in the hydrostatic-limit system (Fig. 5.6b). This means that in a nonhydrostatic system of large β, nonhydrostatically forced waves provide an additional momentum flux, although the additional momentum flux is small compared to the total momentum flux. Figure 5.6c shows the spectral gravity-wave momentum flux above the convective forcing M_{3k} as a function of k in the case of $\beta = 0.5$. The magnitude of the spectral gravity-wave momentum flux M_{3k} decreases with increasing k up to $k \sim 1.6$, and a secondary local maximum exists near $k = k_c$. We can calculate k at the secondary local maximum using $dM_{3k}/dk = 0$. In the case of $\beta = 0.5$, the wave component corresponding to the secondary local maximum is a slantwise (almost horizontally) propagating wave of $k = 1.958$ and $m = 0.204$. The slope of the wave propagation is $m/k = 0.104$. Because m is very small and positive when $k \sim k_c$, we can approximate M_{2k} for a very small $m = \varepsilon > 0$ using Eq. (5.25).

$$M_{2k} = -\frac{\varepsilon\beta a^2}{8} e^{-2ak}\left(h_2^2 - h_1^2\right)\left(z^2 - h_1^2\right). \tag{5.26}$$

The above approximation indicates that the nonhydrostatically generated additional gravity-wave momentum flux is proportional to the nonhydrostaticity factor. The above approximation also indicates that the magnitude of the nonhydrostatically forced

momentum flux increases with increasing height and that above the convective forcing is larger for deeper convective forcing.

Figures 5.2c and 5.2d show that the alternating updrafts and downdrafts are upstream tilted above the convective forcing, so the tilted waves transport wave energy vertically. As already mentioned, these tilted alternating updrafts and downdrafts mainly provide an additional momentum flux above the height of the convective forcing top ($z = h_2$). Note that another upstream tilted wave exists above the convective forcing and that the sign of the vertical velocity above the convective forcing is opposite to the total vertical velocity (compare Figs. 5.1c and 5.2c and Figs. 5.1d and 5.2d). For this reason, the additional momentum flux in the nonhydrostatic system is small even though the nonhydrostatically generated alternating updrafts and downdrafts provide a meaningful amount of momentum flux. In other words, in nonhydrostatic system, some portion of transported wave energy above the convective forcing is downstream shifted.

The result of our study shows that convective forcing in a nonhydrostiatic system can provide an additional gravity-wave momentum flux above the convective forcing. Considering the importance of the parameterization of convectively forced gravity-wave drag in large-scale or climate models, its parameterization in a nonhydrostatic system needs to be further developed.

In the viscid system, using Eq. (5.24), we can obtain the gravity-wave momentum flux.

$$M_{1k} = \frac{a^2}{4k} e^{-2ak} (X_R^2 + X_I^2) \times \left(M_R \sinh 2M_I z - M_I \sin 2M_R z\right) \times \left\{e^{-2M_I h_1} + e^{-2M_I h_2} - 2e^{-M_I (h_1 + h_2)} \cos M_R (h_2 - h_1)\right\} \quad \text{for } 0 \le z \le h_1, \qquad (5.27a)$$

$$
\begin{aligned}
M_{2k} = -\frac{a^2}{4k} e^{-2ak} (X_R^2 + X_I^2) \times \\
&\Big\langle M_R \Big[e^{-2M_I z} \Big\{ \cosh 2M_I h_1 - e^{-M_I (h_1+h_2)} \cos M_R (h_2 - h_1) \\
&+ \cos 2M_R h_1 - e^{-M_I (h_2-h_1)} \cos M_R (h_1 + h_2) \Big\} - e^{-2M_I h_2} \sinh 2M_I z \\
&+ \Big\{ e^{-M_I (z+h_2)} \cos M_R (z + h_2) - e^{-M_I (z+h_1)} \cos M_R (z + h_1) \\
&+ e^{M_I (z-h_2)} \cos M_R (z - h_2) - e^{-M_I (z-h_1)} \cos M_R (z - h_1) \Big\} \Big] \\
&- M_I \Big[e^{-M_I (h_1+h_2)} \sin M_R \{ 2z - (h_2 - h_1) \} \\
&+ e^{-M_I (h_2-h_1)} \sin M_R \{ 2z - (h_1 + h_2) \} - e^{-2M_I h_2} \sin 2M_R z \\
&+ \Big\{ e^{-M_I (z+h_2)} \sin M_R (z + h_2) - e^{-M_I (z+h_1)} \sin M_R (z + h_1) \\
&- e^{M_I (z-h_2)} \sin M_R (z - h_2) - e^{-M_I (z-h_1)} \sin M_R (z - h_1) \Big\} \Big] \Big\rangle
\end{aligned}
$$

for $h_1 < z \le h_2$, (5.26b)

$$
\begin{aligned}
M_{3k} = -\frac{a^2}{4k} e^{-2ak} (X_R^2 + X_I^2) M_R e^{-2M_I z} \times \\
&\{ \cosh 2M_I h_1 + \cos 2M_R h_1 + \cosh 2M_I h_2 + \cos 2M_R h_2 \quad \text{for } z > h_2. \\
&- 2 \cos M_R (h_1 + h_2) \cosh M_I (h_2 - h_1) \\
&- 2 \cos M_R (h_2 - h_1) \cosh M_I (h_1 + h_2) \}
\end{aligned}
\qquad (5.26c)
$$

Figure 5.7 shows the vertical profiles of gravity-wave momentum flux in the cases of ν = 0.01, 0.3, and 0.7 for various values of β. For ν = 0.01, the magnitude of the gravity-wave momentum flux above the convective forcing increases with increasing β, which is similar to that in the inviscid-limit system. This is due to the nonhydrostatically forced slantwise propagating gravity waves of $k \lesssim k_c$ which contribute to the secondary local maximum of the spectral momentum flux (Fig. 5.7a). For larger ν, however, the magnitude of the gravity-wave momentum flux above the convective forcing decreases as β increases (Figs. 5.7b and 5.7c).

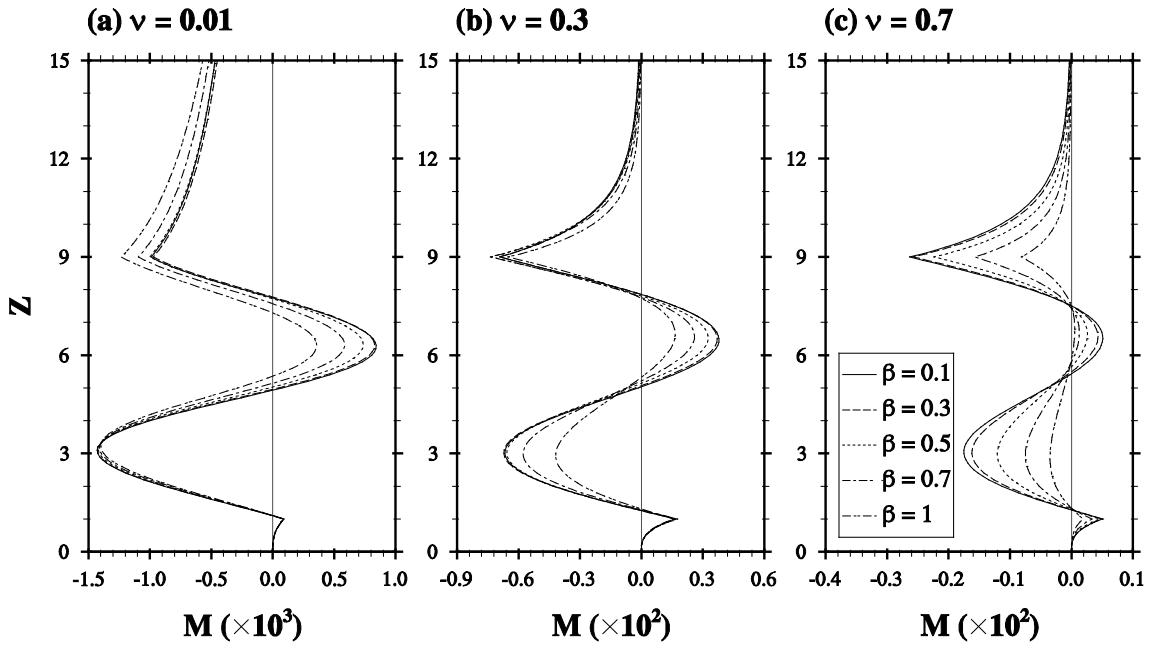

Figure 5.7. Vertical profiles of gravity-wave momentum flux in the cases of ν = (a) 0.01, (b) 0.3, and (c) 0.7 for β = 0.1, 0.3, 0.5, 0.7, and 1.

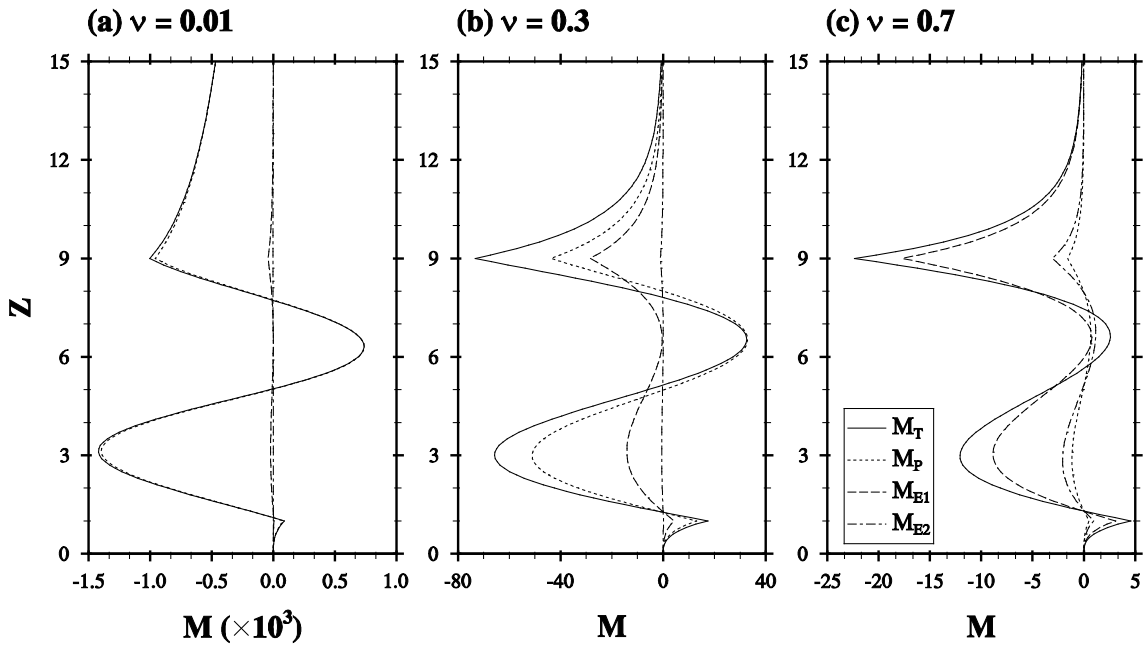

Figure 5.8. Vertical profiles of the gravity-wave momentum flux of total and each mode in the cases of β = 0.5 and v = (a) 0.01, (b) 0.3, and (c) 0.7.

Figure 5.8 shows the vertical profiles of the gravity-wave momentum flux of total and each mode in the cases of β = 0.5 and ν = 0.01, 0.3, and 0.7. For ν = 0.01, the propagating mode takes the largest portion of the total momentum flux (Fig. 5.8a). As the viscous coefficient increases, the portion of the momentum flux of evanescent mode 1 increases (Figs. 5.8b and 5.8c). For ν = 0.7, the gravity-wave momentum flux of the propagating mode is almost dissipated, whereas the gravity-wave momentum flux of evanescent mode 1 is dominant. The critical viscous coefficient $\nu_c = 1/(2\sqrt{2}\beta)$ for β = 0.1, 0.3, 0.5, 0.7, and 1 are 3.54, 1.18, 0.71, 0.51, and 0.35, respectively. Therefore, the propagating mode is effectively dissipated by relatively weak viscous effects. Accordingly, the nonhydrostatic effects on convectively forced flows are easily weakened in a nonhydrostatic system of large β.

6 Dynamics of orographic-convective flows in a two-layer nonhydrostatic atmosphere

6.1 Introduction

Convectively forced internal gravity waves are regarded as a main source of momentum fluxes with high frequency, especially in summer. The momentum fluxes transported by horizontally/vertically propagating internal gravity waves deposit their energy through wave breaking/drag, and the wave drag has an important role in controlling the upper atmosphere (Eliassen and Palm 1960; Bretherton 1969; Linzen 1981; Holton 1982); for this reason, the convectively forced internal gravity waves have been actively investigated for decades.

Parameterizations of the convectively gravity wave drag have been proposed based on theoretical studies of the momentum fluxes induced by convective heating. Kim et al. (2003) reviewed the gravity-wave drag parameterizations in numerical climate models, and highlighted the importance of understanding in the spectrum of the gravity waves in developing new parameterizations. In a stably stratified hydrostatic atmosphere, vertically propagating internal gravity waves are induced, and they transport the wave energy vertically with vertically monotonic waves in steady-state (Chun and Baik 1998, 2002). Beres et al. (2004) and Song and Chun (2005, 2008) theoretically investigated and formulated the convectively forced momentum fluxes spectrum under two- and three-dimensional frameworks. Parameterizations based on those studies are applied to large-scale numerical models, and they have a role in improving the numerical climate

simulations (Beres et al. 2005; Song et al. 2007).

In a nonhydrostatic atmosphere, in which the vertical scale of a system cannot be neglected compared to the horizontal scale of the system, non-negligible inertial terms in the vertical momentum equation generate a distinct pattern of convectively forced mesoscale flows. Woo et al. (2013) numerically investigated the nonhydrostatic effects on the convectively forced flows. Woo et al. (2013) showed that the alternating cells of updraft/downdraft are induced downstream of the convection and that the cells have specific horizontal length scales, which depend on the static stability and the basic-state wind speed in a strongly nonhydrostatic single-layer atmosphere. Chapter 5 showed that the alternating cells are horizontally tilted internal gravity waves and provide additional vertical momentum flux; however, the convectively forced internal gravity waves and their effects on the vertical momentum fluxes in the nonhydrostatic atmosphere with static stability jump and the basic-state wind shear need further investigations.

The investigations of the characteristics of topographically forced internal gravity waves in a nonhydrostatic atmosphere with static stability jump and the basic-state wind shear have seen some progress. Broutman et al. (2002, 2003) examined the behavior of mountain waves in hydrostatic and nonhydrostatic atmospheres using the ray theory. Vosper (2004) and Teixeira et al. (2017) also showed that the mountain lee waves can be trapped by stability changes due to temperature inversion. Based on Wurtele et al. (1987), Keller (1994) examined the flow patterns, wave reflections, and momentum fluxes of topographically forced internal gravity waves in a two-layer nonhydrostatic atmosphere. In a nonhydrostatic atmosphere, a number of distinct resonance waves with characteristic horizontal wavenumbers are generated; however, the theories of topographically forced

waves cannot be directly adapted to convectively forced waves because 1) the source of convectively forced waves is continuously distributed above the surface in the vertical, while the source of topographically forced waves is at the bottom, 2) convectively forced waves are thermally forced waves, while topographically forced waves are mechanically forced waves, and 3) convective forcing is spatially and temporally varying, while topographic forcing is temporally fixed.

This study examines the characteristics of convectively forced gravity waves in a two-layer nonhydrostatic atmosphere. The governing equations and analytic solutions for the convectively forced flows are provided in section 6.2. The convectively forced flows in a two-layer nonhydrostatic atmosphere and the characteristics of resonant waves are analyzed in section 6.3.1. In section 6.3.2, analyses of the gravity-wave momentum fluxes in the stratosphere factoring in various environmental factors are provided.

6.2 Governing equations and solutions

In this study, we consider a two-dimensional linear Boussinesq system in steady-state including a convective diabatic forcing. Since we consider a nonhydrostatic atmosphere, the inertial terms in the vertical momentum equation are not neglected. The governing equations in perturbation variables are as follows:

$$Uu_x + wU_z = -\pi_x, \tag{6.1}$$

$$Uw_x = -\pi_z + b, \tag{6.2}$$

$$Ub_x + N^2 w = \frac{g}{c_p T_0} q, \tag{6.3}$$

$$u_x + w_z = 0, \tag{6.4}$$

where u and w are the perturbation horizontal and vertical velocities, respectively, π is the perturbation kinematic pressure, b is the perturbation buoyancy, U is the basic-state wind speed, N is the buoyancy frequency, g is the gravitational acceleration, c_p is the specific heat of air at constant pressure, T_0 is the reference temperature, and q is the diabatic forcing function.

Figure 6.1 presents the schematic of a two-layer atmosphere considered in this study. The lower and upper layers represent the troposphere and the stratosphere, respectively, and the tropopause height is H. In the troposphere, the basic-state wind speed has a constant wind shear ($U = U_0 + sz$, where U_0 is the basic-state wind speed at the surface and s is the basic-state wind shear), while the basic-state wind is constant in the stratosphere ($U = U_H$). In this study, U_0 and s are positive. The stratospheric buoyancy frequency N_S is larger than the tropospheric buoyancy frequency N_T.

The Green function method is used to solve Eq. (6.1)–(6.4) (Han and Baik, 2009, 2010). The perturbation vertical velocity induced by a finite-depth diabatic (hereafter, convective) forcing is obtained by integrating the analytic solution for the perturbation vertical velocity induced by a line-type diabatic forcing at $z = h$, which is given below, with respect to h from convection bottom height h_1 to convection top height h_2.

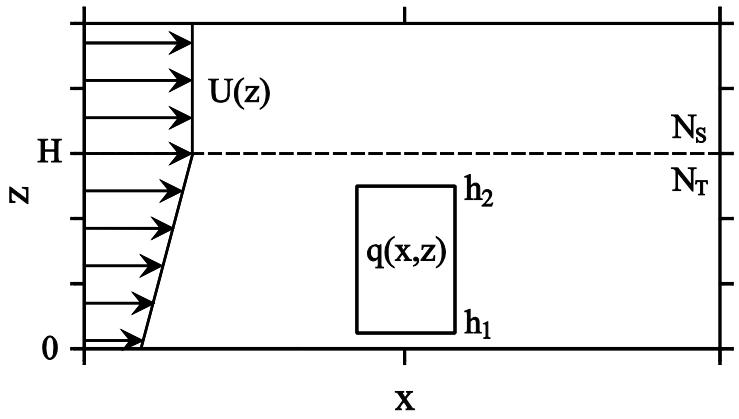

Figure 6.1. Structure of a two-layer atmosphere in the presence of convective forcing considered in this study.

$$q(x) = q_0 \left(\frac{a^2}{x^2 + a^2} - \frac{ab}{x^2 + b^2} \right) \delta(z - h). \tag{6.5}$$

Here, q_0 and a are the strength and the half-width of the bell-shaped diabatic forcing, respectively, b is a constant ($b > a$), and δ is the Dirac delta function.

Equations (6.1)–(6.4) are combined into a single equation in w as follows.

$$U^2 \left(w_{xx} + w_{zz} \right) + N^2 w = \frac{g}{c_p T_0} q, \tag{6.6}$$

To derive the ordinary differential equation for the perturbation vertical velocity in the wavenumber space, the Fourier transformation of Eq. (6.6) is taken ($x \rightarrow k$).

Due to the two layers having different vertical structures of the basic-state wind speed, the general solutions for the perturbation vertical velocity have different forms as follows:

$$\hat{w}_{\mathrm{T1}} = A_1 Z^{1/2} K_{i\mu}(\xi) + B_1 Z^{1/2} L_{i\mu}(\xi) \text{ for } 0 \le z \le h, \tag{6.7a}$$

$$\hat{w}_{\mathrm{T2}} = A_2 Z^{1/2} K_{i\mu}(\xi) + B_2 Z^{1/2} L_{i\mu}(\xi) \text{ for } h \le z \le H, \tag{6.7b}$$

$$\hat{w}_{\mathrm{S}} = C e^{imz} + D e^{-imz} \text{ for } z > H. \tag{6.7c}$$

Here, $Z = U/U_0$, $m = (N_S^2/U_H^2 - k^2)^{1/2}$, and $Ki_\mu(\xi)$ and $L_{i\mu}(\xi)$ are the modified Bessel functions with purely imaginary order $i\mu$ [$\mu = (\mathrm{Ri} - 0.25)^{1/2}$; $\mathrm{Ri} = N_T^2/s^2$ is Richardson

number] and argument ξ (= Uk/s), and the modified Bessel functions $Ki_\mu(\xi)$ and $L_{i\mu}(\xi)$ are defined by the modified Bessel function of the first kind $I_{\pm i\mu}(\xi)$ as follows (Wurtele et al. 1987; Duster 1990; Keller 1994).

$$K_{i\mu}(\xi) = \frac{i\pi}{2}\frac{I_{i\mu}(\xi) - I_{-i\mu}(\xi)}{\sinh \mu\pi}, \tag{6.8a}$$

$$L_{i\mu}(\xi) = \frac{\pi}{2}\frac{I_{i\mu}(\xi) + I_{-i\mu}(\xi)}{\sinh \mu\pi}, \tag{6.8b}$$

Chapter 5 describes the behavior of each wave component depending on the horizontal wavenumber k in a nonhydrostatic single-layer atmosphere. In the stratosphere in which the basic-state wind speed and static stability are uniform, if $k < N_S/U_H$ ($k > N_S/U_H$), then the wave component is sinusoidal and represents a vertically propagating wave (exponential and vertically decaying wave) with the vertical wavenumber m (with the decaying rate $m' = im$). The second term on the RHS of Eq. (6.7c) is nonphysical and is to be deleted due to the upper radiation condition ($D = 0$ with $U_H > 0$).

In the troposphere, the wave components which are represented by modified Bessel functions $K_{i\mu}(\xi)$ and $L_{i\mu}(\xi)$ can be interpreted in a similar way. If $\xi \lesssim \mu$ ($\xi \gtrsim \mu$), then the wave component is oscillatory (exponential), and the behavior changes from oscillatory (exponential) to exponential (oscillatory) when $\xi \approx \mu$ (c.f., Figs A1 and A2 in Wurtele et al. 1987). When $\xi \gg \mu$, the asymptotic behaviors of $K_{i\mu}(\xi)$ and $L_{i\mu}(\xi)$ are exponentially decaying and amplifying with the argument ξ, respectively, and are expressed as

$$K_{i\mu}(\xi) \approx \left(\frac{\pi}{2\mu}\right)^{1/2} e^{-\xi}, \tag{6.9a}$$

$$L_{i\mu}(\xi) \approx \left(\frac{\pi}{2\mu}\right)^{1/2} \frac{e^{\xi}}{\sinh(\mu\pi)}. \tag{6.9b}$$

On the other hand, when $\xi \ll \mu$, the asymptotic behavior of $K_{i\mu}(\xi)$ and $L_{i\mu}(\xi)$ is sinusoidal and are $\pi/2$ out of phase with each other. Each is expressed as

$$K_{i\mu}(\xi) \approx \left(\frac{\pi}{2\mu}\right)^{1/2} \exp\left(-\frac{\mu\pi}{2}\right) \sin\left[\mu\left(\ln\mu - \ln\frac{\xi}{2} - 1\right) + \frac{\pi}{4}\right], \tag{6.10a}$$

$$L_{i\mu}(\xi) \approx \left(\frac{\pi}{2\mu}\right)^{1/2} \exp\left(-\frac{\mu\pi}{2}\right) \cos\left[\mu\left(\ln\mu - \ln\frac{\xi}{2} - 1\right) + \frac{\pi}{4}\right]. \tag{6.10b}$$

The choice of $L_{i\mu}(\xi)$ as the pair of the modified Bessel function of the second kind $K_{i\mu}(\xi)$ is introduced by Miller (1950), and various characteristics of $K_{i\mu}(\xi)$ and $L_{i\mu}(\xi)$ are described in Dunster (1990).

To find the coefficients A_1, A_2, B_1, B_2, and C, the no-slip bottom boundary condition [$\hat{w}_{T1}(z = 0) = 0$] and the interfacial boundary conditions at $z = h$ and $z = H$ are applied as follows:

$$\hat{w}_{T1}(z = h) = \hat{w}_{T2}(z = h), \tag{6.11a}$$

$$\hat{w}_{T2,z}(z = h) - \hat{w}_{T1,z}(z = h) = \hat{F}, \tag{6.11b}$$

$$\hat{w}_{T2}(z = H) = \hat{w}_{S}(z = H), \tag{6.11c}$$

$$\hat{w}_{\mathrm{T2},z}(z=H)=\hat{w}_{\mathrm{S},z}(z=H), \tag{6.11d}$$

where

$$\hat{F}(k,z)=\frac{gq_0a}{c_pT_0s^2}\left(e^{-ak}-e^{-bk}\right)\delta(z-h). \tag{6.11e}$$

Then, the solution for the perturbation vertical velocity forced by line-type diabatic forcing in the wave number space is

$$\hat{w}_{\mathrm{T1}}=-\frac{U_h\hat{F}}{s\pi}\sinh(\mu\pi)\frac{(K_h-RL_h)}{(K_0+RL_0)}Z^{\frac{1}{2}}\left\{L_0K_{i\mu}(\xi)-K_0L_{i\mu}(\xi)\right\}\ \text{for } 0\le z\le h, \tag{6.12a}$$

$$\hat{w}_{\mathrm{T2}}=-\frac{U_h\hat{F}}{s\pi}\sinh(\mu\pi)\frac{(L_0K_h-K_0L_h)}{(K_0+RL_0)}Z^{\frac{1}{2}}\left\{K_{i\mu}(\xi)-RL_{i\mu}(\xi)\right\}\ \text{for } h\le z\le H, \tag{6.12b}$$

$$\hat{w}_{\mathrm{S}}=\frac{U_h\hat{F}}{s\pi}\sinh(\mu\pi)\frac{(L_0K_h-K_0L_h)}{(K_0+RL_0)}Z_H^{\frac{1}{2}}\left(K_H-RL_H\right)e^{im(z-H)}\ \text{for } z>H, \tag{6.12c}$$

where

$$U_\zeta=U(z=\zeta), \tag{6.12d}$$

$$Z_\zeta=Z(z=\zeta), \tag{6.12e}$$

$$K_\zeta=K_{i\mu}(U_\zeta k/s),\ L_\zeta=L_{i\mu}(U_\zeta k/s), \tag{6.12f}$$

$$R = \frac{\frac{s}{2}K_H + U_H k K_H' + imU_H K_H}{\frac{s}{2}L_H + U_H k L_H' + imU_H L_H}. \tag{6.12g}$$

Here, R is the complex reflection coefficient at the tropopause.

The solution for the perturbation vertical velocity forced by a convective diabatic forcing can be obtained by integrating Eqs. (6.12a)–(6.12c) with respect to h from h_1 to h_2 as follows:

$$\hat{w}_1 = \int_{h_1}^{h_2} \hat{w}_{\mathrm{T1}} dh \quad \text{for } 0 \le z \le h_1, \tag{6.13a}$$

$$\hat{w}_2 = \int_{h_2}^{z} \hat{w}_{\mathrm{T1}} dh + \int_{z}^{h_2} \hat{w}_{\mathrm{T2}} dh \quad \text{for } h_1 \le z \le h_2, \tag{6.13b}$$

$$\hat{w}_3 = \int_{h_1}^{h_2} \hat{w}_{\mathrm{T2}} dh \quad \text{for } h_2 \le z \le H, \tag{6.13c}$$

$$\hat{w}_4 = \int_{h_1}^{h_2} \hat{w}_{\mathrm{S}} dh \quad \text{for } z > H. \tag{6.13d}$$

The solution can be obtained analytically by the relations below.

$$\begin{aligned}\int_{h_1}^{h_2} U_h K_{i\mu}(\xi_h)\, dh &= \frac{s}{k^2}\int_{\xi_1}^{\xi_2} \xi_h K_{i\mu}(\xi_h)\, d\xi_h \\ &= i\frac{s\pi}{k^2}\left(\frac{\xi_h}{2}\right)^{2-i\mu}\left\{\xi_h^{2i\mu}\Gamma\left(\frac{i\mu}{2}+1\right){}_1\tilde{F}_2\left[\frac{i\mu}{2}+1; i\mu+1, \frac{i\mu}{2}+2; \left(\frac{\xi_h}{2}\right)^2\right]\right. \\ &\quad \left. - 2^{2i\mu}\Gamma\left(1-\frac{i\mu}{2}\right){}_1\tilde{F}_2\left[1-\frac{i\mu}{2}; 1-i\mu, 2-\frac{i\mu}{2}; \left(\frac{\xi_h}{2}\right)^2\right]\right\}\Bigg|_{\xi_1}^{\xi_2},\end{aligned} \tag{6.14a}$$

$$\int_{h_1}^{h_2} U_h L_{i\mu}\left(\xi_h\right) dh = \frac{s}{k^2}\int_{\xi_1}^{\xi_2} \xi_h L_{i\mu}\left(\xi_h\right) d\xi_h$$

$$= -\frac{s\pi}{k^2 \sinh\left(\mu\pi\right)}\left(\frac{\xi_h}{2}\right)^{2-i\mu}$$

$$\times\left\{\xi_h^{2i\mu}\Gamma\left(\frac{i\mu}{2}+1\right){}_1\tilde{F}_2\left[\frac{i\mu}{2}+1; i\mu+1, \frac{i\mu}{2}+2; \left(\frac{\xi_h}{2}\right)^2\right]\right.$$

$$\left. +2^{2i\mu}\Gamma\left(1-\frac{i\mu}{2}\right){}_1\tilde{F}_2\left[1-\frac{i\mu}{2}; 1-i\mu, 2-\frac{i\mu}{2}; \left(\frac{\xi_h}{2}\right)^2\right]\right\}\Bigg|_{\xi_1}^{\xi_2}, \tag{6.14b}$$

where

$$\xi_j = \xi\,(z = h_j), \tag{6.14c}$$

$${}_1\tilde{F}_2\left[\alpha; \beta_1, \beta_2; \xi\right] = \frac{1}{\Gamma(\beta_1)\Gamma(\beta_2)}\sum_{n=0}^{\infty}\frac{(\alpha)_n}{(\beta_1)_n(\beta_2)_n}\frac{\xi^n}{n!}. \tag{6.14d}$$

Here, ${}_1\tilde{F}_2\left[\alpha; \beta_1, \beta_2; \xi\right]$ is the regularized hypergeometric function and $\Gamma(\beta)$ is the gamma function. In this study, however, we numerically integrate Eq. (6.13) to simplify the calculation and to easily handle and analyze the solution.

The inverse Fourier transform of the numerically integrated solution in Eq. (6.13) is taken ($k \rightarrow x$) using the Euler forward scheme. The grid size Δk and the number of the grids N_k are varied case by case to avoid numerical blow-ups triggered by the calculations involving Bessel functions. Some caveats to calculating the solutions are described in section 4 of Keller (1994). In this study, we consider the nonhydrostatic atmosphere with the basic-state wind shear which is determined by three Richardson numbers (Ri = 9, 36,

and 144) with and without stability jump at the tropopause (N_S = 0.02 s^{-1} when the stability jump exists). When Ri = 9, 36, and 144, the basic-state wind speeds at z = 12 km are U_H = 50, 30, and 20 m s^{-1} and s = 3.33 × 10^{-3}, 1.66 × 10^{-3}, and 0.83 × 10^{-3} s^{-1}, respectively, when U_0 = 10 m s^{-1} and N_T = 0.01 s^{-1} (Table 6.1). The line-type diabatic forcing is located at $z = h$ = 8 km and the convective diabatic forcing is located from $z = h_1$ = 1 km to $z = h_2$ = 11 km vertically. The half-widths a = 10 km for both of the diabatic forcings, and $b = 5a$. The magnitude of both diabatic forcings is q_0 = 1 J kg^{-1} s^{-1} and the reference temperature is T_0 = 273.15 K.

6.3 Results and discussion

6.3.1 Convectively forced flows and gravity waves

The perturbation vertical velocity fields induced by line-type diabatic forcing without stability jump are shown in Figure 6.2. Downstream of the convective forcing, horizontal wavy patterns appear clearly. Resonant waves with different horizontal wavenumbers are superposed to form the wavy patterns. Without the stability jump (R = 0), the perturbation vertical velocity has singularities at the zeros of K_0 [see Eqs. (6.12a)–(6.12c)]. When the denominator of Eqs. (6.12a)–(6.12c) goes to zero, the horizontal the wave component e^{ikx} and the vertical wave components $K_{i\mu}(\xi)$ and $L_{i\mu}(\xi)$ corresponding to wavenumber k are amplified. Because the wave strength is exponentially decreasing with k [see Eq. (6.11e)], wave components corresponding to relatively long wavelengths are strongly amplified. Since the zeros of $K_{i\mu}(\xi)$ depend only on Richardson number, the tropospheric basic-state wind shear determines the horizontal wavelengths of resonant waves when the tropospheric static stability is fixed.

Ri	U_H (m s^{-1})	s ($\times 10^{-3}$ s^{-1})	L_x at zeros of $K_{i\mu}(\xi_0)$ (km)
9	50	3.33	7.2, 20.9, 60.3
36	30	1.66	9.4, 15.9, 26.9, 45.5, 76.9
144	20	0.83	7.7, 10.0, 13.0, 17.0, 22.0, 28.6, 37.2, 48.3, 62.8

Table 6.1. The basic-state wind speed at z = 12 km, basic-state wind shear s, and the horizontal wavelengths corresponding to the zeros of $K_{i\mu}(\xi_0)$ for the case of Richardson numbers 9, 36, and 144.

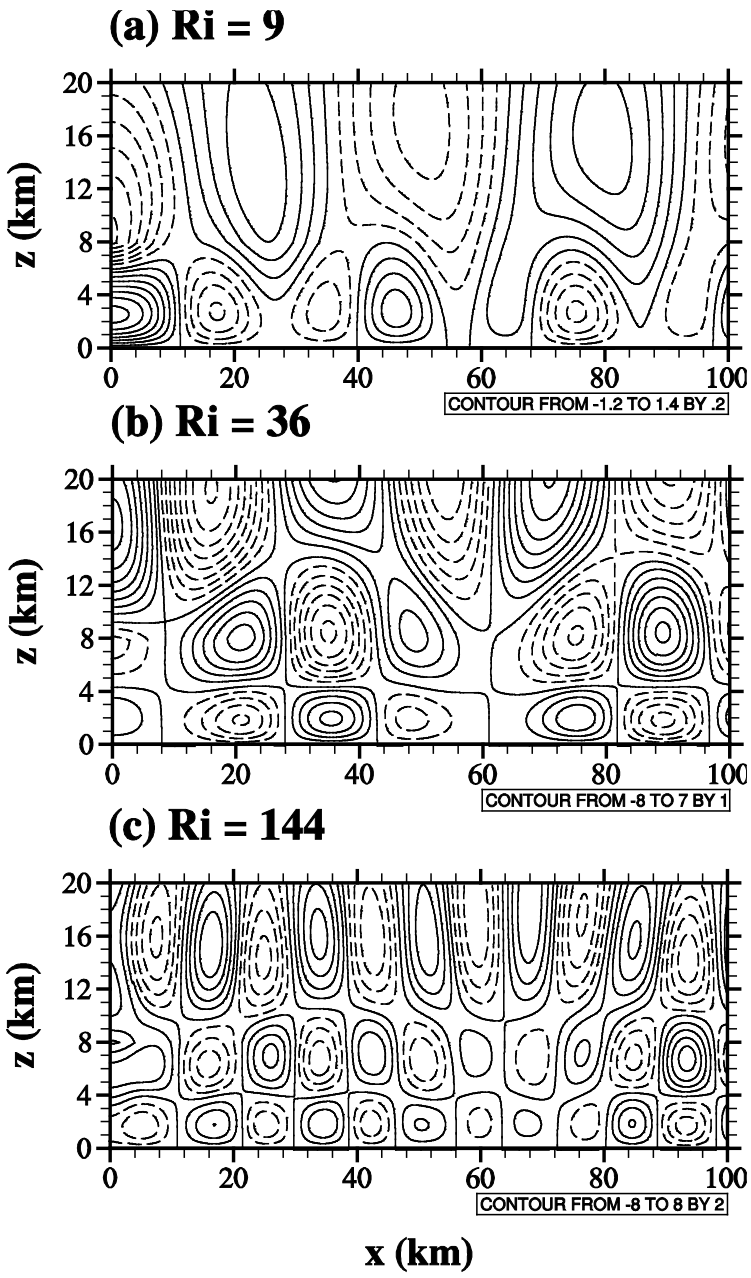

Figure 6.2. Perturbation vertical velocity induced by line-type forcing at h = 8 km without stability jump at the tropopause in the case of Ri = (a) 9, (b) 36, and (c) 144. The contour line informations are given at the bottom of each panel.

The dash-dot line in Fig. 6.3 is the horizontal wavelength (= $2\pi/k$) corresponding to $\xi_0 = \mu$ as a function of Richardson number and shows that the resonant wave corresponding to wavelengths longer than ~10 km satisfies $\xi_0 < \mu$. For this reason, the sinusoidal asymptotic form of $K_{i\mu}(\zeta)$ and $L_{i\mu}(\zeta)$ in Eq. (6.10) can approximate the behavior of resonant waves. Figure 6.3 also shows the horizontal wavelengths corresponding to the zeros of sinusoidal asymptotic form of $K_{i\mu}(\zeta)$ as

$$L_{xn} = \frac{\pi U_0}{s} \exp\left[\frac{1}{\mu}\left(n - \frac{1}{4} \right)\pi + 1 - \ln \mu \right]. \tag{6.15}$$

The possible wavelengths of resonant waves are broadly but discretely distributed depending on Richardson number. The wavelengths of the possible resonant waves shorter than 100 km and satisfying $\xi_0 < \mu$ are listed in Table 6.1. When Ri = 9, the resonant waves corresponding to wavelengths ~20.9 km and ~60.3 km appear in the lower and the upper atmospheres, respectively (Fig. 6.2a). For a fixed horizontal wavelength (or k), the argument of the Bessel function increases with the basic-state wind speed. For this reason, the resonant waves with short wavelength (large wavenumber) are trapped as the argument of the Bessel function approaches or overtakes μ, so that the wave components behave exponentially rather than sinusoidally (Fig. 6.2a). As the basic-state wind shear becomes smaller, the horizontal wavelengths of the resonant waves decrease and resonant waves with relatively shorter horizontal wavelengths can approach high altitude (Fig. 6.2b and 6.2c).

Figure 6.4 shows the convectively forced perturbation vertical velocity fields without stability jump. The flow patterns are made by superposing the flows induced -

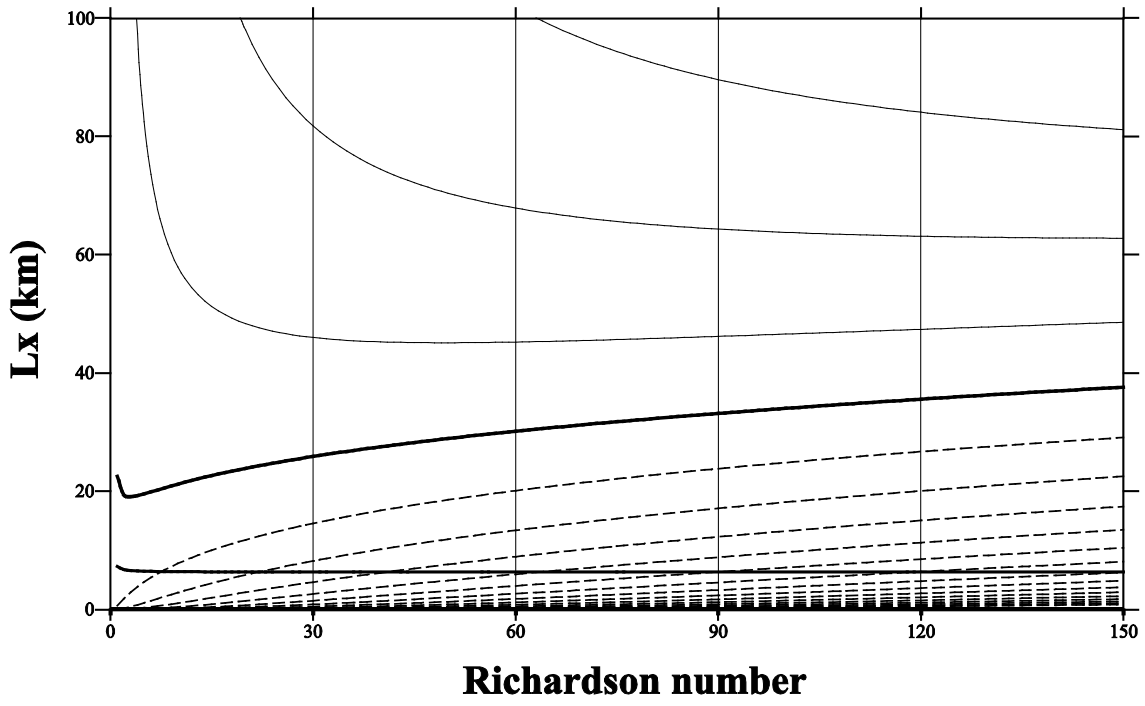

Figure 6.3. The horizontal wavelengths corresponding to the zeros of sinusoidal asymptotic forms of $K_{i\mu}(\xi_0)$ in Eq. (6.10a) as a function of Richardson number. The thick solid lines are for $n = 0$ and the thin solid (dashed) lines are corresponding to $n = 1$, 2, and 3 ($n = -15, -14, \ldots, -1$) [see Eq. (6.15)]. The sinusoidal asymptotic form of $K_{i\mu}(\xi_0)$ is valid when L_x is longer than the dash-dot line on which $\xi_0 = \mu$ is valid.

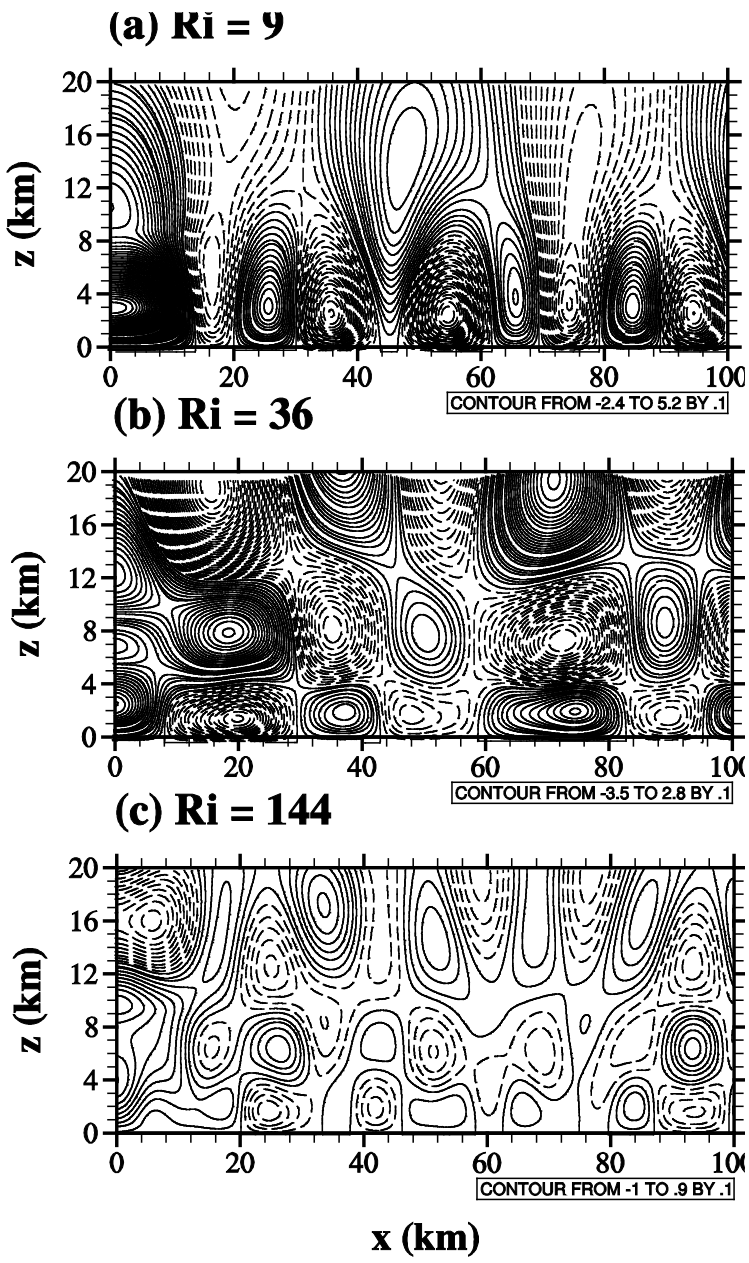

Figure 6.4. The same as Fig. 6.2 except for the perturbation vertical velocity induced by convective forcing distributed from h_1 = 1 km to h_2 = 9 km.

by line type diabatic forcings which are continuously distributed from $z = h_1$ to $z = h_2$. As a result, strong and deep upward motions are induced around the convection center. The composition of various resonant waves with different phases and strengths makes for a complex wave structure, especially in the case with high Ri (Fig. 6.4c), while the horizontal wavelength of the resonant waves looks similar to those in the case of the line-type diabatic forcing. Convectively forced resonant waves with weaker wind shear are weaker than those with stronger wind shear, while those induced by a line-type diabatic forcing are stronger (Fig. 6.2c and 6.4c).

The contribution of the resonant waves to the entire fields is as follows:

$$w_{\mathrm{T1}} = -\frac{2U_h}{s}\sinh(\mu\pi)Z^{\frac{1}{2}} \times \sum_{j=1}^{N}\hat{F}_j\left\{L_{0j}K_{i\mu}(\xi_j) - K_{0j}L_{i\mu}(\xi_j)\right\}\mathrm{Re}\left\{i\frac{\left(K_{hj} - RL_{hj}\right)}{\left(K'_{0j} + RL'_{0j}\right)}e^{ik_j x}\right\} \quad \text{for } 0 \le z \le h, \tag{6.16a}$$

$$w_{\mathrm{T2}} = -\frac{2U_h}{s}\sinh(\mu\pi)Z^{\frac{1}{2}} \times \sum_{j=1}^{N}\hat{F}_j\left(L_{0j}K_{hj} - K_0L_{hj}\right)\mathrm{Re}\left\{i\frac{\left\{K_{i\mu}(\xi_j) - RL_{i\mu}(\xi_j)\right\}}{\left(K'_{0j} + RL'_{0j}\right)}e^{ik_j x}\right\} \quad \text{for } h \le z \le H, \tag{6.16b}$$

$$w_{\mathrm{S}} = \frac{2U_h}{s}\sinh(\mu\pi)Z_H^{\frac{1}{2}} \times \sum_{j=1}^{N}\hat{F}_j\left(L_{0j}K_{hj} - K_0 jL_{hj}\right)\mathrm{Re}\left\{i\frac{\left(K_{Hj} - RL_{Hj}\right)}{\left(K'_{0j} + RL'_{0j}\right)}e^{i\{k_j x + m(z-H)\}}\right\} \quad \text{for } z > H. \tag{6.16c}$$

In Eq. (6.16), terms with subscript j are the values corresponding to the wavenumber of j-th zero of denominator $K_0 + RL_0$, and N is the number of zeros. In the troposphere, the horizontal wave component e^{ikx} is separated from the vertical wave components $K_{i\mu}(\xi)$ and $L_{i\mu}(\xi)$, which means the the resonant waves do not transport the wave energy vertically. In the stratosphere, however, the resonant waves vertically transport wave energy from the tropopause.

Figure 6.5 shows the perturbation vertical velocity fields induced by the line-type diabatic forcing with stability jump at the tropopause. As discussed, the resonant waves are tilted upstream in the stratosphere, which indicates that the wave energy is vertically transported upward. Moreover, in the upper troposphere, the resonant waves are tilted downstream, which indicates downward propagating wave components above the line-type diabatic forcing due to the gravity-wave reflection at the tropopause. The wave energy source in the stratosphere is the nonhydrostatically generated resonant waves at the tropopause level. For this reason, wave energy, which is transmitted and transported in the stratosphere, strongly depends on Richardson number, the height of the diabatic forcing, and the tropopause height.

Convectively forced perturbation vertical velocity fields in Fig. 6.6 show that the cellular structure of the resonant waves in the troposphere is aligned vertically compared to those induced by a line-type forcing. Similar to the case with a line-type forcing, resonant waves in the upper troposphere (in the stratosphere) are tilted downstream (upstream). The vertically aligned wavy structure in the troposphere shows that the wave energy source of the stratosphere is less sensitive to the tropopause height if the change in the distance between the tropopause and the convection top height is smaller.

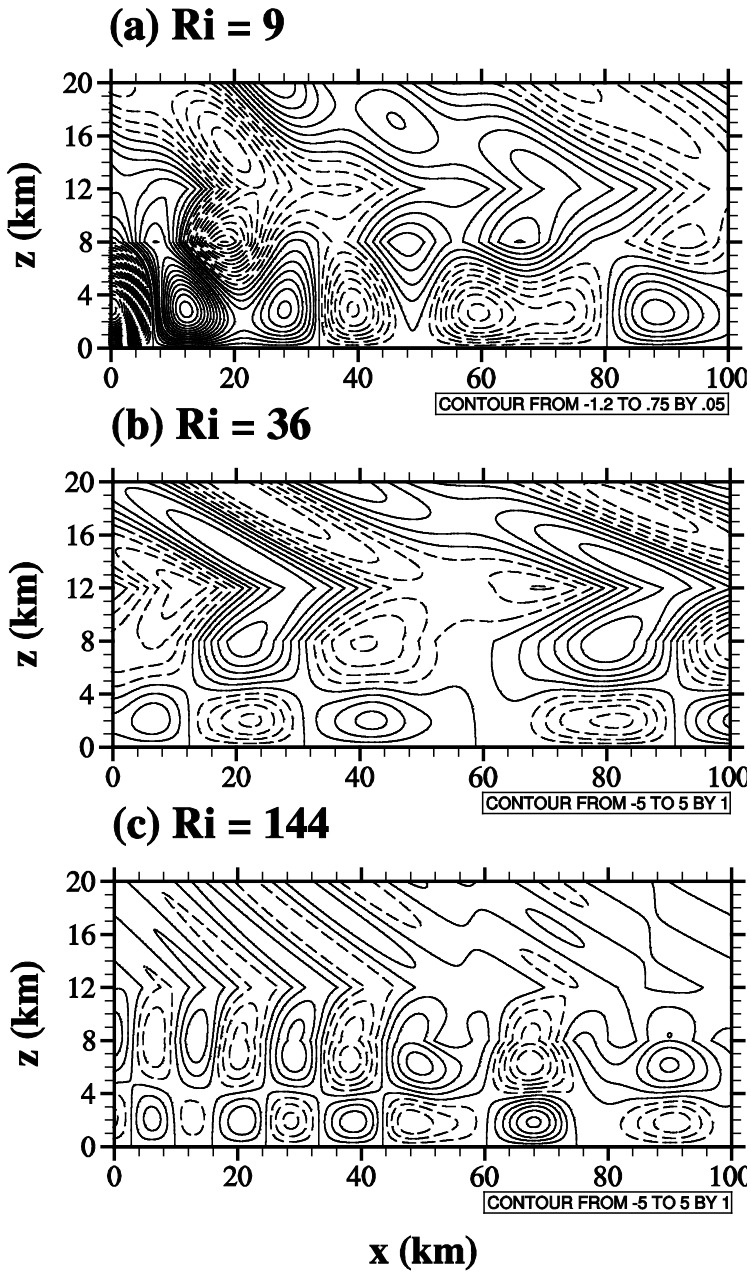

Figure 6.5. The same as Fig. 6.2 except for the cases with stability jump at the tropopause.

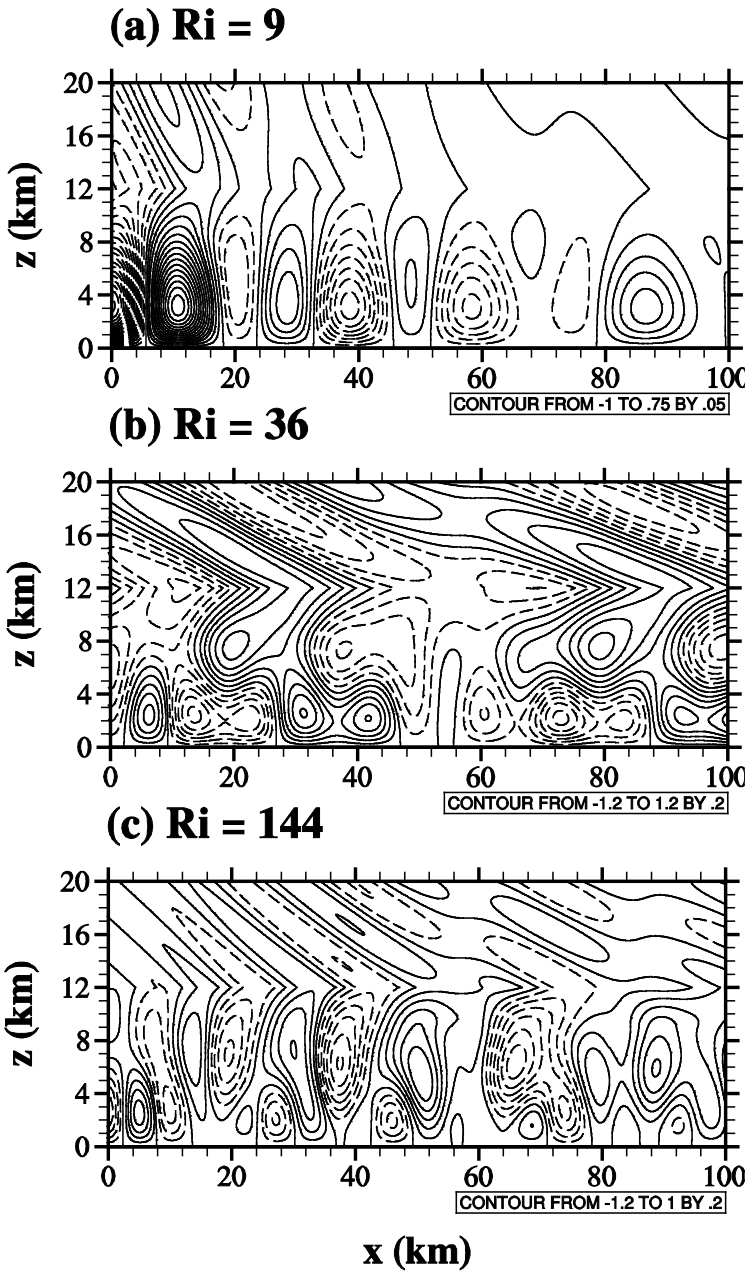

Figure 6.6. The same as Fig. 6.3 except for the cases with stability jump at the tropopause.

6.3.2 Gravity-wave momentum fluxes

As discussed in Section 6.3.1, resonant waves without stability jump do not transport wave energy vertically. However, the stability jump at the tropopause (existence of the higher stability layer aloft) ensures the vertical propagation of wave energy toward the upper atmosphere. Because the wave components are trapped at a certain height (when $\xi_0 \approx \mu$) given a Richardson number and the wavelength of the resonant wave, the wave energy cannot be transported far aloft without stability jump. In this section, we examine the gravity-wave momentum fluxes of the resonant waves in the stratosphere which are transmitted through the tropopause.

Using the Fourier transformed continuity equation [$\hat{u}_i = (i/k)\partial\hat{w}_i/\partial z$], we can analytically obtain the perturbation horizontal velocity and the momentum fluxes in the stratosphere induced by a line-type diabatic forcing as follows.

$$M_S = \int_{-\infty}^{\infty} u_S w_S dx = \frac{4U_h^2}{s^2}\sinh^2(\mu\pi) Z_H \times \sum_{j=1}^{N} \hat{F}_j^2 \left(L_{0j}K_{hj} - K_{0j}L_{hj}\right)^2 \frac{K_{Hj}^2 - \mathrm{Re}\{R\}K_{Hj}L_{Hj} + |R|^2 L_{Hj}^2}{K_{0j}'^2 + \mathrm{Re}\{R\}K_{0j}'L_{0j}' + |R|^2 L_{0j}'^2}. \quad (6.17)$$

Here, the orthogonality of the sinusoidal function with respect to the wavenumber is used. Due to the ($e^{-ak} - e^{-bk}$) term in $\hat{F}$ [Eq. (6.11e)], the resonant wave component with a longer wavenumber tends to have a stronger momentum flux. The gravity-wave reflection at the tropopause also affects the stratospheric momentum flux, and this effect depends on the tropopause height [Eq. (6.17)].

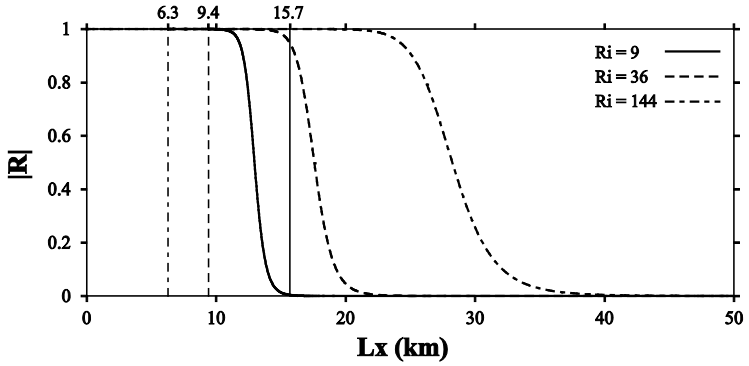

Figure 6.7. The magnitude of the complex reflectivity in Eq. (6.12g) for the cases Ri = 9, 36, and 144.

Figure 6.7 shows the magnitude of the complex reflectivity $|R|$ in Eq. (6.12g) as a function of the horizontal wavelength. The tropopause totally reflects resonant waves that correspond to short wavelength. In the case of weak wind shear (high Ri), a wider range of shorter waves are totally trapped in the troposphere. In the case of strong wind shear (Ri = 9), relatively shorter waves than in the case of weak shear can pass through the tropopause. The resonant waves corresponding to L_x from ~11.1 km to ~14.0 km can be partially transmitted. However, the transmitted resonant waves cannot vertically propagate because the critical wavelength in the stratosphere ($k_c = N_S/U_H$) is 15.7 km. The wave components are thus in the evanescent mode in the stratosphere (see Chapter 5).

Section 6.5.1 shows that the Bessel functions $K_{i\mu}(\xi)$ and $L_{i\mu}(\xi)$ for most of the resonant waves can be approximated by the sinusoidal asymptotic forms [Eq. (6.10)]. Then, $(L_{0j}K_{hj} - K_{0j}L_{hj}) = -(\pi/2\mu)e^{-\mu\pi}\sin[\mu\ln(Z_h/Z_0)]$ and Eq. (6.17) can be analytically integrated with respect to h as follows:

$$
\begin{aligned}
M_S = \frac{4}{s^2}\sinh^2(\mu\pi) Z_H \Bigg[& U_1^3 \left\{ \mu\cos\left(\mu\ln\frac{U_1}{U_0}\right) - 3\sin\left(\mu\ln\frac{U_1}{U_0}\right)\right\} \\
& - U_2^3 \left\{ \mu\cos\left(\mu\ln\frac{U_2}{U_0}\right) - 3\sin\left(\mu\ln\frac{U_2}{U_0}\right)\right\}\Bigg] \\
& \times \sum_{j=1}^{N} \hat{F}_j^2 \frac{K_{Hj}^2 - \mathrm{Re}\{R\}K_{Hj}L_{Hj} + |R|^2 L_{Hj}^2}{K_{0j}'^2 + \mathrm{Re}\{R\}K_{0j}'L_{0j}' + |R|^2 L_{0j}'^2}.
\end{aligned}
\tag{6.18}
$$

Here, U_j (j = 1 and 2) is the basic-state wind speed at $z = h_j$. Equation (6.18) shows that the stratospheric momentum fluxes of the transmitted resonance waves can be positive or negative depending on Richardson number, the tropopause height, and the bottom and top

heights of convection. The magnitude of the stratospheric momentum fluxes needs to be calculated and analyzed further.

7 Modeling of orographic-convective precipitation: Shallow and warm clouds

7.1 Introduction

Aerosol particles play a role in controlling precipitation characteristics as cloud condensation nuclei (CCN) or ice nuclei (IN). Rosenfeld (1999) and Andreae et al. (2004) showed evidence that smoke aerosols from forest fires can inhibit rainfall. Urban pollution also suppresses downstream rainfall and snowfall (Rosenfeld 2000). The suppression effect of aerosol particles on precipitation has been reproduced in various numerical studies (e.g., Givati and Rosenfeld 2004; Khain et al. 2004; Xie et al. 2013). These numerical studies showed that the size distribution of small-sized cloud droplets in an aerosol-rich condition supresses precipitation. Many observational and numerical studies have shown that air pollution in mountainous areas, such as the western United States, inland of Israel, and northern China, also suppresses precipitation (Givati and Rosenfeld 2004; Jirak and Cotton 2006; Rosenfeld and Givati 2006; Rosenfeld et al. 2007; Guo et al. 2014).

Precipitation over mountainous areas has been investigated for a long time (Barros and Lettenmaier 1994; Roe 2005; Houze 2012). To systematically study orographic precipitation, many theoretical methods have been designed (e.g., Smith and Lin 1982; Lin 1986; Smith and Barstad 2004). However, it is difficult to standardize the detailed characteristics of orographic precipitation because orographic precipitation is sensitive not only to microphysical processes but also to many factors, such as mountain

geometry, static stability, and basic wind speed (Chu and Lin 2000; Colle 2004; Sever and Lin 2017). Colle (2004), Pathirana et al. (2005), and Roe and Baker (2006) examined the sensitivity of orographic precipitation by changing mountain geometry (mountain height and width) and basic wind speed. These studies assess the importance of mountain barrier effects and the roles of mountain waves on shallow orographic precipitation in a macroscopic viewpoint. The mountain height and width modify the strength of orographic convection by controlling upslope steepness. A narrow-mountain with steep upslope angle sometime results in more precipitation over the leeside of the mountain (Roe and Baker 2006). However, the sensitivity of orographic precipitation to mountain geometry is highly dependent on other factors as well, and wide-mountains with gentle upslopes sometimes result in more precipitation over the leeside of mountain (Pathirana et al. 2005). To examine the effects of upslope steepness on orographic precipitation, asymmetric mountains with different upslope steepnesses but fixed downslope geometry should be considered. Sensitivity tests in this study concentrate on the sensitivity of macroscopic features and microphysical processes in the generation and development stages of orographic precipitation.

Mountain geometry and environmental factors can determine the convective development of orographic clouds. (Dudis 1972; Durran and Klemp 1982; Hernandez-Duenas et al. 2015). Cannon et al. (2012, 2014) numerically studied the conditions for the generation of complex orographic convection. Under convection-prone conditions, orographic convection constructs a cellular or a banded structure (Kirshbaum and Durran 2004, 2005). A well-developed orographic convection has been reported in many studies using field campaign data (Smith et al. 2012; Minder et al. 2013; Wang and Kirshbaum,

2015) and has been numerically simulated using high-resolution models (Kirshbaum and Smith 2009; Panosatti et al. 2016; Sever and Lin 2017).

Many bulk and bin microphysics schemes have been developed for numerical simulations of clouds and precipitation. Bin microphysics models predict the number concentration of each hydrometeor in each size bin (e.g., Khain et al. 2000; Lynn et al. 2005a, b). The detailed representation of microphysical processes in bin microphysics models provides more accurate numerical results than the numerical results obtained by bulk microphysics models. However, bin microphysics models require much more computational resources, and less studies have used bin microphysics models. Khain et al. (2005) used a bin microphysics model to study aerosol effects on deep convective precipitation. Aerosol effects on shallow convective precipitation have also been studied using bin microphysics models (Wyszogrodsky et al. 2011; Blyth et al. 2013; Grabowski et al. 2015; Lee et al. 2015).

The effects of aerosol particles on orographic precipitation are even more complicated. Under the influence of mountain geometry and other environmental factors, the complex interactions of dynamical, thermal, and microphysical processes determine the characteristics of orographic precipitation. Several researchers have numerically examined aerosol effects on orographic precipitation using bulk microphysics models and have shown that aerosols reduce the total precipitation amount over mountains (Creamean et al. 2015; Yang et al. 2016). Studies using bin microphysics models have provided an insight for understanding very detailed microphysical processes associated with orographic precipitation influenced by aerosols, including the evolution of the size distributions of hydrometeors (Lynn et al. 2007; Xue et al. 2010; Xiao et al. 2014, 2015).

However, aerosol effects on orographic precipitation from cellular or banded convective clouds are still poorly understood. Recently, Nugent et al. (2016) studied aerosol effects on orographic-convective precipitation with and without the basic wind using an aerosol-aware bulk model. To understand aerosol effects on precipitation from convective orographic clouds more clearly, numerical simulations using a bin microphysics model are needed.

In this study, we examine aerosols effects on orographic precipitation from shallow convective clouds using a bin microphysics model. A particular attention is given to the sensitivity to upslope steepness. Section 7.2 presents the experimental design of simulations. The simulation results are provided and discussed in section 7.3. The macroscopic and microphysical properties of orographic precipitation are presented in section 7.3.1. The sensitivity of orographic precipitation to aerosol number concentration and the sensitivity of aerosol effects on orographic precipitation to upslope steepness are examined in section 7.3.2 and section 7.3.3, respectively.

7.2 Experimental design

7.2.1 Model description

The numerical model used in this study is the Weather Research and Forecasting (WRF) model, version 3.6.1, coupled with the bin microphysics scheme of the Hebrew University Cloud Model (HUCM) (Skamarock et al. 2008; Lee and Baik 2016). The detailed description of the HUCM is given in Khain and Sednev (1996) and Khain et al. (2000, 2004). The WRF-bin model considers 43 mass-doubling bins. The aerosol size

distribution $N(r_a)$ is calculated using the Kölher equation and the Twomey equation as follows (Kölher 1936; Twomey 1959; Khain et al. 2000):

$$\frac{dN}{d\ln r_a} = \frac{3}{2} N_0 k \left(\frac{4A^3}{27Br_a^3} \right)^{k/2}, \tag{7.1}$$

where r_a is the aerosol radius, N_0 is the aerosol number concentration (here, CCN number concentration) at 1% supersaturation, k (= 0.8 in this study) is a constant, A is the curvature-effect-related coefficient, and B is the solution-effect-related coefficient. The radius of the largest aerosol is 2 μm. The initial aerosol number concentration in the vertical is constant up to 2 km height and then decreases exponentially with an *e*-folding height of 2 km. We only consider warm microphysical processes in this study. In the WRF-bin model, a liquid drop larger (smaller) than r = 40 μm is categorized as a raindrop (cloud droplet).

7.2.2 Simulation settings

To examine orographic precipitation, we construct two-dimensional simulations (Fig. 7.1a). The bell-shaped mountain is considered, whose height is given by

$$h(x) = h_m \frac{a^2}{x^2 + a^2}. \tag{7.2}$$

Here, h_m (= 1 km) is the maximum height and a is the half-width of the bell-shaped mountain. The leeward-width is constant ($a = a_2$ = 10 km for $x \geq 0$ km), while the

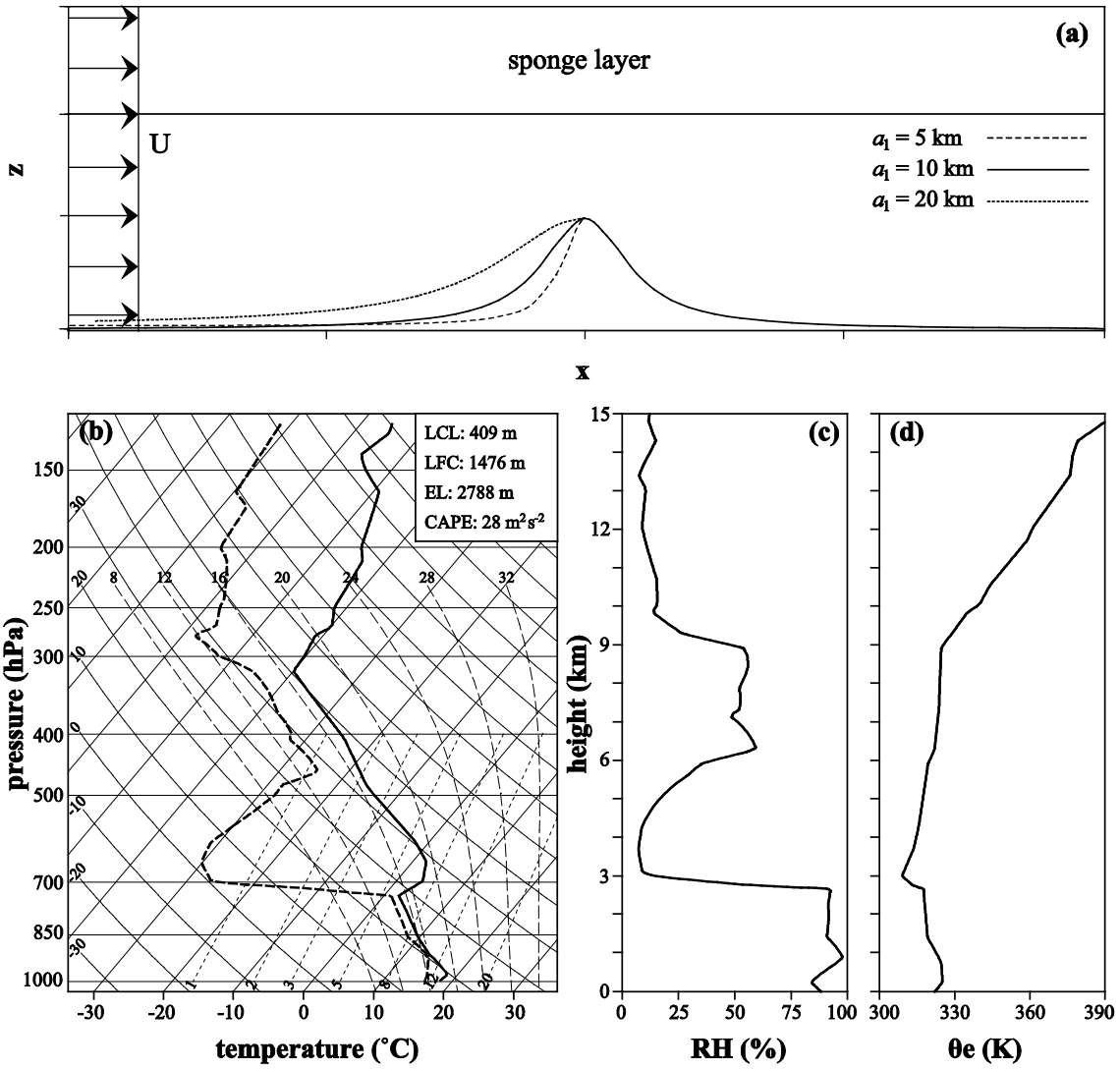

Figure 7.1. (a) Schematic diagram of the simulation configuration. The dashed (dotted) ridge line is for the case of narrow (wide) windward-width of the mountain. (b) Skew T-log P diagram, (c) relative humidity profile, and (d) equivalent potential temperature profile of the sounding data at Osan, South Korea at 00 UTC 19 September 2012.

	N_0 (cm^{-3})	a_1 (km)
CLN	100	10
CNT	500	10
PLT	2500	10
CLNn	100	5
CNTn	500	5
PLTn	2500	5
CLNw	100	20
CNTw	500	20
PLTw	2500	20

Table 7.1 Names and the corresponding aerosol number concentrations at 1% supersaturation N_0 and the half-width of the mountain upslope a_1 for the nine cases.

windward-width determined by $a = a_1$ (for $x < 0$ km) varies. We classify simulation cases into three groups based on the aerosol number concentration at 1% supersaturation N_0. The clean (CLN), control (CNT), and polluted (PLT) cases are simulated by considering N_0 = 100, 500, and 2500 cm^{-3}, respectively. Based on the windward-width (upslope steepness) of the mountain a_1, each group is subdivided into three cases (Table 7.1). The n and the w at the end of each case title indicate narrow (a_1 = 5 km) and wide (a_1 = 20 km) windward-width of the mountain, respectively. In this study, the uniform background wind speed U = 10 m s^{-1} is considered.

Sounding data of Osan, South Korea at 00 UTC on 19 September 2012 is used to simulate orographic precipitation from shallow convective clouds. Figures 7.1b, 7.1c, and 7.1d show the skew T-log P diagram, relative humidity profile, and equivalent potential temperature profile of the sounding data, respectively. Figure 7.1b gives the basic information about the thermodynamic structure. At the surface, the temperature is 17.8°C and the relative humidity is 86%. Although the level of free convection (LFC) is 1476 m, orographic clouds are generated at the lifting condensation level (LCL) of 409 m, which is below the mountain top. The surface height $h(x) = z_{LCL}$ is located at $x = -x_{LCL} \sim -1.2a_1$. Above the equilibrium level (EL) of 2788 m, a strong inversion layer is present, which prevents convective developments there. The temperature at EL is 2.2°C; this indicates that warm microphysical processes are adequate for simulating warm clouds.

The horizontal domain size is 1000 km with the grid size of 250 m. The open boundary condition is applied in the x-direction. The vertical domain size is 15 km, with a 5-km-depth sponge layer at the top. There are 401 terrain-following levels in the vertical direction. The WRF-bin model is integrated for 12 h with the time step of 0.6 s. The

spatial resolution in this study is appropriate to resolve the active cellular/banded convection involved in orographic-convective precipitation (Kirshbaum and Durran 2004; Kirshbaum and Smith 2008). With the exception of the bin microphysics scheme and basic turbulent/diffusion parameterization, other parameterizations, such as shortwave/longwave radiation, boundary layer, and surface physics, are not considered in the simulations.

7.3 Results and discussion

7.3.1 General characteristics of the simulated orographic precipitation

Figures 7.2 and 7.3 show the vertical velocity, the cloud droplet mixing ratio, and the raindrop mixing ratio at t = 1 and 6 h, respectively. In the begining (earlier than t = 1 h), shallow and cellular orographic-convective clouds develop over the mountain (not shown). At t = 1 h, the first convective cell that touches the mountain slope is located at $x \sim -x_{\mathrm{LCL}}$. A comparison of time scales related to orographic precipitation can give us a clue for the relative importance of given orographic-precipitation-related process (Jiang and Smith, 2003). Miglietta and Rotunno (2009) and Cannon et al. (2012) compared the convection time scale τ_{c} and the advection time scale τ_a which are defined as

$$\tau_{\mathrm{c}} = \frac{H_{\mathrm{c}}}{\sqrt{\mathrm{CAPE}}} \text{ and } \tau_{\mathrm{a}} = -x_{\mathrm{LCL}}/U, \tag{7.3}$$

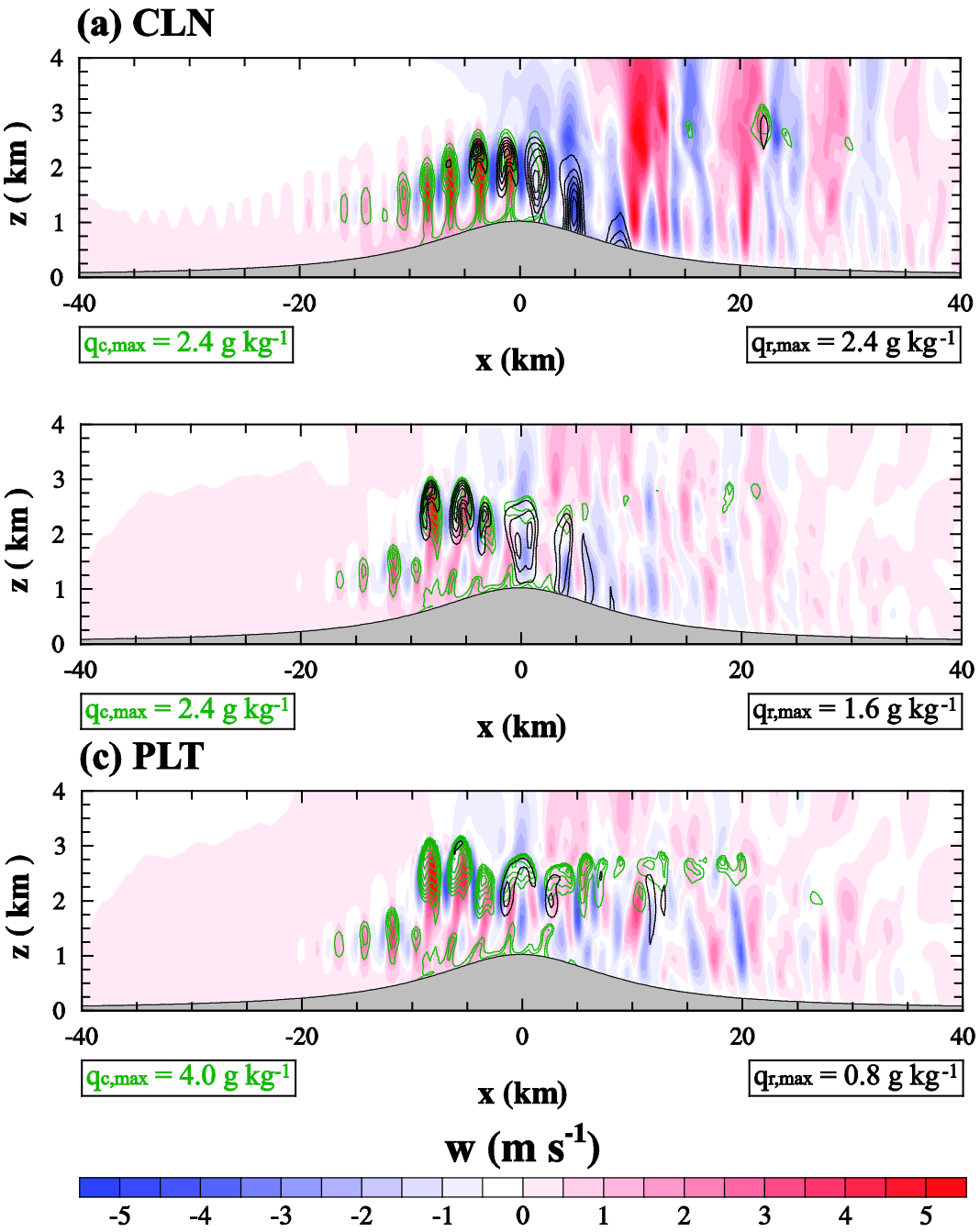

Figure 7.2 Fields of vertical velocity (shaded), cloud droplet mixing ratio (green contours), and raindrop mixing ratio (black contours) at t = 1 h in (a) CLN, (b) CNT, and (c) PLT. The contour interval is 0.4 g kg^{-1} and the maximal values of contour lines for cloud droplet and raindrop mixing ratio in each panel are presented on the bottom boxes.

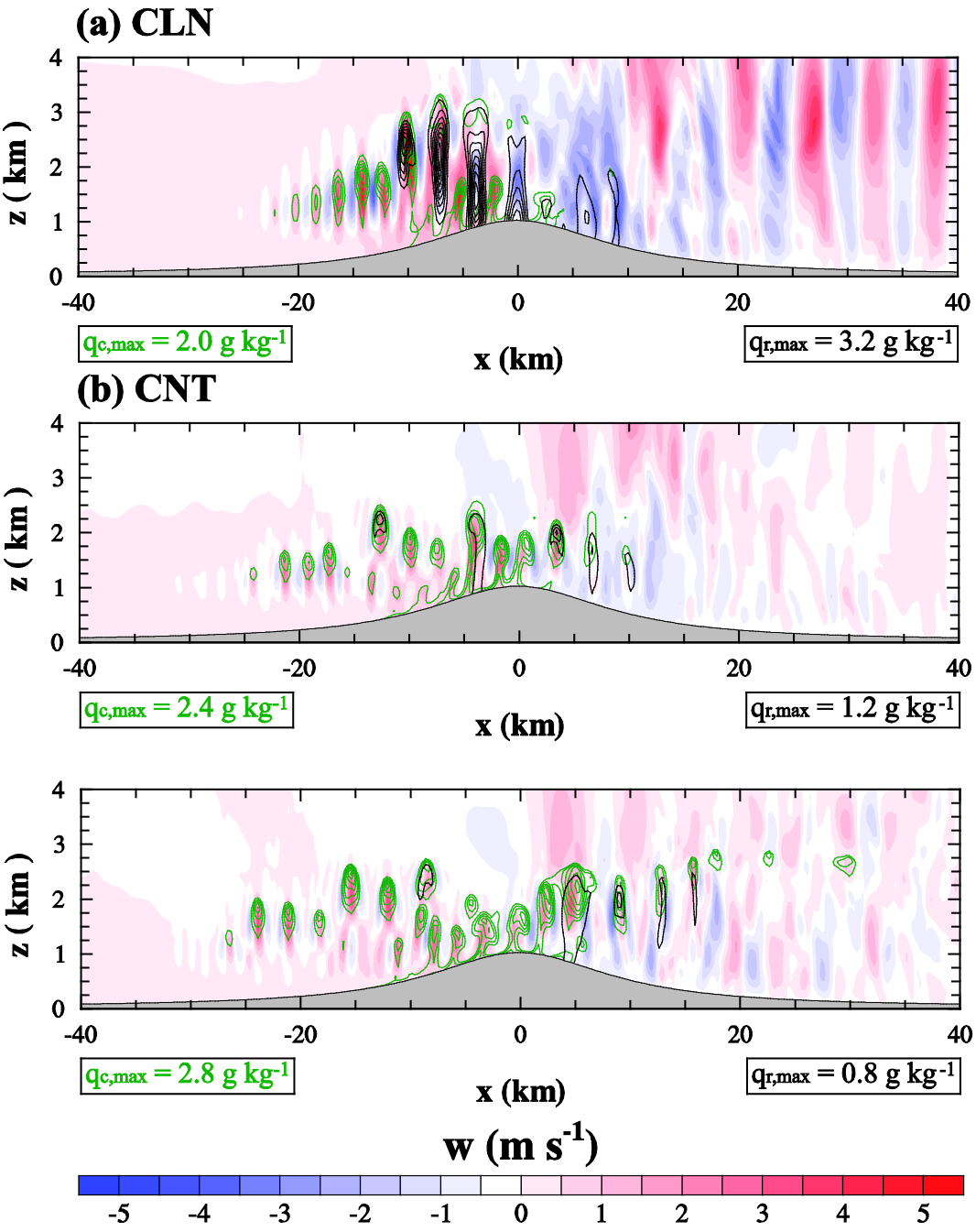

Figure 7.3 The same as Fig. 7.2, but at t = 6 h.

where H_c is the vertical length scale of convection ($z_{EL} - z_{LCL}$ = 2379 m in this study) and CAPE stands for the convective available potential energy. In the case with a_1 = 10 km and U = 10 m s^{-1}, τ_c ~ 450 s and τ_a ~ 1200 s. This means that orographic clouds generated at LCL can be fully developed up to EL before they reach the top of the mountain. Note that CAPE is calculated from LFC, not from LCL. In this case, the condensational heating provides an additional energy, and the updrafts over the upslope associated with the mountain waves strengthen the upward motion in the convective clouds.

Potential instability, which is determined by the sign of $d\theta_e/dz$, determines the type of orographic clouds (stratiform or convective). As shown in Fig. 1d, $d\theta_e/dz$ is less than –0.1 K m^{-1} in two layers, which are z = (0.7, 1.4) and (2.7, 3.0) in km. Kirshbaum and Durran (2004) showed that there can be a case in which convection does not develop even in the region of negative $d\theta_e/dz$. They suggested that N_m^2, where N_m is the moist Brunt-Väisälä frequency, can discriminate the possibility of convective development (unstable when $N_m^2 < 0$). Both formulas introduced by Lalas and Einaudi (1974) and Durran and Klemp (1982) show that N_m^2 is added by ($-dq_w/dz$) times a positive value, where q_w is the total water mixing ratio. For this reason, the development of convection in the layer z = (2.7, 3.0) km, in which the relative humidity steeply decreases (Fig. 7.1c), is weak or inhibited, while many convective cells can be developed in the layer z = (0.7, 1.4) km (see Figs. 7.1c and 7.1d).

Cloud droplets in orographic shallow convective clouds grow primarily through collision/coalescence. Over the mountain upslope, strong orographic uplift and strong convective updrafts enhance the growth of cloud droplets into large raindrops. Large raindrops with a fast enough terminal velocity can fall and reach the surface. A large

portion of liquid drops pass over the mountain peak by advection, so that the rainfall is concentrated over the mountain downslope. Downdrafts associated with mountain waves help the sedimentation of liquid drops by accelerating their fall speed, but also they enhance the evaporation of small raindrops and cloud droplets, so that they turn into water vapor before reacing the surface. At early stages, the transiently developed precipitating convection is propagated downstream [c.f., regime III in Chu and Lin (2000)]. From t ~ 6 h, the overall patterns of the flow and the hydrometeor distribution maintain a quasi-steady state. Hereafter, the snap shot at t = 6 h and the accumulated variables in the range t = 6–12 h are used for analysis.

7.3.2 Aerosol effects on the orographic precipitation

Figure 7.4 shows the horizontal distribution of accumulated surface precipitation amount from t = 6 to 12 h in CLN, CNT, and PLT. The total surface precipitation amount in the entire domain P_{tot}, the local maximum surface precipitation amount P_{max}, and the location x_{max} at which P_{max} occurs are listed in Table 7.2. The total surface precipitation amount decreases as N_0 increases, and the local maximum precipitation amount in CLN is 3.2 and 4.9 times in CNT and PLT, respectively. Generally, the surface precipitation is distributed more broadly in PLT than in CLN and CNT. As N_0 gets larger, the cloud droplet mixing ratio gets higher, while the raindrop mixing ratio gets lower (Figs. 7.2 and 7.3).

As in many previous studies, an increase in the number of CCN enhances nucleation into cloud droplets and results in a higher cloud droplet mixing ratio (Khain et al. 2004, 2005; Lynn et al. 2007; Xiao et al. 2014, 2015). However, the larger number of

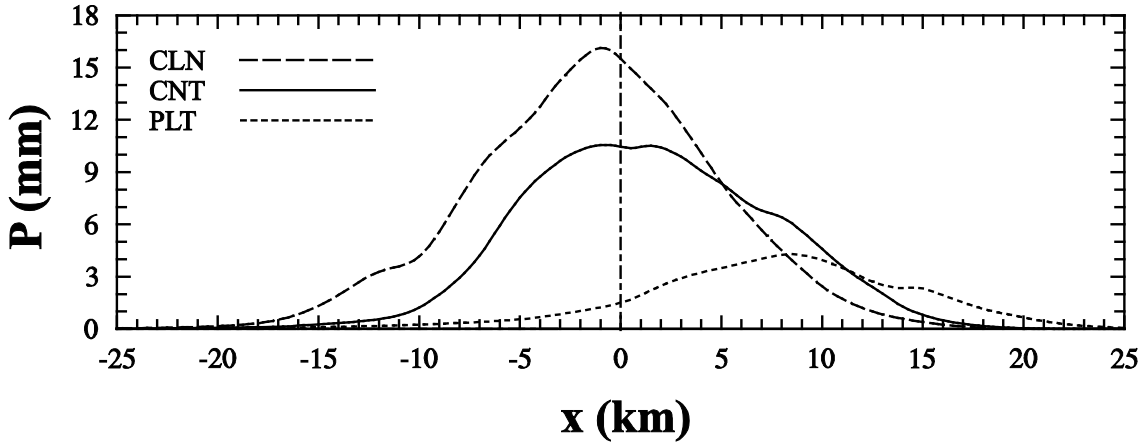

Figure 7.4 Accumulated surface precipitation amount from t = 6 to 12 h in the cases with a_1 = 10 km. The dash-dotted line indicates the x-location of the mountain peak (x = 0 km).

	P_{TOT} (mm)			P_{MAX} (mm)			x_{MAX} (km)		
a_1 (km)	5	10	20	5	10	20	5	10	20
CLN	1091	1175	1269	30.0	21.9	12.9	6.5	0.5	–6.3
CNT	621	779	1102	17.2	12.5	11.2	12.3	3.0	–1.3
PLT	181	365	538	4.4	4.5	6.9	17.5	8.5	–0.8

Table 7.2. Total surface precipitation amount in the entire domain from t = 6 to 12 h P_{tot}, the local maximum surface precipitation amount P_{max}, and the location x_{max} at which P_{max} occurs.

cloud droplets causes a decrease in the average size of liquid drops, and the growth of cloud droplets into raindrops is reduced. As a result, the total surface precipitation amount is smaller in PLT compared to the other cases. In CLN, however, active growth into raindrops causes a rapid sedimentation of liquid drops. In PLT, a large portion of liquid drops are advected downstream of the mountain peak, and the surface precipitation is distributed more broadly on the leeside of the mountain.

Table 7.3 shows the condensation, evaporation, and precipitation rates integrated over the mountain upslope and downslope within 100 km in the horizontal direction and 3 km in the vertical direction. Condensation is more active than evaporation over the mountain upslope, and evaporation is more active than condensation over the mountain downslope. Over both the mountain upslope and downslope, differences in condensation and evaporation rates between PLT and CNT are higher than those between CNT and CLN. The generated net liquid drops over the mountain upslope fall onto ground or are advected toward the leeward side of the mountain. The precipitation rates are 89%, 195%, and 445% on the downslope compared to those on the upslope in CLN, CNT, and PLT, respectively. In CLN, more precipitation occurs on the upslope than on the downslope, while more precipitation is distributed on the downslope in CNT and PLT.

To analyze the size distribution of liquid drops that pass over the mountain peak, we calculate the advection rate of liquid drops over the mountain peak ($x = 0$) as follows (Fig. 7.5):

$$A(r) = \rho_w \int_{h_m}^{h_m+H} q_l(r, x=0, z) U(x=0, z) dz, \tag{7.4}$$

	C_{up} (kg s^{-1})			E_{up} (kg s^{-1})			P_{up} (kg s^{-1})		
a_1 (km)	5	10	20	5	10	20	5	10	20
CLN	2.14	2.47	2.70	0.39	0.77	1.04	0.43	2.88	4.99
CNT	2.24	2.66	3.11	0.62	1.14	1.49	0.17	1.22	3.79
PLT	2.44	3.10	3.45	0.83	1.76	2.20	0.08	0.31	1.87
	C_{down} (kg s^{-1})			E_{down} (kg s^{-1})			P_{down} (kg s^{-1})		
CLN	1.12	0.61	0.36	1.22	0.70	0.40	4.63	2.56	0.90
CNT	1.57	0.64	0.40	1.70	0.71	0.51	2.71	2.38	1.31
PLT	3.34	1.52	0.73	3.58	1.74	0.89	0.76	1.38	1.15
	C_{down}/C_{up}			E_{down}/E_{up}			P_{down}/P_{up}		
CLN	0.52	0.25	0.13	3.13	0.91	0.38	10.77	0.89	0.18
CNT	0.70	0.24	0.13	2.74	0.62	0.34	15.94	1.95	0.35
PLT	1.37	0.49	0.21	4.31	0.99	0.40	9.50	4.45	0.61

Table 7.3 Condensation, evaporation, and precipitation rates over the mountain upslope (C_{up}, E_{up}, and P_{up}) integrated from $x = -100$ to $x = 0$ km and those over the mountain downslope (C_{down}, E_{down}, and P_{down}) integrated from $x = 0$ to $x = 100$ km below $z = h(x) + 3$ km. The ratio of each rate over the mountain downslope to the corresponding rate over the mountain upslope is also presented.

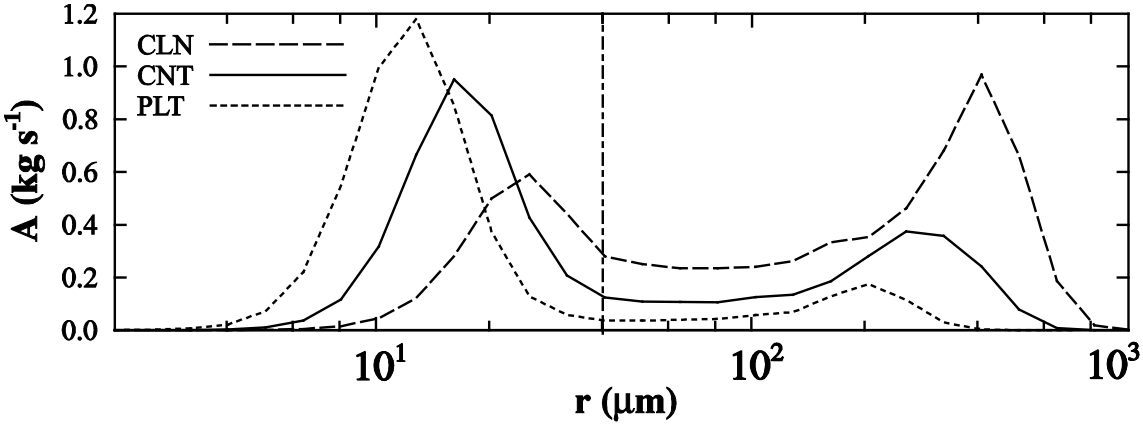

Figure 7.5 Size distribution of the accumulated advection rate of liquid drops (kg s^{-1}) over the mountain peak from t = 6 to 12 h as a function of drop radius in the cases with a_1 = 10 km. The dash-dotted line indicates the size-boundary between cloud droplet and raindrop (r = 40 μm).

where ρ_w is the density of liquid water, H (= 3 km) is the vertical depth of the integration, q_l is the liquid drop mixing ratio, and U is the horizontal velocity. The size distribution of liquid drops has a double-peak structure in the size ranges of cloud droplets and raindrops. As discussed, most of liquid drops are cloud droplets in PLT. Compared to CLN and CNT, the average size of cloud droplets is smaller in PLT. In CLN, more than half the mass of the advected liquid drops is the mass of raindrops, and the average size of raindrops is larger than those in CNT and PLT due to the faster growth of cloud droplets. The large amount of drops between two peaks in CLN indicates that the growth from cloud droplets to raindrops is active in convective clouds near the mountain peak.

To examine the effects of aerosols on the spatial characteristics of the size distribution of liquid drops, the difference in the mass and number size distributions of liquid drops between PLT and CLN as a function of the horizontal location and the height above the surface is given in Fig. 7.6. In PLT, relatively small cloud droplets are distributed over both the mountain upslope and downslope (Fig. 7.6a). In CLN, larger cloud droplets are located in the horizontally narrow region mainly over the mountain upslope. Over the mountain peak, larger raindrops are also located in CLN, while smaller raindrops are located farther downstream in PLT. The active condensation in PLT results in a strong latent heat release. The strong latent heat release generates active convection over the mountain, and the convective clouds can reach a high altitude (Fig. 7.6b). Because the initial CCN number concentration in PLT is 25 times higher than that in CLN, the number concentration of very small droplets over the entire domain is clearly higher in PLT (Fig. 7.6c) than in CLN. In PLT, small raindrops get smaller through

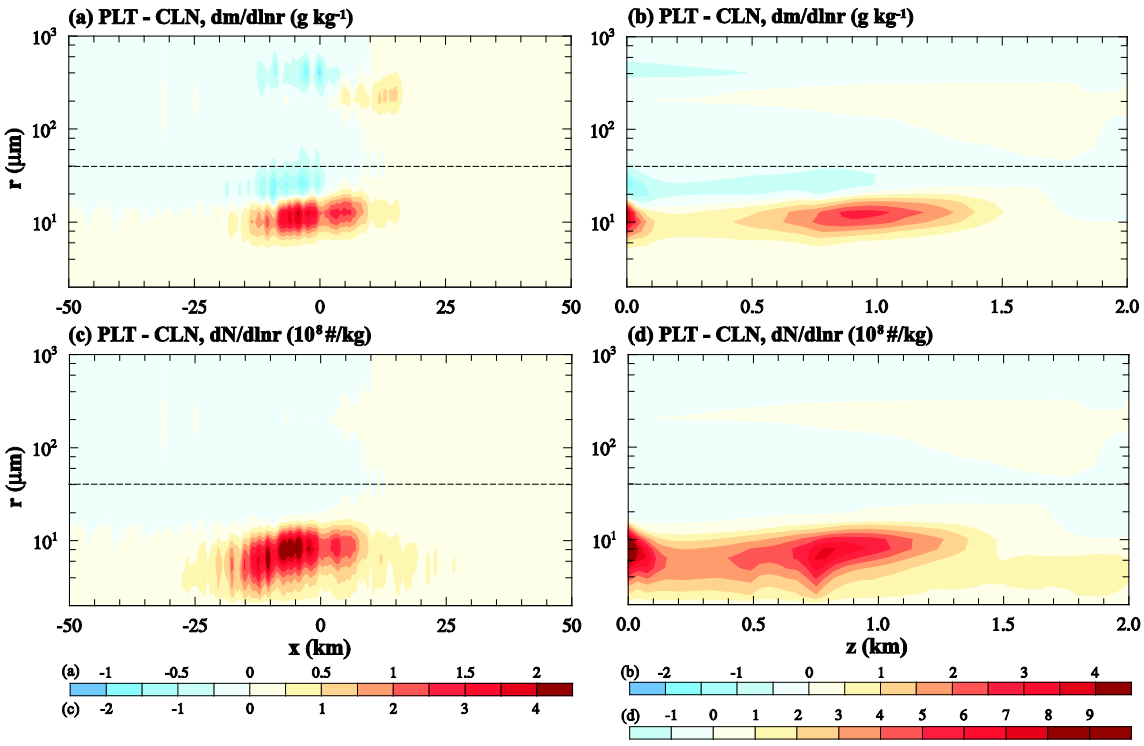

Figure 7.6 Differences in (a, b) mass size distribution and (c, d) number size distribution between PLT and CLN as a function of (a, c) *x* and (b, d) height above the surface.

evaporation while falling. As a result, many raindrops are located at higher altitudes, rather than near the surface, compared to CLN in which the mass distribution of raindrops near the surface is higher than PLT. Similar to the mass distribution in Fig. 7.6b, most cloud droplets are in the convection area and near the surface, and their size is very small in PLT (Fig. 7.6d).

7.3.3 Sensitivity of the aerosol effects on the orographic precipitation to the mountain upslope angle

Changing the half-width of the windward side of the mountain controls the upslope steepness and the advection timescale [Eq. (7.3)]. Figure 7.7 is the same as Fig. 7.2 except for CLNn, CNTn, and PLTn at t = 6 h. In the cases with narrow windward-width, a steeper upslope rapidly lifts moist air; this results in an increase in the maximum precipitation rate in CLNn and CNTn (Table 7.2). However, the shorter windward-width and advection timescale (τ_a ~ 600 s) cause a reduced condensation rate over the upslope (Table 7.3) and a decreased precipitation rate. In PLTn, less cloud droplets over the mountain upslope and downslope grow into raindrops on a shortened advection time scale. Thus, cloud droplets evaporate rapidly due to the downdrafts associated with mountain waves (Table 7.3). Therefore, aerosol effects on the total precipitation amount and maximum precipitation rate become more remarkable in the cases of the narrow windward-width. Smaller size distribution of liquid drops over the mountain peak causes increases in x_{MAX} (Table 7.2 and Fig. 7.9a). A more remarkable aerosol effects, that is, a decrease in total precipitation amount and a downstream shift of the location of the maximum precipitation amount, can also be seen from the horizontal distribution of the

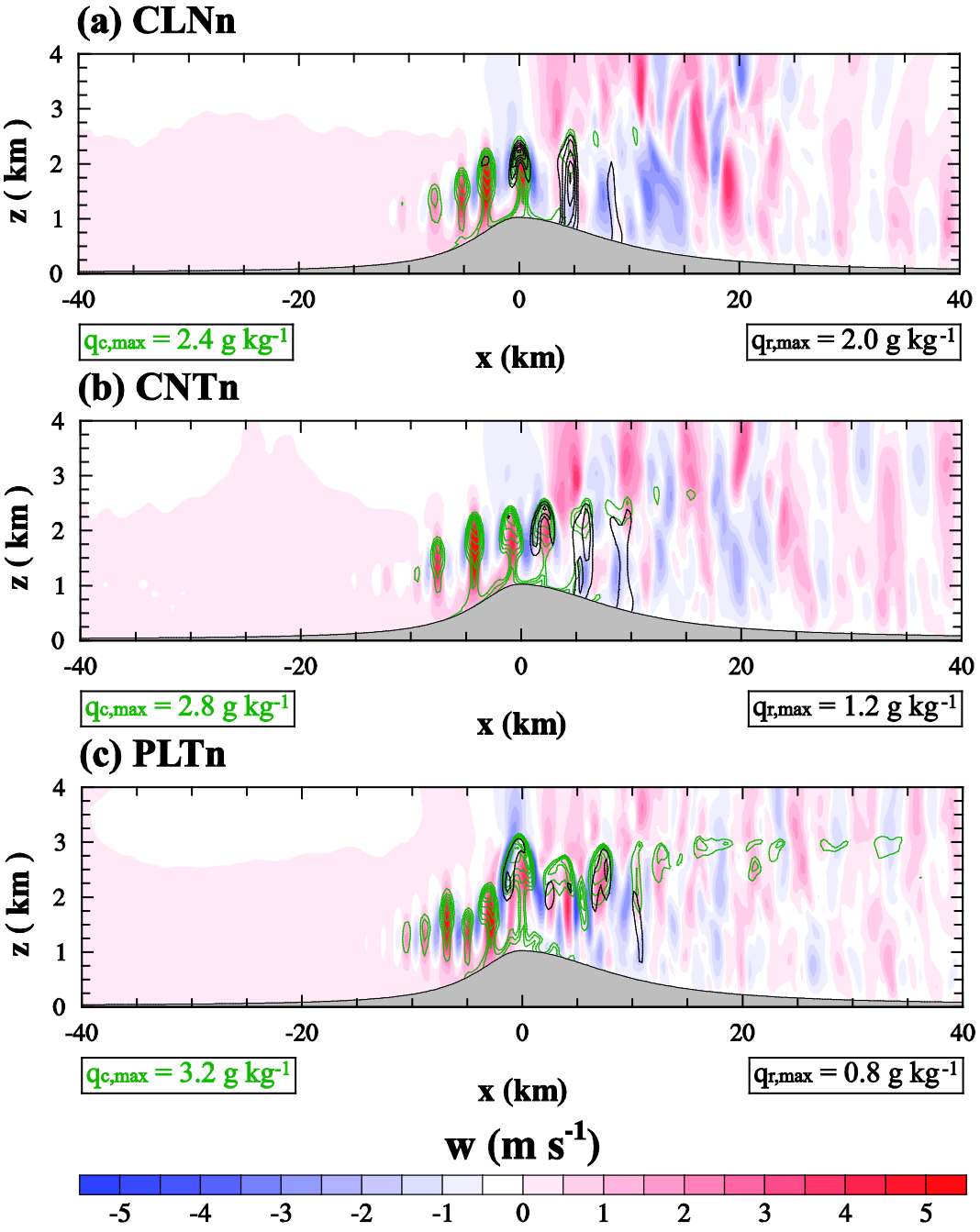

Figure 7.7 The same as Fig. 7.2 except for (a) CLNn, (b) CNTn, and (c) PLTn at t = 6 h.

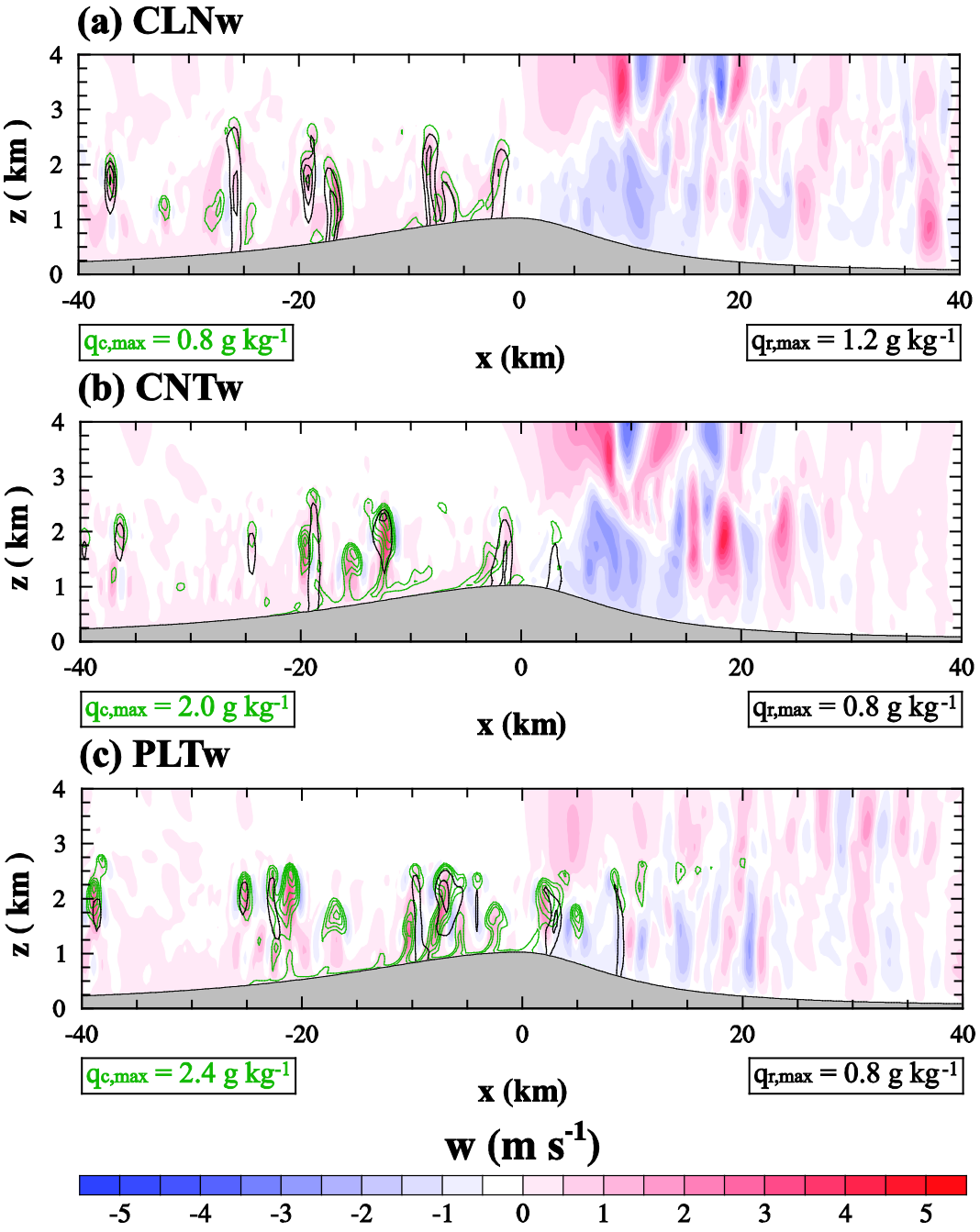

Figure 7.8. The same as Fig. 7.2 except for (a) CLNw, (b) CNTw, and (c) PLTw at t = 6 h.

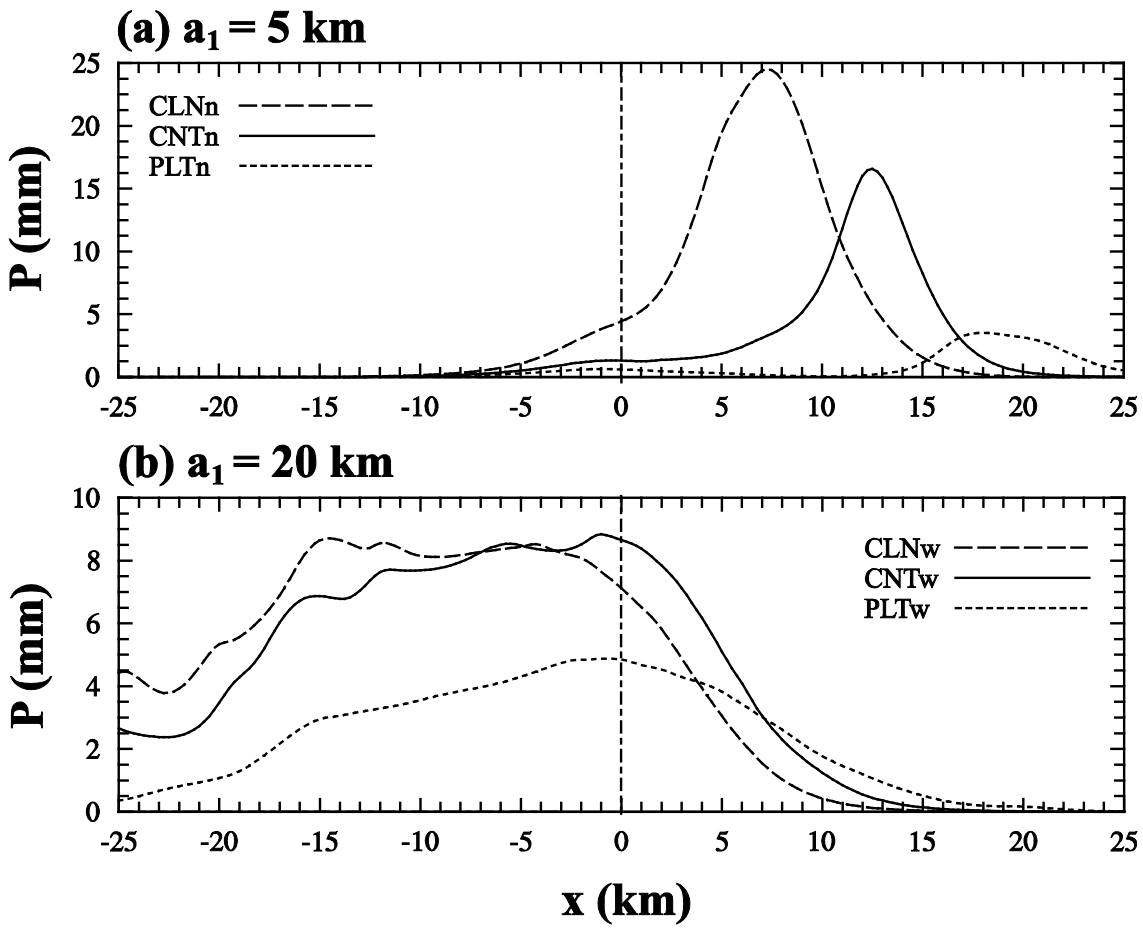

Figure 7.9. Accumulated surface precipitation amount from t = 6 to 12 h in the cases with a_1 = (a) 5 km and (b) 20 km. The dash-dotted line indicates the x-location of the mountain peak (x = 0 km).

accumulated surface precipitation amount in Fig. 7.9a.

Figure 7.8 is the same as Fig. 7.2 except for CLNw, CNTw, and PLTw at t = 6 h. In the cases with wide windward-width, there are greater chances for cloud droplets to grow and for liquid drops to fall onto the surface over the long distance of the mountain upslope on a longer advection time scale (τ_a ~ 2400 s). For this reason, a large amount of drops are precipitated out onto the surface before the advected hydrometeors reach the mountain peak. The horizontal distribution of the accumulated surface precipitation amount in Fig. 7.9b shows a broader rainfall distribution over the mountain upslope and a smaller amount of precipitation over the mountain downslope. The slower growth of cloud droplets in PLTw results in a smaller precipitation amount and the location of maximum precipitation amount being farther downstream than those in CLNw and CNTw, while $x_{\max}$ is located on the mountain upslope in these all cases (Table 7.2). Compared to the cases with narrow windward-width and with the symmetric mountain, there is a smaller decrease in the total precipitation amount and in the maximum precipitation amount due to higher-N_0 in the cases with wide windward-width.

The advection rate of liquid drops over the mountain peak as a function of drop radius in the case with narrow windward-width given in Fig. 7.10a shows that a larger number of cloud droplets are generated and advected over the mountain peak due to the stronger uplift by the steeper upslope. However, shorter advection timescale results in the smaller number of large raindrops. The average size of raindrops in CNTn is smaller than those in CLNn and PLTn. The larger size distribution of raindrops in CLNn is due to the lower aerosol number concentration. On the other hand, having more active and deeper convection in PLTn results in a larger size distribution than CNTn. In the cases with wide

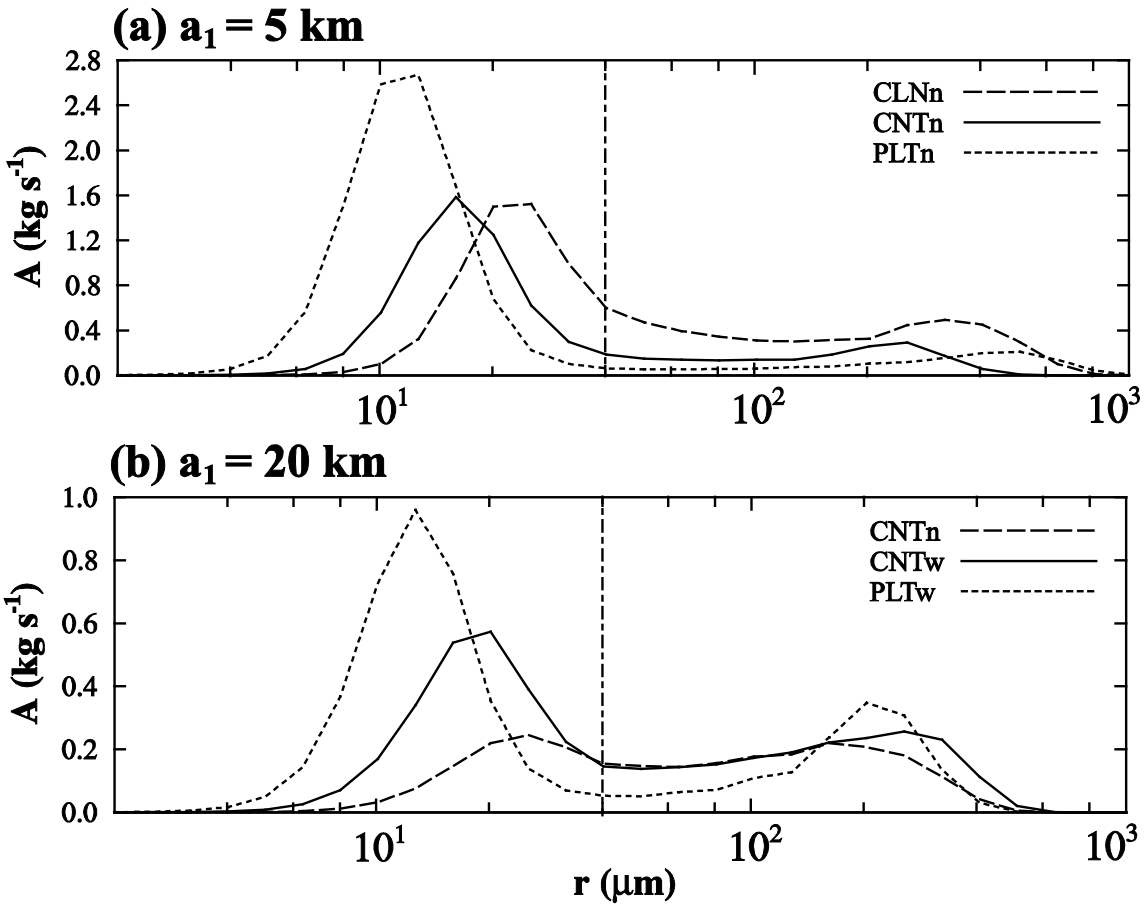

Figure 7.10. Accumulated advection rate of liquid drops over the mountain peak from t = 6 to 12 h as a function of drop radius in the cases with a_1 = (a) 5 km and (b) 20 km. The dash-dotted line indicates the size-boundary between cloud droplet and raindrop (r = 40 μm).

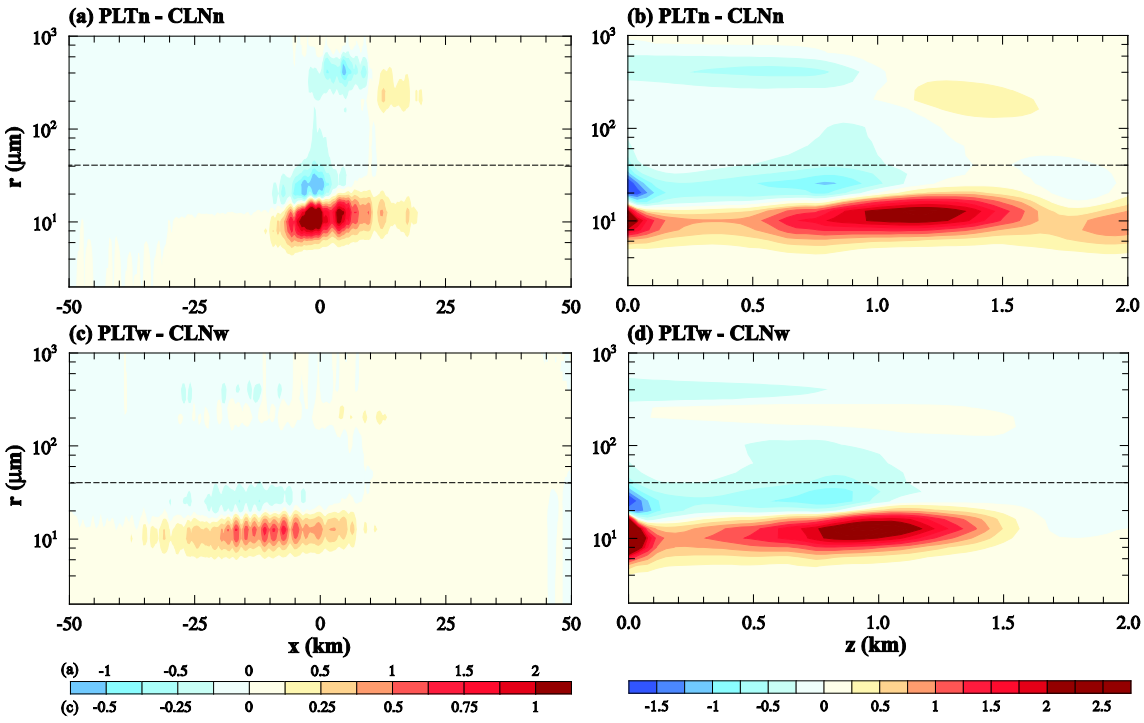

Figure 7.11. Differences in mass size distribution (g kg^{-1}) between (a, b) PLTn and CLNn and (c, d) PLTw and CLNw as a function of (a, c) *x* and (b, d) height above the surface.

windward-width, the long distance upslope provides a better opportunity and time for cloud droplets to grow, so that a large portion of raindrops are precipitated out onto the wide mountain upslope. As a result, the amount of drops that are advected over the mountain peak is small in all cases (Fig. 7.10b). In these cases, the average size of raindrops in CNTw is larger than those in CLNw and PLTw. In CLNw, the faster growth of liquid drops results in more precipitation on the upslope and the decrease in the advected large-sized raindrops over the mountain peak. The smaller size distribution in PLTw is due to the higher aerosol number concentration, while the smaller precipitation amount on the upslope results in the higher advection rate of raindrops over the mountain peak. In the cases with both narrow and wide windward-widths, the double peak pattern is not clearly compared to the cases with the symmetric mountain due to the lack of the advected raindrops over the mountain peak (Figs. 7.5 and 7.9). Note that the change of the size distribution due to the change of the aerosol number concentration is not monotonic, especially for the size distribution of raindrops.

Figure 7.11 presents the differences in mass size distribution between PLTn and CLNn and between PLTw and CLNw as functions of the horizontal location and the height above the surface. In the cases with narrow windward-width, the steeper upslope generates stronger and deeper convection, and the strengthening is outstanding in PLTn compared to that in CLNn (Figs 7.11b), so that the total precipitation amount and the maximum precipitation rate are larger than the cases with the symmetric mountain and the wide windward-width. Although the advection rate of raindrops is lower over the mountain peak due to the insufficient advection time (Fig. 7.9a), cloud droplets grow into raindrops over the downslope. Because the average size of liquid drops is smaller in

PLTn than in CLNn, longer advection time is needed for cloud droplets to grow into large-sized raindrops that have enough terminal velocity to precipitate. As a result, the downstream shifting of the maximal precipitation amount location is clearly seen, but the size difference between PLTn and CLNn is smaller than the cases with the symmetric mountain (Fig. 7.11a).

In the cases with wide windward-width, shallower convection is generated compared to the cases with narrow windward-width over the upslope (Figs. 7.11c and 7.11d). Compared to the cases with narrow windward-width and with the symmetric mountain, clearly distinguished size distributions of cloud droplets and raindrops between PLTw and CLNw are observed in the cases with wide windward-width (Fig. 7.11c) because generation, growth, and precipitation occur almost uniformly over a wider range of the mountain upslope. Because most of the precipitable water are consumed over the wider upslope, the aerosol effects on the total precipitation amount and the location of the maximum precipitation amount are not as obvious.

8 Modeling of orographic-convective precipitation: Deep and mixed-phase clouds

8.1 Introduction

Since aerosol particles act as cloud condensation nuclei (CCN) or ice nuclei (IN) in the atmosphere, aerosol loading controls precipitation characteristics through complex aerosol-cloud-precipitation interactions. To understand the role of aerosol particles in controlling the precipitation characteristics, many researchers have extensively investigated the impacts of aerosols on clouds and precipitation (e.g., Khain, 2009; Tao et al., 2012; Fan et al., 2016).

Precipitation over a mountainous region, called orographic precipitation, is affected by various factors, such as static stability, background wind speed, environmental humidity, and mountain geometry (Colle 2004; Pathirana et al. 2005; Roe and Baker 2006). However, the sensitivity of orographic precipitation to the environmental factors and mountain geometry is generally caused by orographic precipitation from shallow clouds because in broad ranges of the environmental factors and mountain geometry, the downdraft associated with mountain waves restricts convective development of orographic clouds. Several studies have investigated orographic precipitation in a conditionally unstable atmosphere and have categorized the behavior of convective orographic clouds based on convective available potential energy (CAPE), mountain width, and the Froude number ($F = U/Nh_m$), where U is the background wind speed, N is the buoyancy frequency, and h_m is the maximum height of

the mountain (e.g., Chu and Lin 2000; Chen and Lin 2005; Chen et al. 2008; Miglietta and Rotunno 2009; Sever and Lin 2017).

Many previous studies have shown that an increase in aerosol number concentration usually results in a decrease in surface precipitation from shallow convection (Xue and Feingold 2006; Cheng et al. 2007; Fan et al. 2012) and in an increase in surface precipitation from deep convection (Khain et al. 2005; Rosenfeld et al. 2008; Clavner et al. 2018). Many studies have shown that air pollution causes suppression of orographic precipitation in mountainous regions (Givati and Rosenfeld 2004; Jirak and Cotton 2006; Rosenfeld and Givati 2006; Rosenfeld et al. 2007; Guo et al. 2014). Xiao et al. (2015) showed that an increase in aerosol number concentration results in the enhanced orographic precipitation, but its effects on deep convective orographic precipitation have not yet been studied as much.

Bin microphysics models predict each size bin for each hydrometeor (e.g., Khain et al. 2000; Lynn et al. 2005a, b). To investigate the microphysical processes under orographic precipitation more precisely, numerical studies of orographic precipitation using bin microphysics scheme are recently carried out (Lynn et al. 2007; Xue et al. 2010; Xiao et al. 2014, 2015). However, almost all studies of orographic precipitation using bin microphysics scheme are limited to orographic precipitation from shallow clouds.

This study aims to understand how windward mountain upslope controls aerosol effects on orographic precipitation from deep convective clouds. In Section 8.2, the experimental design for simulations is described. Section 8.3.1 and 8.3.2 present the characteristics for orographic precipitations from deep convective clouds and their

dependencies on aerosol number concentration. The sensitivity of aerosol effects on orographic precipitation to windward mountain upslope is discussed in Section 8.3.3.

8.2 Experimental design

In this study, the Weather Research and Forecasting (WRF) model, version 3.6.1, coupled with the Hebrew University Cloud Model (HUCM) is used (Skamarock et al. 2008; Lee and Baik 2016). The model is the same as in Chapter 7 except that the mixed-phase microphysical processes are included. This model predicts seven hydrometeor types [liquid drop, ice crystal (column, plate, and dendrite), snow, graupel, and hail] and aerosol which are subdivided into 43 mass-doubling bins. The detailed descriptions of the HUCM are provided in Khain et al. (2000, 2004, 2011).

Two-dimensional simulations are conducted to examine orographic precipitation from deep convective clouds. Figure 8.1 shows a schematic of the simulations. The bell-shaped mountain, defined as in Eq. (8.1), triggers orographic clouds by a forced uplift:

$$h(x) = h_m \frac{a^2}{x^2 + a^2}. \tag{8.1}$$

Here, h_m (= 2 km) is the maximum height and a (= a_1 for x < 0 km and = a_2 = 10 km for x ≥ 0 km) is the half-width of the bell-shaped mountain. As in Chapter 7, we classify simulation cases by aerosol number concentration at 1% supersaturation N_0 [= 100 cm^{-3} for CLN (clean), = 500 cm^{-3} for CNT (control), and = 2500 cm^{-3} for PLT (polluted)] and the windward-width (upslope steepness) of the mountain a_1 (= 5 km for narrow, = 10 km

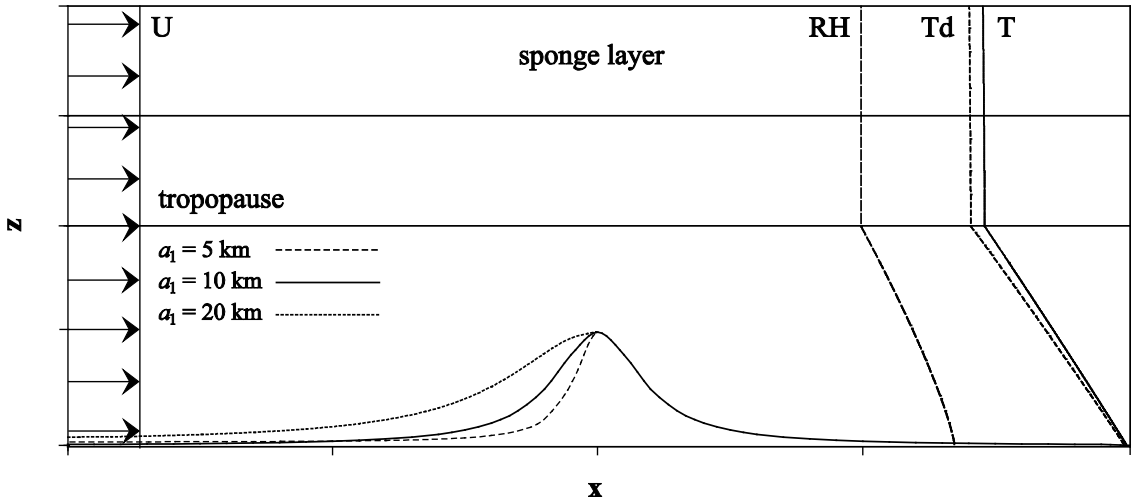

Figure 8.1. The schematic of the simulations. The dashed, solid, and dotted upslope ridge are for the case of narrow windward-width (steep upslope), symmetric, and wide windward-width (gentle upslope) mountain. In this study, the tropopause is located at z = 12 km. Vertical profiles of temperature T, dew point temperature T_d, and relative humidity RH are roughly described.

for control, and = 20 km for wide). Table 7.1 provides the name and specific setting for each case. The background wind speed U = 10 m s^{-1} is constant in the vertical.

To generate vigorous convective orographic clouds, a modified vertical sounding of Weisman and Klemp (1982) is used. In this study, the potential temperature θ and the relative humidity H are defined as follows.

$$\theta(z) = \begin{cases} \theta_0 \left(1 + \dfrac{N^2 z}{g} \right) \text{for } z \le z_{\text{tr}}, \\ \theta_{\text{tr}} \exp\left[\dfrac{g}{c_p T_{\text{tr}}} (z - z_{\text{tr}}) \right] \text{for } z > z_{\text{tr}}, \end{cases} \tag{8.2}$$

$$H(z) = \begin{cases} H_0 \left[1 - \dfrac{3}{4} \left(\dfrac{z}{z_{\text{tr}}} \right)^{5/4} \right] \text{for } z \le z_{\text{tr}}, \\ H_{\text{tr}} \text{ for } z > z_{\text{tr}}, \end{cases} \tag{8.3}$$

where θ_0 (= 298.15 K) and θ_{tr} [H_0 (= 0.9) and H_{tr}] are the potential temperature [the relative humidity] at the surface and the tropopause height z_{tr} (= 12 km), respectively, T_{tr} is the temperature at the tropopause height, c_p is the specific heat of air at constant pressure, N (= 0.01 s^{-1}) is the buoyancy frequency, and g is the gravitational acceleration. By fixing N, the Froude number is easily controlled. The skew T-log P diagram of this sounding is depicted in Fig. 8.2. The lifting condensation level (= 750 m) is located below the mountain top, so orographic clouds can be generated by a forced uplift. Because of the highly unstable vertical structure of the sounding (CAPE = 4448 J), deep and strong convection can be developed through the tropopause. A horizontal domain of 200 km with Δx = 250 m is considered. The vertical domain size is 20 km with a sponge

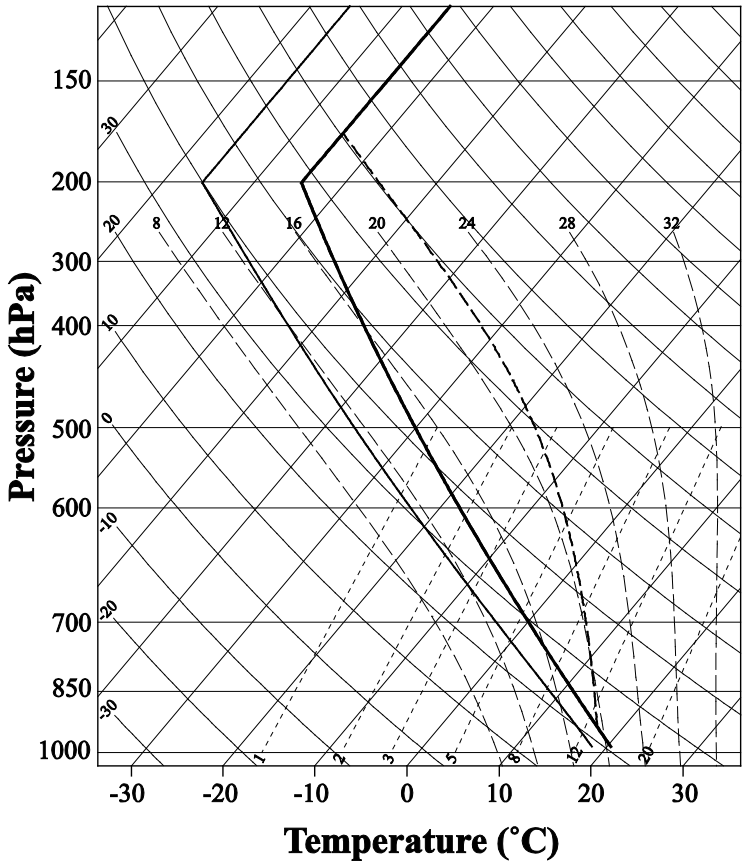

Figure 8.2. Skew T-log P diagram of the simulations. This sounding is modified version of the sounding in Weisman and Klemp (1982).

layer of 5-km-depth and with 401 terrain-following levels. Horizontally, the open boundary condition is considered. Each case is integrated by the WRF-bin model for 12 h with the time step of 0.6 s. However, the early 6-h results will be examined for the reason given in Section 8.3.1. Except for the bin microphysics scheme and basic turbulent/diffusion parameterization, other parameterizations are not considered.

8.3 Experimental design

8.3.1 General characteristics of the simulated orographic precipitation

Figure 8.3 shows the mixing ratio of the liquid drop (bluish shading), low-density ice particles (greenish shading), which are ice crystal and snow, and high-density ice particles (black contours), which are graupel and hail, and wind vectors of the CNT case. From early on, orographic clouds are generated over the upslope. In the subcritical condition ($F < 1$), on the other hand, flows are converged in a thin layer and are accelerated over the downslope. As a result, a hydraulic jump occurs and a strong updraft is generated over the downslope (Fig. 8.3a). This deep convective system is downstream advected by the downslope wind, and results in heavy precipitation lee of the mountain (Fig. 8.3b). After the transiently generated deep convective system is advected downstream of the mountain, the two departed cloud systems are clearly seen in the lower and upper layers (Fig. 8.3c). In the lower layer, orographic clouds only with liquid drops are present. Because of the downdraft associated with mountain waves, shallow orographic clouds cannot be developed vigorously in the stratified atmosphere. In the

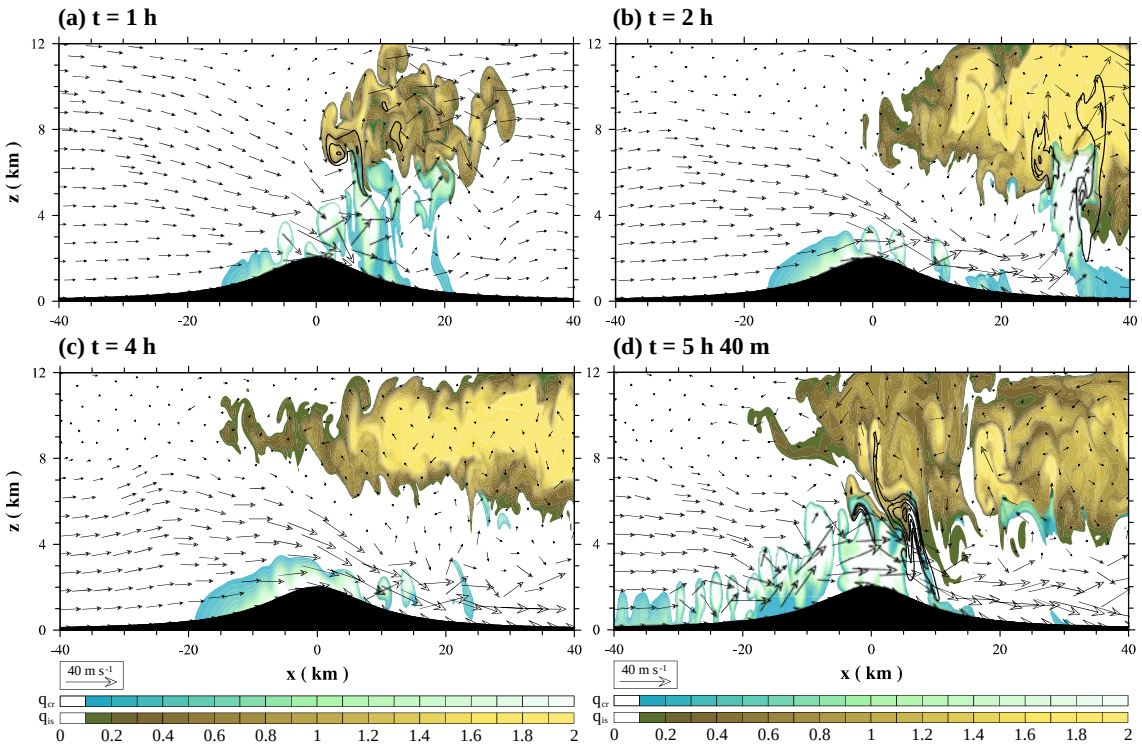

Figure 8.3. Mixing ratio of the liquid drop (bluish shading), low-density ice particle (greenish shading), which are ice crystal and snow, and high-density ice particle (black contours), which are graupel and hail, and wind vectors in CNT at t = (a) 1 h, (b) 2 h, (c) 4 h, and (d) 5 h 40 m. The contour interval of the high-density ice particle mixing ratio is 0.02 g kg^{-1}.

upper layer, where the weak updraft associated with mountain waves is located, ice crystals are generated and are grown into snow particles. Because this updraft associated with mountain waves is in phase with negative perturbation horizontal velocity, the upper-layer cloud with low-density ice particles is extended upstream if negative perturbation horizontal velocity exceeds the background wind speed. After $t \sim 4$ h, the lower-level stratiform orographic clouds are transformed into cellular-type convective orographic clouds due to the condensational latent heating and are extended upstream. Occasionally, some deep convective cloud cells deeply develop and interact with the upper-layer mixed-phased cloud. This interaction results in intermittent heavy precipitation by melting of high-density ice particles or direct precipitation of graupel or hail (Fig. 8.3d).

Figure 8.4 shows the Hovmöller diagrams of the surface rain rate (shaded) and ice-phased precipitation rate (contoured only for 0.01 mm h^{-1}) in CLN, CNT, and PLT. As described earlier, the transiently generated deep convective system is advected downstream while the orographic precipitation occurs steadily near the mountain. This pattern is of regime III in Chu and Lin (2000). In CNT and PLT, orographic precipitation is extended upstream from $t \sim 5$ h. In all cases, ice-phased precipitation is dominant near and lee of the mountain peak after $t \sim 6$ h because the freezing level gets lower with time. In this study, we focus on how the aerosol number concentration and the upstream steepness of the mountain affect the surface rainfall over a mountainous area through the interaction between deep convective orographic clouds and upper-level mixed-phased clouds. For this reason, the averaged and accumulated variables from $t = 4$ to 6 h are given particular attention in this study in order to avoid the time periods during which the influence of the

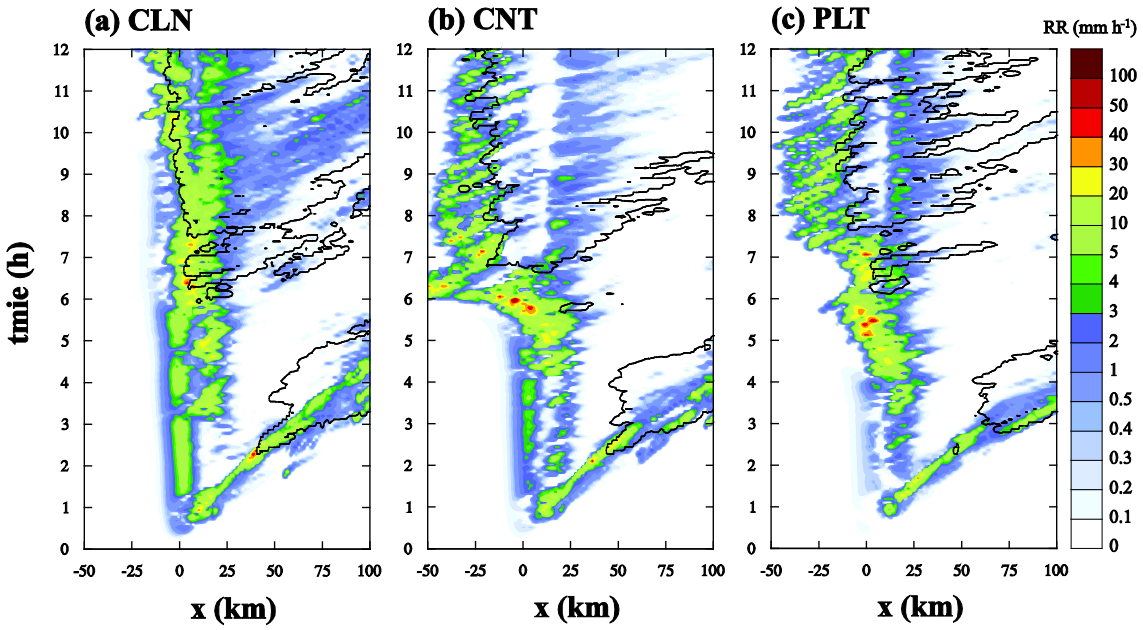

Figure 8.4. Hovmöller diagrams of the surface rain rate (shaded) and ice-phased precipitation rate (contoured only for 0.01 mm h^{-1}) in CLN, CNT, and PLT.

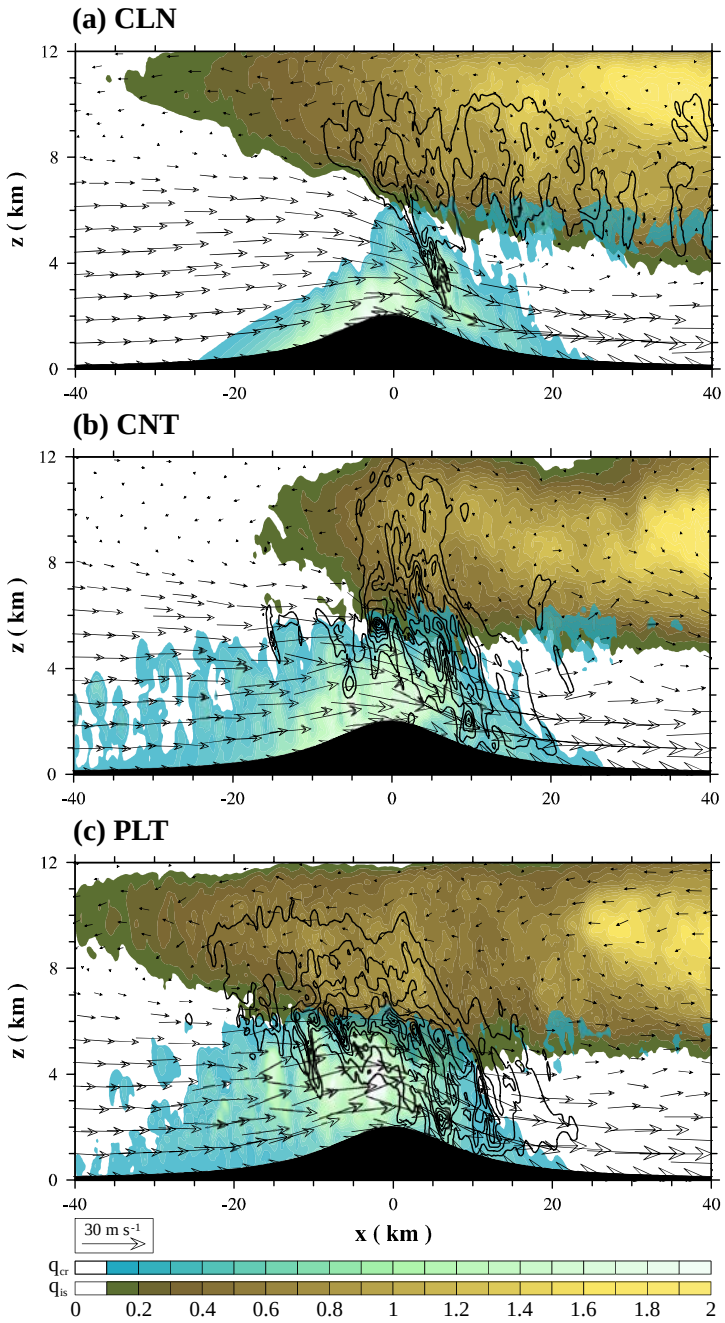

Figure 8.5. Averaged mixing ratio of the liquid drop (bluish shading), low-density ice particles (greenish shading), which are ice crystal and snow, and high-density ice particles (black contours), which are graupel and hail, and wind vectors from t = 4 to 6 h in (a) CLN, (b) CNT, and (c) PLT. The contour interval of the high-density ice particle mixing ratio is 0.05 g kg^{-1}.

transiently developed deep convective system (t = 0–4 h) is strong and the time period during which ice-phased precipitation is dominant (t = 6–12 h).

8.3.2 Aerosol effects on orographic precipitation

Figure 8.5 shows the averaged mixing ratio of the liquid drop, low-density ice particle, and high-density particle, and wind vectors in CLN, CNT, and PLT from t = 4 to 6 h. In this period, lower-level convective orographic clouds are developed over the mountain. In the case with higher aerosol number concentration, the higher number of condensates results in a stronger condensational latent heating which results in a deeper and stronger convection. As a result, many liquid drops can interact with ice particles in the upper-level cloud and are frozen into ice crystals above the freezing level. Both pathways result in higher mixing ratio of the high-density ice particles in the case with higher aerosol number concentration. The high-density ice particles grow via riming in both the lower- and upper-level clouds and result in the enhancement of surface precipitation amount via melting or direct sedimentation. Figure 8.6 and Table 8.1 show that an increase in aerosol number concentration causes increases in the total and maximum precipitation amounts and upstream shifting of the location of the maximum precipitation. This dependency of the precipitation characteristics on the aerosol number concentration the opposite of the case of shallow, warm orographic precipitation which is described in Chapter 7. However, the increase in the total and maximum precipitation amount caused by an increase of aerosol loading is reported by many previous studies (Khain et al. 2005; Rosenfeld et al. 2008; Xiao et al. 2015; Clanvner et al. 2018).

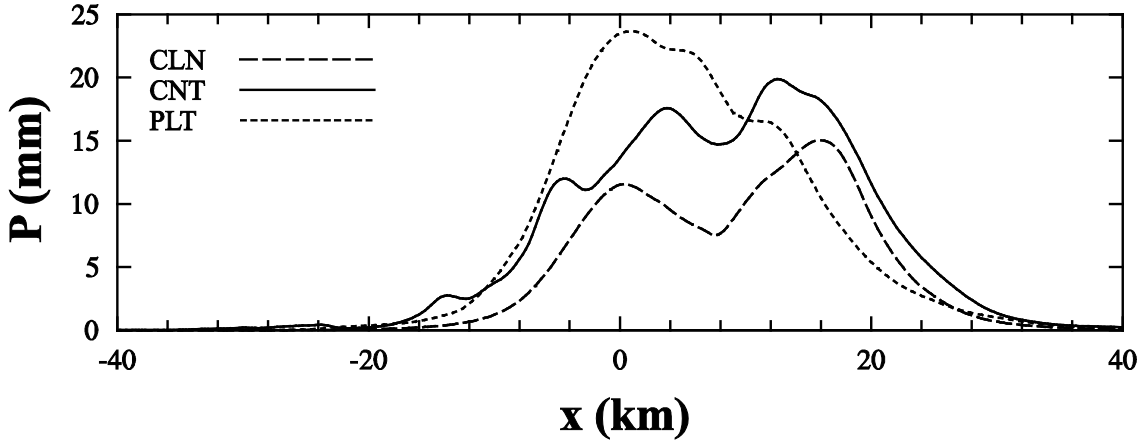

Figure 8.6. Accumulated precipitation amount from t = 4 to 6 h as a function of x in CLN, CNT, and PLT.

	P_{tot} (mm)			P_{max} (mm)			x_{max} (km)		
a_1 (km)	5	10	20	5	10	20	5	10	20
CLN	1755	1298	1711	15.8	15.0	33.7	2.0	16.0	3.8
CNT	1000	2022	2551	10.6	19.9	29.3	16.0	12.5	–2.0
PLT	1260	2071	1394	11.8	23.7	25.2	14.0	1.0	4.8

Table 8.1. Total surface precipitation amount from x = –50 to 50 km and from t = 4 to 6 h P_{tot}, the local maximum surface precipitation amount P_{max}, and the location x_{max} at which P_{max} occurs.

Figure 8.7 shows the vertical profiles of temperature change due to microphysical processes over the upslope (x = –50–0 km) and the downslope (x = 0–50 km) of the mountain. On both sides, nucleation is strongest in PLT. Over the upslope, nucleation rate decreases with height, while nucleation is strongest at agl ~ 5 km over the downslope (Figs. 8.6a and 8.6f). A greater number of condensates over the upslope in PLT results in stronger condensational latent heating over the upslope and also a stronger evaporative cooling over the downslope compared to the other cases (Figs. 8.7b and 8.7g). Over the upslope, many liquid drops are frozen into ice crystals (Fig. 8.7d), and the ice crystals grow through the WBF process in PLT (Figs. 8.7b and 8.7c). In CLN, similar processes, such as the strong freezing and the WBF process, are stronger than in the other cases over the downslope (Figs. 8.7g–i). The riming process between grown ice-phased particles and liquid drops is mainly responsible for the enhanced surface precipitation through mixed-phase processes (Figs. 8.7e and 8.7j).

Along with the aforementioned processes, the upstream extension of the upper-level cloud provides the environment to enhance the mixing ratio of high-density ice particles via riming when lower-level convective clouds develop through the freezing level. This environment is caused by the advection of ice particles by negative horizontal velocity associated with mountain waves over the mountain peak (see Figs. 8.3 and 8.5). Figure 8.8 presents the size distributions of accumulated advection rate of hydrometeors over the mountain peak (x = 0) as a function of z. The advection rate is obtained by the equation,

$$A(r_H, z) = \rho_H(r_H) u(x=0, z) q_H(r_H, x=0, z) / d \ln r_H, \qquad (4)$$

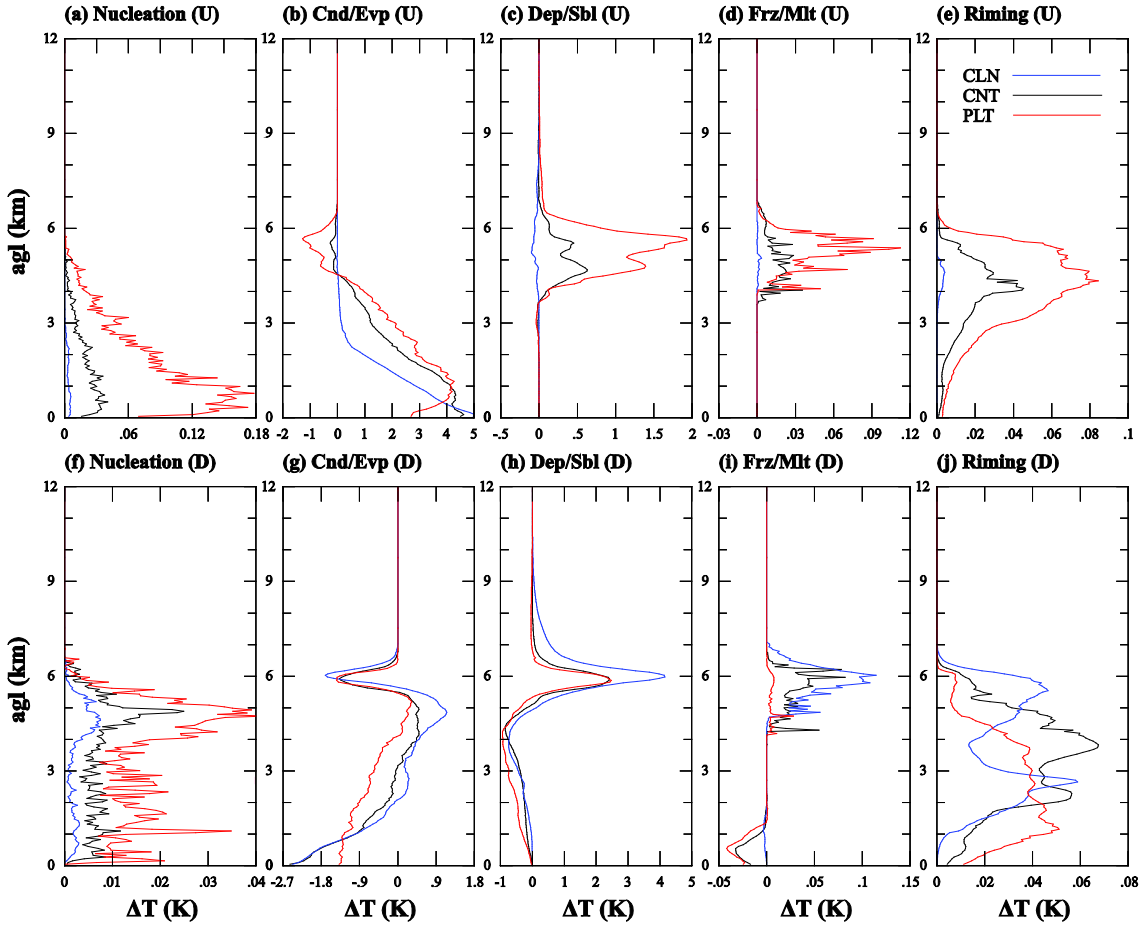

Figure 8.7. Vertical profiles of temperature change due to nucleation, condensation/evaporation, deposition/sublimation, freezing/melting, and riming over the upslope (x = –50–0 km) and downslope (x = 0–50 km) of the mountain in CLN, CNT, and PLT.

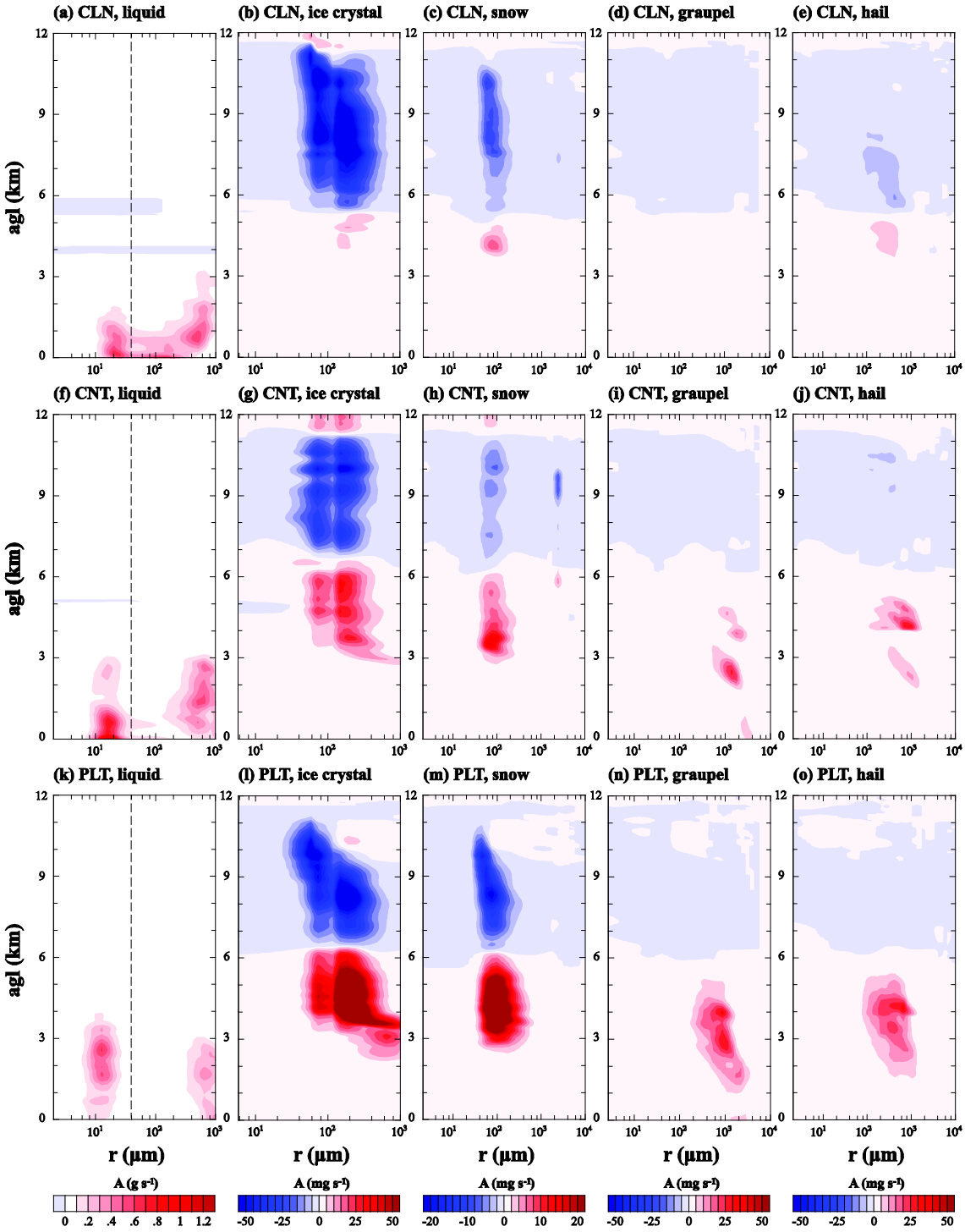
(a) CLN, liquid
(b) CLN, ice crystal
(c) CLN, snow
(d) CLN, graupel
(e) CLN, hail
(f) CNT, liquid
(g) CNT, ice crystal
(h) CNT, snow
(i) CNT, graupel
(j) CNT, hail
(k) PLT, liquid
(l) PLT, ice crystal
(m) PLT, snow
(n) PLT, graupel
(o) PLT, hail
agl (km)
r (μm)
A (g s⁻¹)
A (mg s⁻¹)

Figure 8.8. Size distributions of accumulated advection rate of liquid drop, columnar ice crystal, snow, graupel, and hail through $x = 0$ as a function of z in CLN, CNT, and PLT. Dashed lines in (a, f, k) indicate $r = 40$ μm which is the boundary size between cloud droplet and raindrop.

where ρ_H (r_H) is the density of each hydrometeor as a function of the size of particle, u is the horizontal velocity, and q_H is the mixing ratio of each hydrometeor.

When aerosol number concentration is higher, the size of cloud droplets is smaller and the lower-level convective clouds can achieve higher altitude (Figs. 8.8a, 8.8f, and 8.8k). The positive advection rate of columnar ice crystal below agl ~ 6 km is very high in PLT, while there is almost no positive advection rate in CLN (Figs. 8.8b, 8.8g, and 8.8i) due to the the stronger/weaker freezing into ice crystal and stronger/weaker WBF process over the upslope in PLT/CLN cases (Figs. 8.7b–d). Similarly, the negative advection rate in the higher level is higher in CLN than in the other cases. Over the mountain peak, lower-level convective orographic clouds are developed and are overlapped with upper-level cloud in PLT (Fig. 8.5c). In the upper-level cloud, many ice crystals grow into snow particles, some portion of which are advected over the upslope side (Fig. 8.8m). These snow particles grow further in the overlapped layer over the upslope through riming (Fig. 8.7e), the type is converted into graupel and hail, and again advected over the mountain peak (Figs. 8.8n and 8.8o). The graupel and hail particles melt and enhance surface precipitation (Fig. 8.7i). In CLN, however, the overlapping of lower and higher clouds occurs only in the narrow area over the mountain peak (Fig. 8.5a). Although many ice particles which are generated and grown over the downslope are advected over the mountain peak, their further growth is limited. Moreover, ice particles cannot reach the surface over the downslope, even though their growth via riming is active (Fig. 8.7j). For this reason, the total and maximum precipitation amount in CLN is smaller than in the other cases.

8.3.3 Sensitivity of aerosol effects on orographic precipitation to upslope steepness

In Chapter 7, the sensitivity of aerosol effects on orographic precipitation to upslope steepness is examined. As discussed in Chapter 7, Fig. 8.9 shows that the decrease in precipitation amount and the downstream shift of the location of the maximum precipitation are clearly seen in the cases with a_1 = 5 km (Fig. 8.9a–c) and are ambiguous in the cases with a_1 = 20 km (Fig. 8.9d–f) early on (t = 0–4 h). As the simulation continues, however, the sensitivity changes in different ways depending on the cases. In the cases with a_1 = 5 km, the upstream extension of the precipitation area starts earlier in PLTn and CLNn than in CNTn. This results in the lighter total and maximum precipitation in CNTn compared to the other cases (Table 8.1). In the cases with a_1 = 20 km, the broad precipitation region over the mountain is clearly seen in all cases. In CLNw and PLTw, however, the upstream extension of the precipitation area does not occur. This results in heavier total precipitation in CNTw compared to the other cases (Table 8.1).

Figure 8.10 shows the averaged mixing ratio of the liquid drop, low-density ice particle, and high-density particle, and wind vectors in CLNn, CNTn, and PLTn from t = 4 to 6 h. In CNTn, narrow lower-level orographic clouds are generated over the upslope due to the narrow upslope. Although the high-density ice particles affect precipitation over the downslope, the interaction between lower- and upper-level clouds is weaker compared to the other cases. Surface precipitation is concentrated over the downslope and the upslope precipitation amount is very small in CNTn (Fig. 8.11a). In CLNn and PLTn, the upper-level cloud is upstream extended and this clearly affects the upslope surface precipitation amount (Fig. 8.11a). Compared to CNTn, the upstream extension of lower-

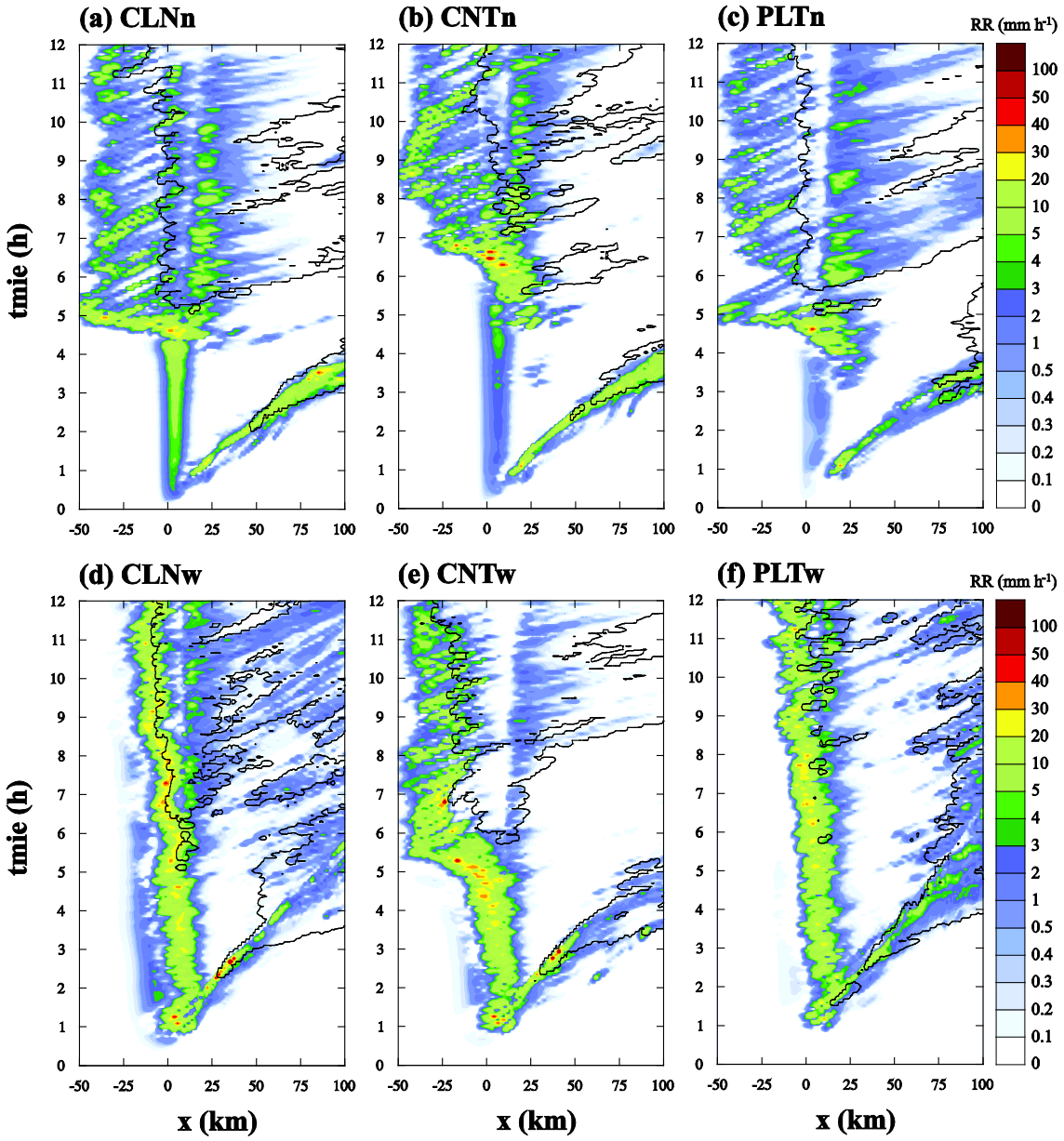

Figure 8.9. Hovmöller diagrams of the surface rain rate (shaded) and ice-phased precipitation rate (contoured only for 0.01 mm h^{-1}) in CLNn, CNTn, PLTn, CLNw, CNTw, and PLTw.

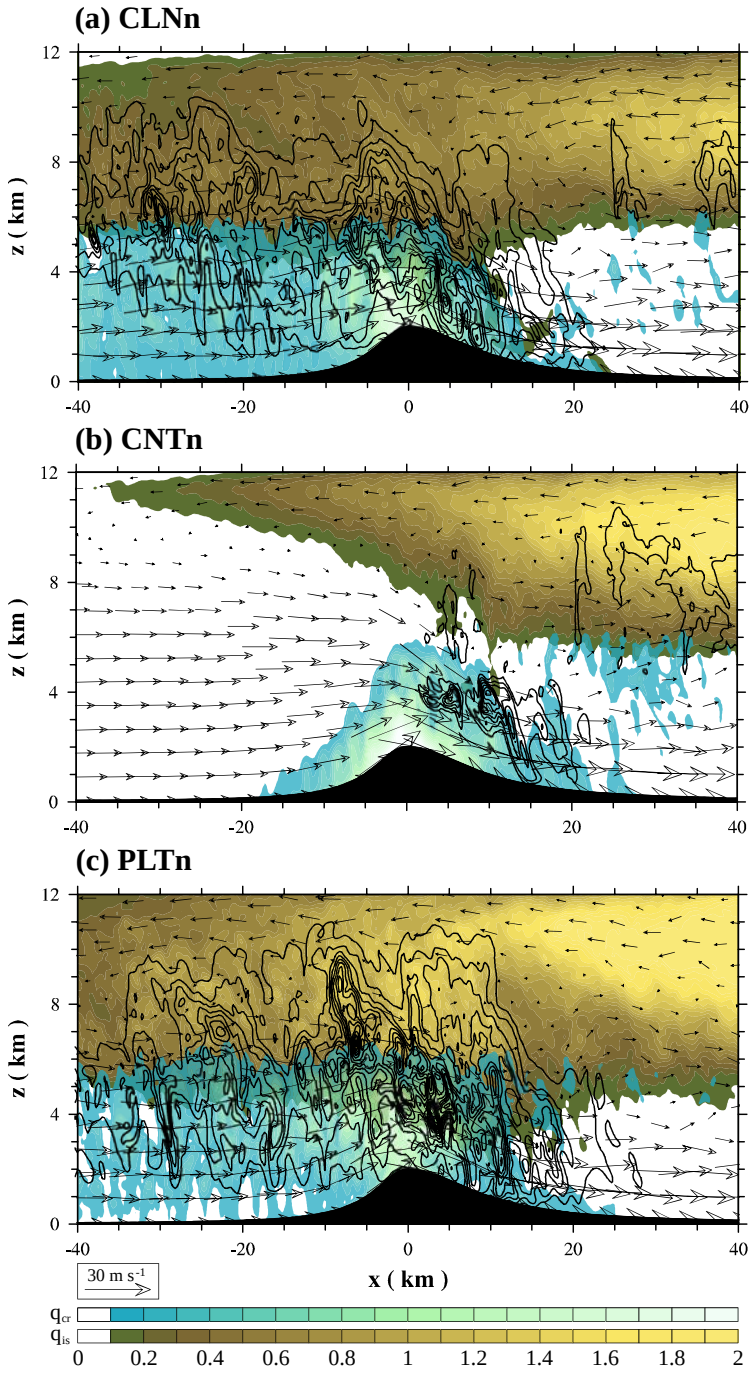

Figure 8.10. The same as Fig. 8.5 except for (a) CLNn, (b) CNTn, and (c) PLTn.

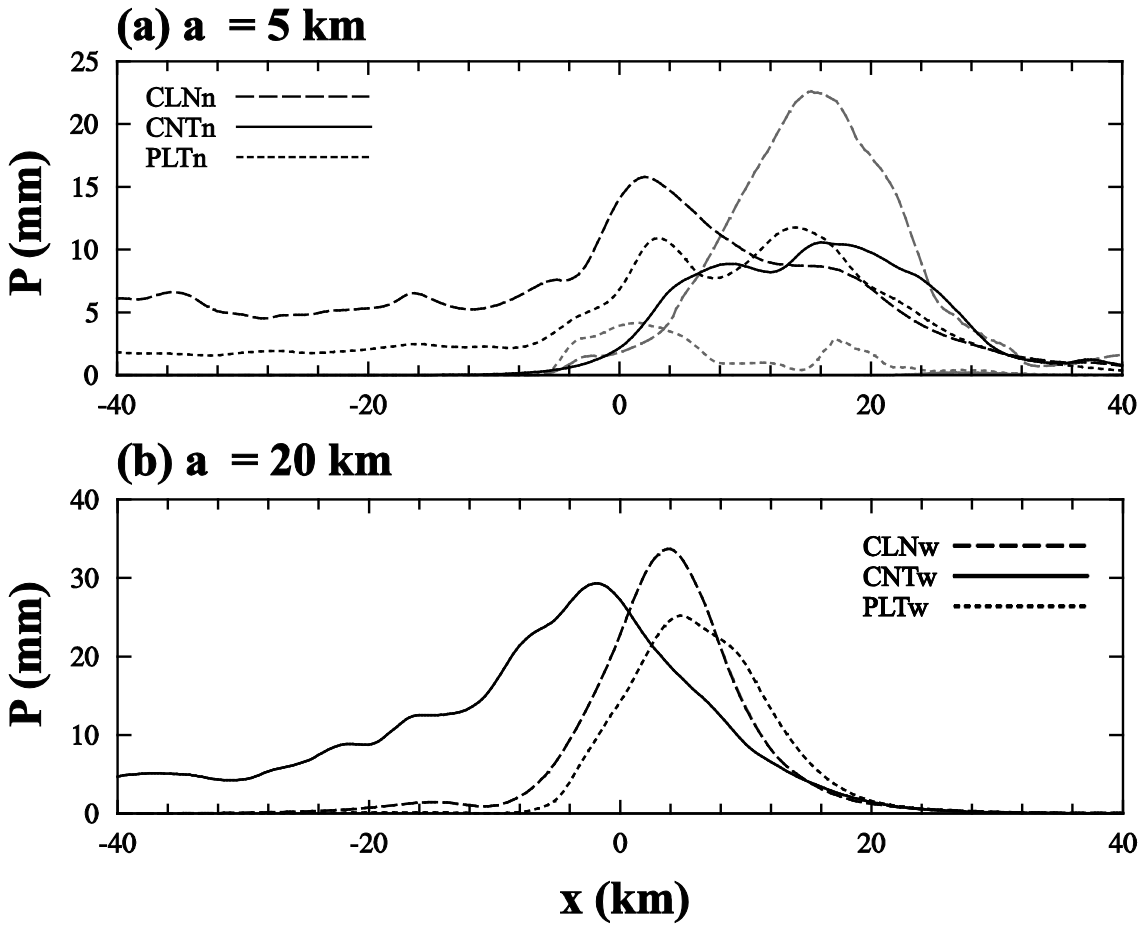

Figure 8.11. Accumulated liquid (black) and ice (gray) precipitation amount and from t = 4 to 6 h as a function of x in the cases with (a) a_1 = 5 km and (b) 20 km.

level clouds is more apparent in PLTn. Ice-phased precipitation is strongest in CLNn compared to the other cases (Fig. 8.11a).

Over the upslope and downslope, nucleation is strongest in PLTn. As discussed in Chapter 7, in these cases, nucleated cloud droplets do not grow sufficiently until they reach the mountain peak during the short advection time scale over the upslope, even though the steep upslope generates strong convection over the upslope. For this reason, the mass content of cloud droplets is larger and the mass of rain drops is smaller compared to the cases with the symmetric mountain (compare Figs. 8.8a, 8.8f, and 8.8k and Figs. 8.13a, 8.13f, and 8.13k). In the case with a higher aerosol number concentration, the strong condensational latent heating generates deeper convective clouds over the upslope and many small liquid drops freeze above the freezing level (Figs. 8.12b and 8.12d). Compared to the other cases, WBF process is strongest in PLTn (Figs. 8.12b and 8.12c). Similar to PLT, frozen and grown ice particles expense further growth via strong riming over both the upslope and the downslope and result in heavy surface precipitation via melting or direct sedimentation of ice-phased particles (Figs. 8.11a, 8.12e, 8.12j, and 8.13i–o). In CLNn, lower-level clouds with liquid drops can develop through the freezing level. Because of the faster growth of liquid drops (Fig. 8.13a), frozen ice particles are bigger here than in the other cases (Fig. 13b). As a result, the sizes of high-density ice particles are very large resulting in the heavy liquid- and ice-phased precipitation (Figs. 8.11a, 8.13d, and 8.13e). In CNTn, however, the weaker condensational latent heating than PLTn and the slower growth of liquid drops than CLNn result in weak lower-level convection (Fig. 8.13a). For this reason, the interaction between lower- and upper-level clouds is inhibited over the upslope (Fig. 8.12b–e). However, the advected liquid drops

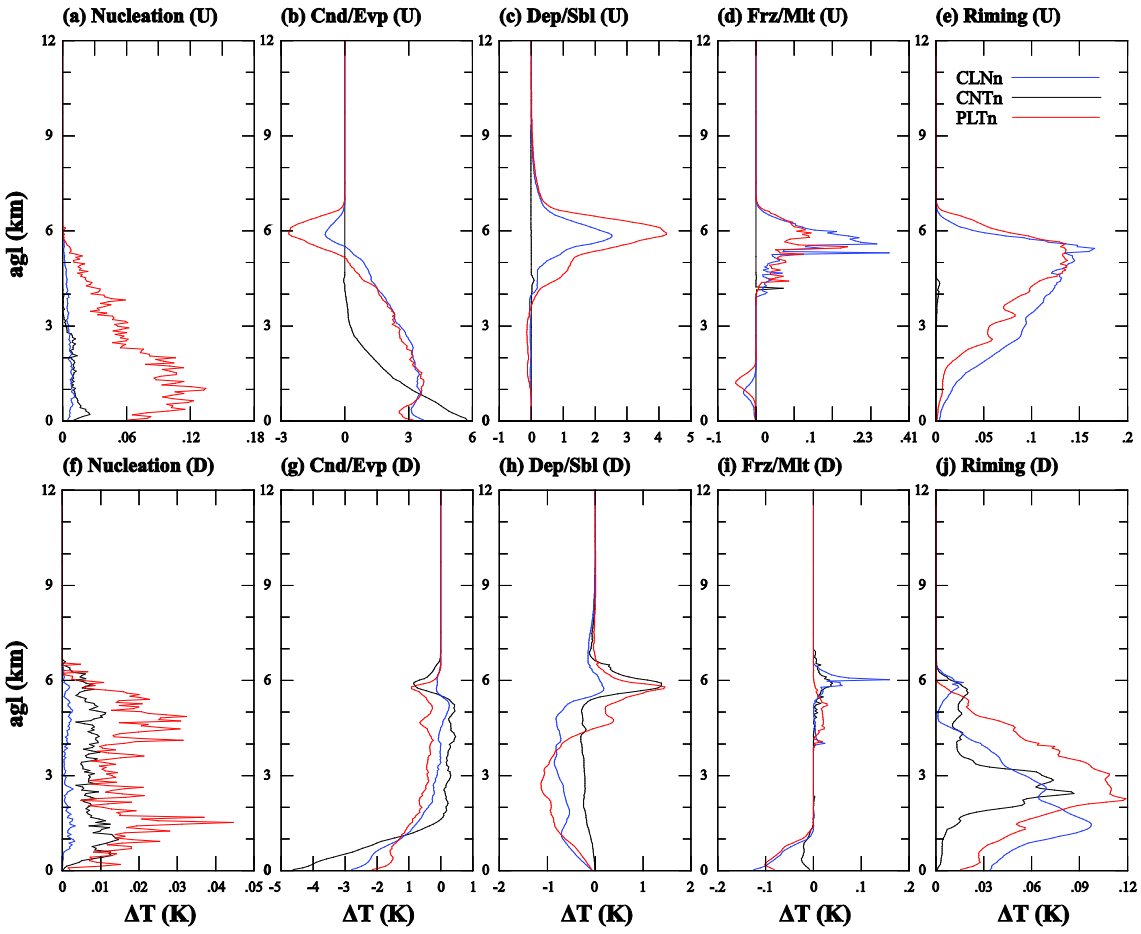

FIG. 8.12. The same as Fig. 8.7 except for the cases with a_1 = 5 km.

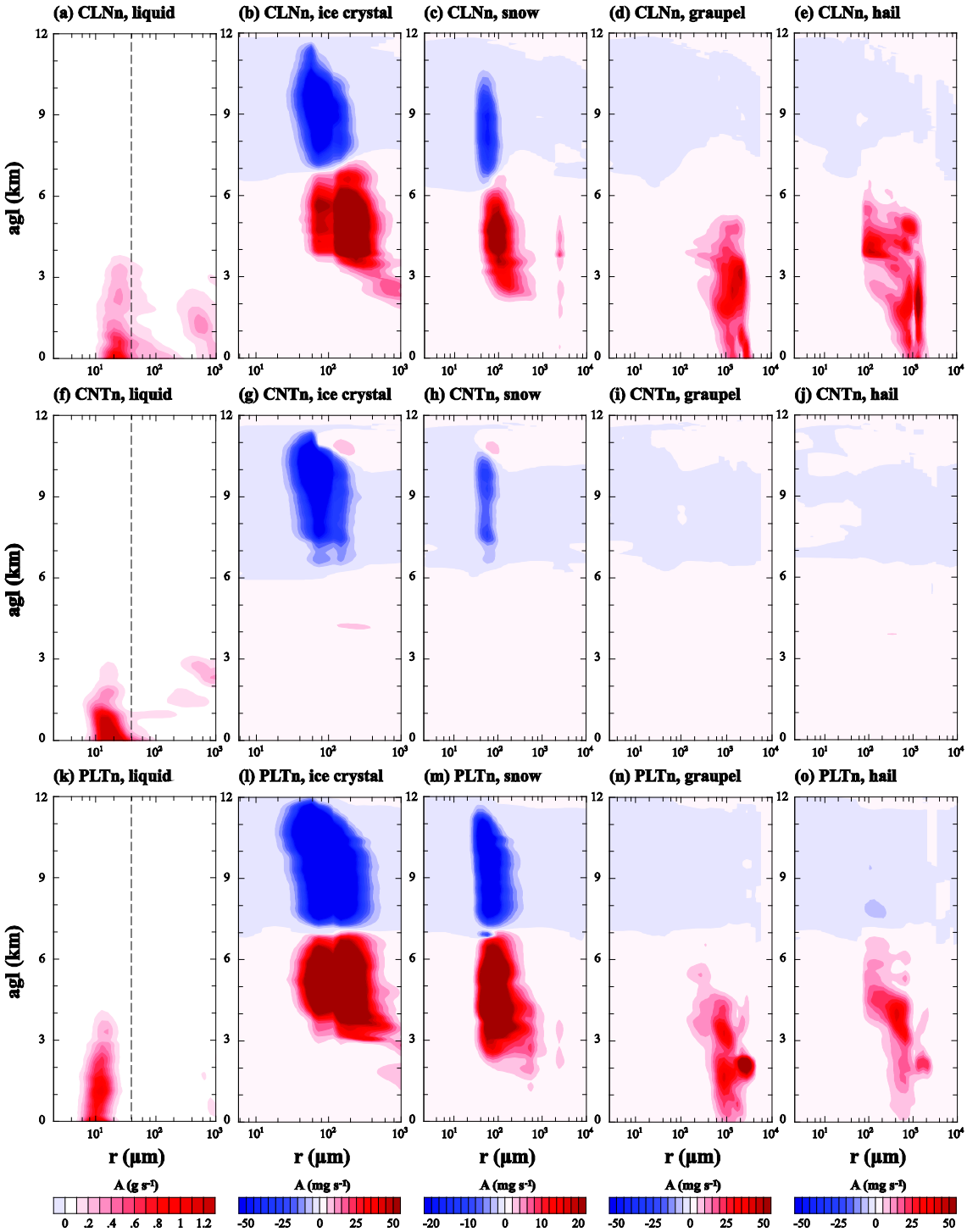

FIG. 8.13. The same as Fig. 8.8 except for the cases with a_1 = 5 km.

over the mountain peak grow further and freeze over the downslope, and the ice crystals grow via the WBF process and riming (Figs. 8.12g–j). As a result, downslope-concentrated precipitation occurs in CNTn (Fig. 8.11a).

Figure 8.14 shows the averaged mixing ratio of the liquid drop, low-density ice particle, and high-density particle, and wind vectors in CLNw, CNTw, and PLTw from *t* = 4 to 6 h. Over the wide upslope, wider and weaker convective orographic clouds are generated compared to the cases with symmetric mountain and a narrow upslope. In CLNw and PLTw, lower- and upper-level clouds interact only near the mountain peak (Figs. 8.14a and 8.14c). In CNTw, however, the interaction over the upslope exists due to the upstream extension of the lower-level clouds (Fig. 8.14b). For this reason, the total precipitation amount is largest in CNTw (Table 8.1). The surface precipitation is concentrated over the downslope in CLNw and PLTw, and is smaller in PLTw than in CLNw (Table 8.1 and Fig. 8.11b).

As discussed in Chapter 7, cloud droplets sufficiently grow into raindrops over the wide upslope. For this reason, the mass of raindrops is larger than the mass of cloud droplets over the mountain peak (Fig. 8.16a, 8.16f, and 8.16k). Similar to the other cases, the nucleation rate is largest in PLTw over the upslope and the downslope (Figs. 8.15a and 8.15f). In CNTw, many ice crystals are generated by freezing and growth into snow particles via the WBF process at agl ~ 6 km over the downslope (Figs. 8.15g–i). These low-density ice particles are advected over to the upslope side (Figs. 8.15g and 8.15h). Besides, the freezing rate is strongest in CNTw (Fig. 8.15d). Low-density ice particles generated over the upslope and advected from the downslope grow further into high-density ice particles via deposition and riming, and again get advected over to the

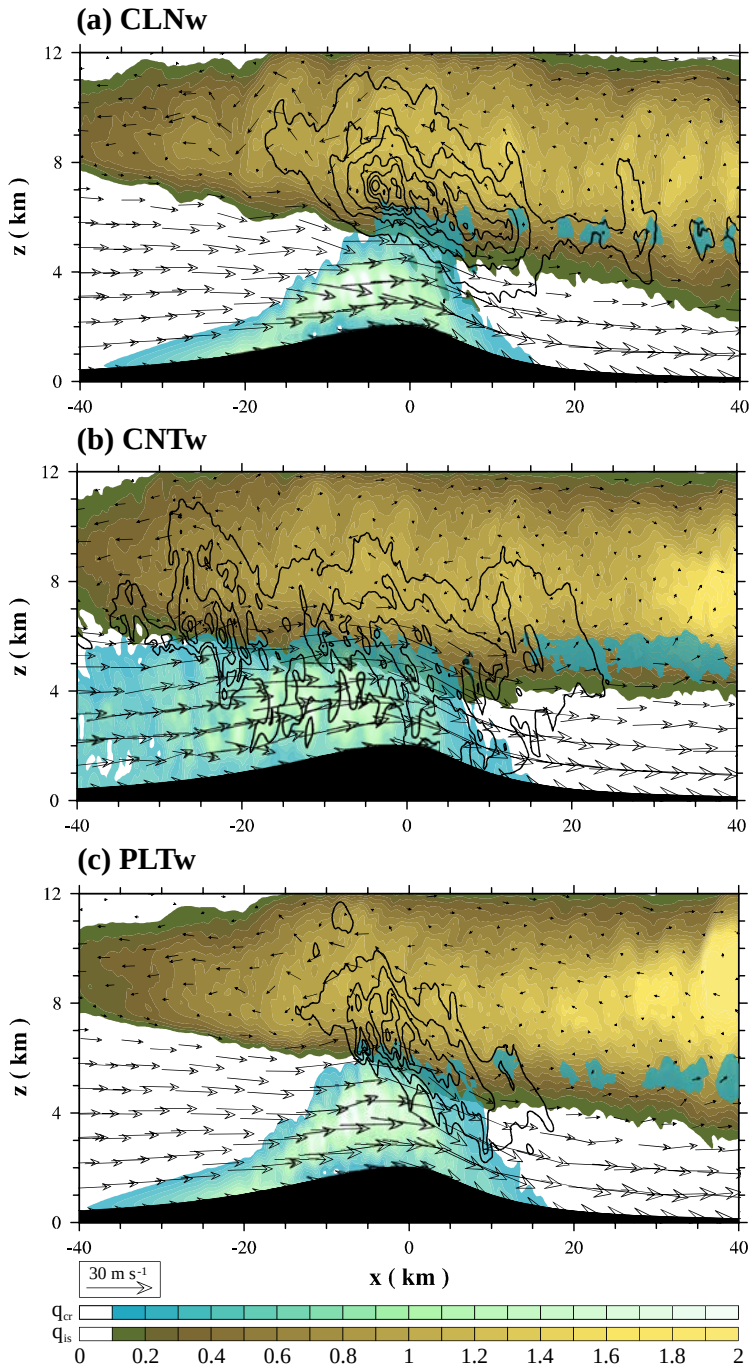

FIG. 8.14. The same as Fig. 8.5 except for (a) CLNw, (b) CNTw, and (c) PLTw.

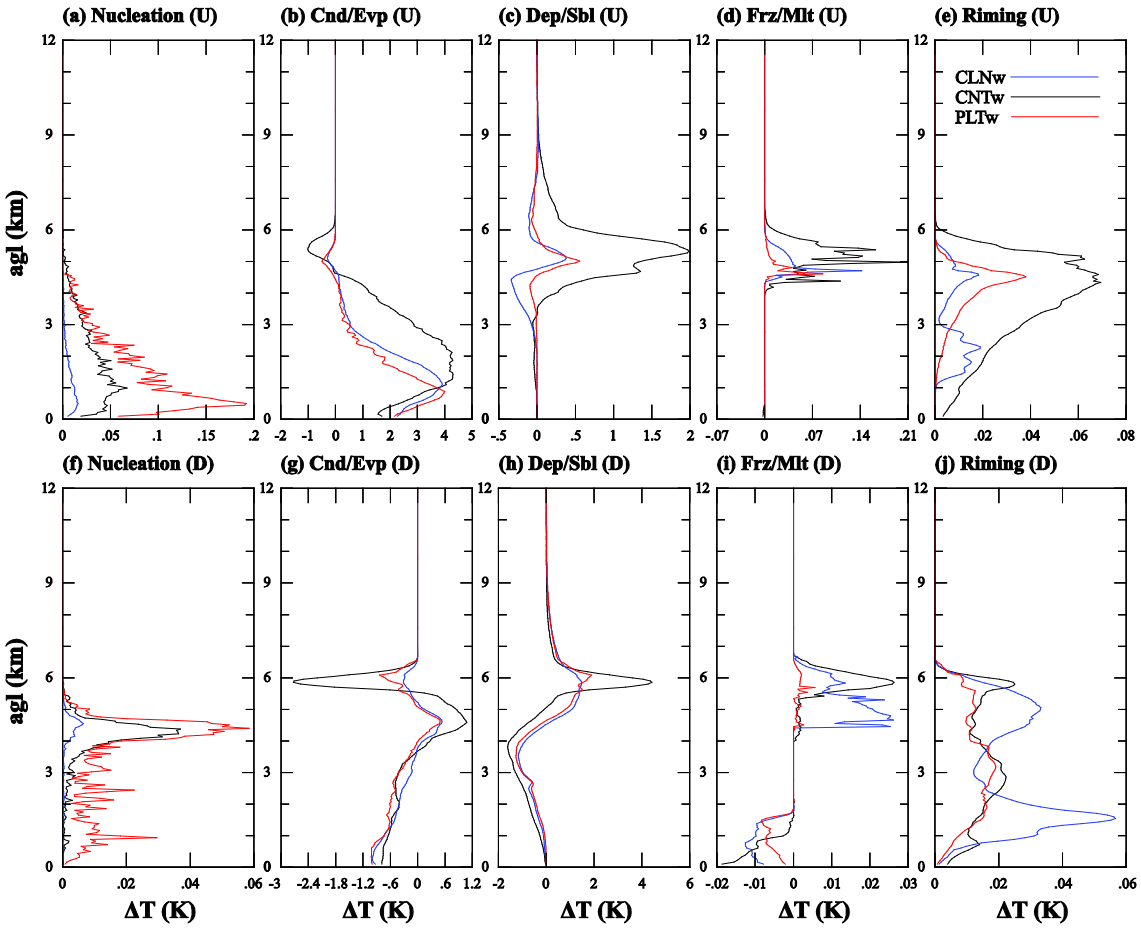

FIG. 8.15. The same as Fig. 8.7 except for the cases with a_1 = 20 km.

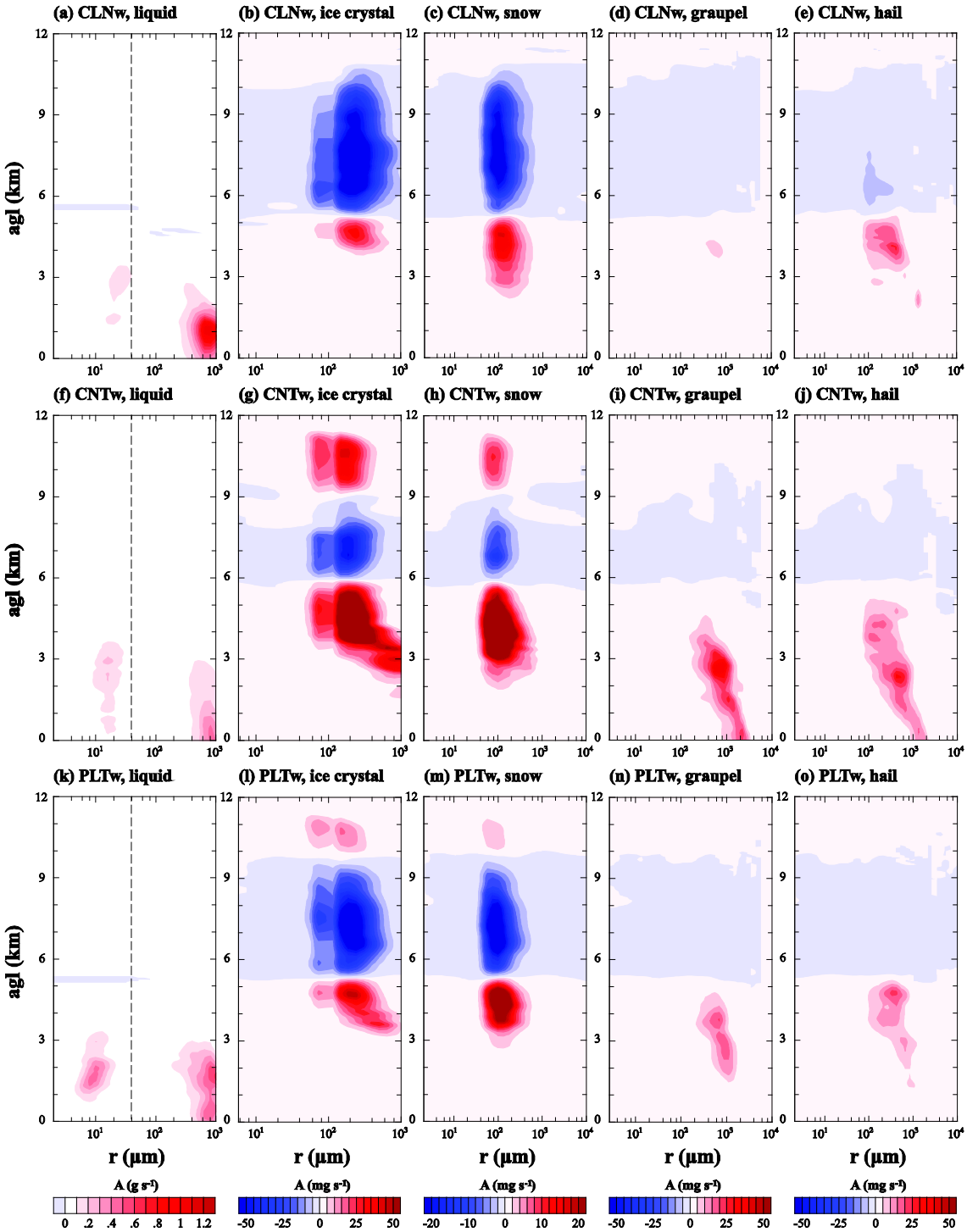

FIG. 8.16. The same as Fig. 8.8 except for the cases with a_1 = 20 km.

Downslope side (Figs. 8.15b–e and 8.16g–j).The melted high-density ice particles enhance surface precipitation via melting. In CLNw and PLTw, however, such mixed-phase processes are inhibited. In CLNw, the fast growth of liquid drops results in a smaller amount of cloud droplets, which are the first source of ice crystals above the freezing level (Fig. 8.16a). In PLTw, weak convection in the cases with gentle upslope is not sufficient for small-sized liquid particles to finally generate large-sized ice particles (Fig. 8.16k).

9 Modeling of orographic precipitation over Taebaek Mountains in South Korea

9.1 Introduction

In Chapter 7 and Chapter 8, the idealized simulations of orographic precipitations with various aerosol number concentrations and mountain geometries are performed. Both chapters suggest how orographic precipitation from shallow-warm clouds and deep, mixed-phase clouds is controlled by the aerosol loading and the upslope steepness. This chapter examines aerosol effects on orographic precipitation over a real mountainous area, the Taebaek Mountains located on the eastern side of the Korean peninsula.

Because of the north-southerly enlongated geometry and the steep upslope angle of the Taebaek Mountains, the moist air advected from East Sea frequently leads to precipitation events over the Taebaek Mountains. Regarding the Youngdong region (eastern side of the Taebaek Mountains), however, most of the studies focus on the wintertime heavy snowfall event (e.g., Seo and Jhun 1991; Seo and Lee 1996; Lee 1999; Lee and Kim 2008; Lee et al. 2011; Jung et al. 2012; Lee and Xue 2013). In recent decades, aerosol effects on orographic precipitation over the Taeback Mountains have been studied, mainly concerned with cloud seeding and anthropogenic pollution (Kim et al. 2005; Bae et al. 2015; Yang et al. 2015). But the study of aerosol effects on orographic precipitation over the Taebaek Moutains in summer time is not sufficiently done as of yet.

This study examines aerosol effects on orographic precipitation by numerically simulating a real precipitation event over the Taebaek Mountains in summer using the

WRF-bin model. Section 9.2 provides experimental design. In section 9.3.1, the detailed case description with model verification is provided. Aerosol effects on orographic precipitation over the Taebaek Mountains are examined in Section 9.3.2.

9.2 Experimental design

A precipitation event over the Taebaek Mountains from 26 to 27 June 2015 is selected. To simulate the orographic precipitation, the Weather Research and Forecasting (WRF) model version 3.7.1 coupled with the Hebrew University Cloud Model (HUCM) is used (Skamarock et al. 2008; Lee and Baik 2016). The detailed description of the model is given in Chapter 7, Chapter 8, and Khain et al. (2000, 2004, 2011). By changing the aerosol number concentration at 1% supersaturation N_0 [= 30 cm^{-3} for CLN (clean), = 300 cm^{-3} for CNT (control), and = 3000 cm^{-3} for PLT (polluted)], three cases are considered. Table 9.1 and Fig. 9.1a provide detailed description of the simulation. Figure 9.1b shows the terrain height in the innermost domain, locations of the observatories used in this study, and the two lines named C1 and C2 for the cross section analyses. The model integrates for 42 h from 06 UTC 25 June to 00 UTC 27 June. Only the last 21 h is used for the analysis.

9.3 Results and discussion

9.3.1 Precipitation case

Figure 9.2 shows observed and simulated weather charts at 850 hPa height. From 21 KST 25, a low pressure system develops in southwest of Korean peninsula and

	domain 1	domain 2	domain 3
horizontal grid size	25 km	5 km	1.667 km
horizontal grid numbers	120 × 120	211 × 211	211 × 211
vertical grid levels	41		
PBL scheme	Yonsei University Scheme (Hong et al. 2006)		
cumulus scheme	Kain-Fritsch (Kain 2004)	none	
radiation scheme	longwave: RRTM (Mlawer et al. 1997) shortwave: Dudhia (Dudhia 1989)		
land surface scheme	5-layer thermal diffusion (Dudhia 1996)		
surface-layer scheme	MM5 similarity (Paulson 1970; Dyer and Hicks 1970; Webb 1970; Beljaars 1994; Zhang and Anthes 1982)		
Initial/boundary data	RDAPS (UM 12kmL70) data		

Table 9.1. Model configuration of each domain and parameterization list in the WRF model simulations.

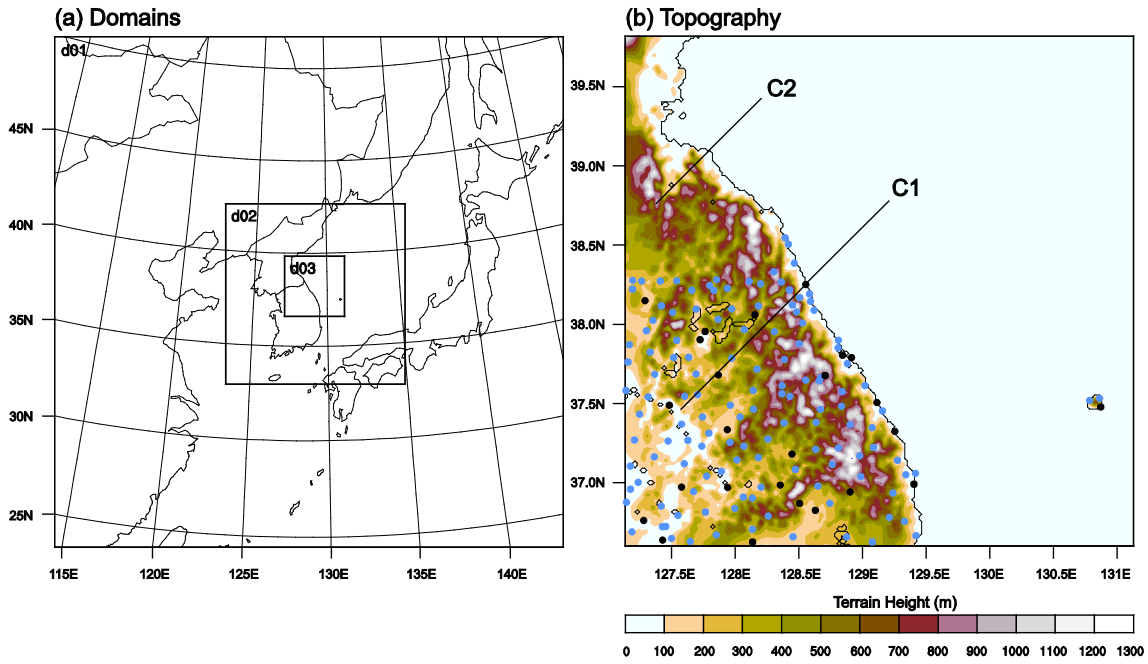

Figure 9.1. (a) Three nested simulation domains and (b) terrain height in the innermost domain with observation location. Black and light blue dots indicate automated synoptic observing system (ASOS) and Automatic Weather System (AWS) observatories, respectively. Two lines named C1 and C2 are for the cross sections which are given in Figs. 9.7 and 9.8, respectively.

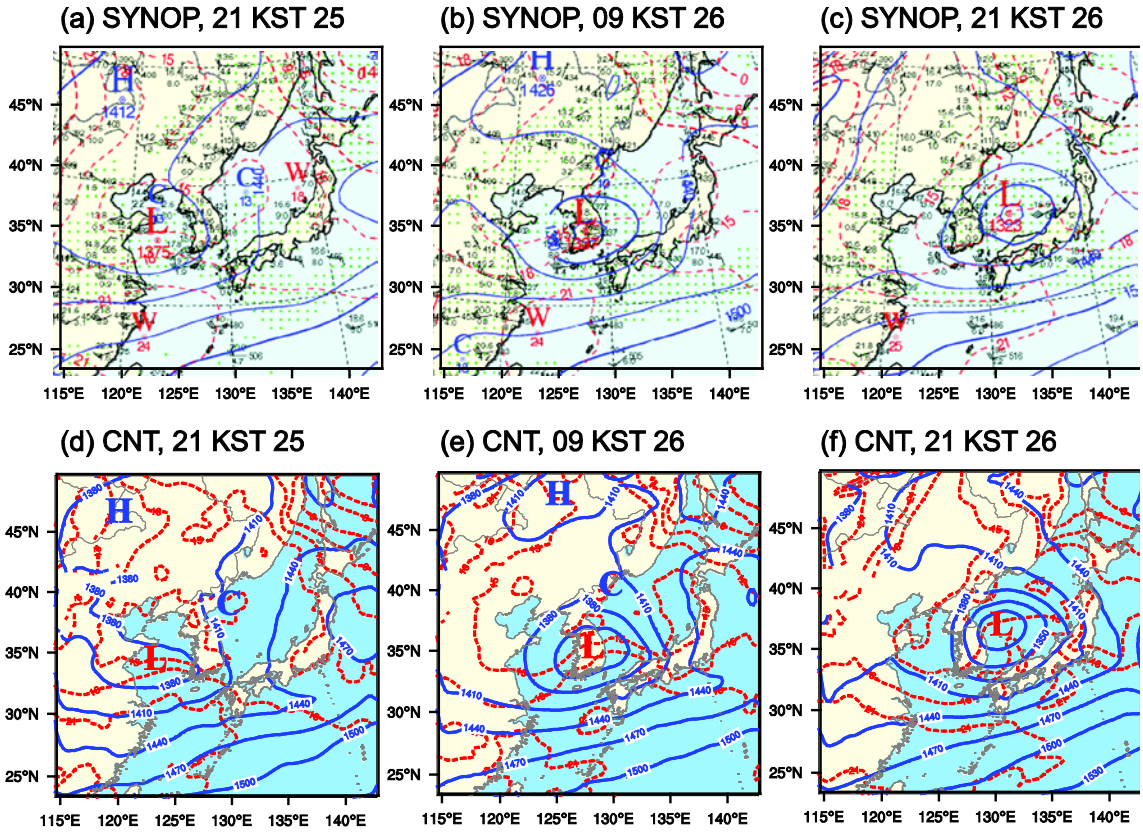

Figure 9.2. (a–c) Observed and (d–f) simulated (CNT case) geopotential height (gpm) and temperature (℃) at 850 hPa height at 21 KST 25, 09 KST 26 and 21 KST 26.

passes over the southern Korean peninsula. As the low pressure system moves to the East Sea, a strong and consistent easterly is generated over Youngdong region. When the low pressure system is located over the East Sea, the main flow changes into the northeasterly. Overall, the synoptic patterns are well simulated by the WRF-bin model (Figs. 9.2d–f). Observed and simulated 21-h accumulated surface precipitation amount are given in Fig. 9.3. Note that the observed precipitation amount on the northern region of Korean peninsula is not available. The simulations overestimate the surface precipitation amount, while simulating well the overall patterns over the Taebaek Mountains.

9.3.2 Aerosol effects on orographic precipitation

To compare precipitation patterns between CLN and PLT cases, the differences in 21-h accumulated surface precipitation amount between CLN and CNT and PLT and CNT are given in Fig. 9.4. Although the signs of the differences are different depending on location, the signs of differences in the Youngdong region are mainly negative and positive in CLN and PLT, respectively. Figure 9.5 shows the differences of the 21-h averaged vertically integrated cloud droplet mixing ratio and the raindrop mixing ratio between CLN and CNT, and between PLT and CNT. As the aerosol number concentration increases, the cloud droplet mixing ratio decreases and the raindrop mixing ratio increases for the most part. Note that, however, there are negative and positive differences near the line C2 in Figs. 9.5c and 9.5d, respectively. Figure 9.6 shows that ice particles might have a role in making different precipitation characteristics between the region near the lines C1 and C2.

Figure 9.7 shows the vertical cross sections through the line C1 of the cloud

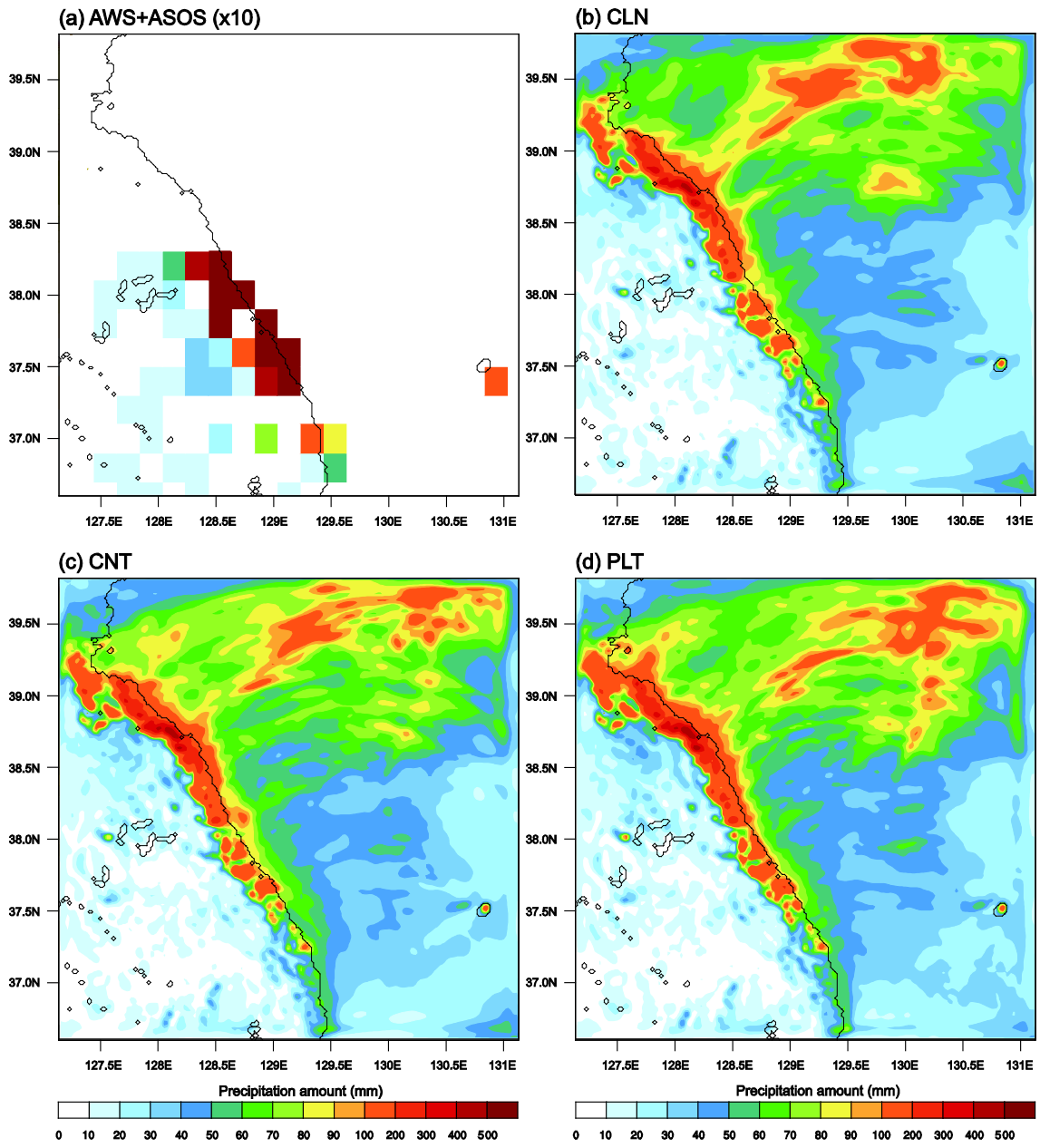

Figure 9.3. (a) Observated by AWS and ASOS and (b–d) simulated 21-h accumulated surface precipitation amount.

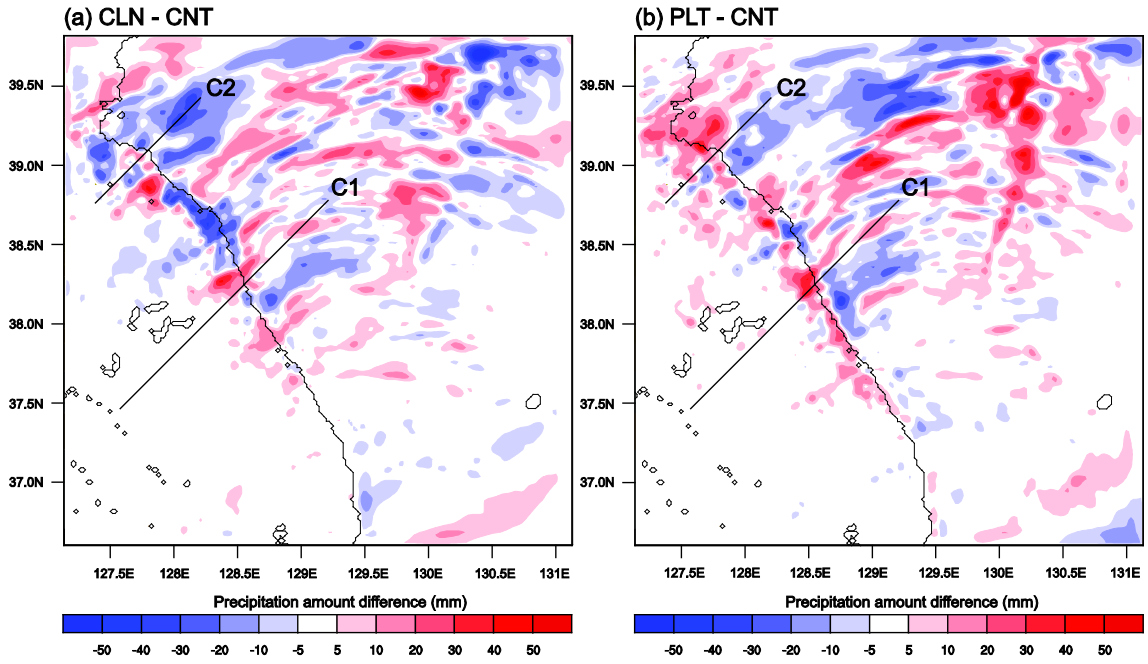

Figure 9.4. Differences in 21-h accumulated surface precipitation amount between (a) CLN and CNT and (b) PLT and CNT.

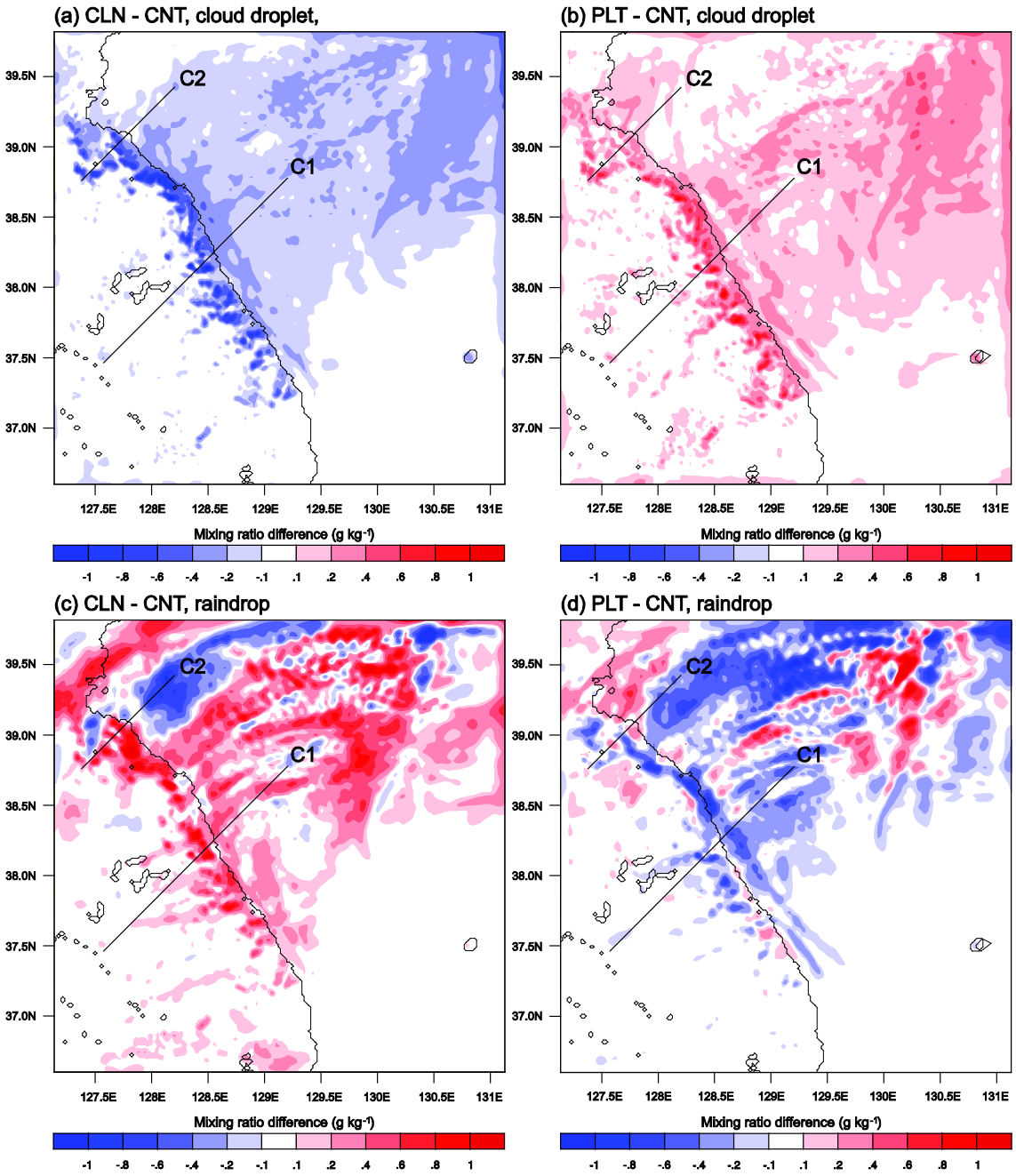

Figure 9.5. Differences in 21-h averaged vertically integrated (a, b) cloud droplet mixing ratio and (c, d) raindrop mixing ratio between (a, c) CLN and CNT and (b, d) PLT and CNT.

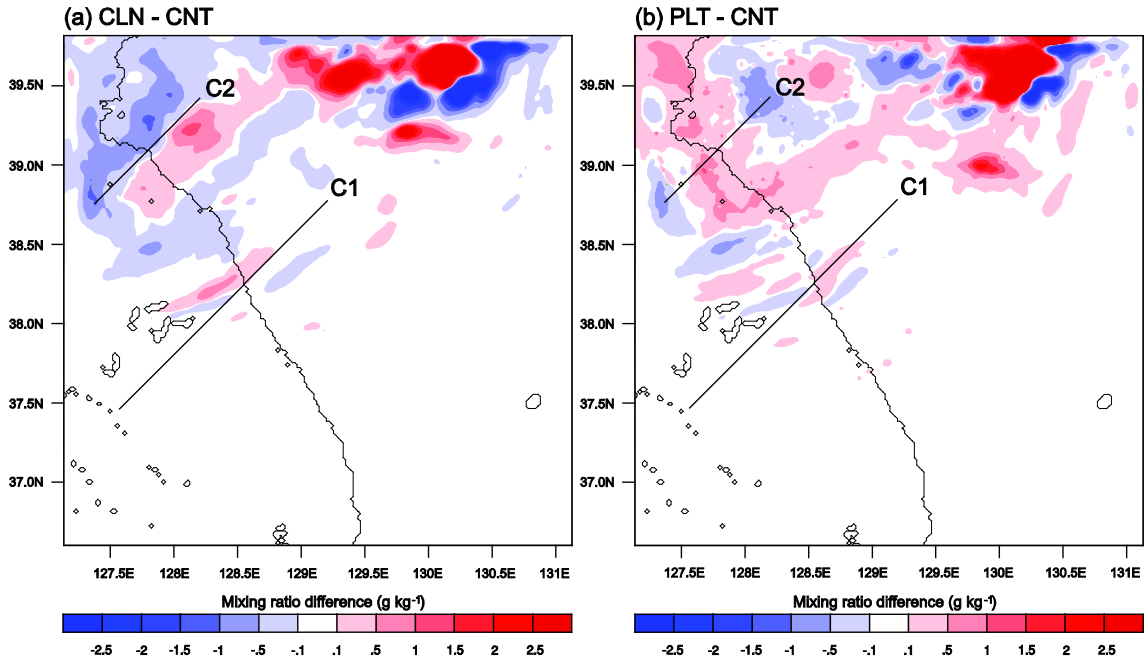

Figure 9.6. Differences in 21-h averaged vertically integrated ice crystal and snow mixing ratio between (a) CLN and CNT and (b) PLT and CNT.

droplet and raindrop mixing ratios. Line C1 passes through Sokcho and the near-Hongcheon automated synoptic observing system (ASOS) observatories (Fig. 9.1b) and the $x = 0$ is located at the coast. In this region, the orographic clouds are warm clouds. As we discussed in Chapter 7, an increase in aerosol number concentration results in an increase in the cloud droplet mixing ratio and the decrease in raindrop mixing ratio. However, in this case, both the increase and decrease of aerosol number concentration result in an increase of surface precipitation amount over the mountain upslope (Fig. 9.4). In CLN, the faster growth of cloud droplets over the steep upslope results in a higher raindrop mixing ratio than in CNT (Fig. 9.7a). In PLT, the difference in the raindrop mixing ratio between PLT and CNT is small, while the cloud droplet mixing ratio is higher in PLT than CNT, which also results in an increase of the surface precipitation amount over the mountain upslope (compare Figs. 9.7b and 9.7c).

Figure 9.8 shows vertical cross sections through line C2 of the liquid drop mixing ratio and the low- and high-density ice particle mixing ratios. Line C2 passes through the local maximum terrain height near Mt. Kumgang (Fig. 9.1b) and where $x = 0$ is located at the coast. Note that the orographic clouds in this region are mixed-phase clouds. Both the low- and high-density ice particle mixing ratios increase as the aerosol number concentration increases, while the liquid drop mixing ratio changes little. As discussed in Chapter 8, an increase in ice particle mixing ratio in higher-level cloud results in enhanced surface precipitation via melting of the ice particles.

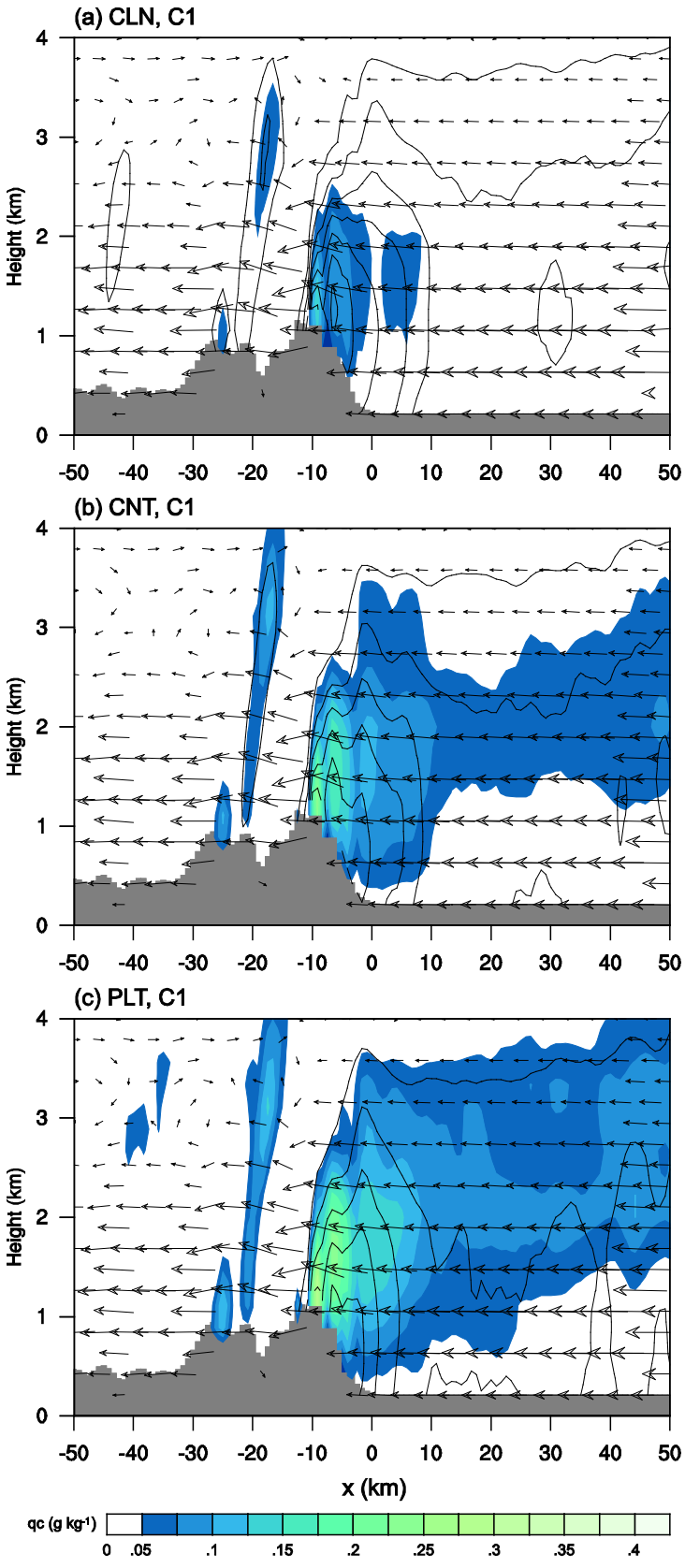
(a) CLN, C1
(b) CNT, C1
(c) PLT, C1
Height (km)
x (km)
qc (g kg-1)
0
.05
.1
.15
.2
.25
.3
.35
.4

Figure 9.7. Vertical cross sections through the line C1 of 21-h averaged cloud droplet mixing ratio (shaded) and raindrop mixing ratio (contoured) in (a) CLN, (b) CNT, and (c) PLT. The contour interval is 0.05 g kg^{-1}.

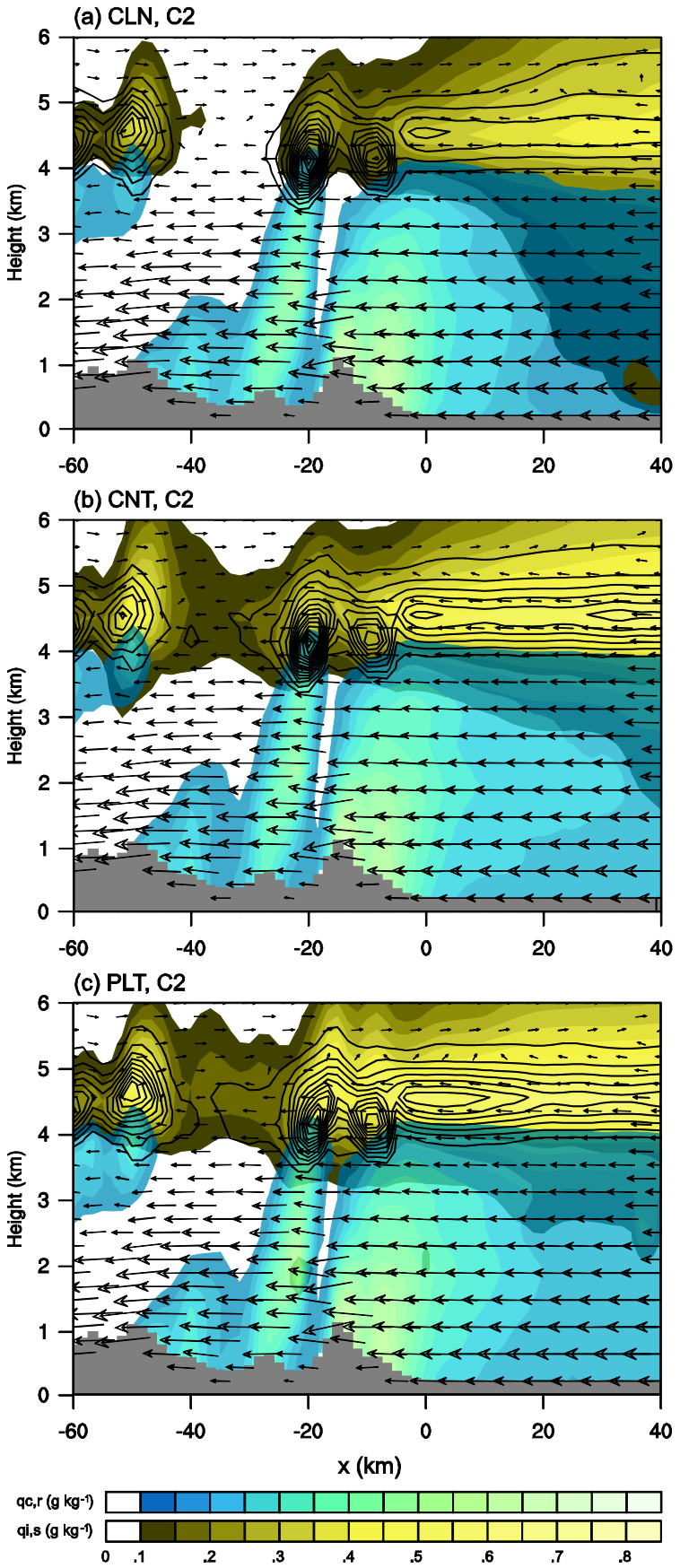
(a) CLN, C2
(b) CNT, C2
(c) PLT, C2
Height (km)
x (km)
qc,r (g kg-1)
qi,s (g kg-1)
0 .1 .2 .3 .4 .5 .6 .7 .8

Figure 9.8. Vertical cross sections through the line C2 of 15-h averaged liquid drop mixing ratio (bluish shaded), low-density ice particle mixing ratio (greenish shaded), and high-density ice particle mixing ratio (contoured) in (a) CLN, (b) CNT, and (c) PLT. The contour interval is 0.05 g kg^{-1}.

10 Summary and conclusions

The theoretical study in Chapter 2 is an extension of our previous study (Ganbat et al. 2015b) by including a basic-state wind and a mountain mechanical forcing to further examine the interactions between urban breezes and mountain slope winds. We showed how interactions between urban breezes and mountain slope winds vary diurnally and are different from a location another. Going further, we showed that the degree of interactions between urban breezes and mountain slope winds are sensitive to the mountain height and the basic-state wind speed and that the basic-state wind direction is an important factor which significantly affects these interactions. This study demonstrates the importance of linear mesoscale dynamics of local winds in city/mountain areas.

In this theoretical study, the buoyancy frequency, i.e., the basic-state stability, is assumed to be constant and a two-dimensional airflow system is adapted. Noticing the importance of basic-state stability in thermally and mechanically forced winds/flows and the typical geometries of cities, the time-varying basic-state stability and its extension to three dimensions need to be taken into account in future research. In this theoretical study, the Coriolis force is neglected. The effects of the Coriolis force on the interactions between urban breezes and mountain slope winds deserve an investigation. Although the linear dynamics can explain many aspects of the interactions between urban breezes and mountain slope winds, there may be other aspects of the interactions that cannot be explained by linear dynamics or in which nonlinear dynamics is important. A challenging

research topic would be to examine the nonlinear interactions between urban breezes and mountain slope winds using nonlinear theories or simple nonlinear dynamical models.

In Chapter 3, to examine the dynamics of urban breeze circulation (UBC) in a rotating system, particularly of the reversed UBC, we constructed a linearized, two-dimensional, hydrostatic, Boussinesq airflow system in a calm atmosphere with a specified thermal forcing which represents the diurnally varying urban heating. To represent the diurnal variation of UBC, the daily steady solution and the diurnally varying solution are linearly superposed.

It was confirmed that reversed UBC appears early in the morning. Similar to the frictional coefficient, the Coriolis parameter plays a role in damping the strength of UBC. The occurrence condition, strength, and vertical structure of the reversed UBC were examined. The Coriolis force as well as the urban heating alters the occurrence time of the reversed UBC. For a strong viscous system, the reversed UBC occurs only in high latitudes with low occurrence possibility. An analysis of the solutions for a simple oscillation-type model also shows that the Coriolis force alters the occurrence time and strength of the reversed UBC.

Observational evidence of reversed UBC has not been reported yet. The detection of the reversed UBC might not be as straightforward because various kinds of atmospheric flows/circulations interact nonlinearly depending on the geographical location and because real urban areas are very complex. Nevertheless, the detection of a reversed UBC early in the morning may be possible if synoptic and other mesoscale flows are very weak. In the presence of reversed UBC, the near-surface thermal structure and pollutant dispersion can be modified. Reversed UBC are expected to be observed.

In this study, we considered constant static stability to simplify the mathematical problem. In the real atmosphere, however, static stability varies diurnally and diurnally varying static stability can significantly affect the strength and the vertical structure of UBC. The dynamics of UBC or the reversed UBC with diurnally varying static stability deserves an investigation. In this study, we considered a two-dimensional dynamical frame. In three dimensions, the horizontal structure of urban heating can be represented by a circular or an elliptic shape, thus closely imitating the real urban heating. The extension to three dimensions in the study of the dynamics of UBC or the reversed UBC would be an interesting research topic.

In Chapter 4, we theoretically examined the linear dynamics of orographic-convective flows in a two-layer hydrostatic atmosphere. The two-dimensional, linear, steady-state, inviscid, nonrotating system that includes an orographic mechanical forcing and a convective diabatic forcing was solved to obtain the analytic solutions for the perturbation velocities. The analytic solutions are the superposition of the solutions forced by the orographic and convective forcings. We examined the resultant orographic-convective flows according to changes in basic-state wind, stratospheric static stability, and location of the convection relative to the mountain. The deep upward motion forced by the convective forcing located upslope of the mountain is positively combined with the orographic uplift. The convectively forced upward motion is deeper and causes a deeper updraft layer in the case with wind shear than in the case without wind shear. The stability jump between the troposphere and stratosphere acts to strengthen the resultant flows owing to the wave reflections at the tropopause. We calculated the ratio of the convectively forced vertical velocity to the orographically forced vertical velocity at the

cloud base over an upslope location of the mountain to further understand the linear interaction of orographically forced flows with convectively forced flows.

To understand the roles of wave reflection at the tropopause, the resultant wave strength and phase shift angle due to the infinite reflections of gravity waves at the tropopause were analyzed. The reflectivity R_0 converges to $(N_S - N_T)/(N_S + N_T)$ for large Ri, and increases with increasing N_S for a given Ri. The phase shift angle θ_0 is negative in the wide range of N_S and Ri. However, there are some conditions under which the phase is reversed in the opposite direction. The wave reflection at the tropopause strengthens the symmetric structure of the orographically forced internal gravity waves and the anti-symmetric structure of the convectively forced internal gravity waves in the troposphere.

The vertical fluxes of the horizontal momentum in the stratosphere were analytically obtained and calculated with different N_S and Ri. Since the momentum flux is a nonlinear variable, the total momentum fluxes contain a component related to the nonlinear interaction between convectively and orographically forced waves. Each momentum flux component is constructed by multiplication of the factors related to the nonlinearity parameter of each forcing, the horizontal structure of each forcing, the vertical structure of the atmosphere (basic-state wind speed and static stability), the bottom and top heights of the convective forcing, and the wave transmission through the tropopause. The nonlinear interaction component is the geometric average of the components forced by both forcings except that the factor related to the horizontal structure of the forcing is a function of the location of the convection relative to the mountain and the horizontal scales of both forcings. It was found that the nonlinear interaction component has an order of magnitude comparable to each of the

orographically and convectively forced components, which can increase or decrease the total momentum fluxes depending on the location of the convection relative to the mountain. The parameterizations of orographic and convective gravity wave drags have considered both wave components separately. In some situations, however, the interaction component between orographic and convective forcings cannot be negligible compared to the component forced by a sole forcing. The parameterization of the interaction generated gravity wave drag deserves for an in-depth investigation.

In this study, we considered orographic-convective flows in a hydrostatic system. In a nonhydrostatic system, orographically and convectively forced internal gravity waves propagate horizontally or slantwise as well as vertically. Some dynamics associated with nonhydrostatic effects on orographically forced flows has been theoretically examined (Wurtele et al. 1987; Keller 1994). Woo et al. (2013) described nonhydrostatic effects on convectively forced flows using a nonlinear dynamical model. In a future study, nonhydrostatic effects on orographically and convectively forced flows need to be examined.

In Chapter 5, we examined nonhydrostatic effects on convectively forced mesoscale flows and gravity-wave momentum flux by solving the equations governing small-amplitude perturbations in a linearized, two-dimensional, steady-state, nonrotating, and Boussinesq airflow system with prescribed convective forcing. The nonhydrostaticity factor β (= U/Na) appears in the nondimensionalized vertical momentum equation.

In an inviscid-limit system, the solutions are divided into the propagating mode for $k \leq k_c$ and the evanescent mode for $k > k_c$, where $k_c = \beta^{-1}$ is the critical horizontal wavenumber. For very small β, the flow is close to the hydrostatic flow. As β increases,

an alternating wavy pattern of updrafts and downdrafts appears downstream of the convective forcing and its horizontal wavelength is $2\pi\beta$. The alternating updrafts and downdrafts correspond to almost horizontally propagating gravity waves of the propagating mode with the horizontal wavenumber $k \sim k_c$. The momentum flux analysis indicates that the slantwise (almost horizontally) propagating gravity waves provide an additional momentum flux above the convective forcing and that its magnitude increases with increasing β and increasing convective-forcing depth.

In a viscid system, unlike in the inviscid-limit system, the solution cannot be explicitly separated into two modes. Each wave component has a vertically propagating part and a vertically decaying part simultaneously. In this study, the propagating mode and two evanescent modes are classified by comparing the vertical wavenumber M_R and the decay rate M_I. The k-range of the propagating mode becomes narrow as the viscous coefficient increases. As a result, the alternating updrafts and downdrafts downstream of the convective forcing are dissipated due to the viscous effect. For $\nu \geq \nu_c$, where $\nu_c = 1/(2\sqrt{2}\beta)$, the propagating mode is disappear. For large ν, the magnitude of the momentum flux above the convective forcing decreases as β increases because the momentum flux of the propagating mode easily dissipates in the case of larger β.

In this study, we considered an airflow system with uniform basic-state wind speed and static stability. To study the general characteristics of nonhydrostatic effects on convectively forced flows in a more realistic framework, the vertical variations of basic-state wind speed and static stability need to be included. In their study of mountain waves, Wurtele et al. (1987) and Keller (1994) showed that there are a number of nonhydrostatically forced resonant waves with various horizontal wavelengths in a

nonhydrostatic atmosphere with basic-state wind shear and a stability jump at the tropopause. Unlike the mountain forcing, which is a mechanical forcing at the surface, the convective forcing is a thermal forcing that can generate gravity waves in a range of altitudes where the forcing is located. Thus, the convectively forced flows in a nonhydrostatic non-uniform atmosphere can reveal some features different from topographically forced flows, which also deserves an investigation.

In Chapter 6, convectively forced internal gravity waves in a two-layer nonhydrostatic atmosphere are investigated. For this, an analytic solution for the perturbation vertical velocity forced by line-type diabatic forcing is obtained. The convectively forced perturbation vertical velocity fields are obtained using the Green function method. In the troposphere with constant basic-state wind shear, the wave components form modified Bessel functions of the purely imaginary order of μ and argument $\xi = Uk/s$. The wave components in the stratosphere are sinusoidal or exponential depending on the horizontal wave number compared to N_S/U_H.

Downstream of the diabatic forcing, resonant waves corresponding to the horizontal wavelength of the zeros of the denominator, which is the composition of the modified Bessel functions and the complex reflectivity, of the solution are nonhydrostatically generated. Without stability jump at the tropopause, the horizontal wavelengths of the resonant waves are the zeros of $K_{i\mu}(\xi_0)$. Relatively short waves are trapped at a certain height because the wave behavior changes from sinusoidal to exponential. Most of the resonant waves are in the range of the sinusoidal asymptotic of the modified Bessel function. Using that fact, the wavelengths of resonant waves in the case of Ri = 9, 36, and 144 are approximated.

Stability jump at the tropopause conditionally totally or partially reflects and transmits the resonant waves. Relatively short waves are totally trapped in the troposphere by the gravity-wave reflection and the window is broader in the case with stronger wind shear. The transmitted resonant waves vertically propagate in the stratosphere and transport wave energy. The characteristics and magnitude of the stratospheric momentum fluxes need to be further examined.

In Chapter 7, based on the numerical simulations using the WRF model, which includes the bin microphysics scheme, the effects of aerosol number concentration on orographic precipitation from shallow convective clouds and their sensitivity to windward mountain slope were examined. Forced uplift due to a bell-shaped mountain generates orographic precipitation. By changing the aerosol number concentration and the half-width of the mountain upslope, nine simulation cases are constructed.

Because of the potentially unstable low-level structure, the orographic uplift generates shallow cellular-structured convective orographic clouds. As the aerosol number concentration increases, the total and maximum surface precipitation amounts decrease and the maximum surface precipitation amount occurs far downstream. In the polluted case, a greater number of cloud droplets is generated, and the resultant average size of liquid drops is smaller. This small size distribution of cloud droplets inhibits the growth of cloud droplets into raindrops and suppresses surface precipitation. However, as the surface precipitation amount decreases on the upslope, more liquid drops are transported to the lee of the mountain. As a result, the surface precipitation amount on the downslope is larger than that on the upslope in the cases with higher aerosol number concentrations. Downdrafts associated with the mountain waves act to stimulate the

sedimentation of liquid drops and the evaporation of small-sized liquid drops. The advection rate of liquid drops over the mountain peak as a function of drop size exhibits a double-peak pattern, which is constructed by a large enough amount of grown raindrops from cloud droplets during the advection toward the mountain peak. This feature is more prominent in the clean case.

The advection timescale is one of the key parameters for determining the amount and distribution of precipitation. The narrow mountain upslope rapidly generates strong convections due to its steep upslope angle; however, the growth into raindrops is not completed over the upslope due to the short advection timescale. In these cases, strong and concentrated downslope precipitation occurs. Over the wide upslope, orographic convection produces precipitation over the long advection timescale. In these cases, a large amount of precipitation occurs and most of precipitable water is consumed over the upslope; these result in a smaller amount of downslope precipitation. The effects of aerosol number concentration, which are the decrease in the total surface precipitation amount and the downstream shift of the location of the maximum precipitation, are weak in the cases with the wide upslope because there is a long enough advection timescale to grow into raindrops from cloud droplets and to consume the precipitable water through upslope precipitation even in the polluted cases. Both in the cases with narrow and wide windward-widths, the double-peak structure of the size distribution of advection rate of liquid drops is not clear compared to the control cases due to having not enough advection timescales to form raindrops in the cases with narrow windward-width and the large amount of large-sized raindrop consumption by precipitation over the upslope in the cases with wide windward-width, respectively.

Many studies have reported the importance of ice processes in orographic precipitation. Although aerosol particles mainly reduce the orographic precipitation amount, melted ice particles in the mixed-phase orographic precipitation can enhance the precipitation amount. However, the precise microphysics under the complicated convective orographic precipitation from deep, mixed-phase clouds need to be examined using a bin microphysics model. The sensitivity of deep, mixed-phase convective orographic precipitation to mountain geometry, static stability, and basic wind speed deserves an investigation.

In Chapter 8, the sensitivity of aerosol effects on orographic precipitation from deep convective clouds to windward mountain slope is examined using the WRF model coupled with bin microphysics scheme. The aerosol number concentration and the windward-width of bell-shaped mountain are controlled to construct nine simulation cases.

In early stage, orographic precipitation near the mountain occurs mainly from lower-level clouds, and its dependency on the aerosol number concentration and upslope steepness is similar to that in the cases with warm shallow convective clouds which is discussed in chapter 7. As time goes on, lower-level convective clouds vigorously develop and an upper-level mixed-phase cloud extends upstream depending on the case, and strong interactions between lower- and upper-level clouds result in strong precipitation via melting or direct sedimentation of ice-phased particles if both conditions are satisfied.

In the cases with symmetric mountain, an increase in the aerosol number concentration results in stronger lower-level convection and stronger mixed-phase

processes (freezing, WBF process, and riming). As a result, total and maximum precipitation amounts are enhanced in the case with high aerosol number concentration. In the cases with a steep upslope and a gentle upslope, the trends are not monotonic. In CLNn, strong convection generated by a steep upslope and the fast growth of liquid drops and ice particles result in strong precipitation. In PLTn, even though the growth of liquid drops is slow, the large condensational latent heating also results in strong precipitation. In the middle of the two cases, the slower growth of liquid drops than CLNn and the weaker condensational latent heating than PLTn inhibit the interaction between lower- and upper-level clouds, and mixed-phase processes in CNTn result in weak precipitation. In CNTw, even though the gentle upslope generates a weak orographic uplift, the condensational latent heating provides additional energy. As a result, convection can develop through the freezing level, and the mixed-phase processes enhance the surface precipitation. In CLNw, the weak condensational latent heating and the lesser amount of cloud droplets by fast growth of liquid drops result in the inhibition of the interaction between lower- and upper-level clouds. In PLTw, the slow growth of liquid drops results in the inhibition of the interaction even though the condensational latent heating is strong.

In this study, the sounding of a stably stratified atmosphere with a large CAPE is used to simulate deep convective clouds in the presence of mountain waves. If CAPE is not large, downdrafts associated with mountain waves restrict the development of convection. In the present study, it is shown that the development of lower-level convection through the freezing level is one of the conditions to reach active interactions between lower- and upper-level clouds. For this reason, choosing soundings with different CAPEs can make totally different results from those in this study. Not only

considering different aerosol number concentrations and mountain geometries, but also considering different vertical soundings deserve further investigations.

In Chapter 9, a real orographic precipitation event over the Taebaek Mountains is numerically simulated using the WRF-bin model. To examine aerosol effects on orographic precipitation, three cases with different aerosol number concentrations are considered. Two different aerosol effects on orographic precipitation are observed and investigated.

Near Sokcho, orographic clouds are warm-phased. As discussed in Chapter 7, an increase in aerosol number concentration results in an increase of cloud droplet mixing ratio and a decrease of raindrop mixing ratio. However, the changes of the surface precipitation amount are not monotonic. Increases in raindrop mixing ratio in CLN and in the cloud droplet mixing ratio in PLT both result in enhanced surface precipitation. Near Mt. Kumgang, ice particles in the higher-level cloud play an important role in controlling the surface precipitation amount. In this region, the increase in aerosol number concentration results in an increased surface precipitation amount through the increase of ice-phased particle mixing ratio.

This study investigated orographic precipitation from warm and mixed-phased stratiform clouds in summer. As discussed in Chapter 7 and Chapter 8, orographic precipitation from convective orographic clouds has different characteristics compared to that from stratiform orographic clouds. A more detailed investigation of the sensitivity of aerosol effects on convective orographic precipitation in a real case is needed.

References

Alexander, M. J., and J. R. Holton, 2004: On the spectrum of vertically propagating gravity waves generated by a transient heat source. *Atmos. Chem. Phys.*, **4**, 923–932.

Alexander, M. J., J. H. Richter, and B. R. Sutherland, 2006: Generation and trapping of gravity waves from convection with comparison to parameterization. *J. Atmos. Sci.*, **63**, 2963–2977.

Andreae, M. O., D. Rosenfeld, P. Artaxo, A. A. Costa, G. P. Frank, K. M. Longo, and M. A. F. Silva-Dias, 2004: Smoking rain clouds over the Amazon. *Science*, **303**, 1337–1342.

Bae, S. Y., J. I. Jeong, R. J. Park, K.-S. S. Lim, S.-Y. Hong, 2016: Weekly variability of precipitation induced by anthropogenic aerosols: A case study in Korea in summer 2004. *Sci. Total Environ.*, **541**, 1531–1539.

Baik, J.-J., 1992: Response of a stably stratified atmosphere to low-level heating–an application to the heat island problem. *J. Appl. Meteor.*, **31**, 291–303.

Baik, J.-J., and H.-Y. Chun, 1997: A dynamical model for urban heat islands. *Bound.-Layer Meteor.*, **83**, 463□ 477.

Barlag, A.-B., and W. Kuttler, 1990/91: The significance of country breezes for urban planning. *Energy Bldg.*, **15–16**, 291–297.

Barros, A. P., 1994: Dynamics modeling of orographically induced precipitation. *Rev, Geophys.*, **32**, 265–284.

Beljaars, A. C. M., 1994: The parameterization of surface fluxes in large-scale models under free convection. *Quart. J. Roy. Meteor. Soc.*, **121**, 255–270.

Beres, J. H., 2004: Gravity wave generation by a three-dimensional thermal forcing. *J.*

Atmos. Sci., **61**, 1805–1815.

Beres, J. H., M. J. Alexander, and J. R. Holton, 2004: A method of specifying the gravity wave spectrum above convection based on latent heating properties and background wind. *J. Atmos. Sci.*, **61**, 324–337.

Beres, J. H., R. R. Garcia, B. A. Boville, and F. Sassi, 2005: Implementation of a gravity wave source spectrum parameterization dependent on the properties of convection in the Whole Atmosphere Community Climate Model (WACCM). *J. Geophys. Res.*, **110**, D10108.

Blyth, A. M., J. H. Lowenstein, Y. Huang, Z. Cui, S. Davies, and K. S. Carslaw, 2013: The production of warm rain in shallow maritime cumulus clouds. *Quart. J. Roy. Meteor. Soc.*, **139**, 20–31.

Bretherton, C., 1988: Group velocity and the linear response of stratified fluids to internal heat or mass sources. *J. Atmos. Sci.*, **45**, 81–93.

Bretherton, F. P., 1969: Momentum transport by gravity waves. *Quart. J. Roy. Meteor. Soc.*, **95**, 213–243.

Broutman, D., J. W. Rottman, and S. D. Eckermann, 2002: Maslov's method for stationary hydrostatic mountain waves. *Quart. J. Roy. Meteor. Soc.*, **128**, 1159–1171.

Broutman, D., J. W. Rottman, and S. D. Eckermann, 2003: A simplified Fourier method for nonhydrostatic mountain waves. *J. Atmos. Sci.*, **60**, 2686–2696.

Cannon, D. J., D. J. Kirshbaum, and S. L. Gray, 2012: Under what conditions does embedded convection enhance orographic precipitation? *Quart. J. Roy. Meteor. Soc.*, **138**, 391–406.

Cannon, D. J., D. J. Kirshbaum, and S. L. Gray, 2014: A mixed-phase bulk orographic

precipitation model with embedded convection. *Quart. J. Roy. Meteor. Soc.*, **140**, 1997–2012.

Chen, S.-H., and Y.-L. Lin, 2005: Orographic effects on a conditionally unstable flow over an idealized three-dimensional mesoscale mountain. *Meteor. Atmos. Phys.*, **88**, 1–21.

Chen, S.-H., Y.-L. Lin, and Z. Zhao, 2008: Effects of unsaturated moist Froude number and orographic aspect ratio on a conditionally unstable flow over a mesoscale mountain. *J. Meteor. Soc. Japan*, **86**, 353–367.

Cheng, C. T., W. C. Wang, and J. P. Chen, 2007: A modelling study of aerosol impacts on cloud microphysics and radiative properties. *Quart. J. Roy. Meteor. Soc.*, **133**, 283–297.

Choi, H.-J., and H.-Y. Chun, 2011: Momentum flux spectrum of convective gravity waves. Part I: An update of a parameterization using mesoscale simulations. *J. Atmos. Sci.*, **68**, 739–759.

Chu, C.-M., and Y.-L. Lin, 2000: Effects of orography on the generation and propagation of mesoscale convective systems in a two-dimensional conditionally unstable flow. *J. Atmos. Sci.*, **57**, 3817–3837.

Chun, H.-Y., 1995: Enhanced response of a stably stratified two-layer atmosphere to low-level heating. *J. Meteor. Soc. Japan*, **73**, 685–696.

Chun, H.-Y., and J.-J. Baik, 1994: Weakly nonlinear response of a stably stratified atmosphere to diabatic forcing in a uniform flow. *J. Atmos. Sci.*, **55**, 3109–3121.

Chun H.-Y., and J.-J. Baik, 1998: Momentum flux by thermally induced internal gravity waves and its approximation for large-scale models. *J. Atmos. Sci.*, **55**, 3299–3310.

Chun H.-Y., and J.-J. Baik, 2002: An updated parameterization of convectively forced gravity wave drag for use in large-scale models. *J. Atmos. Sci.*, **59**, 1006–1017.

Clanvner, M., W. R. Cotton, S. C. van den Heever, S. M. Saleeby, and J. R. Pierce, 2018: The response of a simulated mesoscale convective system to increased aerosol pollution: Part I: Precipitation intensity, distribution, and efficiency. *Atmos. Res.*, **199**, 193–208.

Clarke, J. F., 1969: Nocturnal urban boundary layer over Cincinnati, Ohio. *Mon. Wea. Rev.*, **97**, 582–589.

Colle, B. A., 2004: Sensitivity of orographic precipitation to changing ambient conditions and terrain geometries: An idealized modeling perspective. *J. Atmos. Sci.*, **61**, 588–606.

Creamean, J. M., A. P. Ault, A. B. White, P. J. Neiman, F. M. Ralph, P. Minnis, and K. A. Prather, 2015: Impact of interannual variations in sources of insoluble aerosol species on orographic precipitation over California's central Sirra Nevada. *Atmos. Chem. Phys.*, **15**, 6535–6548.

Dalu, G. A., and R. A. Pielke, 1989: An analytical study of the sea breeze. *J. Atmos. Sci.*, **46**, 1815–1825.

Dandou, A., M. Tombrou, and N. Soulakellis, 2009: The influence of the city of Athens on the evolution of the sea-breeze front. *Bound.-Layer Meteor.*, **131**, 35–51.

Davies, H. C., and C. Schár, 1986: Diabatic modification of airflow over a mesoscale orographic ridge: A model study of the coupled response. *Quart. J. Roy. Meteor. Soc.*, **112**, 711–730.

Draxler, R. R., 1986: Simulated and observed influence of the nocturnal urban heat island

on the local wind field. *J. Climatol. Appl. Meteor.*, **25**, 1125–1133.

Dudhia, J., 1989: Numerical study of convection observed during the Winter Monsoon Experiment using a mesoscale two-dimensional model. *J. Atmos. Sci.*, **46**, 3077–3107.

Dudhia, J., 1996: A multi-layer soil temperature model for MM5. Preprints, *The Sixth PSU/NCAR Mesoscale Model Users' Workshop*, Boulder, CO, National Center for Atmospheric Research, 49–50.

Dudis, J. J., 1972: The stability of saturated, stably-stratified shear layer. *J. Atmos. Sci.*, **29**, 774–778.

Dunster, T. M., 1990: Bessel functions of purely imaginary order, with an application to second-order linear differential equations having a large parameter. *SIAM J. Math. Anal.*, **21**, 995–1018.

Durran, D. R., 1992: Two-layer solutions to Long's equation for vertically propagating mountain waves: How good is linear theory? *Quart. J. Roy. Meteor. Soc.*, **118**, 415–432.

Durran, D. R., and J. B. Klemp, 1982: On the effects of moisture on the Brunt-Väisälä frequency. *J. Atmos. Sci.*, **39**, 2152–2158.

Dyer, A. J., and B. B. Hicks, 1970: Flux-gradient relationships in the constant flux layer. *Quart. J. Roy. Meteor. Soc.*, **96**, 715–721.

Eliassen, A., and E. Palm, 1960: On the transfer of energy in stationary mountain waves. *Geofys. Publ.*, **22**, 1–23.

Estoque, M. A., and C. M. Bhumralkar, 1969: Flow over a localized heat source. *Mon. Wea. Rev.*, **97**, 850–859.

Fan, J. W., L. R. Leung, Z. Q. Li, H. Morrison, H. B. Chen, Y. Q. Zhou, Y. Qian, and Y. Wang, 2012: Aerosol impacts on clouds and precipitation in eastern China: Results from bin and bulk microphysics. *J. Geophys. Res.*, **117**, D00K36.

Fan, J. W., Y. Wang, D. Rosenfeld, and X. Liu, 2016: Review of aerosol-cloud interactions: Mechanisms, significance, and challenges. *J. Atmos. Sci.*, **73**, 4221–4252.

Fernando, H. J. S., 2010: Fluid dynamics of urban atmospheres in complex terrain. *Annu. Rev. Fluid. Mech.*, **42**, 365–389

Freitas, E. D., C. M. Rozoff, W. R. Cotton, and P. L. Silva Dias, 2007: Interactions of an urban heat island and sea-breeze circulations during winter over the metropolitan area of Sao Paulo, Brazil. *Bound.-Layer Meteor.*, **122**, 43–65

Fritts, D. C., and M. J. Alexander, 2003: Gravity wave dynamics and effects in the middle atmosphere. *Rev. Geophys.*, **41**, 1003.

Ganbat, G., J.-J. Baik, and Y.-H. Ryu, 2015a: A numerical study of the interactions of urban breeze circulation with mountain slope winds. *Theor. Appl. Climatol.*, **120**, 123–135.

Ganbat, G., J. M. Seo, J.-Y. Han, and J.-J. Baik, 2015b: A theoretical study of the interactions of urban breeze circulation with mountain slope winds. *Theor. Appl. Climatol.*, **121**, 545–555.

Givati, A., and D. Rosenfeld, 2004: Quantifying precipitation suppression due to air pollution. *J. Appl. Meteor. Climatol.*, **43**, 1038–1056.

Grabowski, W. W., L.-P. Wang, and T. V. Prabha, 2015: Macroscopic impacts of cloud and precipitation processes on maritime shallow convection as simulated by a large

eddy simulation model with bin microphysics. *Atmos. Chem. Phys.*, **15**, 913–926.

Grimsdell, A. W., M. J. Alexander, P. T. May, and L. Hoffmann, 2010: Model study of waves generated by convection with direct validation via satellite. *J. Atmos. Sci.*, **67**, 1617–1631.

Guo, J. M., Deng, J. Fan, Z. Li, Q. Chen, P. Zhai, Z. Dai, and X. Li, 2014: Precipitation and air pollution at mountain and plain stations in northern China: Insights gained from observations and modeling. *J. Geophys. Res. Atmos.*, **119**, 4793–4807.

Haeger-Eugensson, M., and B. Holmer, 1999: Advection caused by the urban heat island circulation as a regulating factor on the nocturnal urban heat island. *Int. J. Climatol.*, **19**, 975–988.

Han, J.-Y., and J.-J. Baik, 2008: A theoretical and numerical study of urban heat island-induced circulation and convection. *J. Atmos. Sci.*, **65**, 1859–1877.

Han, J.-Y., and J.-J. Baik, 2009: Theoretical studies of convectively forced mesoscale flows in three dimensions. Part I: Uniform basic-state flow. *J. Atmos. Sci.*, **66**, 947–965.

Han, J.-Y., and J.-J. Baik, 2010: Theoretical studies of convectively forced mesoscale flows in three dimensions. Part II: Shear flow with a critical level. *J. Atmos. Sci.*, **67**, 694–712.

Han, J.-Y., and J.-J. Baik, 2012: Nonlinear effects on convectively forced two-dimensional mesoscale flows. *J. Atmos. Sci.*, **69**, 3391–3404

Hernandez-Duenas, G., L. M. Smith, and S. N. Stechmann, 2015: Stability and instability criteria for idealized precipitating hydrodynamics. *J. Atmos. Sci.*, **72**, 2379–2393.

Holton, J. R., 1982: The role of gravity wave induced drag and diffusion in the

momentum budget of the mesosphere. *J. Atmos. Sci.*, **39**, 791–799.

Hong, S.-Y., Y. Noh, J. and Dudhia, 2006: A new vertical diffusion package with an explicit treatment of entrainment processes. *Mon. Wea. Rev.*, **134**, 2318–2341.

Houze, R. A., Jr., 2012: Orographic effects on precipitating clouds. *Rev. Geophys.*, **50**, RG1001, doi:10.1029/2011RG000365.

Iwasaki, T., S. Yamada, and K. Tada, 1989: A parameterization scheme of orographic gravity wave drag with two different vertical partitionings. Part I: Impacts on medium-range forecasts. *J. Meteor. Soc. Japan*, **67**, 11–27.

Jiang, Q., 2003: Moist dynamics and orographic precipitation, *Tellus*, **55A**, 301–316.

Jiang, Q., and R. B. Smith, 2003: Cloud timescales and orographic precipitation. *J. Atmos. Sci.*, **60**, 1543–1559.

Jirak, I. L., and W. R. Cotton, 2006: Effect of air pollution on precipitation along the Front Range of the Rocky Mountains. *J. Appl. Meteor. Climatol.*, **45**, 236–245.

Jung, S.-H., E.-S. Im, and S.-O. Han, 2012: The effect of topography and sea surface temperature on heavy snowfall in the Yeongdong region: A case study with high resolution WRF simulation. *Asia-Pacific J. Atmos. Sci.*, **48**, 259–273.

Kain, J. S., 2004: The Kain-Fritsch convective parameterization: An update. *J. Appl. Meteor.*, **43**, 170–181.

Kang, M.-J., H.-Y. Chun, and Y.-H. Kim, 2017: Momentum flux of convective gravity waves derived from an off-line gravity wave parameterization. Part I: Spatiotemporal variations at source level. *J. Atmos. Sci.*, **74**, 3167–3189.

Keller, T. L., 1994: Implications of the hydrostatic assumption on atmospheric gravity waves. *J. Atmos. Sci.*, **51**, 1915–1929.

Khain, A. P., 2009: Notes on state-of-the-art investigations of aerosol effects on precipitation: A critical review. *Environ. Res. Lett.*, **4**, 015004.

Khain, A. P., A. Pokrovsky, M. Pinsky, A. Seifert, and V. Phillips, 2004: Simulation of effects of atmospheric aerosols on deep turbulent convective clouds using a spectral microphysics mixed-phase cumulus cloud model. Part I: model description and possible applications. *J. Atmos. Sci.,* **61**, 2963–2982.

Khain, A. P., D. Rosenfeld, and A. Pokrovsky, 2005: Aerosol impact on the dynamics and microphysics of deep convective clouds. *Quart. J. Roy. Meteor. Soc.*, **131**, 2639–2663.

Khain, A., D. Rosenfeld, A. Pokrovsky, U. Blahak, and A. Ryzhkov, 2011: The role of CCN in precipitation and hail in a mid-latitude storm as seen in simulations using a spectral (bin) microphysics model in a 2D dynamic frame. *Atmos. Res.*, **99**, 129–146.

Khain, A. P., and I. Sednev, 1996: Simulation of precipitation formation in the Eastern Mediterranean coastal zone using a spectral microphysics cloud ensemble model. *Atmos. Res.,* **43**, 77–110.

Khain, A. P., M. Ovtchinnikov, M. Pinsky, A. Pokrovsky, and H. Krugliak, 2000: Notes on the state-of-the-art numerical modeling of cloud microphysics. *Atmos. Res.*, **55**, 159–224.

Kim, C.-K., S. S. Yum, S.-N. Oh, J.-C. Nam, and K.-H. Chang, 2005: A feasibility study of winter orographic cloud seeding experiments in the Korean peninsula. *Asia-Pacific J. Atmos. Sci.*, **41**, 997–1014. (in Korean with English abstract)

Kim, Y.-J., S. D. Eckermann, and H.-Y. Chun, 2003: An overview of the past, present and future of gravity-wave drag parameterization for numerical climate and weather

prediction models. *Atmos.-Ocean*, **41**, 65–98.

Kirshbaum, D. J., and D. R. Durran, 2004: Factors governing cellular convection in orographic precipitation. *J. Atmos. Sci.*, **61**, 682–698.

Kirshbaum, D. J., and D. R. Durran, 2005: Atmospheric factors governing banded orographic convection. *J. Atmos. Sci.*, **62**, 3758–3774.

Kirshbaum, D. J., and R. B. Smith, 2008: Temperature and moist-stability effects on midlatitude orographic precipitation. *Quart. J. Roy. Meteor. Soc.*, **134**, 1183–1199.

Kirshbaum, D. J., and R. B. Smith, 2009: Orographic precipitation in the tropics: Large-eddy simulations and theory. *J. Atmos. Sci.*, **66**, 2559–2578.

Lalas, D. P., and F. Einaudi, 1974: On the correct use of the wet adiabatic lapse rate in the stability criteria of a saturated atmosphere. *J. Appl. Meteor.*, **13**, 318–324.

Lee, H., and J.-J. Baik, 2016: Effects of turbulence-induced collision enhancement on heavy precipitation: The 21 September 2010 case over the Korean Peninsula. *J. Geophys. Res. Atmos.*, **121**, 12319–12342.

Lee, H., J.-J. Baik, and J.-Y. Han, 2015: Effects of turbulence on warm clouds and precipitation with various aerosol concentrations. *Atmos. Res.*, **153**, 19–33.

Lee, J. G., 1999: Synoptic structure causing the difference in observed snowfall amount at Taegwallyong and Kangnung. *Asia-Pacific J. Atmos. Sci.*, **35**, 319–334. (in Korean with English abstract)

Lee, J. G., and M. Xue, 2013: A study on a snowband associated with a coastal front and cold-air damming event of 3-4 February 1998 along the eastern coast of the Korean peninsula. *Adv. Atmos. Sci.*, **30**, 263–279.

Lee, J. G., S.-D. Kim, and Y.-J. Kim, 2011: A trajectory study on the heavy snowfall

phenomenon in Yeongdong region of Korea. *Asia-Pacific J. Atmos. Sci.*, **47**, 45–62.

Lee, J. G., and Y. J. Kim, 2008: A numerical simulation study using WRF of a heavy snowfall event in the Yeongdong coastal area in relation to the north easterly. *Atmosphere*, **18**, 339–354. (in Korean with English abstract)

Lee, S.-H., and J.-J. Baik, 2010: Statistical and dynamical characteristics of the urban heat island intensity in Seoul. *Theor. Appl. Climatol.*, **100**, 227–237.

Lemonsu, A., and V. Masson, 2002: Simulation of a summer urban breeze over Paris. *Bound.-Layer Meteor.*, **104**, 463–490.

Li, Y., and J. Chao, 2016: An analytical solution for three-dimensional sea-land breeze. *J. Atmos. Sci.*, **73**, 41–54.

Lin, Y.-L., 1986: A study of the transient dynamics of orographic rain. *Pap. Meteor. Res.*, **9**, 20–44.

Lin, Y.-L., 1987: Two-dimensional response of a stably stratified shear flow to diabatic heating. *J. Atmos. Sci.*, **44**, 1375–1393.

Lin, Y.-L., 2007: *Mesoscale dynamics*. Cambridge University Press, New York, U.S.A., 646 pp.

Lin, Y.-L., and R. B. Smith, 1986: Transient dynamics of airflow near a local heat source. *J. Atmos. Sci.*, **43**, 40–49.

Lin, Y.-L., and S. Li, 1988: Three-dimensional response of a shear flow to elevated heating. *J. Atmos. Sci.*, **45**, 2987–3002.

Lindén, J., and B. Holmer, 2011: Thermally induced wind patterns in the Sahelian city of Ouagadougou, Burkina Faso. *Theor. Appl. Climatol.*, **105**, 229–241.

Linzen, R. S., 1981: Turbulence and stress due to gravity wave and tidal breakdown. *J.*

Geophys. Res., **86**, 9707–9714.

Lynn, B., A. P. Khain, D. Rosenfeld, and W. L. Woodly, 2007: Effects of aerosols on precipitation from orographic clouds. *J. Geophys. Res.*, **112**, D10225, doi: 10.1029/2006JD007537.

Lynn, B. H., A. Khan, J. Dudhia, D. Rosenfeld, A. Pokrovsky, and A. Seifert, 2005a: Spectral (bin) microphysics coupled with a mesoscale model (MM5). Part I: Model description and first results. *Mon. Wea. Rev.*, **133**, 44–58.

Lynn, B. H., A. Khan, J. Dudhia, D. Rosenfeld, A. Pokrovsky, and A. Seifert, 2005b: Spectral (bin) microphysics coupled with a mesoscale model (MM5). Part II: Simulation of a CaPE rain event with a squall line. *Mon. Wea. Rev.*, **133**, 59–71.

Markowski, P, and Y. Richardson, 2010: *Mesoscale meteorology in midlatitudes*, Wiley-Blackwell, Chichester, U.K., 407 pp.

Marsh, D. R., M. J. Mills, D. E. Kinnison, and J.-F. Lamarque, 2013: Climate change from 1850 to 2005 simulated in CESM1(WACCM). *J. Clmate*, **26**, 7372–7391.

McFarlane, N. A., 1987: The effect of orographically excited gravity wave drag on the general circulation of the lower stratosphere and troposphere. *J. Atmos. Sci.*, **44**, 1775–1800.

Miglietta, M. M., and R. Rotunno, 2009: Numerical simulations of conditionally unstable flows over a mountain ridge. *J. Atmos. Sci.*, **66**, 1865–1885.

Miller, J. C. P., 1950: On the choice of standard solutions for a homogeneous linear differential equation of the second order. *Quart. J. Mech. Appl. Math.*, **3**, 225–235.

Minder, J. R., R. B. Smith, and A. D. Nugent, 2013: The dynamics of ascent-forced orographic convection in the tropics: Results from Dominica. *J. Atmos. Sci.*, **70**,

4067–4088.

Mlawer, E. J., S. J. Taubman, P. D. Brown, M. J. Iacono, and S. A. Clough, 1997: Radiative transfer for inhomogeneous atmospheres: RRTM, a validated correlated-k model for the longwave. *J. Geophys. Res.*, **102**, 16663–16682.

Nugent, A. D., C. D. Watson, G. Thompson, and R. B. Smith, 2016: Aerosol impacts on thermally driven orographic convection. *J. Atmos. Sci.*, **73**, 3115–3132.

Oke, T. R., 1973: City size and the urban heat island. *Atmos. Environ.*, **7**, 769–779.

Olfe, D. B., and R. L. Lee, 1971: Linearized calculations of urban heat island convection effects. *J. Atmos. Sci.*, **28**, 1374–1388.

Oliveira, A., R. D. Bornstein, and J. Soares, 2003: Annual and diurnal wind patterns in the city of São Paulo. *Water, Air Soil Pollut.: Focus*, **3**, 3–15.

Orlanski, I., 1975: A rational subdivision of scales for atmospheric processes. *Bull. Amer. Meteor. Soc.*, **56**, 527–530.

Palmer, T. N., G. J. Shutts, and R. Swinbank, 1986: Alleviation of a systematic westerly bias in general circulation and numerical weather prediction models through an orographic gravity wave drags parameterization. *Quart. J. Roy. Meteor. Soc.*, **112**, 1001–1039.

Panosatti, D., S. Böing, L. Schlemmer, and J. Schmidli, 2016: Idealized large-eddy and convection-resolving simulations of moist convection over mountainous terrain. *J. Atmos. Sci.*, **73**, 4021–4041.

Pathirana, A., S. Herath, and T. Yamada, 2005: Simulating orographic rainfall with a limited-area, non-hydrostatic atmospheric model under idealized forcing. *Atmos. Chem. Phys.*, **5**, 215–226.

Paulson, C. A., 1970: The mathematical representation of wind speed and temperature profiles in the unstable atmospheric surface layer. *J. Appl. Meteor.*, **9**, 857–861.

Pierrehumbert, R. T., 1986: An essay on the parameterization of orographic gravity wave drag. *Proc. Seminar/Workshop on Observation, Theory, and Modeling of Orographic Effects*, Vol. 1, Reading, U.K., ECMWF, 251–282.

Queney, P., 1948: The problem of airflow over mountain: A summary of theoretical studies. *Bull. Am. Meteor. Soc.*, **29**, 16–26.

Roe, G. H., 2005: Orographic precipitation. *Annu. Rev. Earth. Planet. Sci.*, **33**, 645–671.

Roe, G. H., and M. B. Baker, 2006: Microphysical and geometrical controls on the pattern of orographic precipitation. *J. Atmos. Sci.*, **63**, 861–880.

Rosenfeld, D., 1999: TRMM observed first direct evidence of smoke from forest fires inhibiting rainfall. *Geophys. Res. Lett.*, **20**, 3105–3108.

Rosenfeld, D., 2000: Suppression of rain and snow by urban and industrial air pollution. *Science*, **287**, 1793–1796.

Rosenfeld, D., and A. Givati, 2006: Evidence of orographic precipitation suppression by air pollution-induced aerosols in the western United States. *J. Appl. Meteor. Climatol.*, **45**, 893–911.

Rosenfeld, D., J. Dai, X. Yu, Z. Yao, X. Xu, X. Yang, and C. Du, 2007: Inverse relationship between amounts of air pollution and orographic precipitation. *Science*, **315**, 1396–1398.

Rosenfeld, D., U. Lohmann, G. B. Raga, C. D. O'Dowd, M. Kulmala, S. Fuzzi, A. Reissell, and M. O. Andreae, 2008: Flood or draught: How do aerosols affect precipitation? *Science*, **321**, 1309–1313.

Rotunno, R., 1983: On the linear theory of the land and sea breeze. *J. Atmos. Sci.*, **40**, 1999–2009.

Ryu, Y.-H., and J.-J. Baik, 2013: Daytime local circulations and their interactions in the Seoul metropolitan area. *J. Appl. Meteor. Climatol.*, **52**, 784–801.

Ryu, Y.-H., J.-J. Baik, and J.-Y. Han, 2013a: Daytime urban breeze circulation and its interaction with convective cells. *Quart. J. Roy. Meteor. Soc.*, **139**, 401–413.

Ryu, Y.-H., J.-J. Baik, K.-H. Kwak, and N. Moon, 2013b: Impacts of urban land-surface forcing on ozone air quality in the Seoul metropolitan area. *Atmos. Chem. Phys.*, **13**, 2177–2194.

Savijärvi, H., and J. Liya, 2001: Local winds in a valley city. *Bound.-Layer Meteor.*, **100**, 301–319.

Seo, E.-K., and J.-G. Jhun, 1991: A case study of the heavy snowfalls occurred in the Korean peninsula from 29 January to 1 February 1990. *J. Korean Meteor. Soc.*, **27**, 165–179. (in Korean with English abstract)

Seo, K.-H., and D.-K. Lee, 1996: Analysis and simulation of orographic rain in the middle part of the Korean peninsula. *Asia-Pacific J. Atmos. Sci.*, **32**, 511–533. (in Korean with English abstract)

Sever, G., and Y.-L. Lin, 2017: Dynamical and physical processes associated with orographic precipitation in a conditionally unstable uniform flow: Variation in basic-state wind speed. *J. Atmos. Sci.*, **74**, 449–466.

Shreffler, J. H., 1978: Detection of centripetal heat-island circulations from tower data in St. Louis. *Bound.-Layer Meteor.*, **15**, 229–242.

Shreffler, J. H., 1979: Heat island convergence in St. Louise during calm periods. *J. Appl.*

Meteor., **18**, 1512–1520.

Simpson, J. E., 1994: *Sea breeze and local wind*. Cambridge University Press, Cambridge, U. K., 234 pp.

Skamarock, W. C., J. B. Klemp, J. Dudhia, D. O. Gill, D. M. Barker, M. G. Duda, X. Huang, W. Wang, and J. G. Powers, 2008: A description of the advanced research WRF version 3. NCAR Tech Note, NCAR/TN-475+STR, 8 pp., Natl. Cent. For Atmos. Res., Boulder, Colorado, U.S.A.

Smith, R. B., 1979: The influence of mountains on the atmosphere. *Adv. Geophys.*, Vol. 21, Academic Press, 87–230.

Smith, R. B., 1980: Linear theory of stratified hydrostatic flow past an isolated mountain. *Tellus*, **32**, 348–364.

Smith, R. B., and I. Barstad, 2004: A linear theory of orographic precipitation. *J. Atmos. Sci.*, **61**, 1377–1391.

Smith, R. B., J. R. Minder, A. D. Nugent, T. Storelvmo, and D. J. Kirshbaum, 2012: Orographic precipitation in the tropics: The Dominica experiment. *Bull. Amer. Meteor. Soc.*, **93**, 1567–1579.

Smith, R. B., and Y.-L. Lin, 1982: The addition of heat to a stratified airstream with application to the dynamics of orographic rain. *Quart. J. Roy. Meteor. Soc.*, **108**, 353–378.

Song, I.-S., and H.-Y. Chun, 2005: Momentum flux spectrum of convectively forced internal gravity waves and its application to gravity wave drag parameterization. Part I: Theory. *J. Atmos. Sci.*, **62**, 107–124.

Song, I.-S., and H.-Y. Chun, 2008: A Lagrangian spectral parameterization of gravity

wave drag induced by cumulus convection. *J. Atmos. Sci.*, **65**, 1204–1224.

Song, I.-S., H.-Y. Chun, R. R. Garcia, and B. A. Boville, 2007: Momentum flux spectrum of convectively forced internal gravity waves and its application to gravity wave drag parameterization. Part II: Impacts in a GCM (WACCM). *J. Atmos. Sci.*, **64**, 2286–2308.

Tao, W.-K., J.-P. Chen, Z. Li, C. Wang, and C. Zhang, 2012: Impact of aerosols on convective clouds and precipitation. *Rev. Geophys.*, **50**, RG2001.

Teixeira, M. C., A. Paci, and A. Belleudy, 2017: Drag produced by waves trapped at a density interface in non-hydrostatic flow over an axisymmetric hill. *J. Atmos. Sci.*, **74**, 1839–1857

Twomey, S., 1959: The nuclei of natural cloud formation part II: The supersaturation in natural clouds and the variation of cloud droplet concentration. *Pure. Appl. Geophys.*, **43**, 243–249.

Vosper, S. B., 2004: Inversion effects on mountain lee waves. *Quart. J. Roy. Meteor. Soc.*, **130**, 1723–1748.

Walters, D. N., and Coauthors, 2014: The Met Office Unified Model Global Atmosphere 4.0 and JULES Global Land 4.0 configurations. *Geosci. Model Dev.*, **7**, 361–386.

Wang, C.-C., and D. J. Kirshbaum, 2015: Thermally forced convection over a mountainous tropical island. *J. Atmos. Sci.*, **72**, 2484–2506.

Webb, E. K., 1970: Profile relationships: The log-linear range, and extension to strong stability. *Quart. J. Roy. Meteor. Soc.*, **96**, 67–90.

Weisman, M. L., and J. B. Klemp, 1982: The dependence of numerically simulated convective storms on vertical wind shear and buoyancy. *Mon. Wea. Rev.*, **110**, 504–520.

Woo, S., J.-J. Baik, H. Lee, J.-Y. Han, and J. M. Seo, 2013: Nonhydrostatic effects on convectively forced mesoscale flows. *J. Korean Meteor. Soc.*, **23**, 293–305.

Wurtele, M. G., R. D. Sharman, and T. L. Keller, 1987: Analysis and simulations of a troposphere-stratosphere gravity wave model. Part I. *J. Atmos. Sci.*, **44,** 3269–3281.

Wyszogrodzki, A. A., W. W. Grabowski, and L.-P. Wang, 2011: Activation of cloud droplets in bin-microphysics simulation of shallow convection. *Acta Geophys.*, **59**, 1168–1183.

Xiao, H., Y. Yin, L. Jin, Q. Chen, and J. Chen, 2014: Simulation of aerosol effects on orographic clouds and precipitation using WRF model with a detailed bin microphysics scheme. *Atmos. Sci. Lett.*, **15**, 134–139.

Xiao, H., Y. Yin, L. Jin, Q. Chen, and J. Chen, 2015: Simulation of the effects of aerosol on mixed-phase orographic clouds using the WRF model with a detailed bin microphysics scheme. *J. Geophys. Res. Atmos.*, **120**, 8345–8358.

Xie, X., X. Liu, Y. Peng, Y. Wang, Z. Yue, and X. Li, 2013: Numerical simulation of clouds and precipitation depending on different relationships between aerosol and cloud droplet spectral dispersion. *Tellus B*, **65**, 19054, doi:10.3402/tellusb.v65i0.19054.

Xue, H., and G. Feingold, 2006: Large-eddy simulations of trade wind cumuli: Investigation of aerosol indirect effects. *J. Atmos. Sci.*, **63**, 1605–1622.

Xue, L., A. Teller, R. Rasmussen, I. Geresdi, and Z. Pan, 2010: Effects of aerosol

solubility and regeneration on warm-phase orographic clouds and precipitation simulated by a detailed bin microphysical scheme. *J. Atmos. Sci.*, **67**, 3336–3354.

Yang, H.-Y., S. Chae, J.-Y. Jeong, S.-K. Seo, Y.-S. Park, and B.-J. Kim, 2015: A case study on the impact of ground-based glaciogenic seeding on winter orographic clouds at Daegwallyeong. *J. Korean Earth Sci. Sco.*, **36**, 301–314.

Yang, Y., J. Fan, L. R. Leung, C. Zhao, Z. Li, and D. Rosenfeld, 2016: Mechanisms contributing to suppressed precipitation in Mt. Hua of central China. Part I: Mountain valley circulation. *J. Atmos. Sci.*, **73**, 1351–1366.

Yoshikado, H., 1992: Numerical study of the daytime urban effect and its interaction with the sea breeze. *J. Appl. Meteor.*, **31**, 1146–1164.

Zhang, D.-L., and R. A. Anthes, 1982: A high-resolution model of the planetary boundary layer-sensitivity tests and comparisons with SESAME-79 data. *J. Appl. Meteor.*, **21**, 1594–1609.

초 록

세계적으로 많은 도시들이 산 근처에 위치하고 있다. 산악과 도시가 공존하는 지역에서는 열적 및 지형적으로 유도되는 국지풍이 형성되어 도시 대기로 방출되는 오염물질 수송에 영향을 미친다. 따라서 국지풍 예측을 향상시키고, 도시 환경 문제에 대처하기 위해 열과 산악이 유도하는 국지풍에 대한 깊은 이해가 필요하다. 이 연구에서는 배경류가 존재할 때의 도시풍 순환과 산곡풍 순환 사이의 상호작용을 안정하게 성층화된 대기의 열적-역학적 강제력에 대한 반응이라는 관점으로 이론적으로 연구하였다. 도시의 열적 강제력, 산악의 열적 강제력, 산악의 역학적 강제력이 유도하는 각 해석해의 선형결합을 통해 도시풍 순환과 산곡풍 순환 사이의 상호작용을 볼 수 있었다. 먼저 도시가 산악의 풍하측에 위치하는 경우를 고려하였다. 야간에는 산악의 냉각 및 역학적 강제력에 의해 유도되는 흐름이 도시풍 순환과 양의 상호작용을 통해 산악측 도시지역의 지표 근처 흐름을 강화한다. 주간에는 산악의 가열에 의해 유도되는 흐름이 도시풍 순환과 음의 상호작용을 통해 도시지역 지표 근처 흐름을 약화한다. 도시풍 순환과 산곡풍 순환 사이의 상호작용의 정도는 산악 고도 및 배경류 속도에 따라 달라짐을 보였다. 특히 배경류 속도의 변화는 열적-역학적으로 유도되는 흐름 (내부 중력파)의 강도뿐 아니라 연직 파장과 감쇄율에도 영향을 주었다. 도시가 산악의 풍상측에 위치하는 경우에 대한 분석을 통해 도시풍 순환과 산곡풍 순환 사이의 상호작용에 배경류의 풍향이 중요한 역할을 함을 보였다.

도시풍 순환 (urban breeze circulation; UBC)은 도시 중심을 향한 하층의 흐름, 도시 중심 근처의 상승류, 도시 바깥을 향하는 상층의 흐름, 도시 밖에서의 약한 하강류를 특징으로 하는 열적으로 유도된 중규모 흐름이다. 이전 수치 모형을 이용한 연구들은 이른 아침에 도시풍 순환의 방향이 역전될 수 있음을 보였다. 이 연구에서는 도시 가열의 일변화를 나타내는 열적 강제력에 대한 대기의 반응이라는 관점으로 역전된 도시풍 순환의 역학을 분석하였다. 이를 위해 열적

강제를 포함한 회전계에서 부시네스크 흐름을 만족하는 선형화된 2 차원의 정역학 부시네스크 방정식계를 푸리에 변환법을 이용해 풀었다. 이를 통해 이른 아침에 도시풍 순환의 역전이 일어남을 보였다. 코리올리 변수는 레일리 마찰 계수나 뉴톤 냉각 계수와 비슷한 역할을 하며 도시풍 순환의 강도 및 연직구조에 영향을 주었다. 도시풍 순환의 역전의 발생 조건, 강도, 연직구조를 조사하였다. 도시 가열과 더불어 전향력은 도시풍 순환의 역전 발생 시각을 조절하였다. 강한 마찰계에서는 도시풍 순환의 역전은 고위도에서만 일어나며 발생 가능성은 낮다. 수평 속도에 대한 간단한 진동 모형을 구성하여 역전된 도시풍 순환에 대한 역학적 이해를 도모하였다. 그 결과 또한 전향력이 도시풍 순환의 역전 발생 시각을 조절함을 보였다.

대류 가열이나 산악이 각각 유도하는 흐름에 대한 역학적 연구는 광범위하게 이루어졌으나, 대류 가열과 산악이 함께 유도하는 흐름에 대한 연구는 부족하다. 이 연구에서는 두 층의 성층화된 정역학과 비정역학 대기의 산악-대류 흐름, 중력파 반사 및 운동량 속에 대해 이론적으로 조사하였다. 상층(성층권)은 하층(대류권)보다 높은 정적 안정도를 가지며 배경류는 대류권에서 일정한 시어를 가지며 성층권에서 균일하다. 산악과 대류 강제력을 고려하는 2 차원, 정상상태, 비회전계의 저진폭 섭동 방정식의 해를 해석적으로 구하였다. 산악과 대류가 유도하는 흐름이 배경류 속도, 성층권 정적 안정도, 산악에 대한 대류의 상대적 위치의 변화에 어떻게 영향을 받는지 이해하기 위해 위 해석해를 분석하였다.

두 층의 정역학 대기에서 대류가 유도하는 깊은 상승류는 풍상측 산사면의 산악 강제상승과 양의 상호작용을 하여 상승류를 강화시켰다. 산악과 대류가 유도하는 흐름간의 선형적 상호작용을 더 깊이 이해하기 위해 풍상측 산사면 위 구름 바닥면 고도에서 산악이 유도하는 흐름의 연직속도에 대한 대류가 유도하는 흐름의 연직속도의 비율을 분석하였다. 대류권계면에서의 중력파 반사는 산악-대류 흐름을 조절하는데 중요한 역할을 하였다. 대류권계면에서의 중력파 반사는 산악(대류)가 유도하는 흐름의 대칭(반 대칭) 구조를 강화하는 역할을 하였다. 연직으로 전파되는 수평 운동량 속을 해석적으로 구하였는데, 총 운동량 속은 산악과 대류가 유도하는 파동의 비선형적 상호작용에서 비롯된 성분을 포함하였다.

이 비선형적 상호작용에서 비롯된 성분의 운동량 속은 산악과 대류가 각각 유도하는 파동에 의한 운동량 속과 비슷한 중요도를 가지며, 산악에 대한 대류의 상대적 위치에 영향을 받았다.

단일층 대기에서 대류가 유도하는 흐름에 미치는 비정역학 효과를 조사하기 위해 레일리 마찰과 뉴톤 냉각을 포함한 무차원화 된 지배 방정식계를 고려하였다. 무차원화 된 흐름계는 비정역학성 인자 β (= U/Na, 이 때 U 는 배경류 속도, a 는 대류 강제력의 반폭, N 은 배경 부력 진동수)를 포함한다. 비점성에 가까운 계에서 연직 속도의 해는 전파 모드($k \le \beta^{-1}$, 이 때 k 는 무차원화 된 수평 파수)와 감쇄 모드($k > \beta^{-1}$)로 분리된다. β 가 커지면 대류 강제력의 풍하측에 상승류와 하강류가 반복되는 파동형태가 나타나며 이 때 수평 파장은 임계 수평 파수 $k_c = \beta^{-1}$ 에 대응하는 $2\pi\beta$ 이다. 운동량 속 분석을 통해 상승류와 하강류가 반복되는 형태는 k 가 k_c 보다 조금 작고 전파 모드에 속하며 거의 수평으로 전파되는 중력파이며, 이 중력파는 대류 강제력 위의 운동량 속을 강화시킴을 밝혔다. 점성계에서 연직 속도의 해는 전파 및 감쇄 성분을 동시에 가져 두 모드로 엄밀하게 나눌 수 없다. 이 연구에서는 연직 파수와 감쇄율의 비교를 통해 전파 모드와 두 개의 감쇄 모드를 정의하였다. 점성 계수가 클 때 전파 모드에 해당하는 k 의 범위는 좁아지며 상승류와 하강류가 반복되는 형태는 소산된다. β 가 커지면 대류 강제력 위의 운동량 속을 강화시키는 전파 모드는 점성 계수가 작더라도 효과적으로 사라졌다.

두 층의 비정역학 대기에서 파동 성분은 순 허수를 차수로 갖는 변형 베셀 함수의 형태를 띤다. 성층권에서의 파동 성분은 수평 파수, 대류권 배경류 시어, 성층권 정적 안정도에 따라 정현 혹은 지수 함수 형태를 띤다. 대류 강제력의 풍하측에는 해의 분모가 0 이 되게 만드는 수평 파수에 해당하는 공명파가 비정역학적으로 생성된다. 성층권 안정도 급증이 없을 때 공명파의 수평 파수는 $K_{i\mu}(\xi_0)$의 영점이다. 상대적으로 짧은 파동은 형태가 정현 함수에서 지수 함수로 바뀌므로 어떤 고도에서 갇히게 된다. 대부분의 공명파의 수평 파장은 변형 베셀 함수의 정현 함수 점근 범위에 해당하는데, 이를 이용하여 Ri = 9, 36, 144 의 경우에 해당하는 공명파의 파장을 근사하였다. 성층권의 안정도 급증은 조건적으로 공명파를 전반사 혹은 부분반사 시켰다. 상대적으로 짧은 파장의 파동은 중력파 반사에 의해

대류권에 갇히며 중력파를 투과시키는 파장 영역은 배경류 시어가 클수록 넓었다. 투과된 공명파는 성층권에서 연직으로 전파하며 파동 에너지를 수송한다.

다양한 풍상측 산사면의 너비를 갖는 산악 위 얕거나 깊은 대류운에서 발생하는 지형성 강수에 미치는 에어로졸 효과를 상세 미세물리 방안을 포함한 Weather and Research Forecasting 모형를 이용하여 수치적으로 연구하였다. 잠재 불안정한 대기의 산악에 의한 강제 상승은 세포 형태의 지형성 대류운을 형성하였다.

얕고 온난한 구름의 경우, 높은 에어로졸 수농도는 많은 구름방울 형성을 야기한다. 그 결과, 구름방울의 빗방울로의 성장이 제한되고 총/최대 강수량이 감소하며 최대 강수량이 풍하측 먼 곳에서 나타났다. 또한 보다 강한 응결 잠열 방출이 강한 대류를 만들어 작은 크기의 물방울이 깊은 층에 걸쳐 분포하였다. 풍상측 산사면 너비가 좁으면 대칭 산악에 비해 급한 경사에 의해 더욱 강한 대류가 더욱 짧은 이류 시간 규모 동안 형성되어 강한 강수가 좁은 영역에 집중되었다. 이에 따라 총 강수량의 감소와 최대 강수량의 풍하측으로의 이동으로 특징되는 에어로졸 효과가 대칭 산악을 고려한 사례에 비해 뚜렷했다. 풍상측 산사면 너비가 넓으면 완만한 경사에 의해 약한 대류가 형성되나 충분히 긴 이류 시간 규모 동안 넓은 경사면 위에서 물방울의 상당량이 강수를 통해 소모되었다. 산악의 강수량과 최대 강수량의 위치는 산사면 경사가 보다 급한 경우 에어로졸 수농도에 보다 민감하였다.

깊고 혼합상의 구름의 경우, 발생 초기의 지형성 강수는 주로 하층 구름에 의해 발생되며, 에어로졸 수농도와 풍상측 산사면 경사가 지형성 강수에 미치는 영향은 얕고 온난한 구름의 경우와 비슷하였다. 이후 몇몇 사례에서 하층 구름이 깊게 발달하고 상층 구름이 풍상측으로 확장되었으며, 두 조건이 만족되었을 때 상하층 구름의 상호작용은 얼음상 알갱이가 녹거나 직접 떨어져 강한 강수를 야기했다. 대칭 산악을 고려한 경우 상호작용 중의 혼합상 과정(결빙, WBF 과정, 결착)은 에어로졸 수농도가 높을수록 강하게 나타나 강수량 증가로 이어졌다. 비대칭 산악을 고려한 경우 이 경향은 일관되지 않았다. 풍상측 산사면이 급한 경우, 청정 사례보다 느린 물방울 성장과 오염 사례에 비해 약한 응결 잠열 방출이 상하층 구름의 상호작용과 혼합상 과정을 제한하여 통제 사례에서의 지표 강수량이 가장

적었다. 반면 풍상측 산사면이 완만한 경우에는 청정 사례에 비해 강한 응결 잠열 방출과 오염 사례에 비해 빠른 물방울 성장이 상하층 구름의 상호작용을 강화시켜 통제 사례에서의 지표 강수량이 가장 많았다.

실제 지형성 강수에 에어로졸이 미치는 영향을 분석하기 위해 세 가지의 에어로졸 수농도를 고려하여 2015 년 6 월 26 일부터 27 일까지 태백산맥에서 발생한 지형성 강수를 수치 모의하였다. 속초 부근에서 발생한 산악 구름은 온난 구름이었으며 이 지역에서 에어로졸 수농도의 증가는 구름방울 혼합비의 증가 및 빗방울 혼합비의 감소를 야기했다. 하지만 지표 강수량의 변화는 일관되지 않았다. 청정 사례에서의 빗방울 혼합비 증가와 오염 사례에서의 구름방울 혼합비 증가 모두 지표 강수량을 증가시켰다. 금강산 부근에서는 상층의 구름이 지표 강수량을 조절하는데 중요한 역할을 하였다. 이 지역에서 에어로졸 수농도의 증가는 얼음상 알갱이 수농도를 증가시킴으로써 지표 강수량 증가를 야기했다.

주요어: 안정하게 성층화된 대기, 도시풍 순환, 산악-대류 흐름, 중력파의 운동량 속, 에어로졸-구름-강수 상호작용, 지형성 강수

학 번: 2009-20371